Doctoral Dissertation

Application of Underdetermined Linear Systems to DOA Estimation and Near Field Source Reconstruction

(劣決定線形システムの方向推定と近傍電磁界再構成への応用)

Graduate School of Engineering
Yokohama National University

Thomas Basikolo

July 2018

Yokohama National University
Doctoral Dissertation

APPLICATION OF UNDERDETERMINED LINEAR SYSTEMS TO DOA ESTIMATION AND NEAR FIELD SOURCE RECONSTRUCTION

A Thesis in
Department of Electrical and Computer Engineering
by
Thomas Basikolo

Submitted in Partial Fulfillment
of the Requirements
for the Degree of

Doctor of Engineering

July, 2018

The thesis of Thomas Basikolo was reviewed and approved* by the following:

Hiroyuki Arai
Professor
Thesis Advisor, Chair of Committee

Koichi Ichige
Associate Professor
Co–Supervisor, Review Committee Member

Takehiko Adachi
Professor
Review Committee Member

Toshihiko Baba
Professor
Review Committee Member

Nobuhiro Kuga
Associate Professor
Review Committee Member

*Signatures are on file in the Graduate School.

Don't be afraid, for I am with you.
Don't be discouraged for I am your God.
I will strengthen you and help you.
I will hold you up with my victorious right hand.
Isaiah 41:10.

Abstract

Wireless communication technology is an indispensable technology in this era. It continues to play an important role in our daily activities. New systems are constantly being introduced to live up to substantial amount and variety of applications and desires for new services. The need for technological support to be used for standard tasks has advanced to a level where a strong dependency on high–performance machines is a reality. Mathematics is the foundation of wireless communication systems. It is the path–breaker in the development of state of the art transmission procedures as well as an important instrument in planning and optimization of wireless systems.

In the 5G and Internet of things era, high speeds and efficient systems are desired. Currently, we are experiencing a boom in the number of connected devices. In order to achieve high performance wireless systems, better hardware systems deployed together with robust signal processing algorithms proves to be the best candidate/choice.

With the increasing amount of connected devices, antennas are beginning to be installed in every electronic device. An antenna is very significant part of the wireless communication system. In the future, it is expected that all devices will perform wireless communication. This will therefore lead to the development of a large quantity of antennas. It is easy to imagine that the usage environment of the device will further be versatile according to this social transformation. Simple techniques in terms of reducing the amount of time required for evaluating the performance of an antenna or wireless communication system by speeding up the measurement process are certainly required. On top of that, it is also significant to estimate the system's performance characteristics assuming various environmental conditions.

On the algorithm side, mathematical models plays a huge role since they are the backbone of wireless communication system's algorithms. The basic role played by mathematics (matrices as an example) is indisputable especially when they are applied to modeling and optimization of wireless systems. As the number of users as well as

demand for wireless services increases exponentially, the need for extensive coverage area and higher transmission quality rises. Smart–antenna systems therefore, present a solution to this problem. In this dissertation, we develop mathematical models that achieves improved system performance. These models for wireless communications systems are specifically applied to the problems of underdetermined direction of arrival (DOA) estimation for smart antenna systems and near field to far field reconstruction. The two problems addressed in this dissertation utilizes underdetermined linear systems which is an application area of Matrix Theory.

In Chapter 2, theoretic aspects of the application of underdetermined linear systems to smart antennas is discussed. From current methods applied to DOA estimation problem, we explore the limitations of the current DOA estimation methods. Furthermore, we briefly explore the methods in the reconstruction problem for near field to far field transformation. A reconstruction method of the wave source distribution from measured electromagnetic field by inverse problem is used. Thus, Chapter 2 introduces the numerical methods explored in this dissertation.

In Chapter 3, to improve DOA algorithm's performance as well as achieve improved DOA estimation characteristics, a nested sparse circular array is proposed. This is a circularly configured array, which has the characteristics of conventional circular arrays. Virtual sensors in concentric extension of the proposed array are utilized which achieves increased degrees of freedom. Furthermore, mathematical models are developed to explore the increased degrees of freedom such that the array is capable of underdetermined DOA estimation. By using the method developed in Chapter 3, we are capable of estimating mores sources (impinging signals) arriving at the array with fewer sensors (antenna elements).

In DOA estimation problems, an ideal array model is assumed. In real use case scenario for antenna arrays, mutual coupling affect the system performance in DOA estimation. In Chapter 4, we consider the problem of mutual coupling compensation in which a mutual coupling compensation method is proposed for nested sparse circular array discussed in Chapter 3. The mutual coupling compensation method attains an improved DOA estimation performance, better RMSE, and lower average run–time as compared to cases where conventional mutual coupling compensation methods are employed.

In Chapters 3 and 4, the assumption is that we are employing narrowband signal sources. This is not the case for all systems, since in some cases, wideband signals are used. In Chapter 5, we discuss the case in which wideband signals are employed. The mathematical models proposed in Chapters 3 and 4 are extended to cases where the signal sources are wideband. The underdetermined DOA estimation performance is verified in this chapter in which more sources are estimated as compared to the number of sensors.

Chapter 6 discusses a mathematical model that is applied to antenna measurement problem. For a very large antenna system, it is very difficult to conduct conventional far field measurements in an anechoic chamber. Thus, near field measurement provides a leeway in which the far field can be calculated from the measured near field data without the need of a very large anechoic chamber by utilizing near field to far field transformation techniques. Therefore, we discuss a hemispherical near field measurement technique in this chapter. In the far field reconstruction procedure, the effect of real ground (earth) is considered.

In Chapter 7, the discussion from chapter 6 is extended to the case in which a vehicular mounted antenna is considered. In this case, the whole body of the vehicle affect the performance of the antenna. Thus, we do not consider the antenna only, but we consider the whole system as device under test. An antenna's performance in the system provides an insight in terms of how we can improve the antenna performance. The near field is measured hemispherically and far field is reconstructed which includes the effect of real ground. In this chapter, we first consider a simple system and evaluate the performance of the technique. This is further applied to a real car model.

Table of Contents

Chapter 1

Introduction 1

List of Figures

Chapter 1

Introduction

1.1 Background

Wireless communications has become an essential part of life to most people. It is playing an ever increasing role in the consumer market [1], [2]. Currently, we have devices that interconnect automatically and devices that enable communication from distance wirelessly. Wireless communication therefore is defined as the transfer of information or power across two or more points not connected by an electrical conductor [3], [4]. In this technology, electromagnetic waves are used by a network or a terminal such as radio frequency (RF), infrared, laser, visible light and acoustic energy as a substitute of wire conductors for telecommunications [5].

In wireless communications, radio waves are the most commonly used [3]. In the electromagnetic spectrum, the radio wave frequency ranges from 20 kHz to 300 GHz [6], [7]. With radio waves, distances (range) can be short; a few meters in the case of bluetooth and television remote control or the distance can be very large; millions of kilometers for deep–space radio communications [3]. Various applications of radio wireless technology continues to emerge. In the last decade, we have experienced a boom in the Internet of Things (IoT) sensors, driverless vehicles etc. By the year 2020, the 5G network will support 50 billion connected devices as well as 212 billion connected sensors and it will permit access to 44 zettabytes (ZB) of data [8], [9], [10]. These connected devices will range from smart–phones and tablets to smart watches, cars, machinery, appliances, and remote monitoring devices [9], [11]. As shown in Fig. 1.1, almost everything will be connected to the internet wirelessly [12]. Currently, connected devices are generating massive amounts of data. This has led to a data driven society where wireless technologies are employed to transmit data, which supports people's daily life. Since high–speed communication is significant, we have also experienced the advent of 5G technologies in which billions of smart sensors are connected at high–speed data rates of up to 10Gbps.

Although wireless communication technology has different applications, mobile communication has a great economic consequence in today's world. Since the introduction of GSM in the early 1990s which is still the dominant mobile communications standard, mobile communications has had an enormous impact on our social life [13]. The importance of mobile communications continues to grow with new fields of application. The telecommunications industry has become broader as compared to as it was in the past [14]. Now, it encompasses several service providers which includes; telephone companies, wireless carriers, internet service providers (ISPs), cable system operators, and satellite operators [14], [15]. As the telecommunications field evolve, the industry today includes software–based applications having a communications emphasis as well as intermediate layers of software incorporated into end–to–end communication services. The industry further includes suppliers of telecommunications equipment and software products sold directly to consumers and service providers [14].

New systems of mobile communication are being introduced regularly to live up to the great variety of applications and desires for new services. This advancement would have been impossible without the digitalization of mobile communication in which mathematics performed an indispensable role [13]. Mathematics is the foundation of information

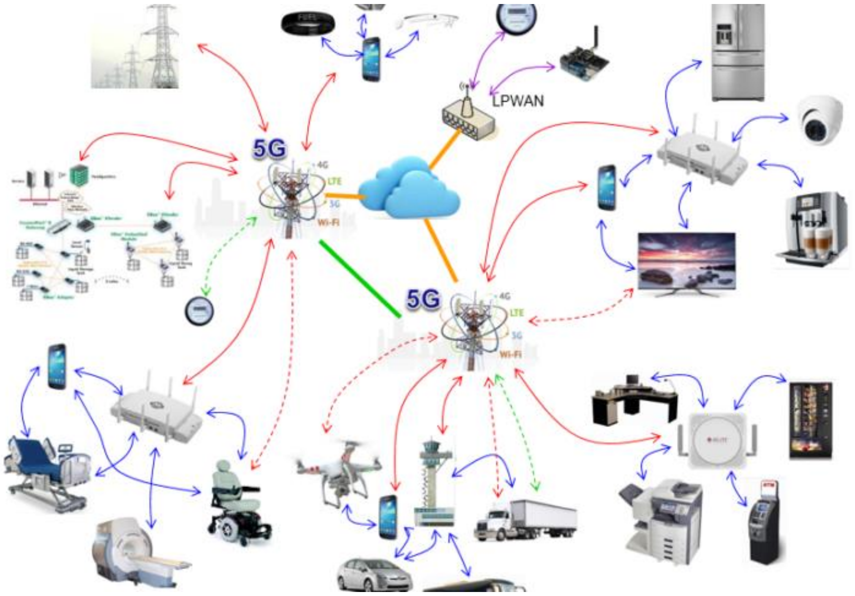

Figure 1.1: Basic idea in IoT in which everything is connected by Internet [12].

and communication theory. It is the path–breaker in the advancement of new transmission procedures as well as an essential instrument in planning and optimization of mobile networks. Some application examples of mathematics in wireless communication technology field include; probability theory and discrete mathematics applied to information theory, and linear algebra, convex optimization and game theory used in the advancement of new transmission methods [13]. Thus, mathematical models are very important in wireless communication systems.

In order to transmit or receive a radio signal, an antenna must be used. An antenna is therefore an essential part of the wireless communication system. The subject of smart antennas is currently enjoying enormous popularity due to the current exponential growth in all forms of wireless communications and sensing [16]. Smart antenna is a name given to antenna systems which are also called adaptive array antennas, digital antenna arrays, and recently, MIMO. Smart antennas are antenna arrays that includes smart signal processing algorithms that is used to identify spatial signal signatures for example direction of arrival (DOA) of the signal, and use them to determine beamforming vectors which are used to track and locate the antenna beam on the mobile/target [17].

The term “smart antenna” generally refers to any antenna array, terminated with a sophisticated signal processor, is capable of adjusting or adapting its own beam pattern in order to emphasize signals of interest and to minimize interfering signals [18]. Smart antennas typically encompass both switched beam and beamformed adaptive systems [19], [20].

The rapid growth of smart antennas has been facilitated by advancing digital signal processing hardware and also by the global interest in wideband wireless applications [16], [21]. Many engineers in the wireless communications field are anticipating to utilize smart antennas to boost capacities, increase signal–to–interference ratios, expand bandwidths, mitigate fading, and on top of that, improve MIMO communications. Smart antennas are also important for defense application because they enable secure communications [22]. On top of that, they can also be used in direction finding, waveform diversity applications, MIMO radar, and multi–mission operations [16].

In smart antennas, two of the main types includes; switched beam smart antennas and adaptive array smart antennas. In the case of switched beam systems, they have several fixed beam patterns available. Thus, a decision is made as to which beam to access at any given point in time which is based on system’s requirements [17], [20], [23]. On the other hand, adaptive arrays allow an antenna array to steer the beam to any direction of interest while simultaneously nulling interfering signals [19]. Beam direction can therefore be estimated using direction–of–arrival (DOA) estimation methods [24], [25]. In engineering applications, in which an incoming wave is detected and/or measured by an array, associated signals at distinct position in space can be processed to extract different types of information including their direction of arrival. In wireless communications, algorithms for estimating DOAs in antenna arrays are often used to increase the capacity and throughput of the wireless network [26].

1.2 Brief Overview of DOA Estimation Methods

Over the last few decades, wireless technology has grown at an alarming rate in which new, as well as improved services have been created at lower costs [27]. This has resulted in an increase in airtime usage and the number of subscribers. As the number of users and the demand for wireless services increases at an exponential rate, the need for wider coverage area and higher transmission quality rises [27]. Smart–antenna systems provide a solution to this problem. Smart antennas leverage the diversity effect at the source and destination. This helps the wireless system to increase data speed as well as reduce the error rate.

1.2.1 Methods for DOA Estimation

DOA estimation techniques using sensor arrays or direction finding has been an important subject in array signal processing [28]. The desired DOA algorithms are the ones that realizes high spatial resolution and low computational complexity. There are different methods to estimate DOA and are divided into three basic categories, classical or conventional methods, subspace–based, and maximum likelihood (ML).

1.2.2 Basic Categories of DOA Estimation

Classical or conventional DOA methods are essentially based on the concepts or theory of beamforming and null steering which requires large number of array elements to provide high resolution. Classical techniques for DOA are the Delay and Sum [29], Bartlett, and the Capon (Minimum Variance Distortionless Response (MVDR)) [30] methods. In classical methods, the idea behind is to scan a beam through space and measure the power received from each direction. From this, the directions from which the largest amount of power is received are taken to be the DOAs [28]. These methods are extremely dependent upon physical size of array aperture, which results in poor resolution and accuracy [27]. Subspace–based algorithms also referred to as high–resolution techniques; offer a good tradeoff between resolution and computational complexity. As opposed to conventional methods, subspace methods exploit the information of the received data resulting in high resolution [28]. Subspace based DOA estimation methods are generally based on the eigen–decomposition [31]. The subspace methods include MUSIC and its variants, Estimation of Signal Parameters via Rotational Invariance Technique (ESPRIT) [32] and the Minimum Norm (Min–Norm) methods. These algorithms deliver information about number of incident signals and DOA of each signal. From the methods discussed, subspace based DOA estimation algorithms such as MUSIC and ESPRIT provide high resolution, more accurate and are not limited to physical size of array aperture.

1.3 Overview of Near Field Techniques

In every wireless communication system, the actual transmission of the waves in free space is carried out by an antenna system [33]. For specific purpose, an antenna system has to stick to particular specifications. Because of different specific purpose an antenna system is used for, different types of antennas are required. In order to characterize the antenna or an antenna system, there is need for antenna measurement. In the field of telecommunications, antenna measurement techniques is defined as the testing of antennas (or antenna systems) to ensure that the antenna or the system meets specifications or simply to characterize it [33], [34]. Typical parameters of antennas that are of particular interest to engineers are gain, beamwidth, radiation pattern, polarization, and impedance [35]. Antenna gain and pattern are measured in the far field. For larger antennas, far field measurements are very difficult to implement and therefore compact measurements or near field measurements comes into play. The near field methods allows one to overcome the weaknesses which, for electrically large radiating systems, make unpractical the measurement of the antenna pattern in a conventional far field range and represent the better choice when complete pattern and polarization measurements are required [36].

In most cases, it is impractical or impossible to make antenna pattern measurements on a conventional far–field range. This may be due to distance to the radiating far field being too long. It may also be impractical to move an antenna from its operating environment to an antenna range, or the desired amount of pattern data may require too much time on a far–field range [37]. For these and other reasons, it is appropriate to determine the far field antenna pattern from measurements made in the radiating near field region. In Fig. 1.2, the different field regions of an antenna are shown.

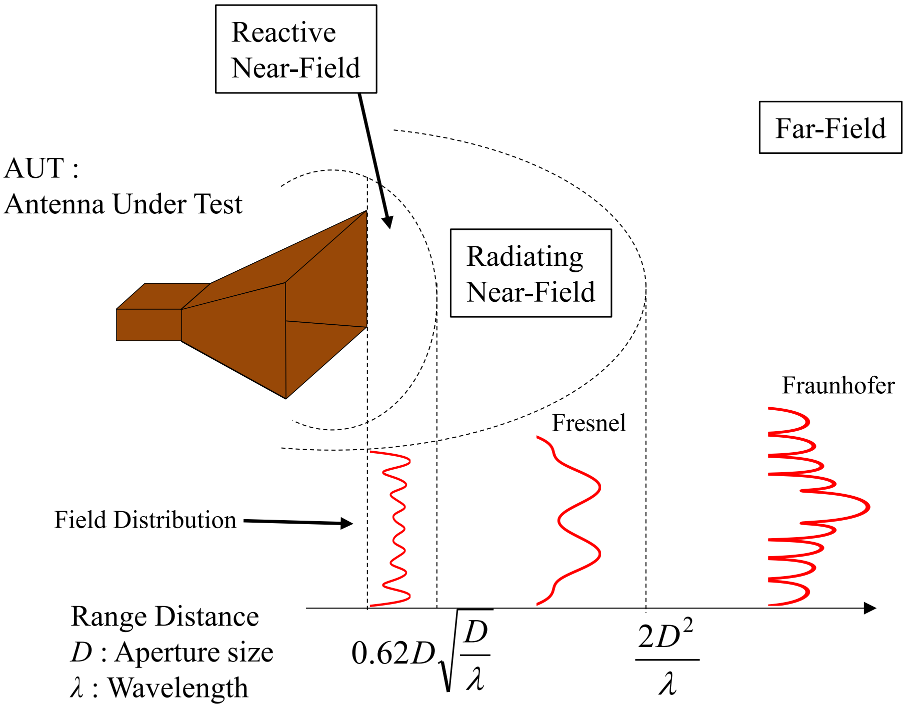

Figure 1.2: Antenna field regions and amplitude pattern shape for different regions.

In near field measurements, one of the several advantages of this method is the reduction in measurement distance. The dimensions of a conventional test range can be reduced by making measurements in the near field. From the measured near field, analytical methods can then be used to transform the measured near field data to compute the far field radiation characteristics [37], [38], [39]. This process or method is what is referred to as near field to far field (NFFF) transformation. Such techniques are frequently used to measure patterns, and often carried out indoors [27]. Therefore, these techniques provide a controlled environment and an all–weather capability, the measurement system is time and cost effective, and the computed patterns are as accurate as those measured in a far field range.

In near field measurements, the near field region of the antenna to be measured is defined by the electrical size determined by the physical size of the antenna under test (AUT) and the measurement frequency. If the aperture diameter of the AUT is D and the wavelength of the measurement frequency is λ. The region where the measurement distance L from the AUT is $L > 2D^2/\lambda$ is defined as a far field and the region of $L \leq 2D^2/\lambda$ is defined as a near–field [40]. In near field measurements, electromagnetic field is measured in the near field region, and characterizing the AUT performance based on the measured information [38]. Near field measurements are mostly performed in an anechoic chamber. This is because the output characteristics are obtained by numerical processing based on the electromagnetic field acquired in a small scale measurement area [40], [41]. The measurement operator does not need to secure an extensive measurement space, and does not have to worry about disturbances by weather and interference waves [27], [41]. Thus, near field measurements for antenna systems have various advantages.

In near field measurements, the electromagnetic field is measured or acquired by moving a measurement probe against the AUT. There are several types of scanning methods using a probe as shown in Fig. 1.3. These methods are largely classified into planar, cylindrical, and spherical near field measurement, largely depending on the scanning method [36], [42], [43].

1.4 Limitations of Current Methods

Wireless technology is beyond shadow of a doubt an appropriate technology for many applications. At the present time, although many people have access to wireless communication technology, it should not be regarded as an all round solution for every networking environment, despite enjoying massive development and advances in recent

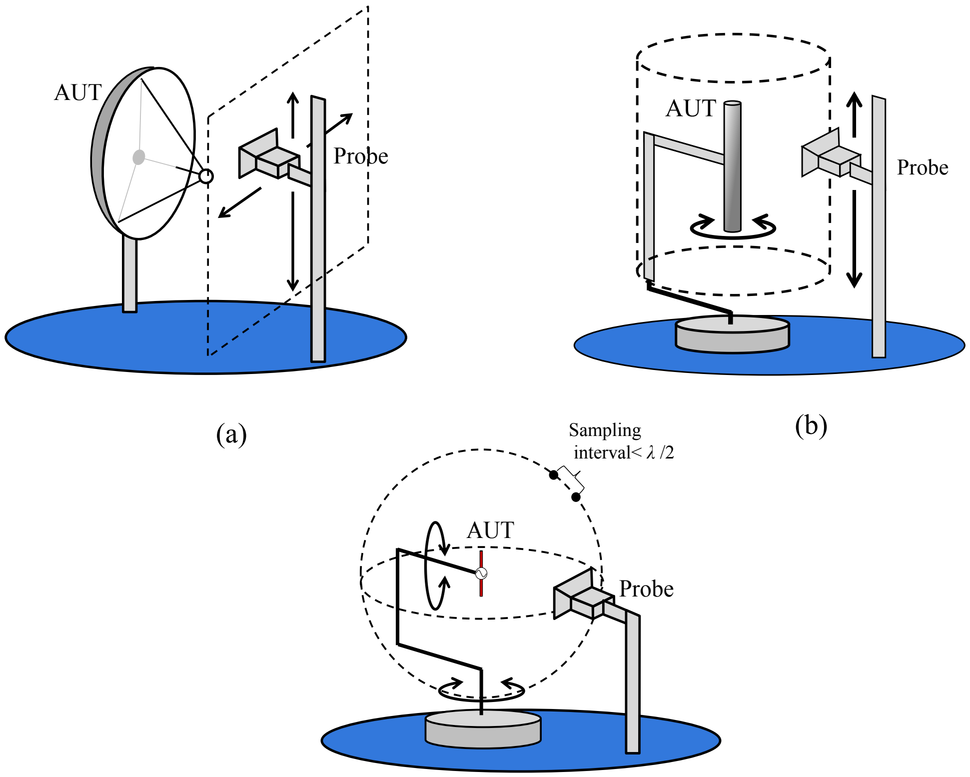

(a) (b) (c)

Figure 1.3: Near field measurement methods (a) Planar scanning, (b) Cylindrical scanning, and (c) Spherical scanning.

years. In various application areas in which mobility is not critical, a hard–wired connection might provide a faster, more reliable as well as more cost–effective solution. In specific scenarios, DOA estimation for example, the size of the array depends on the number of signals to be estimated. Considering MUSIC algorithm for DOA estimation as an example, conventionally, an array with M elements, will be able to resolve $D \leq M - 1$ impinging signals. This implies that for a very large number of sources, the array will be larger which is very costly (in financial and computation sense) as well as complex signal processing techniques are required. Thus, new system is required that is capable of performing underdetermined DOA estimation with better accuracy. Utilizing advanced mathematical techniques, we can be able to resolve this kind of problem.

In another scenario, we consider antenna measurement problem. In antenna measurements, in order to measure the far field of a vehicular mounted antenna or a very large antenna system (electrically large radiating systems), a very large anechoic chamber is required which in most cases is not practical. Thus, near field measurement techniques are utilized for very electrically large antenna systems. Spherical near field measurement technique is the most accurate as well as complex technique. The measurement is usually done in an anechoic chamber in which real use case scenario for the system is not fully taken into account. In the reconstructed far field, only the freespace far field is obtained and the effect of real ground is not taken into account.

1.5 Aim of the Dissertation

1.5.1 Scope

In the current wireless communication field, high data rates is one of the most important component. In order to obtain improved system performance, robust algorithms must be implemented together with better hardware systems. On the algorithm side, mathematical models plays a very important part. Mathematics is the back bone of most wireless communication system technology. This dissertation targets robust mathematical models to be implemented in wireless technology systems to ensure reduced deployment costs. These robust mathematical models also ensures that the overall system performance is not degraded. We therefore deal with two major application scenarios; Advanced signal procession techniques in which more sources are estimated from few sensors (Underdetermined DOA estimation) and Antenna measurement techniques in which hemispherically measured near field data is transformed/reconstructed in the far field including the effect of real ground (earth).

1.5.2 Objectives

The objective of this dissertation is to present novel mathematical techniques that are implemented in wireless communication systems. This is achieved by utilizing advanced techniques in matrix theory in which underdetermined linear systems are utilized. The techniques are robust, cost saving, and enable high performance wireless communications systems.

1.6 Contributions

The contents of this dissertation are divided into two main topics, which falls under mathematical models in wireless communications. The first sub–topic is Underdetermined DOA estimation in which optimization techniques are applied to antenna array to achieve DOA estimation for more sources than sensors. The discussion under this sub–topic mainly focuses on the following

- Proposal of a novel nested circular array antenna called Nested Sparse Circular Array (NSCA).
- A mathematical model based on sparse signal reconstruction or compressive sensing. This method is suited to achieve underdetermined DOA estimation.
- A novel mutual coupling compensation method which improves DOA estimation for the proposed nested sparse circular array.
- An extension of the underdetermined DOA estimation method from narrowband sources to wideband signal sources.

In the second sub–topic, mathematical models in antenna measurement area are discussed. We consider the problem of Near Field to Far field transformation. The discussion focuses on;

- A hemispherical near field measurement technique as compared to conventional spherical near field measurements including the effect of earth on the far field pattern.

- A proposal of the Moore–Penrose pseudo–inverse method for finding current distribution on the AUT.
- Application of near field to far field transformation techniques to vehicular mounted antennas including the effect of earth (real ground).

1.7 Organization of the Dissertation

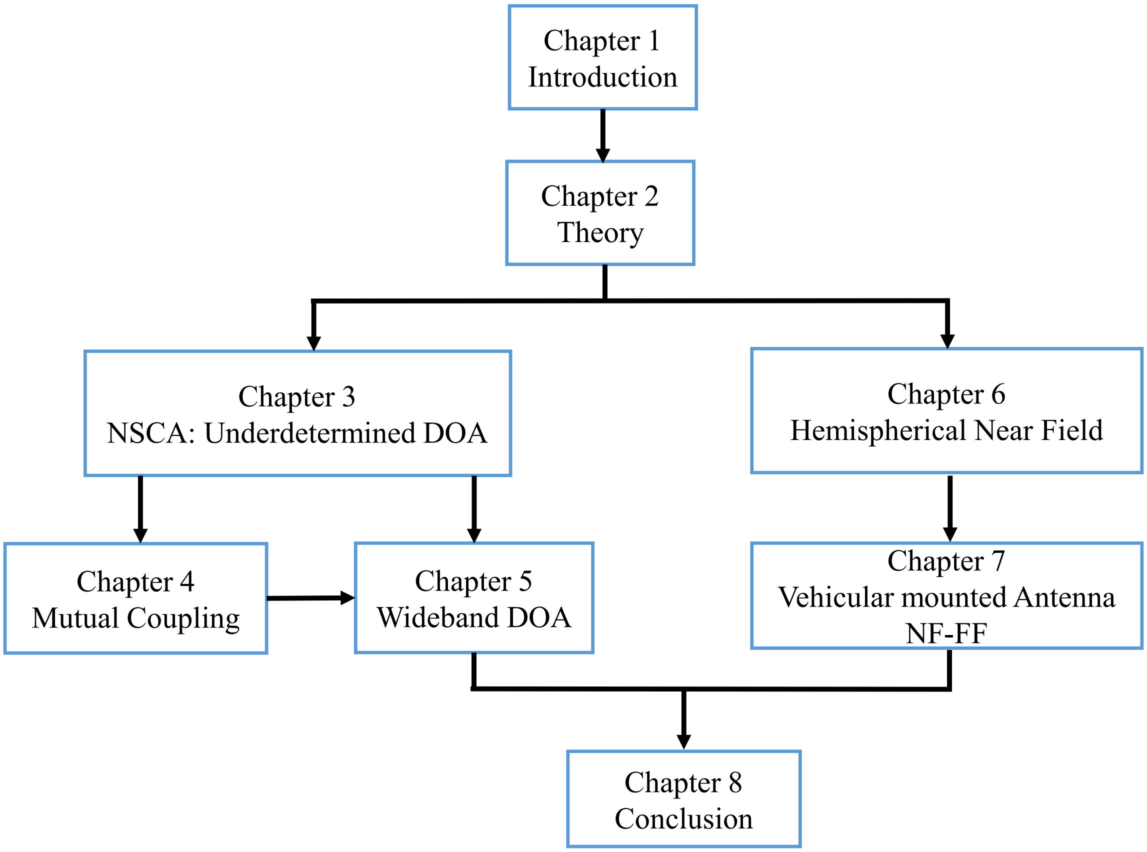

Figure 1.4: Organization of the dissertation.

The remaining part of this dissertation is organized as illustrated in Fig. 1.4. In chapter 2, an overview of mathematical models in wireless communications is presented. An explanation of basic theory in sparse signal reconstruction used in underdetermined DOA estimation is provided. The mathematical models (compressive sensing methods) that are presented in this chapter are used in adaptive antenna arrays for direction of arrival estimation. We further, provide a brief explanation of mathematical models that are used in antenna measurements specifically the ones applied to the problem of near field far field transformation.

In Chapter 3, Nested Sparse Circular array is proposed together with mathematical models used in this array for underdetermined DOA estimation. The proposed mathematical models are robust since we assume sparse signals. In this case, we are able to reconstruct signals from very few observations. This will ensure reduced deployment costs since we can use smaller arrays in the estimation of more signals impinging on the array. Direction of arrival estimation for more sources than sensors (also called underdetermined DOA estimation) using the proposed Nested Sparse Circular array is evaluated through simulations. The DOA estimation spectra, RMSE performance analysis against SNR and number of snapshots (or underdetermined DOA estimation accuracy) is presented. Furthermore, a comparison of different circular array type's performance is discussed in this chapter.

Chapter 4 describes a Mutual Coupling Compensation Method for Nested Sparse Circular Arrays. In this chapter, a novel symmetric banded–like circulant structure for MCM is developed and is used to achieve underdetermined DOA estimation in nested sparse circular arrays proposed in Chapter 3. The work in Chapter 3 is therefore extended to include the effects of mutual coupling in Chapter 4. The proposed Mutual Coupling Compensation method achieves improved DOA estimation performance, better RMSE as well as lower average run–time as compared to cases where conventional Mutual Coupling Compensation Methods are employed.In this mutual coupling method, as the number of snapshots increases, the RMSE performance becomes better.

Chapter 5 discusses the wideband DOA estimation for more sources than sensors. In this chapter, unlike Chapter 3 in which narrowband signals are assumed, we use wideband signals and propose a mathematical model that works with the nested sparse circular array. Furthermore, we utilize the mutual coupling compensation method proposed in Chapter 4 to estimate DOAs. Thus, Chapter 5 is related to Chapter 3 and Chapter 4 since it is an extension of the ℓ_1–based optimization and KR–MUSIC to wideband signals.

Chapter 6 proposes a hemispherical near field far field transformation technique. Antenna measurements techniques uses mathematical models based on Maxwell's equations. From measured near field, current source is determined using Maxwell's equations. By using the method of moments, equivalent electric current source is determined from the hemispherically measured near field data. To calculate the current distribution on the AUT, we propose the Moore–Penrose pseudo–inverse method in this chapter. The simulation and measurement results are discussed in this chapter to verify the performance of the proposed mathematical model applied to this problem. In the reconstructed far field, the effect of real ground (earth) is included which provides an insight into the real world performance of an antenna as compared to conventional freespace measurement results.

Chapter 7 discusses the hemispherical near field far field transformation technique in electrically large systems. In this chapter, a vehicular mounted antenna is discussed. Chapter 7, is directly related to Chapter 6 since the applied mathematical models are equivalent with the difference being that of the DUT model. The reconstructed far field includes the effect of the car body as well as real ground. Far field results for simulation and measurement data is compared in both freespace case and on real ground (earth). Finally, concluding remarks for this dissertation are given in Chapter 8.

Chapter 2

Advanced Mathematical Techniques in Wireless Systems

In this chapter, we formulate advanced mathematical techniques or models in wireless systems that will act as a backbone to problems addressed in this dissertation. Firstly, the problem of sparse signal reconstruction is considered by utilizing the compressive sensing approach. The mathematical preliminaries for DOA estimation problem that will be considered in Chapters 3 – 5 are discussed. We then give several definitions and review important theory related to compressive sensing for accurate signal recovery. Secondly, we give an overview of mathematical models considered in the problem of far field reconstruction from near field measurements which is discussed in Chapters 6 and 7. These two problems considered in this dissertation are optimization problems. Several approaches considered in both underdetermined DOA estimation and near field to far field reconstruction problems are applicable to sparse systems that are too large to be handled by a direct implementation or other direct methods. These kind of problems often arises when numerically solving partial differential equations and in other cases, optimization problems. Therefore, we apply underdetermined linear systems to problems in DOA estimation and near field far field reconstruction in this dissertation.

Sparse Signal Reconstruction: A Compressive Sensing Approach

2.1 Mathematical Preliminaries

Array processing generally deals with signal processing applications that use arrays of spatially separated sensors of the same type [44]. These sensors typically sample an incoming wavefront generated by emitters from the far field. For communication applications, antenna arrays are used. In other applications such as classical radar and sonar, the sensor array is used to focus and steer the energy of a signal in the spatial domain, so that a potential target return is enhanced in favor of surrounding interference, clutter and noise [44]. On transmit, this is done by distributing the signal waveform over the various sensor elements with suitable time delays, which will make the energy from all sensors add coherently in the desired (look) direction, while it is attenuated in other directions. The same technique is used on receive, by first applying the same time delays to sensor outputs, and then summing the result.

In array signal processing, space–time signal model is considered in which both spatial and temporal samples of signals are collected and processed simultaneously [45]. The signal model in signal processing is developed by considering both the physics of electromagnetic (EM) wave propagation and the statistical model of the incoming signals. We consider the most basic case, which is the localization of narrowband sources in the far field of an array. The signal $E(t, \mathbf{r})$ (e.g., EM field) at a time t and location $r = (x, y, z)^T$ is governed by the wave equation [44].

$$\frac{\partial^2 E(t,\mathbf{r})}{\partial x^2} + \frac{\partial^2 E(t,\mathbf{r})}{\partial y^2} + \frac{\partial^2 E(t,\mathbf{r})}{\partial z^2} = \frac{1}{c^2}\frac{\partial^2 E(t,\mathbf{r})}{\partial t^2} \tag{2.1}$$

where c represents the speed of propagation. Assuming a relatively small array of sensors situated in the far–field, the function becomes

$$E(t,\mathbf{r}) = s(t - r/c) \tag{2.2}$$

$s(t)$ as the signal at some origin which is near the sensor array and far from the signal source and r is the distance between the observation point $\mathbf{r}$ and the source. r can be replaced by $\mathbf{r} \cdot \mathbf{u}_r$, where $\mathbf{u}_r$ is a unit vector pointing in the direction of propagation and $\mathbf{r}$ is the coordinates of the observation point [44]. In the narrowband case, signal $s(t) = Ae^{j\omega t}$, which leads to

$$E(t,\mathbf{r}) = Ae^{j\omega(t-\mathbf{r}\cdot\mathbf{u}_r/c)} = Ae^{j(\omega t-\mathbf{r}\cdot\mathbf{k})} \tag{2.3}$$

where $k = \omega/c$ is the wave number and $\mathbf{k} = k\mathbf{u}_r$ is the wave vector. In the Cartesian coordinates $\mathbf{k}$ is given by

$$\mathbf{k} = \begin{bmatrix} k_x \\ k_y \\ k_z \end{bmatrix} = -k \begin{bmatrix} \cos\phi\cos\theta \\ \cos\phi\sin\theta \\ \sin\phi \end{bmatrix} \tag{2.4}$$

where θ represents the azimuth angles and ϕ denotes the elevation angles respectively see Fig. 2.1.

In many applications, the transmitted signal occupies a very small bandwidth B as compared to its center frequency ω. Using a complex–valued representation, such a signal can be expressed as $A(t)e^{j\omega t}$, where the complex amplitude $A(t)$ varies much slower than $e^{j\omega t}$, so that it can be modeled as constant throughout the propagation of the wave across the array [44], [45]. Suppose a narrowband signal is received by an array of M sensors at positions $\mathbf{r}_m$, $m = 1, \cdots, M$ relative to the origin. If the Radio–Frequency (RF) signal $E(t, \mathbf{r}_m)$ is captured by an ideal sensor, and the resulting signal is down–converted to baseband, the resulting output of the m–th sensor is given by

$$x_m(t) = e^{-j\mathbf{k}\cdot\mathbf{r}_m} s(t) \tag{2.5}$$

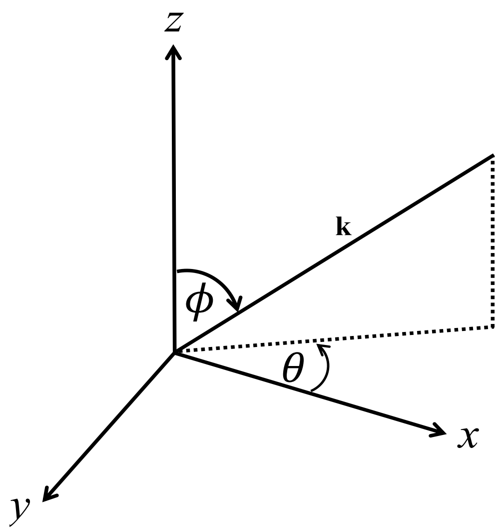

Figure 2.1: Representation of the coordinate System.

From 2.5, considering an M-element array, the output of the array $\mathbf{x}(t)$ is given by

$$\mathbf{x}(t) = \begin{bmatrix} x_1(t) \\ x_2(t) \\ \vdots \\ x_M(t) \end{bmatrix} = \mathbf{a}(\theta,\phi)s(t) \tag{2.6}$$

Where $\mathbf{a}(\theta,\phi)$ is the *steering vector* (or array response vector) given by

$$\mathbf{a}(\theta,\phi) = \begin{bmatrix} e^{-j\mathbf{k}(\theta,\phi)\cdot\mathbf{r}_1} \\ e^{-j\mathbf{k}(\theta,\phi)\cdot\mathbf{r}_2} \\ \vdots \\ e^{-j\mathbf{k}(\theta,\phi)\cdot\mathbf{r}_M} \end{bmatrix} \tag{2.7}$$

When we consider an M-element uniform circular array (UCA) in which D signals are impinging on the array, the element–space steering vector matrix of the UCA may be written as $A = [a_1(\varsigma,\phi), a_2(\varsigma,\phi), \cdots, a_D(\varsigma,\phi)]$, where

$$\mathbf{a}_d(\varsigma,\phi) = [e^{j\varsigma\cos\,(\phi_d-\gamma_0)}, e^{j\varsigma\cos\,(\phi_d-\gamma_1)}, \cdots, e^{j\varsigma\cos\,(\phi_d-\gamma_{M-1})}]^T \tag{2.8}$$

For $d = 1, 2, \ldots, D$, $\varsigma = \kappa r \sin\theta$, r is the radius and $\gamma_{M-1} = 2\pi m/M$, $(m = 0, 1, \cdots, M - 1)$ is the sensor location [46]. In the presence of multiple emitters we can apply the superposition principle resulting in the data model below;

$$\mathbf{x}(t) = A(\theta, \phi)\mathbf{s}(t) + \mathbf{n}(t) \tag{2.9}$$

where $n(t)$ is Additive white Gaussian noise (AWGN). The noise is modeled as a stationary, second–order ergodic, zero–mean spatially and temporally white circular complex Gaussian process. In most cases. In order to estimate the DOAs, estimation is based on a finite set of N samples of $x(t)$, taken at arbitrary time intervals $t_n, n = 1, \cdots, N$. Replacing $x(t_n)$ by the discrete–time notation $x(n)$, we express the available data as

$$\mathbf{x}(n) = \mathbf{A}(\theta, \phi)\mathbf{s}(n) + \mathbf{n}(n), \qquad n = 1, 2, \ldots, N \tag{2.10}$$

Most of the methods employed for DOA estimation use only second–order properties of the data (i.e second–order statistics) [47], [48]. The array correlation matrix is defined as $\mathbf{R}_{xx} = E[\mathbf{x}(n)\mathbf{x}^H(n)]$, where $E[\bullet]$ is statistical expectation and $(\bullet)^H$ denotes complex conjugate and transpose (the Hermitian operator). If the signal and noise vectors are assumed to be independent zero–mean stationary random processes with correlation matrices $\mathbf{R}_{ss} = E[\mathbf{s}(n)\mathbf{s}^H(n)]$ and $\mathbf{R}_{nn} = E[\mathbf{n}(n)\mathbf{n}^H(n)]$ respectively, we obtain

$$\mathbf{R}_{xx} = \mathbf{A}(\theta, \phi)\mathbf{R}_{ss}\mathbf{A}^H(\theta, \phi) + \mathbf{R}_{nn} \tag{2.11}$$

As previously alluded to, the noise is often modeled as spatially white, i.e., $\mathbf{R}_{nn} = \sigma^2\mathbf{I}$, where $\mathbf{I}$ is the $M \times M$ identity matrix and σ^2 is the noise power [44]. If this is not the case, but $\mathbf{R}_{nn}$ is known, then $\mathbf{x}(n)$ can be pre–multiplied by an inverse square–root factor $\mathbf{R}_{nn}^{-1/2}$ of $\mathbf{R}_{nn}$, which renders the resulting noise white (and also alters the steering vectors in a predictable way). The array correlation matrix is approximated from available data by sample correlation matrix

$$\hat{\mathbf{R}}_{xx} = \frac{1}{N}\sum_{n=1}^{N}\mathbf{x}(n)\mathbf{x}^{H}(n) \tag{2.12}$$

Under mild assumptions on the involved random processes, it holds that $\hat{\mathbf{R}}_{xx} \rightarrow \mathbf{R}_{xx}$ as $N \rightarrow \infty$. Many estimation methods are based on properties of the "true" array correlation matrix $\mathbf{R}_{xx}$, but applied to the sample correlation [44]. If the sample size is large enough and the data model is sufficiently good, such an approach can result in highly accurate DOA estimates.

2.1.1 MUSIC Algorithm

MUSIC is an acronym which stands for MUltiple SIgnal Classication [49]. It is a relatively simple and efficient spectral estimation method, which is based on matrix eigenvalue decomposition [50], [51]. In the geometric field, the signal processing of the observation space can be decomposed into signal subspace and noise subspace. In [49], it was proved that these two spaces (signal and noise) are orthogonal [28].

In the analysis of MUSIC algorithm, eigenvectors of signals that corresponds to received signal subspace from the array data covariance matrix which is composed of the noise subspace has the smallest eigenvalue from the covariance matrix of eigenvector. MUSIC algorithm therefore uses the orthogonality between the two complementary spaces to estimate the direction of the signal in space [28]. Noise subspace of all vectors is used to construct the DOA spectrum. The peak position which corresponds to the wave's azimuth and elevation is the spectrum of all spatial directions. Thus, MUSIC algorithm tremendously enhance the resolution direction finding, while adapting to an antenna array of arbitrary shape. In the case of MUSIC algorithm, from covariance matrix;

$$\mathbf{R}_{xx} = \mathbf{A}(\phi)\mathbf{R}_{ss}\mathbf{A}^{H}(\phi) + \sigma^{2}\mathbf{I} \tag{2.13}$$

$$\mathbf{R}_{xx} = \sum_{m=1}^{M}\lambda_m\mathbf{e}_m\mathbf{e}_m^{H} = \mathbf{E}_s\Lambda_s\mathbf{E}_s^{H} + \mathbf{E}_n\Lambda_n\mathbf{E}_n^{H} \tag{2.14}$$

where $\mathbf{E}_s = [\mathbf{e}_1, \mathbf{e}_2, \ldots, \mathbf{e}_D]$ contains all signal, vectors, and the noise eigenvector matrix $\mathbf{E}_n = [\mathbf{e}_{D+1}, \mathbf{e}_{D+2}, \ldots, \mathbf{e}_M]$ obeys $\mathbf{A}^H\mathbf{E}_n = 0$. In this case $D < M$ i.e overdetermined DOA estimation. The sample covariance matrix therefore becomes

$$\hat{\mathbf{R}}_{xx} = \frac{1}{N}\sum_{n=1}^{N}\mathbf{x}(n)\mathbf{x}^H(n) = \hat{\mathbf{E}}_s\hat{\Lambda}_s\hat{\mathbf{E}}_s^H + \hat{\mathbf{E}}_n\hat{\Lambda}_n\hat{\mathbf{E}}_n^H \tag{2.15}$$

The MUSIC method therefore searches for the D largest peaks of the MUSIC pseudo–spectrum

$$\mathbf{D}_{MUSIC} = \frac{1}{\left\|\mathbf{a}^H(\phi)\hat{\mathbf{E}}_n\right\|^2} = \frac{1}{\left\|\mathbf{a}^H(\phi)\hat{\mathbf{E}}_n\hat{\mathbf{E}}_n^H\mathbf{a}(\phi)\right\|^2} \tag{2.16}$$

Thus, the location of the peaks will coincide with the true DOAs.

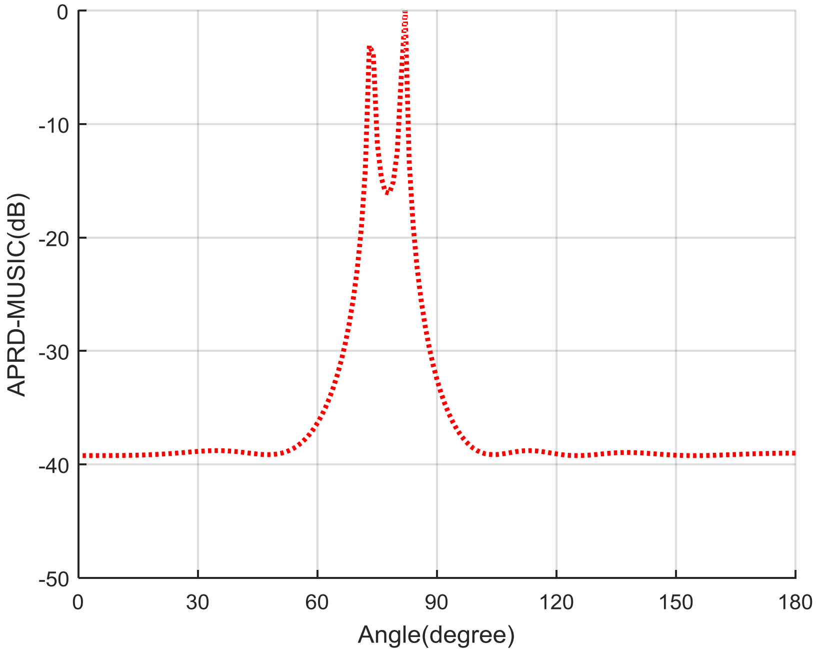

Figure 2.2: MUSIC DOA estimation for 6 element UCA [28].

In Fig. 2.2, the DOA estimation using MUSIC algorithm is shown. The 2 peaks are accurately estimated which coincides with the true DOAs.

2.1.2 Limit of Conventional MUSIC Method in DOA Estimation

In the array signal processing field especially DOA estimation; MUSIC [49] is the most commonly used technique. However, this technique has a notable drawback that it is restricted by the dimensionality of the covariance matrix [52]. The MUSIC algorithm requires the residual subspace of the observation to be reserved only for noise [53]. Hence, using conventional MUSIC algorithm [49], accurate estimation is achieved at the time when the number of impinging DOAs on the array $D < M$. In an overdetermined DOA estimation scenario, MUSIC has the limit of estimating $D = M - 1$ sources. Thus, MUSIC algorithm can resolve up to $M - 1$ DOAs. When the number of sources $D \geq M$, the MUSIC method fails to resolve all the DOAs correctly.

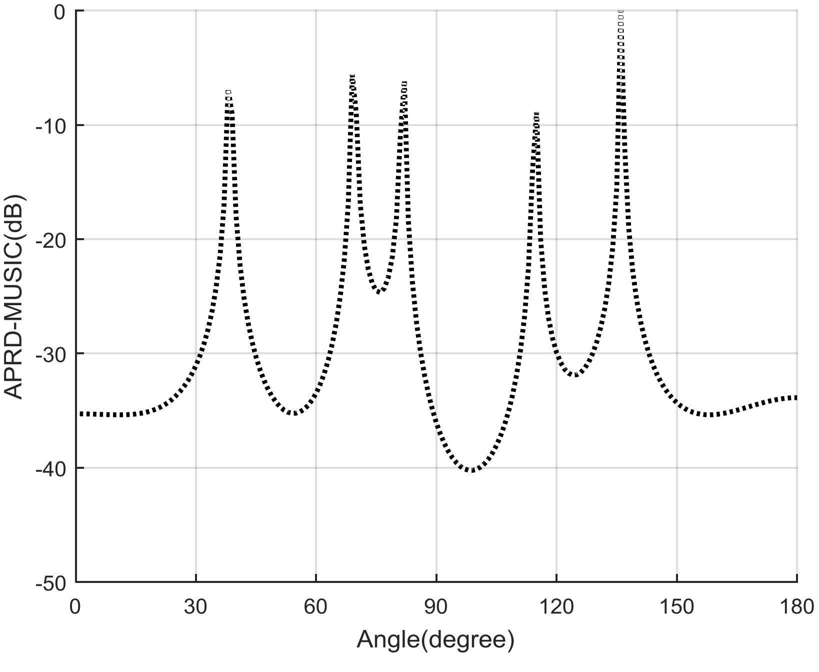

Figure 2.3: Limit of MUSIC DOA estimation for 6 element UCA [28].

To this extent, in order to estimate DOAs of D signals arriving on an array, $M(> D)$ antenna elements (sensors) are required. As the number of sources D approaches M, the DOA estimation performance degrades. One of the solutions to improve the estimation performance of DOA estimation algorithm is to increase the number of sensors. Therefore, a very large sensor array is required for the DOA estimation of a large number of sources.

Another limitation of MUSIC method is that it requires *priori* knowledge on the number of sources which at times may be difficult to obtain [54]. Additionally, MUSIC requires a sufficient number of data snapshots to accurately estimate the data covariance matrix. Moreover, the method can be sensitive to source correlations that tend to cause a rank deficiency in the sample data covariance matrix [54]. Thus, new methods have been proposed that utilizes techniques in sparse representation and compressed sensing methods [55], [56], [57]. The sparse estimation (or optimization) methods can be applied in several demanding scenarios, including cases with no knowledge of the source number, highly or completely correlated sources, and limited number of snapshots such as single snapshot cases [58].

2.2 Compressive Sensing

Compressed sensing is one of the prominent recent application of sparsity–related ideas which is popular and rapidly expanding area of modern signal processing [59], [60]. It is a signal processing technique for efficiently acquiring and reconstructing a signal, which is achieved by finding solutions to underdetermined linear systems. It is also called compressive sensing, or compressive sampling [55], [56]. In this technique, the idea is that the majority of real–life signals, such as images, audio, or video, can be well approximated by sparse vectors, given some appropriate basis, and that exploiting the sparse signal structure can dramatically reduce the signal acquisition cost. Thus, accurate signal reconstruction can be achieved in a computationally efficient way, by using sparse optimization methods [54], [60]. The idea behind this method is based on the principle that, through optimization or mathematical analysis, the sparsity of a signal can be exploited to recover it from far fewer samples than required by the

Shannon–Nyquist sampling theorem.

2.2.1 Shannon–Nyquist Sampling Theorem

In the Shannon–Nyquist sampling theorem, the theorem states that sampling rate of a signal must be at least twice the maximum frequency present in the signal (which is called Nyquist rate). Consider $\mathbf{x}(t)$ to be a signal with Continuous-Time Fourier Transform (CTFT) $\mathbf{X}(\omega)$. If $\mathbf{X}(\omega) = 0$ for all $|\omega| > \pi/\omega$, then $\mathbf{x}(t)$ can be reconstructed from samples $\mathbf{x}(nT)$ using reconstruction formula

$$\mathbf{x}(t) = \sum_{n \in Z} \mathbf{x}(nT) \mathrm{sinc}\left(\frac{t - nT}{T}\right) \tag{2.17}$$

where

$$\mathrm{sinc}(t) = \frac{\sin(\pi T)}{\pi T} \tag{2.18}$$

This asserts that for a signal that is bandlimited to π/T, it can be recovered from its uniformly spaced samples with period T, or sampling rate $f = 1/T$ [59].

In the field of wireless communications especially signal processing, we would like to reconstruct a signal from measured data. In most cases, the information acquisition process is linear, which reduces the problem to solving linear system of equations [61], [62]. In mathematical stipulations, observed data $\mathbf{y} \in \mathbf{C}^m$ is related to signal $\mathbf{x} \in \mathbf{C}^n$ of interest through

$$\mathbf{A}\mathbf{x} = \mathbf{y} \tag{2.19}$$

where matrix $\mathbf{A} \in \mathbf{C}^{n \times m}$ represents the linear measurement process. Thus, we can recover the vector $\mathbf{x} \in \mathbf{C}^n$ by solving the linear system shown above. From the Shannon–Nyquist sampling theorem, the amount of measured data m, ought to be at least as large as the signal length N (in other words, the number of components of $\mathbf{x}$) [61].

This principle described above is the basis for most devices that are being used in current technology. The examples of the areas that apply this principle includes mobile communication, radar, analog–to–digital conversion, and medical imaging. If $m < N$, then the linear system (2.19) is underdetermined and there are infinitely many solutions. Thus, if we do not have additional information, it is impossible to recover the signal $\mathbf{x}$ from measurements $\mathbf{y}$ in the case $m < N$. Although this is the case, under certain assumptions, it is possible to reconstruct or recover signals $\mathbf{x}$ when the number m of measurements available is smaller as compared to the signal length N. We thus introduce some of the algorithms that exist for signal reconstruction. The fundamental assumption that makes all this possible is *sparsity* in which most of the signal's components are zero [61], [63].

2.2.2 Normed Vector Spaces

A normed vector space is described as a vector space over the real or complex numbers, on which a norm is defined [59]. In sparse vectors, ℓ_p–norms play a key role in their treatment. The ℓ_p–norm for $p \in [1, \infty]$ of a vector $\mathbf{x} \in \Re^n$ is defined as

$$\|x\|_p = \begin{cases} \left(\sum_{i=1}^{n} |x_i|^p\right)^{\frac{1}{p}}, & \text{if } p \in [1, \infty), \\ \max\limits_{i=1,2,\ldots,n} |x_i|, & p = \infty \end{cases} \tag{2.20}$$

where $|x_i|$ express the absolute value of the i–th component of $\mathbf{x}$. The two most commonly used ℓ_p–norms are; (i) ℓ_1–norm and (ii) ℓ_2–norm expressed as;

$$\|x\|_1 = \sum_{i=1}^{n} |x_i| \tag{2.21}$$

$$\|x\|_2 = \sqrt{\sum_{i=1}^{n} |x_i|^2} \tag{2.22}$$

In some instances, ℓ_p–norm is extended to cases where $p < 1$. In the case when $0 < p < 1$, ℓ_p–norm as defined above does not satisfy the triangle inequality. Consequently, it cannot be called a norm. Alternately, it is called a quasinorm as it satisfies the weaker version of the triangle inequality (2.23) (i.e it becomes a quasinorm because it fails to satisfy the triangle inequality [59], [62], [63]).

$$\|x+y\|_p \leq c(\|x\|_p + \|y\|_p) \tag{2.23}$$

With $c = 2^{1/p-1}$. The ℓ_p–norms and ℓ_p–quasinorms have different properties for different values of p. This is illustrated in Fig. 2.4. In this figure, a unit sphere is shown for ℓ_p–quasinorms and $\ell_p - -$norms. The choice of p therefore has a significant effect on the properties of the resulting approximation error [60].

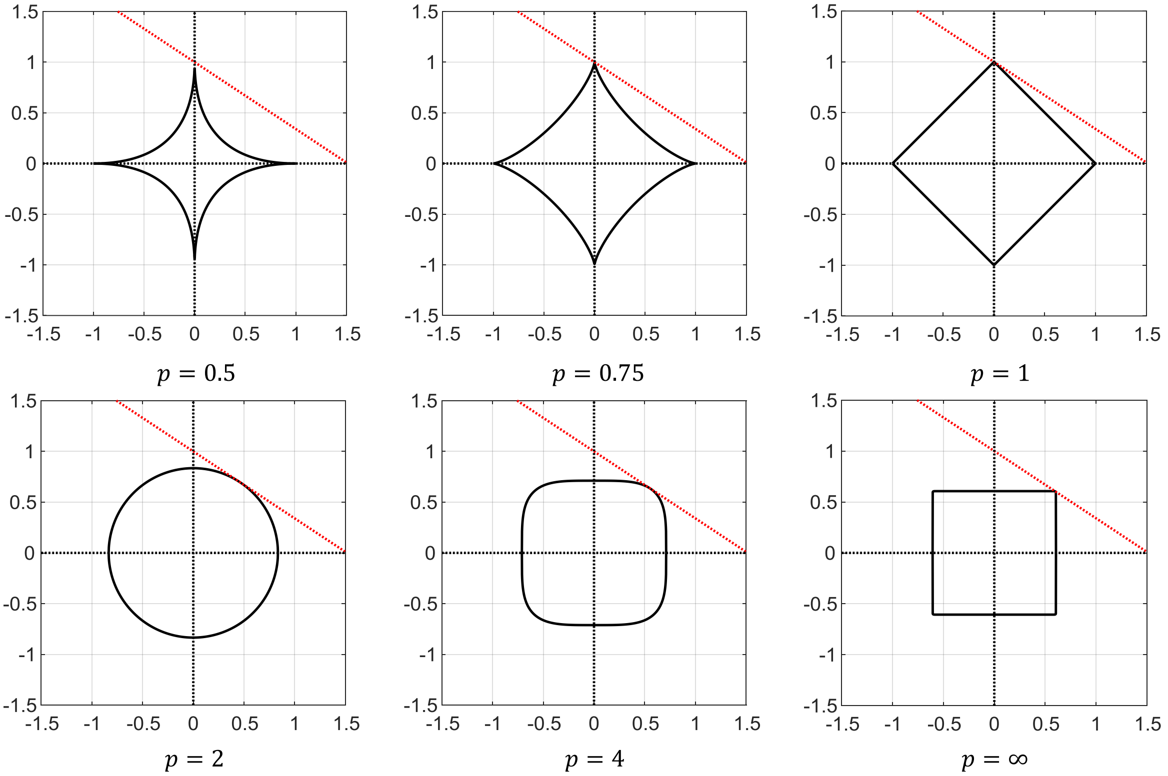

$p = 0.5$ $p = 0.75$ $p = 1$

$p = 2$ $p = 4$ $p = \infty$

Figure 2.4: Normed Vector Spaces unit ball.

2.3 Sparse Signal Recovery

In this section, we consider solving the compressed sensing signal recovery problem; given $\mathbf{y}$ and $\mathbf{A}$, find sparse signal $\mathbf{x}$ such that $\mathbf{y} = \mathbf{Ax}$ (2.19) exactly or approximately [59]. In the compressed sensing field, a sparse signal, which is represented by sparse vector $\mathbf{x}$, is recovered from undersampled linear measurements $\mathbf{y}$, specifically, the system model (2.19) applies for $M << N$ [54]. In this frame of reference, $\mathbf{y}$ is referred to as the compressive data, and $\mathbf{A}$ is sensing matrix. Sparse signal recovery can be formulated as finding a minimum–cardinality solution to a constrained optimization problem [60]. ℓ_0–minimization is one of the approach. The objective function is the cardinality of $\mathbf{x}$, i.e. the number of non-zeros, which is often denoted $\|x\|_0$ and called ℓ_0–norm of $\mathbf{x}$ [60].

Given measurements $\mathbf{y}$ (i.e let $\mathbf{y}$ be the signal that we observe) and the knowledge that the signal $\mathbf{x}$ is sparse. We desire to sparsely represent $\mathbf{y}$ using the model (2.19). We can therefore recover/reconstruct $\mathbf{x}$ as a solution of the combinatorial optimization problem;

$$\textit{noiseless case} \qquad \text{minimize } \|x\|_0 \quad \text{subject to } \mathbf{Ax} = \mathbf{y} \tag{2.24}$$

$$\textit{noisy case} \qquad \text{minimize } \|x\|_0 \quad \text{subject to } \|\mathbf{y} - \mathbf{Ax}\|_2 \leq \epsilon \tag{2.25}$$

Consequently, we search for the sparsest vector consistent with the measured data $\mathbf{Ax} = \mathbf{y}$. Unfortunately, the ℓ_0–minimization problem is NP–hard [61] i.e $\|x\|_0$ is non–convex and therefore difficult to solve. A very computationally efficient recovery technique is basis pursuit or ℓ_1–minimization. This consists of finding a minimizer of the problem.

2.3.1 ℓ_1–norm Minimization

In this method, in order to translate problem (2.19) into a manageable problem, $\|x\|_0$ is replaced with its convex approximation $\|x\|_1$. The practical approach to sparse signal recovery is based on the convex relaxation. In this problem, the ℓ_0–norm is replaced by its tightest convex relaxation, the ℓ_1–norm [54]. A computationally efficient recovery is possible by solving a convex optimization problem:

$$\min \|x\|_1 \quad \text{subject to } \mathbf{A}\mathbf{x} = \mathbf{y} \tag{2.26}$$

This problem can be reformulated as a linear program and accordingly solved by standard optimization techniques easily [60]. Furthermore, even if measurements are contaminated by noise, sparse recovery is still stable in a sense that recovered signal is a close approximation to the original provided that the noise is sufficiently small, and that the design matrix satisfies certain properties such as RIP [55]. A sparse signal can be recovered by solving a "noisy" version of the above ℓ_1–norm minimization problem

$$\min \|x\|_1 \quad \text{subject to } \|\mathbf{y} - \mathbf{A}\mathbf{x}\|_2 \leq \epsilon \tag{2.27}$$

In the presence of noise, (2.27) results in a quadratic optimization problem which is solvable using polynomial time methods [64]. An unconstrained optimization, using the corresponding Lagrangian for some appropriate Lagrange multiplier λ uniquely defined by ϵ, is written as

$$\min_{x} \frac{1}{2} \|\mathbf{y} - \mathbf{A}\mathbf{x}\|_2^2 + \lambda \|x\|_1 \tag{2.28}$$

For some $\lambda > 0$. In order to solve the optimization problem numerically, a matlab based modelling system for convex optimization is used called CVX [65].

2.3.2 Other Algorithms

In this section, we provide an overview of several other common algorithms for sparse signal recovery. There are several approaches such as basis pursuit (in which ℓ_1–norm minimization is an example), greedy algorithms, active set methods, block–coordinate descent, iterative thresholding, and proximal methods [60].

Greedy algorithms are essentially iterative and select columns of **A** homologous to their correlation with measurement $\mathbf{y}$ [59]. In greedy algorithms, Matching Pursuit (MP) is one example. It is a sparse approximation algorithm that comprises of finding the best matching projections of multidimensional data onto the span of an over–complete (in other words, redundant) dictionary [66].

Orthogonal Matching Pursuit (OMP) is another greedy method that builds up the support set of the reconstructed sparse vector iteratively by adding one index to the current support set at each iteration [66], [67]. OMP is an algorithm that is based on Matching Pursuit. The selection operation is greedy on the grounds that the index is chosen to minimize the residual at each iteration [61]. In OMP, the algorithm starts by finding the column of a matrix $\mathbf{A}$ that resembles the most with the residual, and then this column will be added into a set of selected columns [67]. OMP re–compute the coefficients of all variables in the current support, by solving the full OLS problem over the support augmented with the new variable. As the result of this operation, the residual becomes orthogonal to the support variables [61]. The algorithm will update the residuals by projecting the vector $\boldsymbol{b}$ onto the space spanned by the selected columns in the set. After each step, the residuals are orthogonal to all the selected columns. Thus, no column is chosen twice.

Another greedy method is compressive sampling matching pursuit (CoSaMP). It is an effective compressive sensing algorithm that holds rigorous estimation error bounds and low computational complexity, when it is dealing with additive noise signal model in the observation domain [68]. It combines selection of multiple columns per iteration with a pruning step. At each iteration, this methods selects several elements of the support set and then refines this selection [69]. There are multiple extensions and improvements to the basic greedy schemes, including Stagewise OMP (StOMP) [70], regularized OMP (ROMP) [71], and several others [60].

Iterative Hard Thresholding algorithm (IHT) is different from all the previous algorithms [72]. IHT solves a local approximation to the problem. Instead of directly handling the problem, a surrogate objective function is introduced. Each $\mathbf{x}$ can then be optimized independently [60]. The algorithm uses a nonlinear operator that sets all but the largest s elements of its argument to zero [73]. As demonstrated in [72], this method gives near–optimal error guarantees and is robust to noise. The performance guarantees for IHT are uniform but depends on sparsity of the signal and sampling operator.

2.3.3 Sparse Recovery Performance Comparison

In this subsection, we compared the recovery performance of sparse signals by using three compressive sensing algorithms. In this example, ℓ_1–minimization, Orthogonal Matching Pursuit (OMP), and compressive sampling matching pursuit (CoSaMP) algorithms' performance is compared. In terms of the empirical error as a function of sparsity, we observe in both Fig. 2.5 and Fig. 2.6 that ℓ_1–minimization has better performance as compared to OMP and CoSaMP. As the sparsity increases, the error for ℓ_1–minimization is not as pronounced as in the other algorithms. Thus, ℓ_1–minimization is robust in performance as compared to greedy algorithms for both noiseless case Fig. 2.5 and noisy case Fig. 2.6.

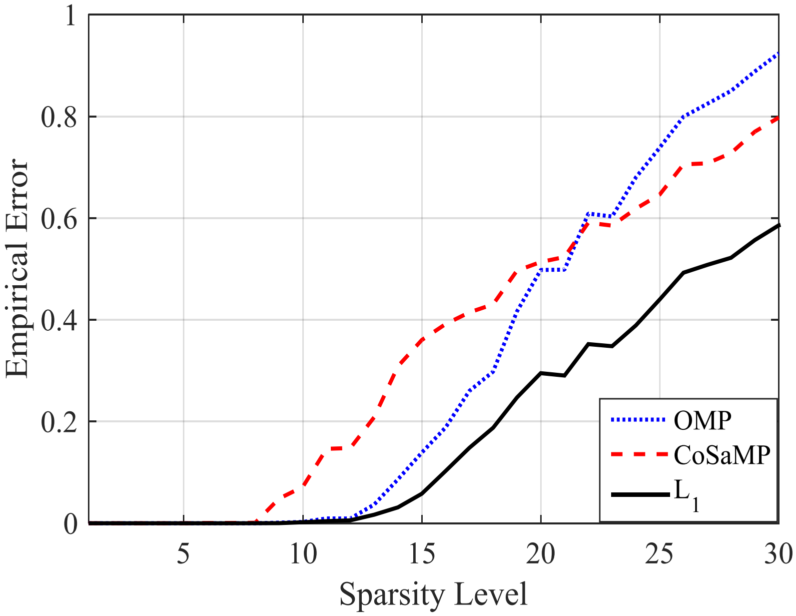

Figure 2.5: Different CS Algorithm recovery performance comparison for noiseless case.

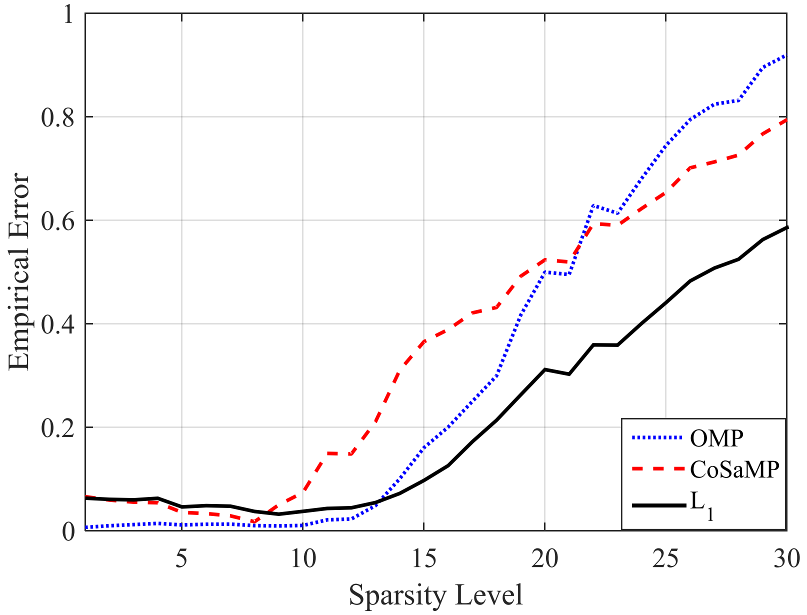

Figure 2.6: Different CS Algorithm recovery performance comparison for noisy case.

Far Field Reconstruction from Near Field Measurements

2.4 Near Field to Far Field Methods

In the field of antenna measurements, near field to far field transformation methods have been extensively investigated in the last five decades [38], [40], [74]. They have been used for applications ranging from cellular phone antennas to large phased arrays and complex multi–beam communication satellite antennas [36], [74]. These methods allow antenna engineers to overcome the shortcomings related to electrically large radiating systems, which makes them unpractical to measure the antenna pattern in a conventional far field range. These methods also represent a better choice when complete pattern as well as polarization measurements are required [36]. On top of that, near field techniques provides significant information to work out the radiating field on the surface of the antenna [75].

In comparison to far field measurements, the size of a conventional test range (such as anechoic chamber) can be reduced by performing near field measurements [27]. From the measured near field information, we can use analytical methods to transform the measured near field data to compute the far field radiation characteristics [37], [38], [39], [76]. These techniques are ordinarily used to measure antenna pattern and are often performed indoors. Consequently, these methods provide a controlled environment and an all-weather capability, and computed patterns are accurate as the patterns measured in a conventional far field range [27]. However, the drawback of such kind of methods is that they require more complex and expensive systems, extensive calibration procedures, sophisticated computer software, and patterns are not obtained in real time.

In the process of measuring the near field data, regular amplitude and phase distributions are measured by a scanning field probe over a preselected surface which may be a plane, a cylinder, or a sphere [27]. Measured information is then transformed to far field using analytical Fourier transform methods. The complexity of the analytical transformation increases from planar to cylindrical, and from cylindrical to spherical surfaces. The choice of the method/technique to be used for near field measurement is primarily determined by the type of antenna or antenna system to be measured. Conventionally, planar system is better suited for high–gain antennas such as phased arrays. This method requires the least amount of computations and no movement of the antenna [77]. In spite of the fact that cylindrical system requires more computations as compared to planar, for most antenna systems, its measuring, positioning, and probe equipment are the least expensive. Of all the three near field measurement systems, spherical system requires the most expensive computation, and antenna and probe positioning equipment, which can become significant for large antenna systems [27]. The spherical near field measurement system is best suited for measurements of low–gain and omnidirectional antennas.

2.4.1 Method of Moment

The Method of Moment (MOM) is a method of transforming differential equations and integral equations into simultaneous equations and numerically solving them [78], [79], [80]. The method of moment in electromagnetic field analysis finds current distribution on the conductor surface by solving integral equation satisfied by electric field on the conductor surface derived from the Maxwell equations. Since it is difficult to solve the integral equation directly, it is possible to numerically solve by spreading current distribution to the sum of piecewise functions and transforming it into simultaneous linear equations (matrix equations). When an electric field $\mathbf{E}^{in}$ enters an antenna or scatterer of perfect conductors, surface current density is generated on the conductor surface S. The scattering electric field $\mathbf{E}^{s}$ generated by this current $\mathbf{J}_s$ depends on the boundary condition on surface S.

$$\mathbf{n}^s \times \left\{ \mathbf{E}^{in}(r) + \mathbf{E}^{s}(r) \right\} = 0, \quad r \text{ on } S \tag{2.29}$$

where, $\mathbf{n}^s$ is a normal vector to surface S. From this equation, electric field integral equation with respect to surface current density $\mathbf{J}_s$ of the conductor surface S is;

$$\mathbf{E}^{in}(r) = j\omega\mu_0 \int_S \bar{G}r, \acute{r} \cdot \mathbf{J}_s(\acute{r}) \times \mathbf{n}^s d\acute{S} \tag{2.30}$$

where $\bar{G}$ is free space Dyadic Green function [81]. The Green function is used to obtain radiation/scattering by arbitrary wave source distribution and shows radiation from the point source as shown in the following equation;

$$\begin{aligned} \bar{G}r, \acute{r} &= \left(\frac{\nabla\nabla}{k^2} + \bar{I} \right) \frac{e^{-jk|r-\acute{r}|}}{4\pi\,|r-\acute{r}|} \\ &= \frac{1}{k^2} \begin{bmatrix} \frac{\partial^2}{\partial x^2} + k^2 & \frac{\partial^2}{\partial x \partial y} & \frac{\partial^2}{\partial x \partial z} \\ \frac{\partial^2}{\partial y \partial x} & \frac{\partial^2}{\partial y^2} + k^2 & \frac{\partial^2}{\partial y \partial z} \\ \frac{\partial^2}{\partial z \partial x} & \frac{\partial^2}{\partial z \partial y} & \frac{\partial^2}{\partial z^2} + k^2 \end{bmatrix} \frac{e^{-jk|r-\acute{r}|}}{4\pi\,|r-\acute{r}|} \end{aligned} \tag{2.31}$$

where k is the propagation constant in free space. In order to solve the electric field integral equation of (2.30), unknown surface current density $\mathbf{J}_s$ is first expanded using basis function (expansion function) $\boldsymbol{f}_n(\acute{r})$ and an unknown current coefficient $\mathbf{I}_n$ is expanded as follows

$$\mathbf{J}_s(\acute{r}) = \sum_{n=1}^{N} \mathbf{I}_n \boldsymbol{f}_n(\acute{r}) \tag{2.32}$$

Therefore, by substituting (2.32) into (2.30) and as well as introducing a weight function $\mathbf{w}_m(r)$, the integral equation of (2.30) becomes;

$$\sum_{n=1}^{N} \mathbf{Z}_{mn}\mathbf{I}_n = \mathbf{V}_m \quad (m = 1, 2, 3, \cdots, N) \tag{2.33}$$

where, the voltage coefficient $\mathbf{V}_m$ is a known coefficient determined by incident electric field $\mathbf{E}^{in}$ and $\mathbf{Z}_{mn}$ is the self and mutual impedance matrix. $\mathbf{V}_m$ and $\mathbf{Z}_{mn}$ are given by the following equations;

$$\mathbf{V}_m = \int_S \mathbf{w}_m(r) \cdot \mathbf{E}^{in}(r) dS \tag{2.34}$$

$$\mathbf{Z}_{mn} = j\omega\mu_0 \int_S \int_S \mathbf{w}_m(r) \cdot G(r, \acute{r}) \cdot \mathbf{f}_n(\acute{r}) d\acute{S} dS \tag{2.35}$$

From the equations above, an unknown current coefficient $\mathbf{I}_n$ can be obtained by solving the simultaneous equations of the formula (2.33) numerically. From the solution, one can obtain the formulas (2.34) and (2.35). Therefore, since the surface current density J_s of the conductor surface can be obtained from the expression (2.32), the scattering electric field from conductor can be calculated.

Therefore, in this dissertation, the moment method is calculated by a point matching method which performed using piecewise linear function (triangular function) given by the following equation for the basis function and trial function.

$$f(n) = \begin{cases} \frac{\sin\, k(\Delta - |z - z_n|)}{\sin\, k\Delta l}, & (|z - z_n| \leq \Delta l) \\ 0, & \text{otherwise} \end{cases} \tag{2.36}$$

A piecewise linear function overlaps adjacent elements and becomes a linear function within each element. By using this function, the current distribution is approximated to a polygonal line together with the current coefficient.

2.4.2 Near Field

The near electromagnetic field generated from the object to be analyzed can be considered by the electromagnetic field generated by the linear current wave source [82]. The near field observation system is shown in Fig. 2.7. The electromagnetic field that the current source $\mathbf{J}$ at the position r_s in the region v forms at the observation point r is represented by the Maxwell equation.

$$\mathbf{E} = -j\omega\mu_0 \left(\mathbf{A} + \frac{\nabla\nabla \cdot \mathbf{A}}{k^2} \right) \tag{2.37}$$

$$\mathbf{H} = \nabla \times \mathbf{A} \tag{2.38}$$

$$\mathbf{A} = \int_v G(r_s, r)\mathbf{J}(r_s)dr_s \tag{2.39}$$

$$G(r_s, r) = \frac{e^{-jk|r-r_s|}}{4\pi\,|r - r_s|} \tag{2.40}$$

$$\nabla = \left(\frac{\partial}{\partial x}, \frac{\partial}{\partial y}, \frac{\partial}{\partial z} \right) \tag{2.41}$$

In order to consider the electromagnetic field generated by the linear wave source, the region v is a line l, and assuming that $\hat{l}$ is a unit tangent vector along a line, the equations (2.37) and (2.38) are the p component of the orthogonal coordinate system about $(p = x, y, z)$, where;

$$\mathbf{E}_p(r) = \frac{jZ_0}{k} \left[\int I(l) \frac{\partial}{\partial p} \left\{ \frac{\partial G(\mathbf{r}_s, \mathbf{r})}{\partial l} \right\} dl - k^2 \int I(l)(\hat{p} \cdot \hat{l}) G(\mathbf{r}_s, \mathbf{r}) dl \right] \tag{2.42}$$

$$\mathbf{H}_p(r) = \int I(l)(\hat{p}'' \cdot \hat{l}) \frac{\partial G(\mathbf{r}_s, \mathbf{r})}{\partial p'} dl - \int I(l)(\hat{p}' \cdot \hat{l}) \frac{\partial G(\mathbf{r}_s, \mathbf{r})}{\partial p''} dl \tag{2.43}$$

Where, (p, p', p'') is obtained by replacing (x, y, z) with circular coordinates. However, equations shown above shows near field in rectangular coordinate system (x, y, z). For

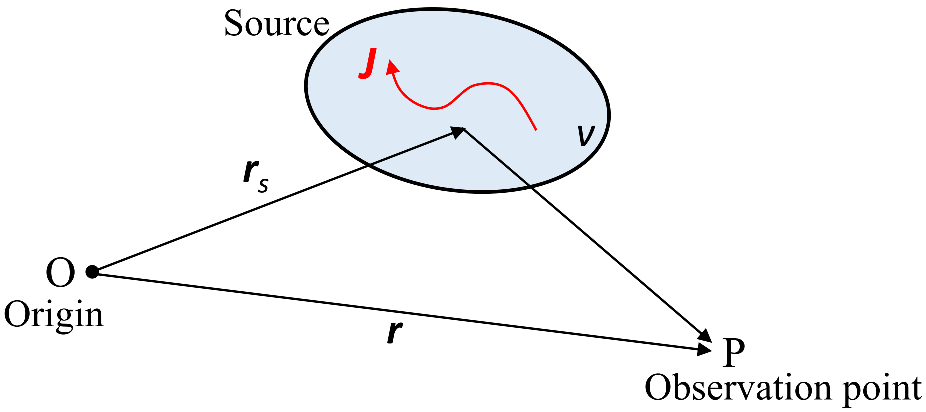

Figure 2.7: Near field observation system.

near field in polar coordinate system (r, θ, ϕ) coordinate transformation is used as follows;

$$\begin{bmatrix} E_r(H_r) \\ E_\theta(H_\theta) \\ E_\phi(H_\phi) \end{bmatrix} = \begin{bmatrix} \sin\theta\cos\phi & \sin\theta\sin\phi & \cos\theta \\ \cos\theta\cos\phi & \cos\theta\sin\phi & -\sin\theta \\ -\sin\phi & \cos\phi & 0 \end{bmatrix} \begin{bmatrix} E_x(H_x) \\ E_y(H_y) \\ E_z(H_z) \end{bmatrix} \tag{2.44}$$

2.4.3 Far Field

Far field is usually defined by the far electric field (E_θ, E_ϕ). It is obtained by setting the observation point at infinity point $(r = \infty)$ in the near electric field equation. The method of moments for a scattered conductor in a semi–infinite space where $z = 0$ is a complete conductor ground plane. The radiation direction from the wave source at the position r_n to the observation point r is uniquely represented by $\hat{r}$. Therefore, the phase change due to the wave source position with respect to the observation point is determined by the inner product of r_n and $\hat{r}$. In addition, the electric field component (E_θ, E_ϕ) generated at the observation point by the wave source in the $\hat{l}_n$ direction is the inner product $(\hat{l}_n \cdot \hat{\theta}, \hat{l}_n \cdot \hat{\phi})$. Therefore, the far field by the linear wave source is given by;

$$E_\theta(r,\theta,\phi) = \frac{jZ_0ke^{-jkr}}{4\pi r}F_\theta(\theta,\phi) \tag{2.45}$$

$$E_\phi(r,\theta,\phi) = \frac{jZ_0ke^{-jkr}}{4\pi r}F_\phi(\theta,\phi) \tag{2.46}$$

$$F_\theta(\theta,\phi) = \sum_{n=1}^{N} \boldsymbol{I}_n \Delta l_n (\hat{l}_n \cdot \hat{\theta}) e^{jkr_n \cdot \hat{r}} \tag{2.47}$$

$$F_\phi(\theta,\phi) = \sum_{n=1}^{N} \boldsymbol{I}_n \Delta l_n (\hat{l}_n \cdot \hat{\phi}) e^{jkr_n \cdot \hat{r}} \tag{2.48}$$

where $\hat{\theta} = (\cos\theta\cos\phi, \cos\theta\sin\phi, -\sin\theta)$, and $(\hat{\phi} = -\sin\phi, \cos\phi, 0)$.

Chapter 3

Underdetermined DOA Estimation using Nested Sparse Circular Arrays

3.1 Introduction

In signal processing area, direction of arrival (DOA) estimation, which is also refereed to as spatial spectra estimation has been an active research area [24], [25], [83]. It is playing a crucial role in many application areas, such as electromagnetic, seismic sensing, and acoustics. The breakthroughs in array signal processing discipline has influenced the development of high resolution DOA estimation techniques for narrowband signals [25], [49] and their wideband extensions [84], [85].

In antenna arrays, DOA estimation nonetheless has been restricted to uniform linear arrays (ULA) and uniform circular arrays (UCA) [50]. On the algorithm side, subspace based methods such as MUSIC [49] for example can resolve up to $(M-1)$ sources for an array with M elements [31], [50]. In order to estimate more sources than the number of physical sensors also refereed to as underdetermined DOA estimation, [86] proposed nested linear arrays. This work on nested arrays was further extended to arrays with higher geometries [87], [88] and co–prime arrays [89]. We thus consider non–uniform circular arrays and propose a novel array structure. The proposed array structure has the ability to provide an increase in degrees of freedom (DOFs) and subsequently is capable of resolving more sources than physical sensors called Nested Sparse Circular Array (NSCA). This proposed array is obtained by combining two or more sub-circular arrays. We demonstrate that by using NSCA, we can achieve underdetermined DOA estimation.

In DOA estimation, uniform circular arrays are of particular importance. They are capable of providing 360° azimuthal coverage and estimate both azimuth and elevation angles simultaneously [90]. In addition to these capabilities, due to their circular symmetry, UCAs also possesses an azimuthally invariant beampattern. Thus, UCAs have a lot of characteristics that makes them useful in terms of estimating DOAs [24]; e.g., directional patterns that are synthesized with UCAs can be electronically rotated in the plane of the array without significant change of beam shape [51]. The geometry of the UCA can further be extended to uniform concentric circular array (UCCA) which comprises of multiple circular arrays or rings in which elements are located on rings with different radius [91]. UCCAs are significant in that they enable wideband DOA estimation as well as 2D-DOA estimation. Thus utilizing concentric arrays in DOA estimation improves estimation accuracy, reduces angular dependency as well as enables wideband DOA estimation.

In recent years, underdetermined DOA estimation which is refereed to as the estimation of more sources than the number of physical sensors available has been receiving considerable interest [92], [93]. One of the most effective approach to underdetermined DOA estimation is to construct a new array that has an extended aperture (from virtual elements) which has higher degrees of freedom as compared to those obtained from the physical array. Sparse spatial sampling in this case provides a remarkable improvement in degrees of freedom, and typical array structures employed include nested linear arrays [86] and co-prime arrays [89], [93], [94]. Recently, a different form but effective DOA estimation technique called ℓ_1–SVD based on sparse signal reconstruction came to light [95]. In single measurement case, ℓ_1 optimization is considered attractive to sparse signal recovery due to its guaranteed recovery accuracy [96], [97]. However, for an array with M sensors, similar to subspace based methods, ℓ_1–based approach in [95] resolve up to $M - 1$ signals impinging on the array.

In earlier works, underdetermined DOA estimation for UCA has barely been considered. In [98], to resolve more than $(M - 1)$ sources, Khatri-Rao (KR) [92] subspace method was considered for quasi–stationary signals applied to UCA. In signal processing, quasi–stationary signals are in a class of nonstationary signals whose signal statics are locally static over a short period of time [92]. Some of the examples of quasi–stationary signals are speech and audio signals. The problem related to using quasi–stationary signals is that this method can not be applied to stationary sources [86].

In order to perform wideband estimation, [99] proposed a Nested Circular Array (NCA). The NCA method proposed in [99] has advantages over conventional methods in that, it is used to eliminate spatial aliasing for counting and DOA estimation of multiple simultaneous speakers. In NCA, each microphone pair is only used in appropriate subband according to its inter-microphone distance which enables the proposed method in [99] to achieve an acceptable performance in both reverberant and noisy conditions. Although this is the case, NCA is basically a Uniform Circular Array in structure and not extension of nested arrays as proposed in [86]. The authors in [99] did not provide any theoretical background of the proposed array structure as has been shown in this chapter. In [100], optimal array structures were evaluated. In this case, optimal and nearly optimal schemes operating both in a periodic and non–periodic form were designed by considering linear compression schemes classified as dense or sparse. In the case of linear array, the length–10 minimal sparse ruler (SR) was found to be an optimal sparse array. On the other hand, its counterpart, length–20 circular SR, which was designed with a length–10 linear SR was found to have sensors or elements positioned on one side of the array which results in angular dependency for DOA estimation hence reduced performance. The performance comparison of the length–20 circular SR to our proposed array configuration NSCA in underdetermined DOA estimation is carried in this chapter.

In this chapter, we firstly propose a new array structure called "*Nested Sparse Circular Array*" that has the ability of estimating more sources than physical sensors. The array is synthesized into a non–uniform concentric array through KR approach. The virtual elements synthesized by the KR approach are inside the original circle which works as a non–uniform concentric circular array and is effective for wideband DOA estimation. Synthesized non–uniform concentric array increases the DOFs and therefore assist us to perform underdetermined DOA estimation for both narrowband and wideband signal models. This makes the proposed NSCA a good candidate for both narrowband and wideband underdetermined DOA estimation. We extend the subspace based approach MUSIC proposed in [49] and used in [92] for quasi–stationary signals to the proposed NSCA. Furthermore, an ℓ_1 optimization method based on compressive sensing or sparse signal recovery is used which takes advantage of the KR product of covariance matrix.

3.2 Nested Sparse Circular Arrays

3.2.1 Nested Array

The class of arrays called nested array was first proposed in [86]. The "two level" nested array as described in [86] is in fact similar to the array structure originally proposed in [101]. Nonetheless, in [86] the concept of nested arrays was generalized to more than two levels such that there is a considerable increase in the degrees of freedom. In the basic case, a two level nested linear array is a series of two interconnected uniform linear array (inner–level 1 and outer–level 2) with the inner ULA having M_1 and the outer ULA having M_2 elements. A two level nested linear array can achieve $2M_2(M_1 + 1) - 1$ freedoms in the co–array using $M_1 + M_2$ elements only [86].

Figure 3.1 also shows the two level nested array. The optimal distribution of sensors in the two levels by finding M_1, M_2 that maximize the total degrees of freedom, $2M_2(M_1 + 1) - 1$, under the constraint of fixed total number of sensors, i.e., $M_1 + M_2 = M$ [45].

M	Optimal M_1, M_2	DOF
even	$M_1 = M_2 = \frac{1}{2}M$	$\frac{M^2-2}{2} + M$
odd	$M_1 = \frac{M-1}{2}, M_2 = \frac{M+1}{2}$	$\frac{M^2-1}{2} + M$

The solution for optimal sensors in the case of even or odd number of elements is given in Table above.

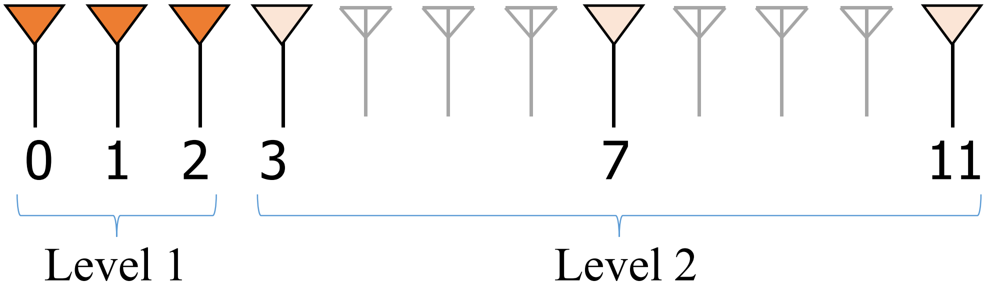

Figure 3.1: A two level nested linear array.

Since linear arrays fails to implement $2D$–DOA estimation which also applies to nested linear arrays, another type of two–dimensional ($2D$) arrays, known as the $2D$ nested arrays, was proposed in [87] and [88], whose difference co–array [102] was demonstrated to have a larger number of virtual elements in $2D$ as compared to the available number of physical sensors and able to accomplish $2D$–DOA estimation. This new class of $2D$ arrays has sensors on lattice(s) whose difference co–array give rise to a virtual $2D$ array with much larger number of elements on a dense lattice [88]. In our concept therefore which is explained in the next section, by utilizing the circular array geometry, we can estimate DOAs both in one and two dimensions.

3.2.2 The Concept of Nested Sparse Circular Array

In case of nested linear array [86], the ability of this array to resolve more sources than physical sensors is dependent on its difference co–array that obtains significantly more degrees of freedom than the original array. In related works, types of Minimum Redundancy arrays (MRAs) [103], [104] were utilized to achieve increased DOFs. The problem with MRAs is that they require an extensive computer search to construct the array [86]. In [105], a joint sparsity approach was used by adopting convex relaxation idea with co–prime arrays for off–grid targets in sparse DOA estimation. A generalization of the co–prime array concept was proposed in [106]. Until recently, most of the work associated with underdetermined DOA estimation has been implemented mainly considering nested linear arrays, co–prime arrays, and MRAs.

In our work, we consider circular arrays and attempt to provide a solution for underdetermined DOA estimation using NSCA. Figure 3.2 shows a nested sparse circular array which has two sub–circular arrays concatenated and a single element at the origin which is used in KR formulation. The center of the NSCA is considered as the origin. For an M–element NSCA, the first and second sub–circular arrays have $(M-1)$ physical elements in total. The first sub–circular array has M_1 physical elements with inter–element spacing of d_1 whilst the second sub–circular array has M_2 physical elements with inter–element spacing of d_2.

For NSCA, spacing $d_1 = 2\pi/((M-1)^2/2)$ and $d_2 = m(M_1+1)d_1$. Employing the union of first and second sub–circular arrays, we obtain the nested sparse circular array. The element positions are given by $C_{first} = m_1 d_1$, where $m_1 = 1, 2, \cdots, M_1$ and $C_{second} = m_2(M_1+1)d_1$, where $m_2 = 1, 2, \cdots, M_2$. The steering vector of the NSCA will be represented by;

$$\mathbf{a}(\theta,\phi) = [1, e^{jkr\sin\theta\cos(\phi-\gamma_1)}, e^{jkr\sin\theta\cos(\phi-\gamma_2)}, \\ \ldots, e^{jkr\sin\theta\cos(\phi-\gamma_{M-1})}]^T \tag{3.1}$$

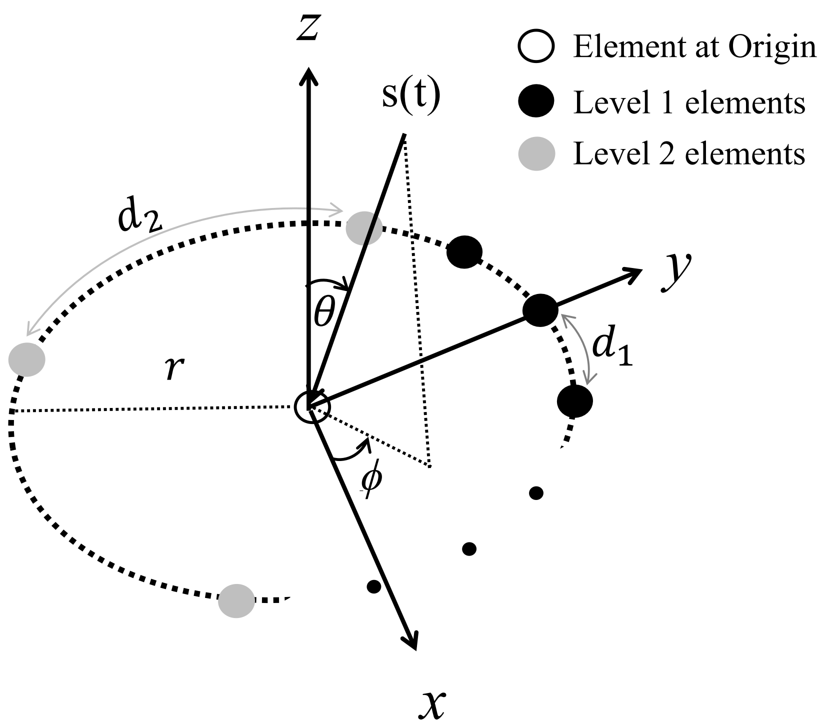

Figure 3.2: A 7 element Nested Sparse Circular Array with one element at the origin.

where γ_m is the angular position of the m-th element. The assumption we make is that elevation angle θ is fixed at 90° [31]. From this, the steering vector of the NSCA given in (3.1) as $\mathbf{a}(\theta, \phi)$ will be reduced to $\mathbf{a}(\phi)$.

To find the virtual elements and extend the array aperture, the Khatri-Rao subspace approach [92] is applied. By using this approach, we can extend the DOFs of the NSCA and be able to perform underdetermined DOA estimation. This approach therefore is described in the following subsection.

3.2.3 The Khatri-Rao Subspace Approach

In several works, increased degrees of freedom has been exploited using different techniques such as augmented matrix approach [103], [104], fourth–order cumulant based methods [107] and quasi–stationary signal based methods [92]. However, these schemes are applied to linear arrays and there is insufficient work related circular array's DOA estimation for more sources than physical sensors. Based on that account, in this subsection and the following, we will exploit the increased degrees of freedom by using the Khatri–Rao subspace approach [92] and extend the KR–MUSIC and ℓ_1–based optimization approach to underdetermined DOA estimation using NSCA.

We extend the Khatri–Rao (KR) subspace approach proposed in [92] to DOA estimation. Consider $\mathbf{A}$ which is an $L \times D$ matrix and $\mathbf{B}$ an $M \times D$ matrix having an identical number of columns, their KR product is given by

$$\mathbf{A} \odot \mathbf{B} = \left[\mathbf{a}_1 \otimes \mathbf{b}_1, \mathbf{a}_2 \otimes \mathbf{b}_2, ..., \mathbf{a}_D \otimes \mathbf{b}_D\right] \tag{3.2}$$

where $\mathbf{A} \odot \mathbf{B}$ results in an $LM \times D$ matrix. The Kronecker product $\mathbf{A} \otimes \mathbf{B}$ is the $LM \times DD$ block matrix:

$$\mathbf{A} \otimes \mathbf{B} = \begin{bmatrix} a_{11}\mathbf{B} & a_{12}\mathbf{B} & \cdots & a_{1D}\mathbf{B} \\ a_{21}\mathbf{B} & a_{22}\mathbf{B} & \cdots & a_{2D}\mathbf{B} \\ \vdots & \ddots & \cdots & \vdots \\ a_{L1}\mathbf{B} & a_{L2}\mathbf{B} & \cdots & a_{LD}\mathbf{B} \end{bmatrix} \tag{3.3}$$

For two vectors $\mathbf{a}$ and $\mathbf{b}$, their Kronecker product is given by

$$\mathbf{a} \otimes \mathbf{b} = \begin{bmatrix} a_1\mathbf{b} \\ a_2\mathbf{b} \\ \vdots \\ a_l\mathbf{b} \end{bmatrix} = \text{vec}(\mathbf{b}\mathbf{a}^T) \tag{3.4}$$

Subsequently, from KR subspace approach,a new array model is found for the proposed NSCA. In the DOA estimation problem formulated in Section 2.1, we apply vectorization to (2.11) to obtain

$$\begin{aligned} \mathbf{y} &= \text{vec}(\mathbf{R}_{xx}) \\ &= \text{vec}\left(\mathbf{A}\mathbf{R}_{ss}\mathbf{A}^H\right) + \text{vec}\left(\sigma_m^2\mathbf{I}\right) \end{aligned}$$

$$=(\mathbf{A}^* \odot \mathbf{A})\mathbf{p} + \sigma_m^2 \mathbf{1}_m^T \tag{3.5}$$

where $\mathbf{p} = [\sigma_1^2, \sigma_2^2, ..., \sigma_D^2]^T$ and $\mathbf{1}_m = [\mathbf{e}_1^T, \mathbf{e}_2^T, ..., \mathbf{e}_M^T]$ and $\mathbf{e}_i$ is a column vector that has all zeros except a 1 at the i–th position. $\mathbf{p}$ in this case is equivalent to source signal vector and noise becomes a deterministic vector that is given by $\sigma_m^2 \mathbf{1}_m$ and can easily be eliminated. In this case of vector $\boldsymbol{y}$ behaves like the array's received signal whose manifold is given by $(\mathbf{A}^* \odot \mathbf{A})$. Hence, $(\mathbf{A}^* \odot \mathbf{A})$ is a manifold of a longer array i.e., array with virtual elements with a larger array aperture than the one when it is not vectorized. Consider $\mathbf{B} = (\mathbf{A}^* \odot \mathbf{A})$, therefore, the steering matrix of array with virtual elements is given by $\mathbf{B} = [\mathbf{b}(\phi_1), \mathbf{b}(\phi_2), ..., \mathbf{b}(\phi_D)]^T$ which is an $M^2 \times D$ matrix. By applying the Kronecker product, $M^2 \times 1$ steering vector is

$$\begin{aligned}
\mathbf{b}(\phi) &= \text{vec}(\mathbf{a}(\phi)\mathbf{a}^H(\phi)) = \mathbf{a}^*(\phi) \otimes \mathbf{a}(\phi) \\
&= \begin{bmatrix} 1 \\ e^{jkr\cos(\phi-\gamma_1)} \\ e^{jkr\cos(\phi-\gamma_2)} \\ \vdots \\ e^{jkr\cos(\phi-\gamma_{M-1})} \end{bmatrix}^* \otimes \begin{bmatrix} 1 \\ e^{jkr\cos(\phi-\gamma_1)} \\ e^{jkr\cos(\phi-\gamma_2)} \\ \vdots \\ e^{jkr\cos(\phi-\gamma_{M-1})} \end{bmatrix} \\
&= \begin{bmatrix} b_1 \\ \vdots \\ b_i \\ \vdots \\ b_{M^2} \end{bmatrix}
\end{aligned} \tag{3.6}$$

for $i = 1, 2, ...M^2$. Instead of using (2.9) in this case, we apply the problem of DOA estimation to the data obtained in (3.5).

3.2.4 Concentric Extension of Nested Sparse Circular Array

In this part of the chapter, we discuss the concept of a non–uniform concentric array which is realized as a consequence of a co–array of the NSCA. The concentric extension of the nested sparse circular array enables an increase in degrees of freedom provided by the co–array, such that we are capable of performing underdetermined DOA estimation.

For an array having M sensors, with the position of an i–th sensor denoted as $\vec{x}_i$, its difference co–array is defined as

$$\mathbf{C}_d = \vec{\boldsymbol{x}}_i - \vec{\boldsymbol{x}}_j,\ \forall i, j = 1, 2, ..., M \tag{3.7}$$

In the difference co–array, $\mathbf{C}_d(i, i)$ refers to the origin of the co–array since $\vec{\boldsymbol{x}}_i - \vec{\boldsymbol{x}}_i = 0$. Although we are able to obtain M^2 distinct pairs of array elements in the co–array using the Khatri–Rao product, some of the positions in the co–array are redundant co–array points. This reduces the number of virtual elements and we therefore end up having less than (M^2) distinct points [108]. The other co–array points therefore are influenced by two distinct pairs $(\vec{\boldsymbol{x}}_i, \vec{\boldsymbol{x}}_j)$ and $(\vec{\boldsymbol{x}}_j, \vec{\boldsymbol{x}}_i)$ with $\vec{\boldsymbol{x}}_i \neq \vec{\boldsymbol{x}}_j$. As illustrated in [108], co–array of a circular array with odd number of elements is $M(M-1)+1$ while for an array with even number of elements is $(M^2/2+1)$ but in our case, the synthesized co–array points were found to be more than in [108].

To synthesize virtual elements developed from the NSCA using the KR product, we consider $\mathbf{b}(\phi)$. From (3.6), let $m, l \in \{C_{first}\ C_{second}\}$. The first $2M$ points will be determined by $1 \otimes e^{jkr\cos(\phi-\gamma_l)}$ and $e^{jkr\cos(\phi-\gamma_m)} \otimes 1$ that are redundant points and the remaining points are given by;

$$\begin{aligned}\mathbf{b}_{ml}(\phi) &= e^{jkr\cos(\phi-\gamma_m)} \otimes e^{jkr\cos(\phi-\gamma_l)} \\ &= e^{jkr\{\cos(\phi-\gamma_m)-\cos(\phi-\gamma_l)\}}\end{aligned} \tag{3.8}$$

from trigonometric addition, $\mathbf{b}(\phi)$ becomes;

$$\begin{aligned}\mathbf{b}_{ml}(\phi) &= e^{-j2kr\{\sin((2\phi-\gamma_m-\gamma_l)/2)\sin((\gamma_m-\gamma_l)/2)\}}\\ &= e^{-j2kr\{\sin(\phi-(\gamma_m+\gamma_l)/2)\sin((\gamma_m-\gamma_l)/2)\}}\end{aligned} \tag{3.9}$$

From this equation, it is observed that we end up with virtual elements located on positions having different radius from the origin implying that using KR approach together with NSCA, we synthesize virtual elements onto a non–uniform concentric circular array. Figure 3.2 shows NSCA whilst in Fig. 3.3, the synthesized version of the array is shown having with virtual elements. This is basically a concentric extension of NSCA.

The number of elements in the concentric extension of the NSCA as shown in Fig. 3.3 (which is given by $\mathbf{C}_d$) determines the values of the cross correlation values in the covariance matrix of the received signal by NSCA [86]. By carefully using cross correlation values, we substantially increase the degrees of freedom, thus, we are able to detect or estimate more number of sources than the number of physical elements using the NSCA. From the synthesized non–uniform concentric circular array, we can easily perform wideband underdetermined DOA estimation as well.

3.2.5 KR–MUSIC based Underdetermined DOA Estimation

We use an ideal MUSIC [49] based approach for exploiting the degrees of freedom of the nested sparse circular array with virtual elements. At first, unknown noise covariance is eliminated and then we perform dimension reduction [92]. In order to get rid of the noise covariance, we consider $\mathbf{q}^{\perp}_{\mathbf{1}_M}$ to denote an orthogonal complement projector, where $\mathbf{q}^{\perp}_{\mathbf{1}_M} = \mathbf{I}_M - (1/M)\mathbf{1}_M\mathbf{1}_M^T$. By operating a projection on (3.5), we obtain

$$\mathbf{y}\mathbf{q}^{\perp}_{\mathbf{1}_M} = (\mathbf{A}^* \odot \mathbf{A})(\mathbf{q}^{\perp}_{\mathbf{1}_M}\mathbf{p})^T \tag{3.10}$$

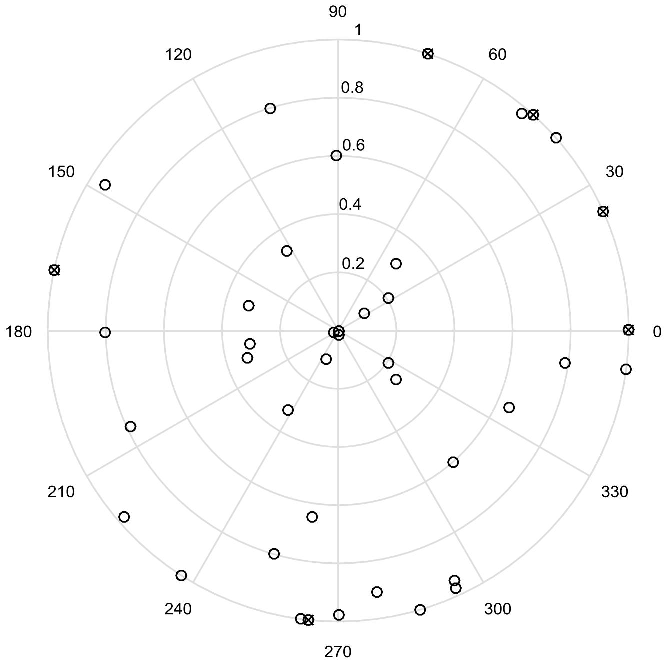

Figure 3.3: Synthesized Concentric extension of Nested Sparse Circular Array. Physical element positions are given by ⊗ and virtual element positions by ∘.

The singular value decomposition (SVD) of $\mathbf{yq}^{\perp}_{\mathbf{1}_M}$ is therefore

$$\mathbf{yq}^{\perp}_{\mathbf{1}_M} = \begin{bmatrix} \mathbf{U}_s \\ \mathbf{U}_n \end{bmatrix} \begin{bmatrix} \sum_s \mathbf{0} \\ \mathbf{0}\ \mathbf{0} \end{bmatrix} \begin{bmatrix} \mathbf{V}_s^H \\ \mathbf{V}_n^H \end{bmatrix}^* \tag{3.11}$$

where $\mathbf{U}_s$ the left and $\mathbf{V}_s$ is the right singular matrix that is associated with nonzero singular values for signals respectively, $\mathbf{U}_n$ and $\mathbf{V}_n$ are the left and right singular matrices associated with zero singular values for noise respectively, and $\sum_s$ is a diagonal matrix whose diagonals contain the nonzero singular values.

It was proved in [92] that for $(\mathbf{A}^* \odot \mathbf{A})$ to yield a full column rank i.e rank $= D$ the sufficient and necessary condition is when $D \leq 2M - 1$. Thus, before applying subspace approach to DOA estimation problem such as MUSIC, we ought to reduce the dimension problem. The dimension reduction idea as proposed in [92] is as follows; Let the virtual array response matrix $(\mathbf{A}^* \odot \mathbf{A}) = \mathbf{GB}$ where $\mathbf{B}$ is a dimensionally reduced virtual array response matrix which is $(2M) \times D$ given by $\mathbf{B} = [\mathbf{b}(\phi_1), \mathbf{b}(\phi_2), ..., \mathbf{b}(\phi_D)]^T$ as compared to one given in (3.6) which is an $M^2 \times D$ matrix and $\mathbf{G}$ is an $(M^2 + M) \times (2M)$ matrix given by

$$\mathbf{G} = \begin{bmatrix} \mathbf{0} \cdots \mathbf{0} & \mathbf{0} & \mathbf{I}_M \\ \mathbf{0} \cdots \mathbf{0} & \mathbf{I}_M & \mathbf{0} \\ \vdots \;\iddots \iddots & \iddots & \vdots \\ \mathbf{0} \;\iddots \iddots & \iddots & \vdots \\ \mathbf{I}_M \, \mathbf{0} \, \mathbf{0} & \cdots & \mathbf{0} \end{bmatrix} \tag{3.12}$$

where $\mathbf{I}_M$ is an $M \times M$ identity matrix, and $\mathbf{0}$ is an $M \times 1$ zero vector. From (3.12), it can verified that $\mathbf{G}$ is column orthogonal [92]. Let $\mathbf{F} = \mathbf{G}^T\mathbf{G}$, this implies that

$$\mathbf{F} = \mathrm{diag}(1, 2, ...M - 1, M, M - 1, ..., 2, 1) \tag{3.13}$$

from (3.10), this problem can therefore result in

$$\begin{aligned} \hat{\mathbf{y}} &= \mathbf{F}^{-\frac{1}{2}}\mathbf{G}^T \left[\mathbf{y}\mathbf{q}^{\perp}_{\mathbf{1}_M}\right] \\ &= \mathbf{F}^{-\frac{1}{2}}\mathbf{G}^T(\mathbf{A}^* \odot \mathbf{A})(\mathbf{q}^{\perp}_{\mathbf{1}_M}\mathbf{p})^T \\ &= \mathbf{F}^{\frac{1}{2}}\mathbf{B}(\mathbf{q}^{\perp}_{\mathbf{1}_M}\mathbf{p})^T \end{aligned} \tag{3.14}$$

the dimension reducing transformation $\mathbf{F}^{-\frac{1}{2}}\mathbf{G}^T$ has orthonormal rows. We apply subspace based method to $\hat{\mathbf{y}}$ that is $(2M - 1) \times 1$. MUSIC is therefore applied to the dimensionally reduced problem, whose spectrum is given by

$$P(\phi) = \frac{1}{\left\|\mathbf{U}_n^H \mathbf{F}^{\frac{1}{2}} \mathbf{b}(\phi)\right\|^2} \tag{3.15}$$

over $\phi \in [0, \pi]$. From this, we pick D largest peaks of $P(\phi)$ as the DOA estimates.

3.2.6 ℓ_1–based Optimization DOA Estimation

Sparse signal representation employs the ideas of enforcing sparsity by ℓ_1 penalization and at the same time, restricting error by ℓ_2–norm which facilitates the reconstruction of sparse signals [95]. Through the sparsity framework, multiple measurements vectors are employed to this problem of estimating an unknown sparse parameter. Thus, the DOA estimation problem is extended to a problem of finding the sparsest solution to an underdetermined linear system [55]. In this work, we develop an ℓ_1–based optimization method initially proposed in [95] and extend it to underdetermined DOA estimation such that we increase the DOFs to $2M$. We consider (3.5) as a sparse signal representation problem given by

$$\mathbf{y} = \mathbf{B}\mathbf{p} + \sigma_m^2 \mathbf{1}_m \tag{3.16}$$

where $\mathbf{B}$ is as defined in section 3.2.3. To extend ℓ_1 penalization to (3.16), we are required to appropriately choose the optimization criteria which is given by; $\min\|\mathbf{p}\|_1$ subject to $\|\mathbf{y} - \mathbf{B}\mathbf{p}\|_2^2 \leq \beta^2$. From this, β is a parameter specifying how much noise we desire to allow. An unconstrained form of this objective function is

$$\min \|\mathbf{y} - \mathbf{B}\mathbf{p}\|_2^2 + \lambda \|\mathbf{p}\|_1 \tag{3.17}$$

The ℓ_2 term in (3.17) forces the residual $\mathbf{y}$–$\mathbf{B}\mathbf{p}$ to be small and the λ term controls tradeoff between the sparsity of the spectrum and residual norm [109].

In a practical setting, $\boldsymbol{y}$ in (3.16) can be estimated from N snapshots such that $\Delta\mathbf{y} = \hat{\mathbf{y}} - \mathbf{y}$. The estimate error [110] is asymptotically normal distribution (AsN), thus

$$\Delta\mathbf{y} = \text{vec}(\Delta\mathbf{R}_{xx}) \sim AsN\left(0_{M^2,1}, \frac{1}{N}\mathbf{R}_{xx}^T \otimes \mathbf{R}_{xx}\right) \tag{3.18}$$

which then leads to

$$\mathbf{W}^{-\frac{1}{2}}\Delta\mathbf{y} \sim AsN\left(0_{M^2,1}, \mathbf{I}_{M^2}\right) \tag{3.19}$$

where $\mathbf{W}^{-\frac{1}{2}} = \sqrt{N}\mathbf{R}_{xx}^{-\frac{T}{2}} \otimes \mathbf{R}_{xx}^{-\frac{1}{2}}$ is the weighting matrix in which $\mathbf{W} = \frac{1}{N}\mathbf{R}_{xx}^T \otimes \mathbf{R}_{xx}$. Let us consider $\hat{\mathbf{p}}$ to be the estimate of $\mathbf{p}$. From this, the DOA estimation problem can be given by the following ℓ_1–norm minimization

$$\min_{\hat{\mathbf{p}}} \|\hat{\mathbf{y}} - \mathbf{B}\hat{\mathbf{p}}\|_2^2 + \lambda \|\hat{\mathbf{p}}\|_1 \tag{3.20}$$

from (3.19) and (3.20) we further deduce that

$$\mathbf{W}^{-\frac{1}{2}} [\hat{\mathbf{y}} - \mathbf{B}\hat{\mathbf{p}}] \sim AsN\left(0_{M^2,1}, \mathbf{I}_{M^2}\right) \tag{3.21}$$

which then results in

$$\mathbf{W}^{-\frac{1}{2}} \|\hat{\mathbf{y}} - \mathbf{B}\hat{\mathbf{p}}\|_2^2 \sim As\chi^2(M^2) \tag{3.22}$$

where $As\chi^2(M^2)$ expresses the asymptotic chi–square distribution with M^2 degrees of freedom. The parameter β is then introduced such that $\left\|\mathbf{W}^{-\frac{1}{2}} [\hat{\mathbf{y}} - \mathbf{B}\hat{\mathbf{p}}]\right\|_2^2 \leq \beta^2$. Therefore, DOA estimation problem is reduced to

$$\min_{\hat{\mathbf{p}}} \|\hat{\mathbf{p}}\|_1 \text{ subject to } \left\|\mathbf{W}^{-\frac{1}{2}} [\hat{\mathbf{y}} - \mathbf{B}\hat{\mathbf{p}}]\right\|_2^2 \leq \beta^2 \tag{3.23}$$

where $\beta = \sqrt{\chi^2(M^2)}$. The problem (3.23) is a second–order cone (SOC) program problem. For numerical solution of this SOC problem, off the shelf optimization softwares such as CVX [65] which is a Matlab Software for Disciplined Convex Programming and SeDuMi [111] can also be used to efficiently solve the SOC problem.

3.3 Simulation Results

3.3.1 Specifications of Simulation

We implement simulation experiments to assess the effectiveness of NSCA in estimating more sources than the number of physical sensors. In this section, numerical examples conducted shows superior performance of the proposed array geometry in terms of degrees of freedom for underdetermined DOA estimation as well as root mean square error (RMSE). For some of the examples presented in this chapter, a 7 element NSCA antenna system ($M = 7$) is examined as shown in Fig. 3.2 with two sub-circular arrays concatenated and one element at the center of the array. 8 narrowband sources ($D = 8$) are impinging on the array from the directions $\phi = [15°, 36°, 46°, 70°, 90°, 112°, 130°, 145°]$, all having the same amount of power. In case when 10 narrowband sources ($D = 10$) are used, $\phi = 54°$ and $162°$ directions are added. In terms of the radius size of the array, $r = \lambda$ is used for the NSCA. The noise is assumed to be spatially and temporally white.

3.3.2 Underdetermined DOA Estimation Spectra

Figure 3.4(a) presents the DOA spectra when we apply the subspace based approach MUSIC for underdetermined DOA estimation. In this case, we observe that all DOAs are resolved correctly and the peaks are sharp but we obtain a low dynamic range. In Fig. 3.4(b) we inspect the DOA spectra of ℓ_1–based optimization for sparse signal recovery in an underdetermined case. In the case of ℓ_1–based optimization, all DOAs are resolved and the estimation is accurate. The peaks in this method are very sharp and we obtain a very high dynamic range. Both methods in Fig. 3.4 requires more snapshots to resolve DOAs correctly but the ℓ_1–based technique have higher dynamic range as compared to MUSIC based method. In Fig. 3.5, DOA estimation spectra for 10 DOAs is shown. This case also has similar results and observations as the one in Fig. 3.4. Both methods use a total number of snapshots of 2000, and an SNR of 0 dB.

3.3.3 SNR Performance Comparison for Underdetermined DOA Estimation

We examine the performance comparison of MUSIC algorithm, the ℓ_1–based optimization technique and the cramer–rao lower bound (CRLB) [112], [113]. This is achieved by examining the RMSE of angular estimates as a function of signal to noise ratio (SNR).

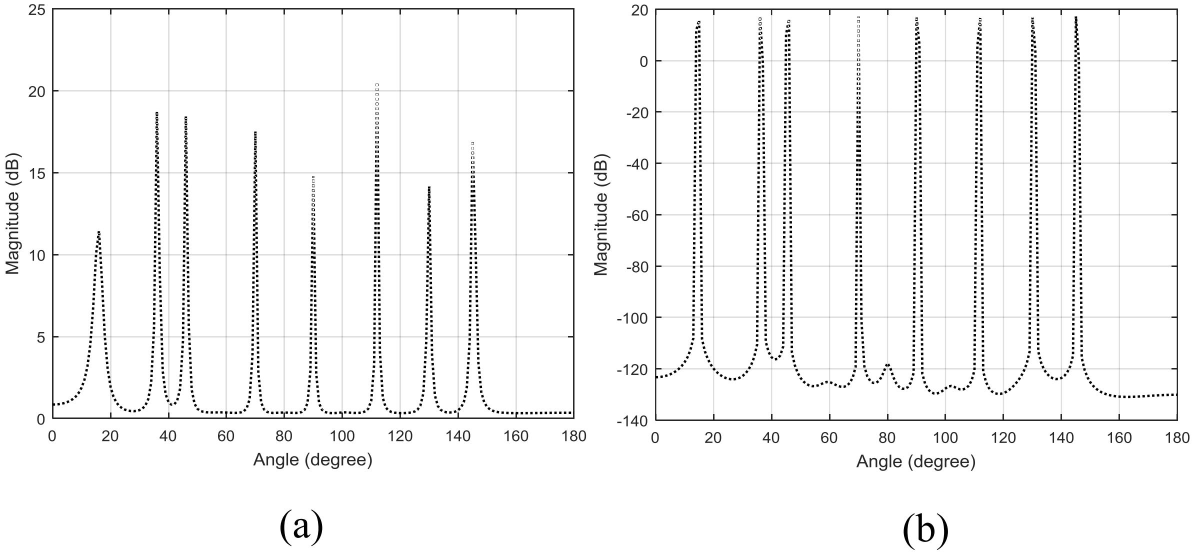

Figure 3.4: DOA estimation spectra using NSCA. $M = 7$, $D = 8$, snapshots = 2000, and SNR = 0 dB in the case of using (a) MUSIC and (b) ℓ_1–based optimization.

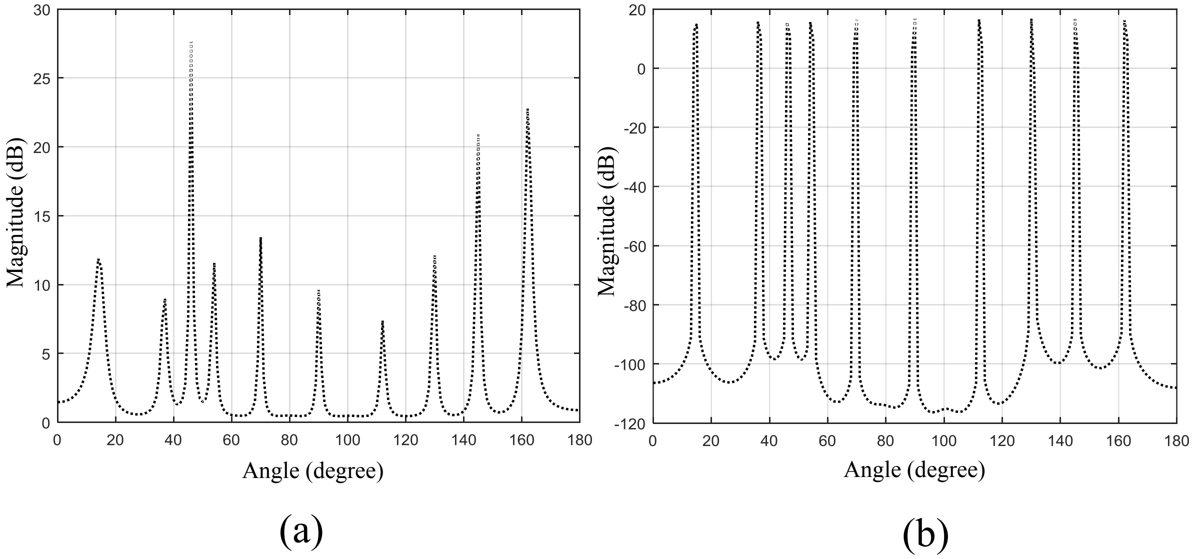

Figure 3.5: DOA estimation spectra using NSCA. $M = 7$, $D = 10$, snapshots = 2000, and SNR = 0 dB in the case of using (a) MUSIC and (b) ℓ_1–based optimization.

Thus, CRLB is used as the benchmark for an unbiased estimator. We perform the comparison for the cases of 8 sources ($D = 8$) and 10 sources ($D = 10$). The performance is found to be not angular dependent since similar observations were made at different angles. The number of trials used in this example is 100. The RMSE is defined as

$$\text{RMSE} = \sqrt{\frac{1}{T_r}\sum_{tr=1}^{T_r}\left\{\frac{1}{D}\sum_{d=1}^{D}(\hat{\phi}_d - \phi_d)^2\right\}} \tag{3.24}$$

where T_r is the number of trials, ϕ_d shows the true DOAs and $\hat{\phi}_d$ represents estimated DOAs. In these simulations, the number of snapshots is 10000.

In Fig. 3.6(a), the RMSE as a function of SNR is presented. In this figure, 8 DOAs are assumed to be impinging on the nested sparse circular array for 10000 snapshots averaged over 100 monte carlo simulations. In both methods, the estimation performance improves as the SNR increases. However, subspace based technique MUSIC has lower RMSE performance as compared to ℓ_1–based optimization method but becomes closer to ℓ_1–based method at an SNR of 20 dB. In Fig. 3.6(b) we observe the RMSE of MUSIC and ℓ_1–based optimization as a function of SNR for 10 DOAs impinging on the NSCA. In this case, the observation is that ℓ_1–based optimization method outperforms subspace method MUSIC. For ℓ_1–based method, it achieves an RMSE of about 0.18 degrees. From the results in Fig. 3.6(a) and (b) ℓ_1–based optimization method is clearly a better method than MUSIC–based method.

3.3.4 Snapshots Performance Comparison for Underdetermined DOA Estimation

In this subsection, we investigate the performance comparison of nested circular array in relation to the RMSE of the angle estimates and the number of snapshots in an underdetermined DOA estimation scenario. We first consider 8 signals arriving on the array in the case of the number of physical elements $M = 7$. We consider an SNR of 20 dB averaged over 100 monte carlo simulations. In Fig. 3.7(a) we observe that the more

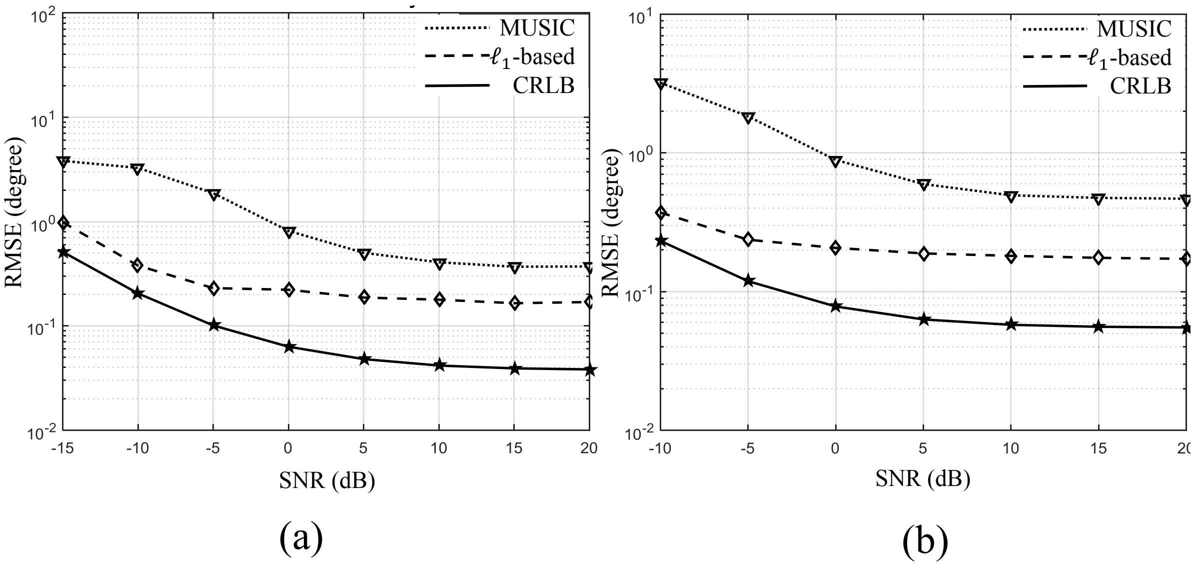

Figure 3.6: RMSE performance versus SNR of MUSIC and ℓ_1–based optimization for underdetermined DOA estimation using NSCA with $M = 7$, Snapshots = 10000 for (a) $D = 8$, and (b) $D = 10$.

snapshots we have, the better the RMSE performance will be. The RMSE of ℓ_1–based optimization method in this figure is better than that subspace based method MUSIC and at 18000 snapshots, its performance becomes closer to the CRLB. For the case of 10 signals impinging on the nested circular as shown in Fig. 3.7(b), we have the same observation in which the increase in the number of snapshots leads to better RMSE performance but the ℓ_1–based optimization method has better RMSE than subspace based technique MUSIC as well.

3.3.5 Degrees of Freedom

In the next example we take into consideration the degrees of freedom obtained by the ℓ_1–based optimization approach. Because of its reduced dimension, MUSIC method obtains *2M-2* degrees of freedom but the extended ℓ_1–based optimization approach has improved DOFs. Figure 3.8 shows the DOA estimation using the ℓ_1–based op-

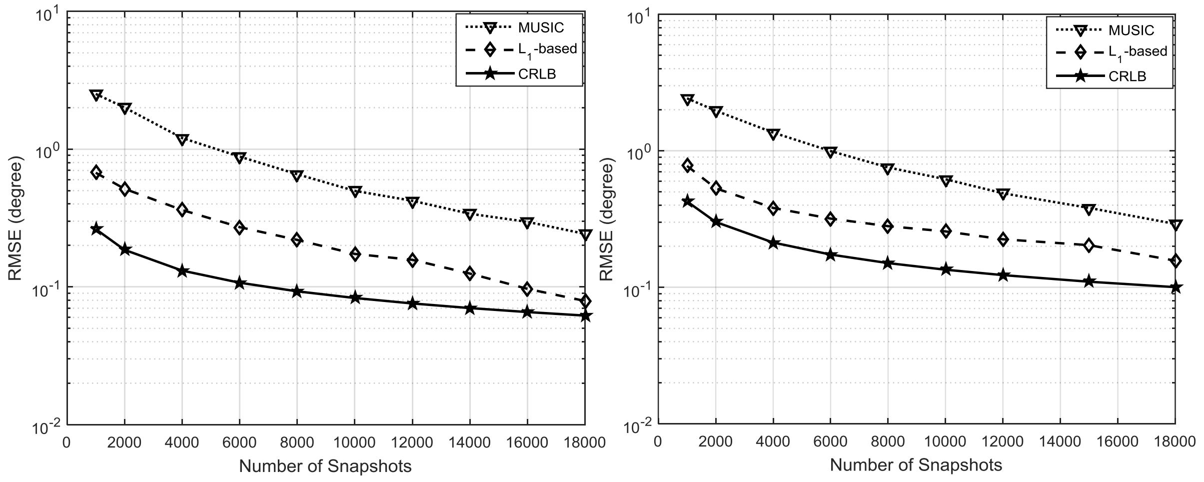

(a) (b)

Figure 3.7: RMSE performance comparison as a function of number of snapshots for NSCA using MUSIC and ℓ_1–based optimization. $M = 7$, SNR = 20 dB for (a) $D = 8$, and (b) $D = 10$.

timization approach for 13 signals impinging on the NSCA from the directions $\phi = [15°, 32°, 43°, 58°, 73°, 80°, 90°, 98°, 112°, 124°, 135°, 145°, 162°]$. Thus the method obtains up to $2M - 1$ degrees of freedom for an array with odd number of sensors.

For the results shown in Fig. 3.8, we considered an array with an odd number of sensors. We therefore extend this analysis to the case in which the array has an even number of sensors. In the case, we consider an array in which the number of sensors is even ($M = 6$). Using the ℓ_1–based optimization technique, the underdetermined DOA estimation achieved $2M$ DOFs which is illustrated in Fig. 3.9.

3.3.6 Average Run–time

The last example in this subsection presents the average CPU run–time as a function of the number of incoming signals. In this problem, we compare the performance of the two algorithms; subspace based method MUSIC and ℓ_1–based optimization using NSCA

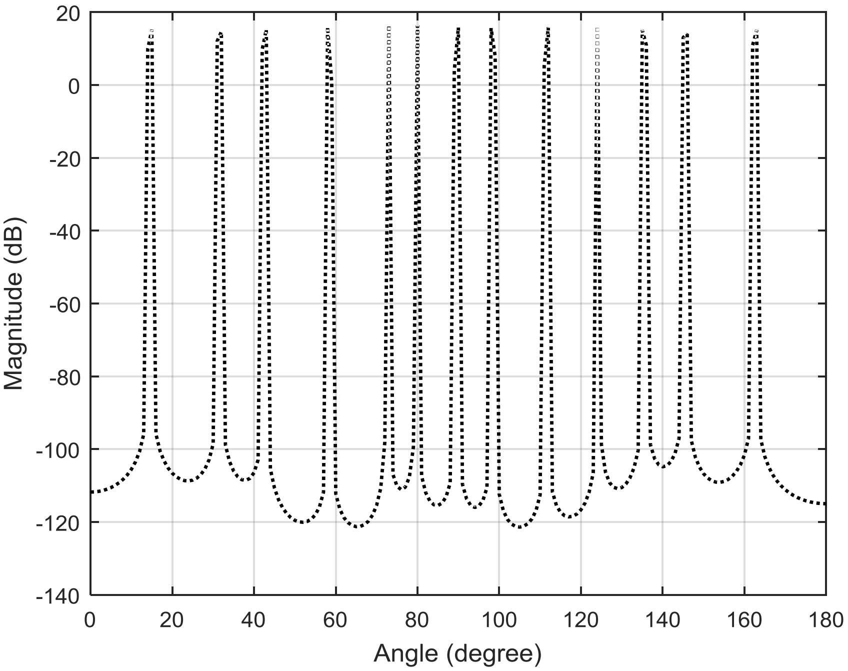

Figure 3.8: Degrees of freedom obtain by ℓ_1-based optimization technique. $D = 13$, Snapshots = 10000.

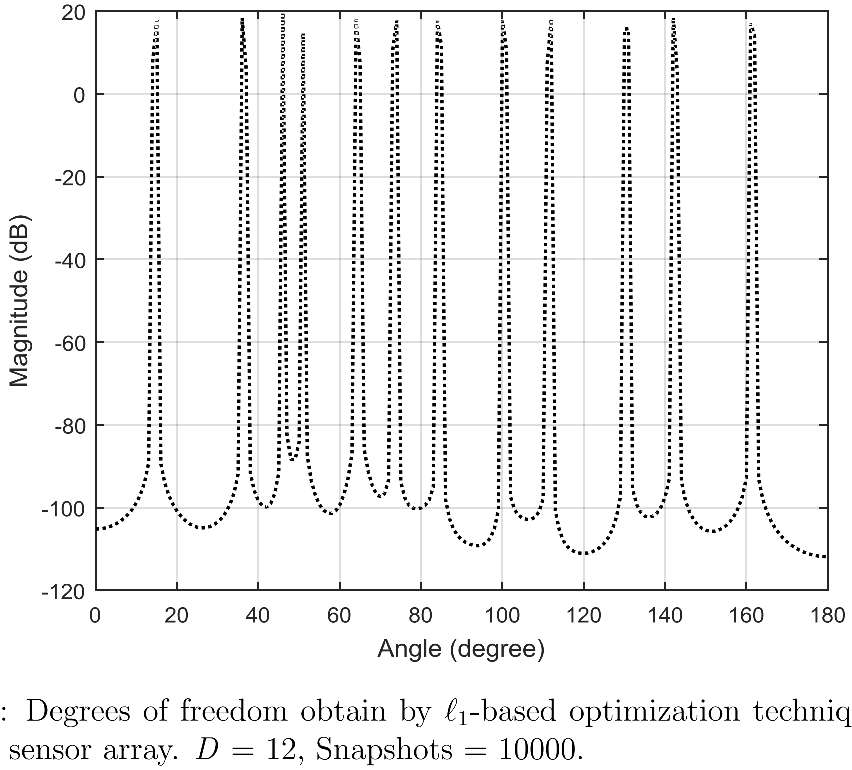

Figure 3.9: Degrees of freedom obtain by ℓ_1-based optimization technique for an even number of sensor array. $D = 12$, Snapshots = 10000.

with different number of signals impinging on the array. In Fig. 3.10, the performance comparison shown. From the results in Fig. 3.10, it is observed that MUSIC requires very little amount of time to run. As compared to MUSIC, the ℓ_1–based optimization technique requires almost twice the amount of time. Although ℓ_1–based optimization method requires much more amount of run time,the method has superior performance as compared to MUSIC in terms of DOA estimation spectra and RMSE.

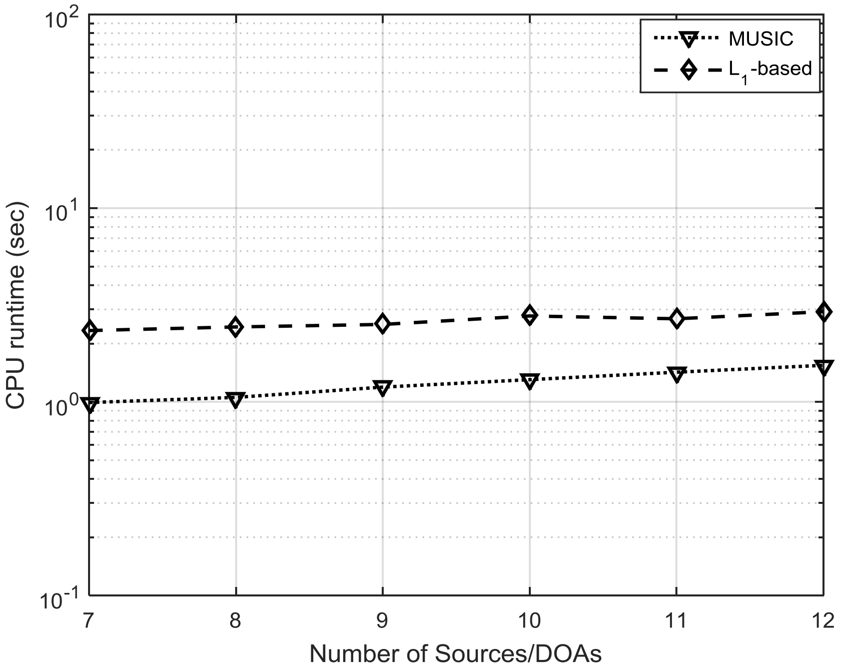

Figure 3.10: Average CPU runtime comparison versus DOAs for MUSIC and ℓ_1–based optimization using NSCA. $M = 7$, $D = 8$, SNR = 20 dB, and Snapshots = 10000.

3.4 Distributed Source Underdetermined DOA Estimation

In the field of array signal processing, the direction of arrival (DOA) estimation problem has the assumption that signals sources are point sources [114]. On the contrary, in reality, signals that are received at an array include not only a direct path signal (which can be regarded as a point source) but are also angularly spread signals. This means that these signals are coherent, phase–delayed, and amplitude–weighted replicas of the direct path signal [115], [116]. As an example, low–elevation radio links are subject to ground reflections resulting in distributed signal source [114]. Therefore, signals detected by an array can then be a continuum of directions [115]. A distributed source model is more suitable for a realistic scenario due to some environmental phenomenon. In this section, we consider distributed sources as applied to underdetermined direction of arrival estimation.

3.4.1 Numerical Simulations for Distributed Sources

To evaluate the performance of distributed source underdetermined DOA estimation using nested sparse circular array, numerical simulations were conducted. We investigate the performance of a 6 element nested sparse circular array ($M = 6$) with 7 narrowband distributed sources ($D = 7$). The distributed sources are impinging on the array from the directions $\phi = [20°, 35°, 65°, 80°, 110°, 130°, 145°]$. In terms of distributed sources, two classes are investigated; (i) same spreading parameter $\rho = 0.7$, and (ii) different spreading parameter values $\rho = [0.6, 0.8, 0.7, 0.6, 0.9, 0.7, 0.8]$.

In Fig. 3.11, the DOA estimation spectrum is presented. In this figure, we compare the case with same spreading parameter ρ in Fig. 3.11(a) and different values spreading parameter ρ in Fig. 3.11(b) of utilizing MUSIC algorithm. In Fig. 3.12, we apply ℓ_1–based optimization algorithm for the two cases as well Fig. 3.12(a) same value of ρ and Fig. 3.12(b) different value of ρ. As observed in Figs. 3.11 and 3.12, all the seven distributed sources are resolved for both case (i) and case (ii). For the case using same spreading parameter ρ (i), it achieves better performance as compared to the case with different spreading parameters (ii). We also note that it is not always the case that all the sources or DOAs can be resolved. When we have smaller SNR values, smaller spreading parameters, and/or fewer samples, there is a high probability of false estimation [116].

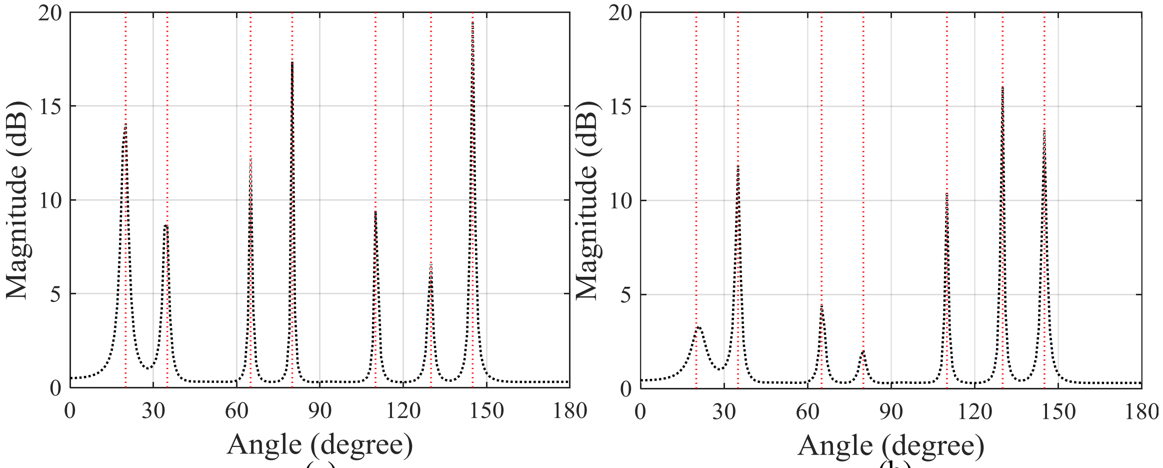

(a) (b)

Figure 3.11: MUSIC DOA estimation spectrum for distributed sources (a) same ρ and (b) different values of ρ , SNR = 10 dB, Number of Snapshots = 1000.

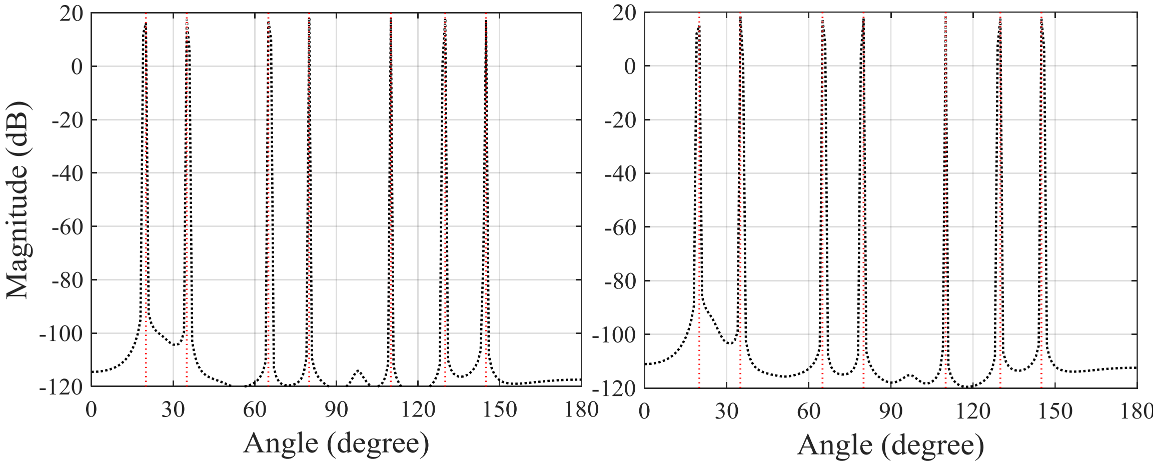

(a) (b)

Figure 3.12: ℓ_1–based optimization DOA estimation spectrum for distributed sources (a) same ρ and (b) different values of ρ , SNR = 10 dB, Number of Snapshots = 1000.

3.4.2 RMSE for Distributed Sources

The RMSE performance as a function of SNR is represented in Fig. 3.13. In Fig. 3.13(a) MUSIC algorithm is applied whilst in Fig. 3.13(b) we use the ℓ_1–based optimization algorithm. In Fig. 3.13(a), we observe that when we have lower SNR levels, both cases of ρ (i) and (ii) have poor performance but as the SNR levels increases, case (i) with same values of ρ obtains better DOA estimation performance as compared to the case (ii) that uses different spreading parameter values. In Fig. 3.13(b), we compare the performance when using ℓ_1–based optimization algorithm. In this figure, we observe that in both cases, with same spreading parameter or different spreading parameter values, the performance does not change. This indicates that ℓ_1–based optimization algorithm has robust performance even when the signal sources are distributed. To this extent, we conclude that the underdetermined DOA estimation accuracy of ℓ_1–based optimization is not affected by angularly spread signal or distributed sources.

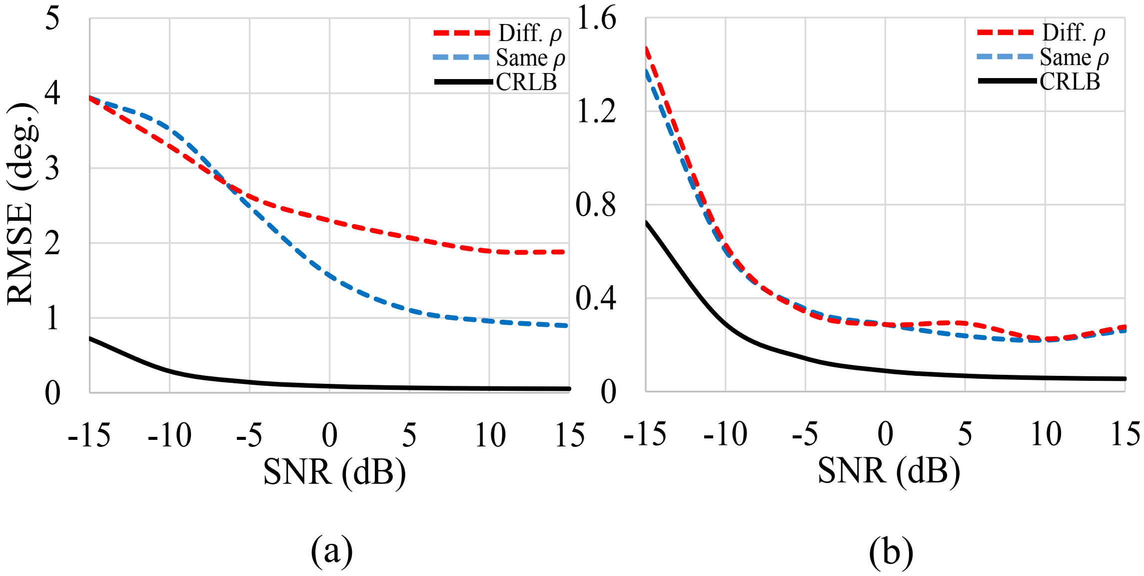

Figure 3.13: RMSE versus SNR performance for distributed sources (a) MUSIC and (b) ℓ_1–based optimization.

3.4.3 Probability of Resolution

In DOA estimation problem, there is an increasing demand for higher accuracy of target angular measurements when using various techniques for angle spectrum estimation. Nearly all the estimation techniques exploit angle information in one way or the other, from the second–order statistics of the array data, in the form of a sensor covariance matrix [117]. Since high resolution is the main motivation for the development of modem spectrum estimation techniques, the resolution capability is undoubtedly the most important performance index of DOA estimation algorithms.

In this subsection, we analyze the probability of the MUSIC and ℓ_1–based optimization algorithm in resolving two spatially separated signal sources in the context of array processing. The problem is tackled in a fashion where the different circular array's probability of resolving signals is compared when using a distributed source signal with same value of spreading parameter ρ. In this comparison, two closely spaced impinging signals are used with $\phi = [20^\circ, 25^\circ]$ for Fig. 3.14(a). In this figure, performance of probability of resolution as a function of SNR is shown. For the two algorithms, ℓ_1–based optimization has better performance since it is able to resolve closed spaced signals for very low SNR levels.

In Fig. 3.14(b), we verify probability of resolution for the two algorithms (MUSIC and ℓ_1–based optimization) as a function of angular change. In this case, we start at an angle ϕ and add $\Delta\phi$ to ϕ. It is verified in Fig. 3.14(b) that ℓ_1–based optimization can resolve very closely spaced signals as compared to MUSIC algorithm.

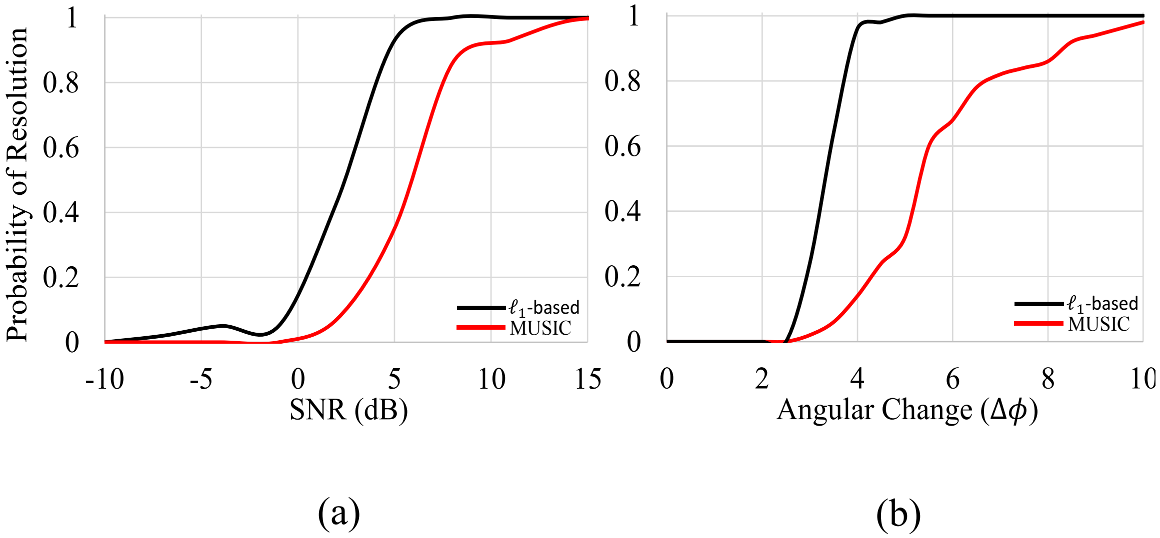

Figure 3.14: probability of resolving closely spaced signals for MUSIC and ℓ_1–based optimization.

3.5 Optimal Array

In circularly configured arrays, there are few geometries that deals with underdetermined DOA estimation, for example, NSCA [47], and SR [100]. In the case of limited number of antenna elements available, the problem of optimum array geometry naturally arises [118]. A class of non uniformly spaced arrays also known as sparse arrays provide a better solution. In [100], optimal array structures were examined. Optimal and nearly optimal schemes operating both in a periodic and non–periodic form were designed by considering linear compression schemes. [99] proposed a nested circular array (NCA) which has advantages over conventional methods in that, it is used to eliminate spatial aliasing for counting and DOA estimation of multiple simultaneous speakers. In NCA, each microphone pair is only used in appropriate sub-band according to its inter–microphone distance which enables the proposed method in [99] to achieve an acceptable performance in both reverberant and noisy conditions. Although this is the case, NCA is basically UCA in structure.

In this section, we analyze the performance of three circular array geometries for underdetermined DOA estimation. By utilizing a sparsity–aware technique with ℓ_1–penalization, we are able to estimate more sources than sensors. In the simulation examples, the results confirms that NSCA is capable of performing underdetermined DOA estimation better than SR and UCA.

As an example in this section, the performance comparison of different array geometries is performed to ascertain an optimal array configuration in underdetermined DOA estimation. We examine 3 circular array configurations shown in Fig. 3.15; (a). Nested Sparse Circular Array (NSCA) proposed in this chapter, (b). the length-20 circular sparse ruler proposed in [100], and (c). Uniform Circular Array (UCA) which is a conventional circular array type and is also similar to an array type considered in [99].

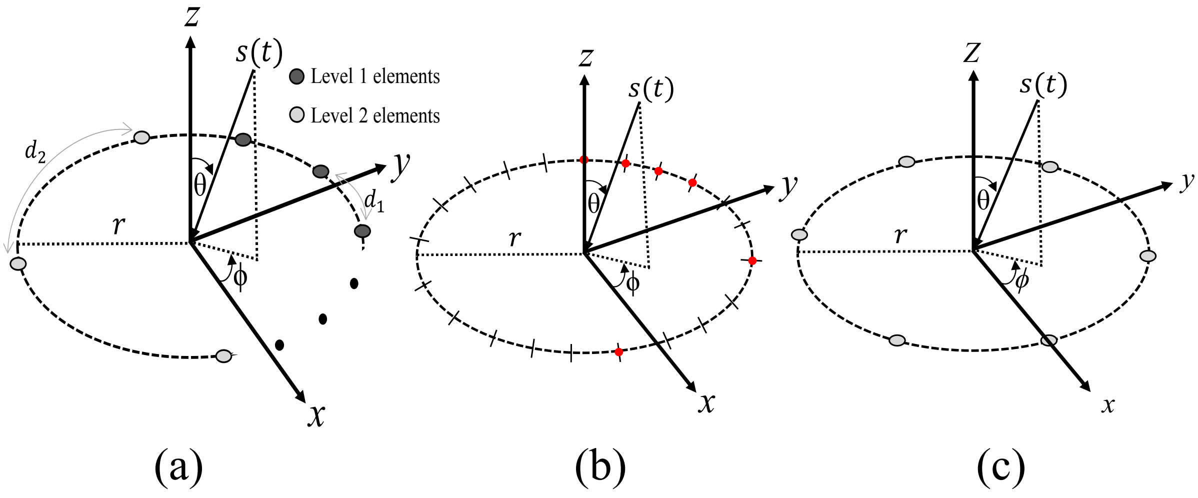

Figure 3.15: Different array geometries (a). Nested Sparse Circular Array (NSCA), (b). the length–20 circular sparse ruler (SR), and (c). Uniform Circular Array (UCA).

3.5.1 Spectra Performance Comparison for Underdetermined DOA Estimation

In this subsection, simulation results for optimum array configuration is reported. We compared NSCA, SR and UCA. In Fig. 3.16, we consider the spectra performance comparison when eight sources are impinging on a six element array with $\phi = [15°, 36°, 46°, 70°, 90°, 112°, 130°, 145°]$. In Fig. 3.16, we observe the spectra for underdetermined DOA estimation for the three arrays compared in this subsection. From this figure, we observe that NSCA has better DOA estimation performance. This is followed by SR whilst UCA has poor performance. In the case of UCA, although the array is capable of resolving the DOAs, there are errors in estimation as well. On top of this, we also observe low dynamic range for UCA estimation performance whilst we have higher dynamic range for NSCA in both (a) MUSIC and (b) ℓ_1–based optimization methods for underdetermined DOA estimation.

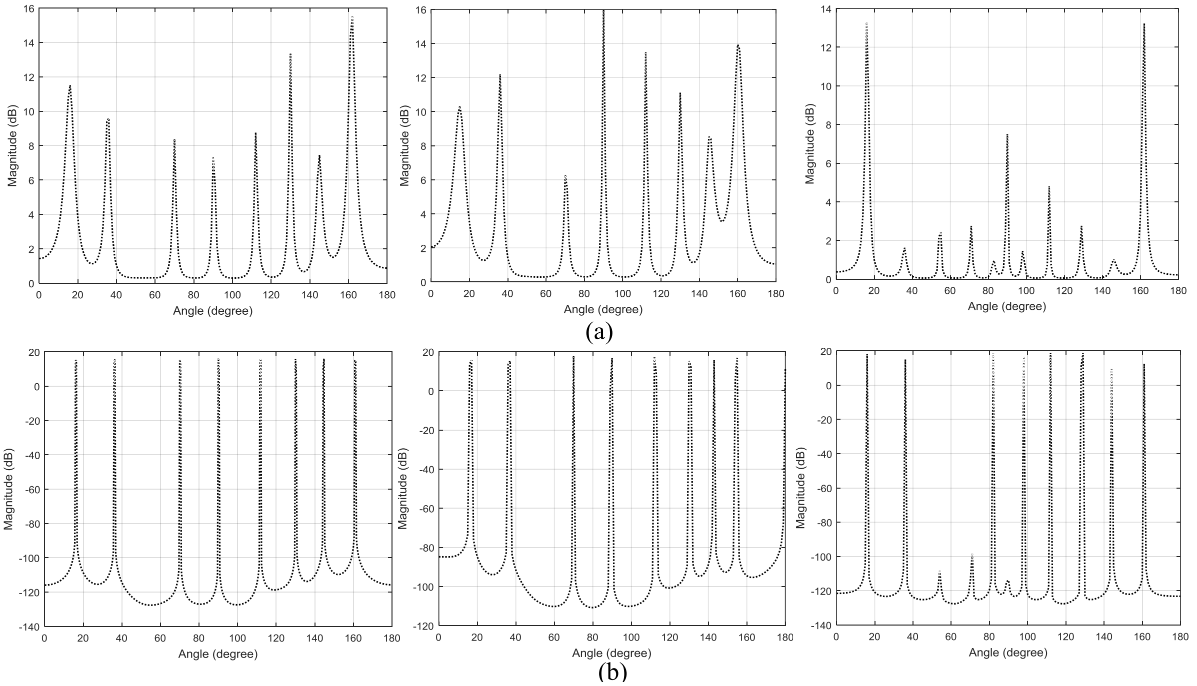

(a)

(b)

Figure 3.16: Underdetermined DOA estimation spectra for different arrays (a). Using MUSIC method, and (b) ℓ_1–based optimization for (NSCA), SR and UCA from left to right.

3.5.2 RMSE Performance Comparison for Underdetermined DOA Estimation

In Fig. 3.17, we consider the accuracy of DOA estimation by examining the RMSE as a function of SNR. In this figure, we compare the RMSE performance when eight sources are impinging on a six element array. As observed in Fig. 3.17 as well as from previous subsection 3.5.1, NSCA has better RMSE performance amongst the different circular array geometries. NSCA configuration provides a better distribution of virtual elements which are significant in the underdetermined DOA estimation [118].

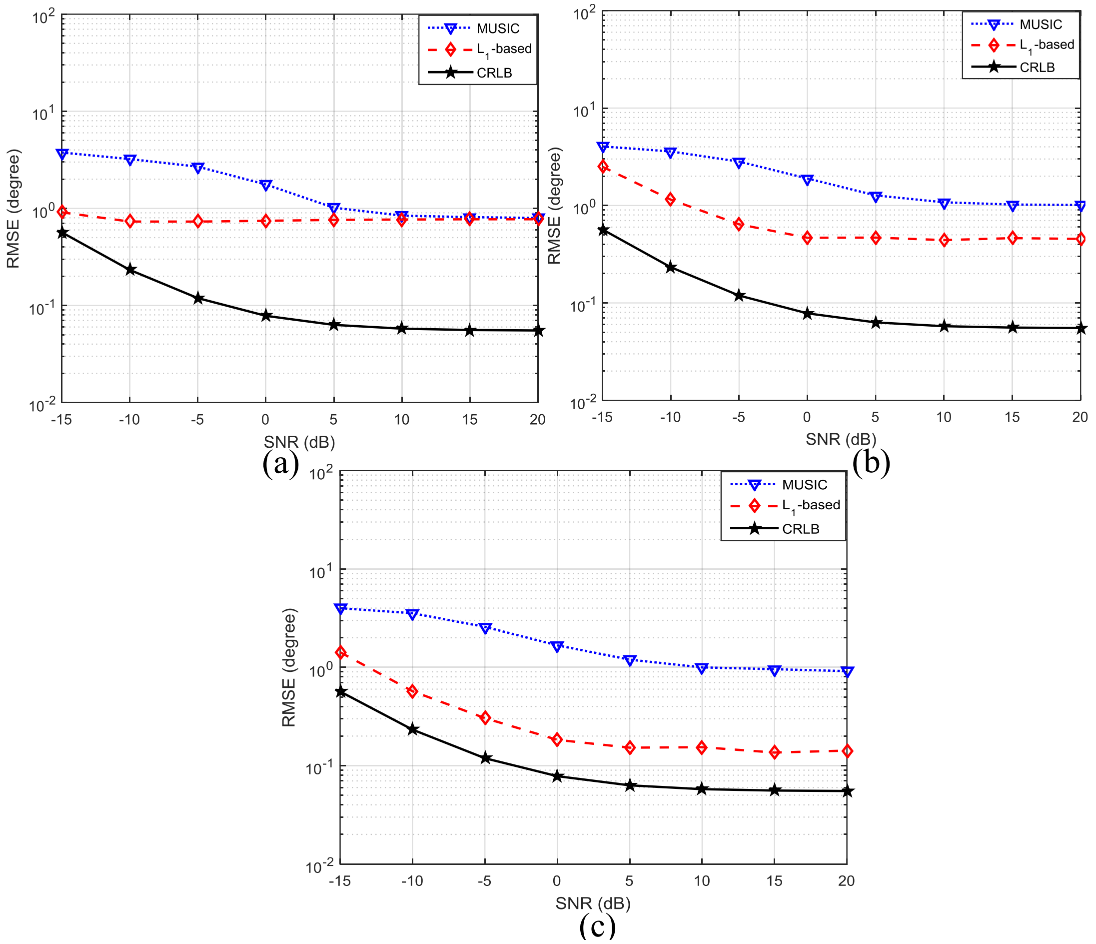

(a) (b) (c)

Figure 3.17: RMSE versus SNR underdetermined DOA estimation comparison for (a) UCA, (b) SR, and (c) NSCA.

3.5.3 Probability of Resolution for Different Arrays

In this subsection, we analyze the probability of the MUSIC and ℓ_1–based optimization algorithms in resolving two spatially separated signal sources in the context of array processing as a continuation of the discussion in subsection 3.4.3. However, in this subsection, the probability of resolution problem is tackled in a fashion where the different circular array's probability of resolving signals is compared. We compare the probability of NSCA, SR, and UCA to resolve closely spaced signals. In Fig. 3.18, we show the probability of resolution for two closely spaced impinging signals $\phi = [20°, 25°]$. In Fig. 3.18(a), MUSIC algorithm is used. In this figure, we observe that NSCA is capable of resolving two closely spaced signals with lower SNR levels as compared to the other two circular geometries (SR and UCA). This is the case as well when using ℓ_1–based optimization method in Fig. 3.18(b) where by NSCA has better probability of resolution.

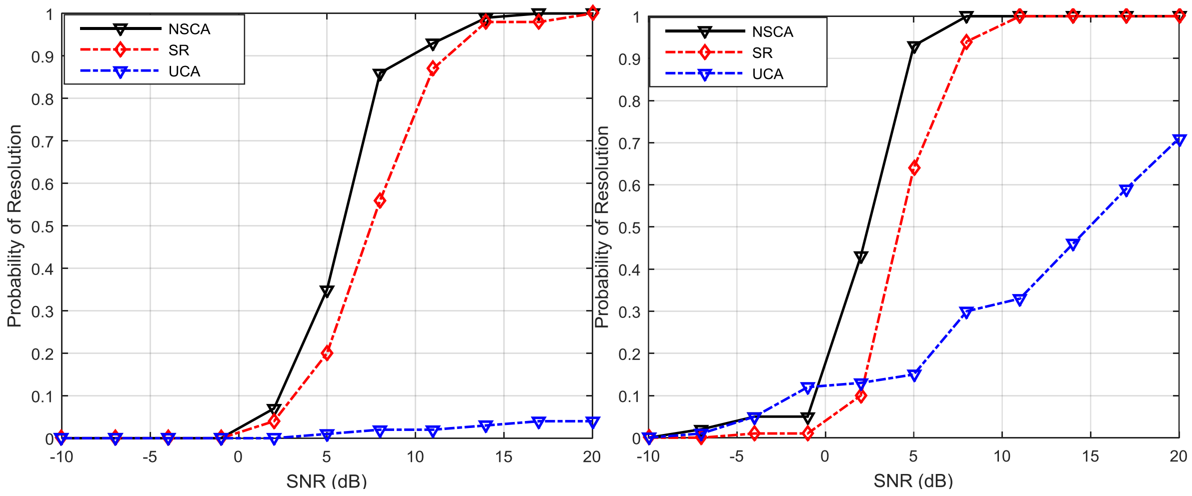

(a) (b)

Figure 3.18: Probability of Resolution for different arrays (a) MUSIC and (b) ℓ_1–based optimization.

3.5.4 Underdetermined DOA Angular Dependency

In the last part of the numerical examples, we examine performance of ℓ_1–based optimization approach in relation to angular dependency. We consider the RMSE comparison of the 3 circular array configurations examined in 3.5. In terms of DOAs, the case of of $(D = 8)$ is used. In terms of the results, we observe RMSE behavior for the 3 circular arrays when the initial DOA values are varied from their initial positions by $\Delta\phi$, where $\Delta\phi$ ranges from 0° to 90°. In Fig. 3.19, we observe that there is very little change in the RMSE behavior for NSCA and UCA while sparse ruler has higher change hence it has higher angular dependency. The NSCA case also obtains better RMSE as compared to the other two configurations over all DOA angles. UCA has no RMSE change as DOAs change in terms of angular dependency between 45° and 90°. Therefore we conclude that NSCA has little angular dependency in the case of $\Delta\phi$ between 0° and 90° and a better RMSE performance as compared to the other two array configurations.

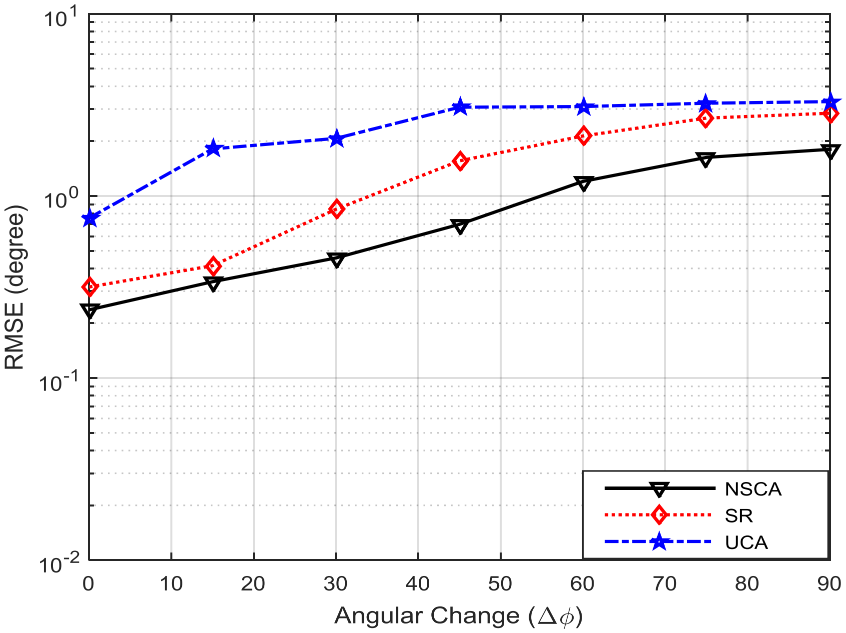

Figure 3.19: Angular dependency of NSCA, SR, and UCA using ℓ_1-based optimization technique for underdetermined DOA estimation. $D = 8$, SNR $= 20$ dB, and Snapshots $= 10000$.

3.6 Summary

In this chapter, a nested sparse circular array was proposed. The proposed array and its geometry solves the problem of underdetermined DOA estimation. The concentric extension of the NSCA provides virtual sensors which are synthesized on a non–uniform concentric circular array. By utilizing the virtual sensors in the concentric extension, the NSCA achieves increased degrees of freedom. In this chapter, two strategies were explored that are used with the NSCA; subspace based technique MUSIC and ℓ_1–based optimization method. In both methods, we confirmed that NSCA has the ability to estimate more sources as compared to the number of physical sensors. We also investigated the RMSE performance in relation to SNR and number of snapshots. We observed that the number of snapshots plays a crucial role in the underdetermined DOA estimation. Using the nested sparse circular array, an increase in the degrees of freedom is guaranteed especially on the ℓ_1–based optimization method which obtains $2M - 1$ degrees of freedom and has no angular dependency. The work was also extended to cases in which signals are distributed. It was confirmed that the underdetermined DOA estimation accuracy of ℓ_1–based method was not affected by distributed sources.

Chapter 4

Mutual Coupling Compensation Method for Nested Sparse Circular Arrays

4.1 Introduction

The problem of evaluating parameters of superimposed signals which utilizes sensor arrays has numerous practical applications and is one of the most researched area in array signal processing. Direction of arrival (DOA) estimation is consequently an active research area in signal processing and plays an important role in various application areas, such as wireless communications, seismic sensing, acoustics, and radar [24], [25], [83]. The advancements in array signal processing discipline have led to high resolution DOA estimation techniques for narrowband signals [25], [49] and wideband signals [84], [85]. In most cases, DOA techniques fall into two general classifications; 1) spectral–based methods and 2) statistical parametric methods. However, the performance of these techniques or strategies are generally restricted which prompted new techniques for sparse signal reconstruction (SSR).

In the last couple of years, linear sparse arrays have received significant attention.

These arrays have an advantage of performing underdetermined DOA estimation, which is the estimation of more number of sources than sensors [119]. Sparse arrays, for example, nested linear arrays [86], co–prime arrays [89], and minimum redundancy arrays (MRAs) [120] achieve increased degrees of freedom (DOFs) and are capable of performing underdetermined DOA estimation. In spite of the fact that this is the case, sparse arrays with a circular configuration has received very little consideration. Due to their geometry, circular arrays are capable of providing 360° azimuthal coverage [24], [31]. On top of this 360° estimation, circular arrays have no or minimal angular dependency, and suitable of performing $2D$–DOA estimation. As a consequence, circular arrays are more advantageous as compared to their linear counterparts.

In a situation or an instance where two antenna elements are closely spaced and one is transmitting, the second element will receive a portion of the transmitted energy. The received amount depends on the separation distance between the antenna elements and their relative orientation [121]. Moreover, antennas re–scatter an amount of any incident wave. In this manner, they act like small transmitters despite the fact that fundamentally, they are only receiving which results in energy interchange between a particular element of an array and a remote point [121]. This effect is a clear manifestation of the mutual coupling that exists between array antennas.

In DOA estimation, most algorithms assume an ideally or perfectly uncoupled array manifold. On the contrary, in practice, the array manifold is often affected by unknown array characteristics such as mutual coupling [24], [122], which seriously degrades the performance of DOA estimation algorithm [123], [124]. In the event that mutual coupling is properly accounted for, the performance loss can be restored [125]. The effects of mutual coupling can neither be completely eliminated nor its variability predicted since the electromagnetic environment encompassing the antenna is evolving [126]. Along these lines, if calibration procedures to estimate and compensate for the mutual coupling are available, design constraints with respect to coupling could be relaxed by antenna designers to improve other aspects of the antenna, without affecting the DOA algorithm's performance [126].

The impact of mutual coupling depends on both type of antenna and array structure. Uniform linear array (ULA) that is well balanced has a banded Toeplitz mutual coupling matrix structure, i.e. coupling between any two equally spaced sensors is the same [127]. In uniform circular arrays (UCA), mutual coupling matrix (MCM) is expressed by three bands; a center band, upper right–hand corner band, and a band at the lower left corner. This entails that a good UCA exhibit a circulant [128] MCM structure [127]. An array having an arbitrary geometry does not have any of these structures with the exception of that the mutual coupling matrix (MCM) is symmetric [129]. Mutual coupling between an antenna array's elements accumulated in MCM depends on the self and mutual impedances between array elements [130]. Several strategies have been proposed with a specific goal of modeling mutual coupling between array elements. In [131] a blind calibration method was proposed in which the mutual coupling coefficients were adjusted by utilizing dummy elements. This technique enhanced estimation accuracy of MUSIC algorithm. In [132], an effective way to correct the actual voltage matrix using the terminal impedance matrix derived from the method–of–moments' (MOM) impedance matrix was proposed which realized invariably superior result as compared to ideal case. However, this approach is complex in terms of implementation and execution, time consuming, and only constrained to overdetermined DOA estimation problem.

In literature, there are several methods that are used to compensate for mutual coupling in ULAs and UCAs. On the other hand at present, there is no existing method for nested sparse circular arrays proposed in [47]. Nested sparse circular array is a circularly configured array in which two sub–circular array are nested together. One part of the array is dense and the other part is sparse. This array has more advantages as contrasted to uniform circular arrays because since it achieves better underdetermined DOA estimation performance, very little angular dependency, capable of $2D$–DOA estimation and wideband underdetermined DOA estimation. To solve the problem of array mutual coupling in nested sparse circular arrays, we propose a simple symmetric banded–like circulant structure for MCM that will be utilized to perform underdetermined DOA estimation. The two strategies; MUSIC and ℓ_1–optimization based on compressive sensing or sparse signal recovery for DOA estimation methods are used in the presence of mutual coupling in this chapter. Simulation results confirms that the proposed simple MCM structure is capable of performing underdetermined DOA estimation for sparse circular arrays without degrading the array performance.

Notations

In this chapter, some of the commonly used notations are given as follows. Capital boldface letters are used to represent matrices (e.g., $\mathbf{A}$). On the other hand, vectors are represented by lowercase boldface letters (e.g., $\mathbf{a}$). A transpose is represented by superscript ^{T}, whilst superscript ^{H} represents conjugate transpose, whereas superscript * represents conjugation without transpose. $\|\bullet\|_p$ represents the ℓ_p norm. The symbol $\odot$ represents the Khatri–Rao product between two matrices of appropriate size and the symbol $\otimes$ is used to represent the left Kronecker product.

4.2 Mutual Coupling Problem Formulation

In this chapter, We examine an M element omnidirectional, nested sparse circular array [47] as shown in Fig. 4.1. We assume D sources that are narrowband having a wavenumber of $k = 2\pi/\lambda$ are arriving on the NSCA from the directions $\phi_1, \phi_2, ..., \phi_D$ where, ϕ is the azimuth angle and λ is wavelength. In the presence of mutual coupling, the received signal vector is given by

$$\boldsymbol{x}(t) = \mathbf{C}\mathbf{A}\mathbf{s}(t) + \mathbf{n}(t) \tag{4.1}$$

where $\mathbf{s}(t)$ is a $D \times 1$ signal vector, and $\mathbf{n}(t)$ is an $M \times 1$ noise vector. $\mathbf{C}$ is the mutual coupling matrix (MCM) and $\mathbf{A}$ is array manifold given by

$$\mathbf{A} = [\mathbf{a}(\phi_1), \mathbf{a}(\phi_2), ..., \mathbf{a}(\phi_D)] \tag{4.2}$$

where $\mathbf{a}$ is the steering vector. The number of sources is a *priori* known or accurately estimated [31], [133]. Furthermore, we assume that signal sources are uncorrelated. As such, the source autocorrelation matrix of $\boldsymbol{s}(\mathrm{t})$ is diagonal. Therefore,

$$\mathbf{R}_{xx} = E[\boldsymbol{x}\boldsymbol{x}^H] = \mathbf{C}\mathbf{A}\mathbf{R}_{ss}\mathbf{A}^H\mathbf{C}^H + \sigma^2\mathbf{I} \tag{4.3}$$

where $\mathbf{R}_{ss}$ is signal covariance matrix given by the diagonal of signal powers and $\mathbf{I}$ is an identity matrix. In order to exploit the increased DOFs, a Khatri-Rao subspace approach [92] is utilized to the DOA estimation problem in the presence of mutual coupling. From (4.3), the covariance matrix is vectorized such that

$$\begin{aligned} \mathbf{y} &= \mathrm{vec}(\mathbf{R}_{xx}) \\ &= \mathrm{vec}(\mathbf{C}\mathbf{A}\mathbf{R}_{ss}\mathbf{A}^H\mathbf{C}^H) + \mathrm{vec}(\sigma^2\mathbf{I}) \\ &= (\tilde{\mathbf{A}}^* \odot \tilde{\mathbf{A}})\mathbf{p} + \mathrm{vec}(\sigma^2\mathbf{I}) \end{aligned} \tag{4.4}$$

in which $\tilde{\mathbf{A}} = \mathbf{C}\mathbf{A}$. From the output signal above, DOA estimation algorithm such as MUSIC or ℓ_1–based optimization approach is applied [47]. Hence, we are capable of performing underdetermined DOA estimation because of increased DOFs from this formulation.

4.3 Proposed Mutual Coupling Matrix for Nested Sparse Circular Arrays

4.3.1 Generic Formulation

In antenna arrays, antenna elements affect each other through mutual coupling. In order to compensate for this effect through signal processing algorithms, a mutual coupling matrix is formulated. This mutual coupling matrix depends upon self and mutual impedances between array elements [130]. One of the earliest methods to model cou-

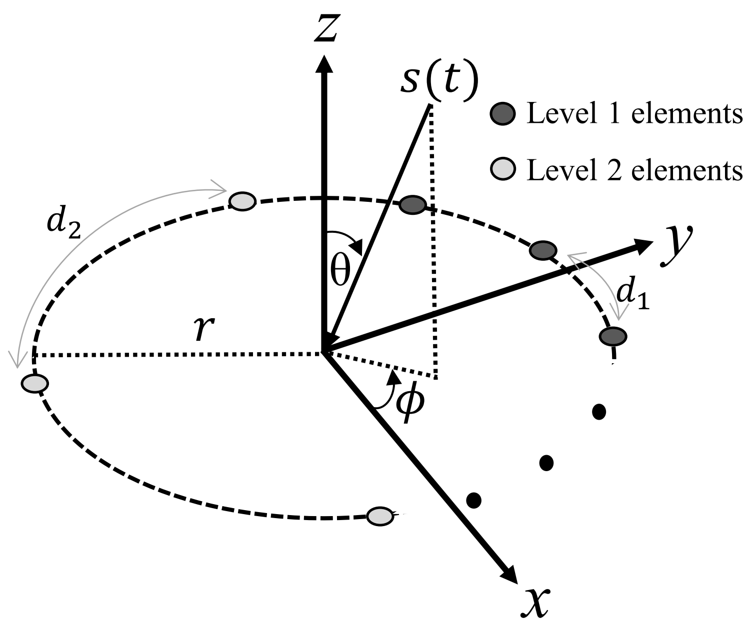

Figure 4.1: A Nested Sparse Circular Antenna Array.

pling matrix is called open–circuit method [124]. In this method, an antenna array is considered as a bilateral terminal network which relates uncoupled voltages with coupled ones using a mutual impedance matrix. An extension of the open–circuit method was proposed in [134], where two types of mutual impedances are depicted; (i) transmission mutual impedance and (ii) re–radiation mutual impedance. Another mutual coupling matrix compensation method was proposed in [135] in which the receiving–mutual impedance method (RMIM) is depicted for use in receive–only antenna arrays. In that capacity, the method provides a more precise coupling model in DOA estimation applications. In RMIM, each antenna pair is considered separately to compute the receiving mutual impedances [130], [135].

In mutual coupling compensation scenario, mutual coupling coefficients between two antenna elements are inversely related to their separation distance in an array [127]. In the case of nested sparse circular arrays, we propose a simple symmetric banded–like circulant matrix to represent the mutual coupling matrix in which the elements of the coupling vector **c** are given by

$$\boldsymbol{c} = [\underbrace{c_0, c_1, c_2, \cdots, c_{L-2}, c_{L-1}, 0, \cdots, 0}_{M}]^T \tag{4.5}$$

where $L = M/2 + 1$, c_0 is self coupling, and $c_{|i-j|}(i, j = 1, 2, ..., L \text{ for } i \neq j)$ denotes the coupling between an i–th element and a j–th element. Since the effect of mutual coupling decreases as the distance between the antenna elements increases, the effect of mutual coupling in the sparse part of the array shown in Fig. 4.1 is assumed to be insignificant and therefore ignored. Thus, the mutual coupling matrix will exhibit a symmetric banded–like circulant matrix structure. In the case of an M–element nested sparse circular array, mutual coupling matrix will be;

$$\mathbf{C} = \begin{bmatrix} c_0 & c_1 & c_2 & \cdots & c_{L-1} & 0 & 0 & \cdots & 0 \\ c_1 & c_0 & c_1 & \cdots & c_{L-2} & 0 & 0 & \cdots & 0 \\ c_2 & c_1 & c_0 & \cdots & c_{L-3} & 0 & 0 & \cdots & 0 \\ \vdots & \vdots & \vdots & \ddots & \vdots & \vdots & \vdots & \cdots & \vdots \\ c_{L-2} & c_{L-3} & c_{L-4} & \cdots & c_0 & 0 & 0 & \cdots & 0 \\ c_{L-1} & c_{L-2} & c_{L-3} & \cdots & c_1 & c_0 & 0 & \cdots & 0 \\ 0 & 0 & 0 & \cdots & 0 & 0 & c_0 & \vdots & 0 \\ \vdots & \vdots & \vdots & \vdots & \vdots & \vdots & \cdots & \ddots & \vdots \\ 0 & 0 & 0 & \cdots & 0 & 0 & 0 & \cdots & c_0 \end{bmatrix} \tag{4.6}$$

The number of unknown coupling coefficients for an M–element nested sparse circular array is L.

4.3.2 Example of a 6 element Nested Sparse Circular Array

In this subsection, we give an example of the proposed mutual coupling matrix. For the NSCA in Fig. 4.1, the symmetric banded-like circulant matrix structure of a 6 element nested sparse circular array will be given by;

$$\mathbf{C} = \begin{pmatrix} c_0 & c_1 & c_2 & c_3 & 0 & 0 \\ c_1 & c_0 & c_1 & c_2 & 0 & 0 \\ c_2 & c_1 & c_0 & c_1 & 0 & 0 \\ c_3 & c_2 & c_1 & c_0 & 0 & 0 \\ 0 & 0 & 0 & 0 & c_0 & 0 \\ 0 & 0 & 0 & 0 & 0 & c_0 \end{pmatrix} \tag{4.7}$$

4.4 DOA Estimation using ℓ_1–based Method in the Presence of Mutual Coupling

Recently, in the field of signal processing, compressive sensing [56] has become extremely popular and is rapidly expanding [60]. The key idea in compressive sensing is that majority of real–life signals can be approximated by sparse vectors. In this way, by exploiting the sparse signal structure, signal acquisition cost can dramatically be reduced, and accurate signal reconstruction can be accomplished in a computationally efficient way [60]. The emerging field of sparse representations therefore, has given renewed interest to the DOA estimation problem [136]. The idea of enforcing sparsity to a general framework using an ℓ_1–SVD method which has applications in a wide variety of practical DOA estimation problems was investigated in [95]. We extend ℓ_1–SVD in [95] to an ℓ_1–based optimization [47] for underdetermined DOA estimation in the presence of mutual coupling such that we can utilize the increase in DOFs using the Khatri–Rao approach. We consider (4.4) as a sparse signal representation problem which is given by

$$\mathbf{y} = (\tilde{\mathbf{A}}^{*} \odot \tilde{\mathbf{A}})\mathbf{p} + \text{vec}(\sigma^2\mathbf{I}) \tag{4.8}$$

In order to extend ℓ_1–penalization to (4.8), we need to appropriately determine an optimization criteria which is

$$\min \|\mathbf{p}\|_1 \text{ subject to } \left\|\mathbf{y} - \tilde{\mathbf{A}}^* \odot \tilde{\mathbf{A}}\mathbf{p}\right\|_2^2 \leq \beta^2 \tag{4.9}$$

where β is a parameter specifying how much noise we wish to allow. Therefore, an unconstrained form of this objective function is

$$\min \left\|\mathbf{y} - \tilde{\mathbf{A}}^* \odot \tilde{\mathbf{A}}\mathbf{p}\right\|_2^2 + \lambda \|\mathbf{p}\|_1 \tag{4.10}$$

The ℓ_2 term in (4.10) forces the residual to be small and λ controls the tradeoff between the sparsity of the spectrum and residual norm [109]. In practice, from N snapshots, the output $\boldsymbol{y}$ in (4.8) can be estimated by $\hat{\mathbf{y}}$ such that $\Delta\mathbf{y} = \hat{\mathbf{y}} - \mathbf{y}$. The error in estimation is asymptotically normal distribution (AsN), therefore

$$\Delta\mathbf{y} = \mathrm{vec}(\Delta\mathbf{R}_{xx}) \sim AsN\left(0_{M^2,1}, \frac{1}{N}\mathbf{R}_{xx}^T \otimes \mathbf{R}_{xx}\right) \tag{4.11}$$

leading to

$$\mathbf{W}^{-\frac{1}{2}}\Delta\mathbf{y} \sim AsN\left(0_{M^2,1}, \mathbf{I}_{M^2}\right) \tag{4.12}$$

where the weighting matrix $\mathbf{W}^{-\frac{1}{2}} = \sqrt{N}\mathbf{R}_{xx}^{-\frac{T}{2}} \otimes \mathbf{R}_{xx}^{-\frac{1}{2}}$ with $\mathbf{W} = \frac{1}{N}\mathbf{R}_{xx}^T \otimes \mathbf{R}_{xx}$. Let $\hat{\mathbf{p}}$ be the estimate of $\mathbf{p}$, the DOA estimation problem can then be given by

$$\min \left\|\hat{\mathbf{y}} - \tilde{\mathbf{A}}^* \odot \tilde{\mathbf{A}}\hat{\mathbf{p}}\right\|_2^2 + \lambda \|\hat{\mathbf{p}}\|_1 \tag{4.13}$$

from (4.12) and (4.13) we further deduce that

$$\mathbf{W}^{-\frac{1}{2}}\left[\hat{\mathbf{y}} - \tilde{\mathbf{A}}^* \odot \tilde{\mathbf{A}}\hat{\mathbf{p}}\right] \sim AsN\left(0_{M^2,1}, \mathbf{I}_{M^2}\right) \tag{4.14}$$

which then results in

$$\mathbf{W}^{-\frac{1}{2}} \left\| \hat{\mathbf{y}} - \tilde{\mathbf{A}}^{*} \odot \tilde{\mathbf{A}} \hat{\mathbf{p}} \right\|_2^2 \sim As\chi^2(M^2) \tag{4.15}$$

where $As\chi^2(M^2)$ denotes the asymptotic chi-square distribution with M^2 DOFs. Hence, a parameter β is introduced such that $\left\| \mathbf{W}^{-\frac{1}{2}} \left[\hat{\mathbf{y}} - \tilde{\mathbf{A}}^{*} \odot \tilde{\mathbf{A}} \hat{\mathbf{p}} \right] \right\|_2^2 \leq \beta^2$. Therefore, DOA estimation can be reduced to

$$\min_{\hat{\mathbf{p}}} \|\hat{\mathbf{p}}\|_1 \text{ subject to } \left\| \mathbf{W}^{-\frac{1}{2}} \left[\hat{\mathbf{y}} - \tilde{\mathbf{A}}^{*} \odot \tilde{\mathbf{A}} \hat{\mathbf{p}} \right] \right\|_2^2 \leq \beta^2 \tag{4.16}$$

where $\beta = \sqrt{\chi^2(M^2)}$. Thus (4.16) is a second–order cone programming problem.

4.5 Simulation Results for DOA Estimation in Presence of Mutual Coupling

4.5.1 Specifications

In order to evaluate the capability of nested sparse circular array in terms of estimating more sources than sensors, we carry out simulation experiments. In the examples given in following subsections, we examine a 6 element nested sparse circular array antenna system ($M = 6$) as shown in Fig. 4.1. We consider eight narrowband sources ($D = 8$) arriving on the array from the directions $\phi = [15°, 36°, 70°, 90°, 112°, 130°, 145°, 162°]$, all with the same amount of power. The radius of the nested sparse circular array is $r = \lambda/2$. The noise is assumed to be spatially and temporally white.

4.5.2 Numerical Mutual Coupling Matrix and Estimation Performance

To evaluate the performance of the proposed approach, we conducted numerical evaluation of NSCA with ($M = 6$) and 8 sources. The number of unknown coupling coefficients is $L = M/2 + 1 = 4$. The coupling vector $\mathbf{c}$ was estimated from random values with the criteria $1 \geq \mathbf{c} \geq 0$ where $\mathbf{c}_0 > \mathbf{c}_1 > \mathbf{c}_2 > \mathbf{c}_3$ depending on element separation. The values were found to be $\mathbf{c} = [1.00 + 0.00\jmath, 0.633 + 0.395\jmath, 0.351 + 0.219\jmath, 0.063 + 0.195\jmath]$. The simplified mutual coupling matrix is shown in Fig. 4.2.

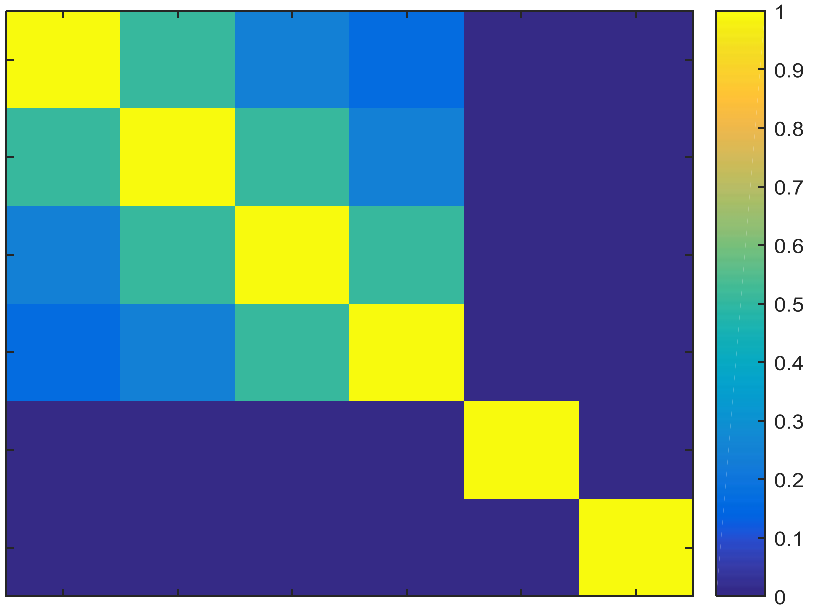

Figure 4.2: A simplified mutual coupling matrix plot for nested sparse circular array.

Figure 4.3(a) shows the spectra for MUSIC algorithm while Fig. 4.3(b) shows spectra for ℓ_1-based optimization approach in an underdetermined DOA estimation case. We observe all DOAs are resolved correctly and peaks are sharp. Even in the presence of mutual coupling, NSCA can detect more sources than sensors. ℓ_1–based method has a very high spectrum range. In terms of detection performance, as observed in Fig. 4.3, ℓ_1–based method offers better results even when we take into consideration mutual coupling effects.

In the next example, we consider the accuracy for underdetermined DOA estimation in presence of mutual coupling. The RMSE performance comparison when MUSIC and ℓ_1-based methods are utilized is examined in Fig. 4.4. Figure 4.4(a) shows the RMSE as a function of SNR for an underdetermined DOA estimation case in which ℓ_1–based method

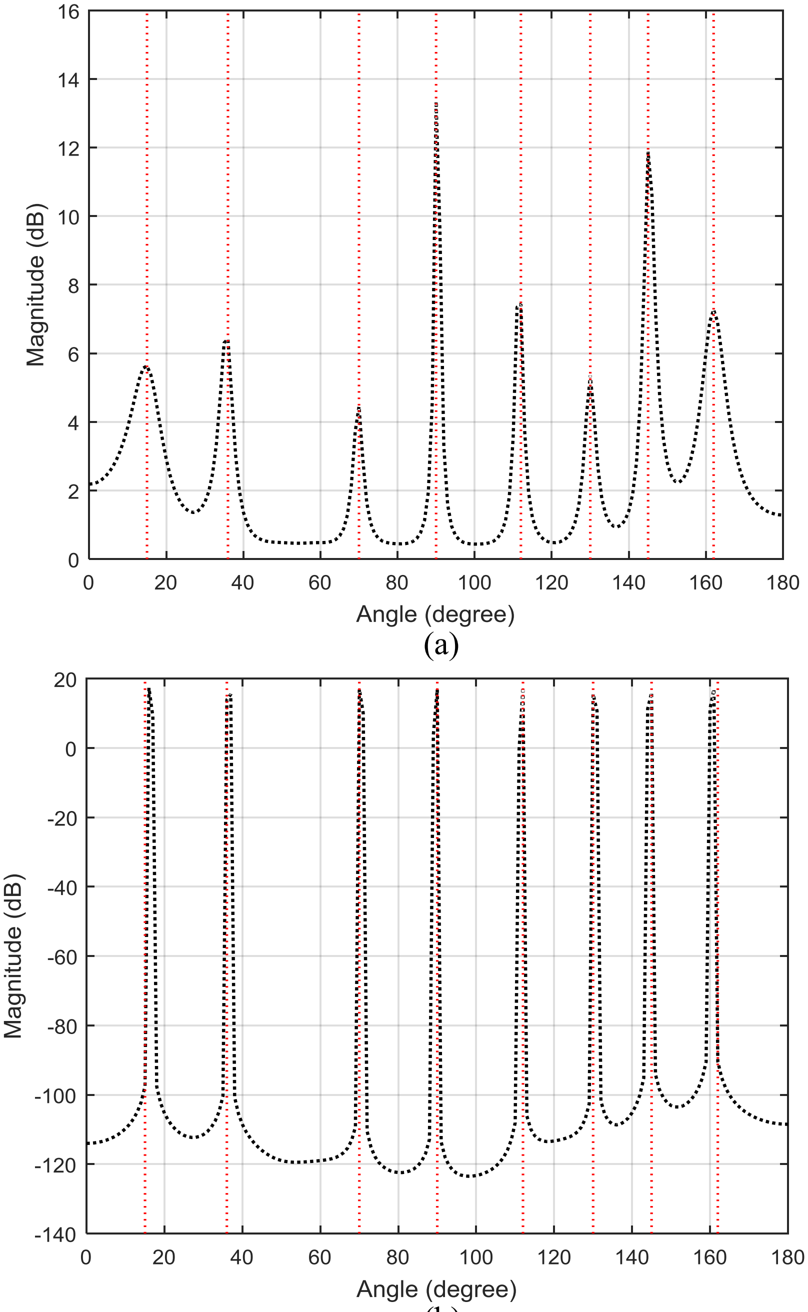

(a)

(b)

Figure 4.3: Underdetermined DOA estimation spectra in the presence of Mutual coupling (a) MUSIC, (b) ℓ_1-based method.

outperforms MUSIC. In Fig. 4.4(b), we present the underdetermined DOA estimation accuracy by employing the RMSE performance comparison as a function of number of snapshots. As the case in Fig. 4.4(a), ℓ_1–based method has superior performance as well.

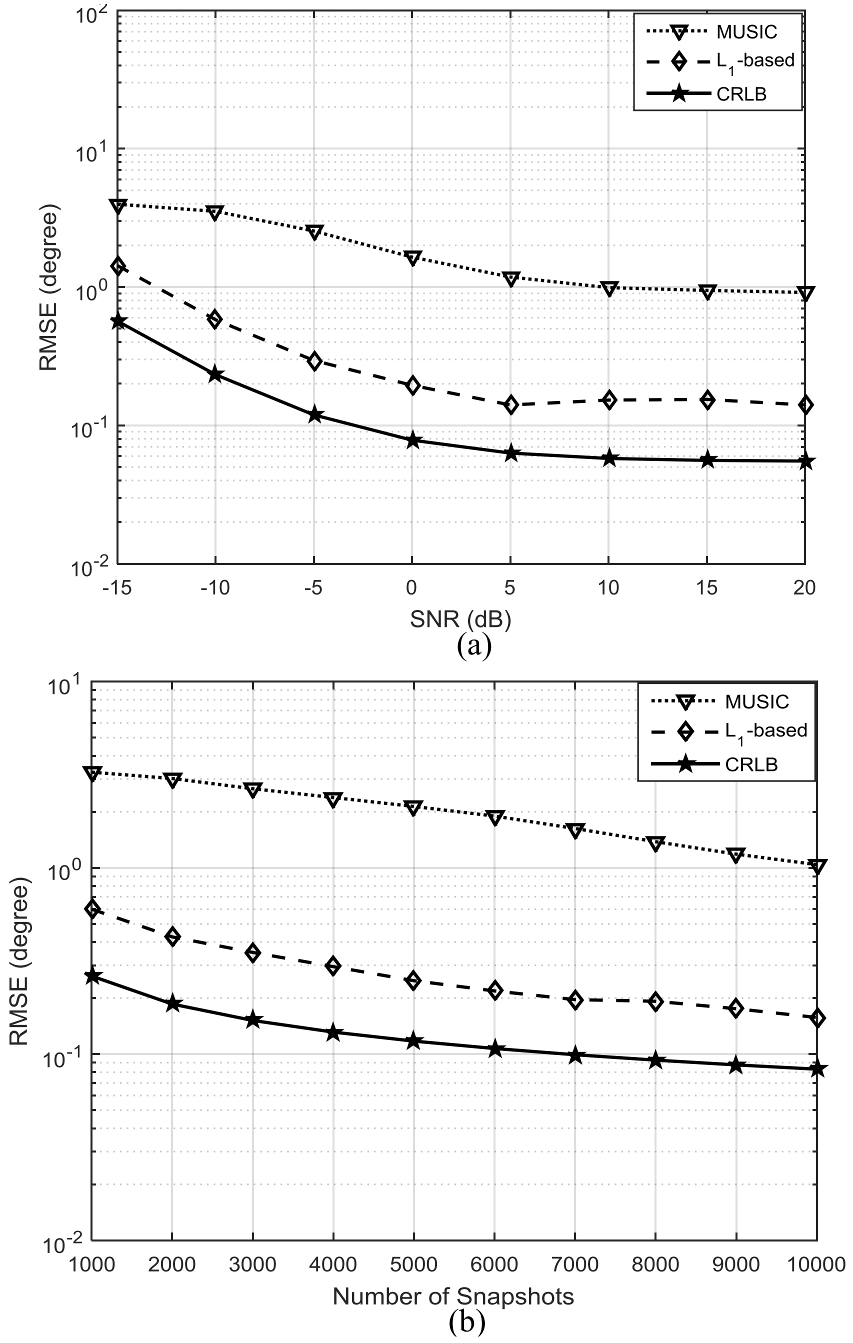

Figure 4.4: Underdetermined DOA estimation RMSE performance in the presence of Mutual coupling versus (a) SNR, (b) number of snapshots.

4.5.3 MCM from Electromagnetic Software

From the formulation in section 4.3, we examine a 6–element nested sparse circular array as an example and obtain its impedance matrix $\mathbf{Z}$ from an electromagnetic simulation software FEKO which uses a method of moments to find $\mathbf{Z}$. The impedance matrix $\mathbf{Z}$ is inversely proportional to the mutual coupling matrix $\mathbf{C}$ i.e $\mathbf{C} = \mathbf{Z}^{-1}$. Hence, if we find the impedance values (i.e elements/entries of the impedance matrix $\mathbf{Z}$), an impedance matrix can be reconstructed from these values. By calculating the inverse of impedance matrix, we obtain mutual coupling matrix. In this example $M = 6$ and $L = 4$, therefore the impedance matrix will be;

$$\mathbf{Z} = \begin{pmatrix} z_{11} & z_{12} & z_{13} & z_{14} & z_{15} & z_{16} \\ z_{21} & z_{22} & z_{23} & z_{24} & z_{25} & z_{26} \\ z_{31} & z_{32} & z_{33} & z_{34} & z_{35} & z_{36} \\ z_{41} & z_{42} & z_{43} & z_{44} & z_{45} & z_{46} \\ z_{51} & z_{52} & z_{53} & z_{54} & z_{55} & z_{56} \\ z_{61} & z_{62} & z_{63} & z_{64} & z_{65} & z_{66} \end{pmatrix} \tag{4.17}$$

From these 36 values, instead of finding all the 36 coupling coefficients (for asymmetric case), the proposed method find only 4 coupling coefficients which tremendously reduces time and effort to calculate the mutual coupling matrix. In the electromagnetic simulation software, the array is modeled using monopole antennas on a ground. We obtained good S_{ii}–parameter values at the frequency of interest 2.45 GHz which are below −10 dB whilst S_{ij}–parameter values are below −15 dB $(i, j = 1, 2, ..., 6; i \neq j)$ which is good for practical applications. The S-parameter values are shown in Fig. 4.5

The self and mutual impedance values evaluated are given in (4.18) where z_{ij} represents the mutual impedance between the i–th element and the j–th element while z_{ii} represents self impedance. The impedance vector to be extracted $\mathbf{z}$ therefore consist of the values z_{11}, z_{12}, z_{13}, and z_{14}. These values are then used to construct the proposed banded-like circulant mutual coupling matrix for the nested sparse circular array.

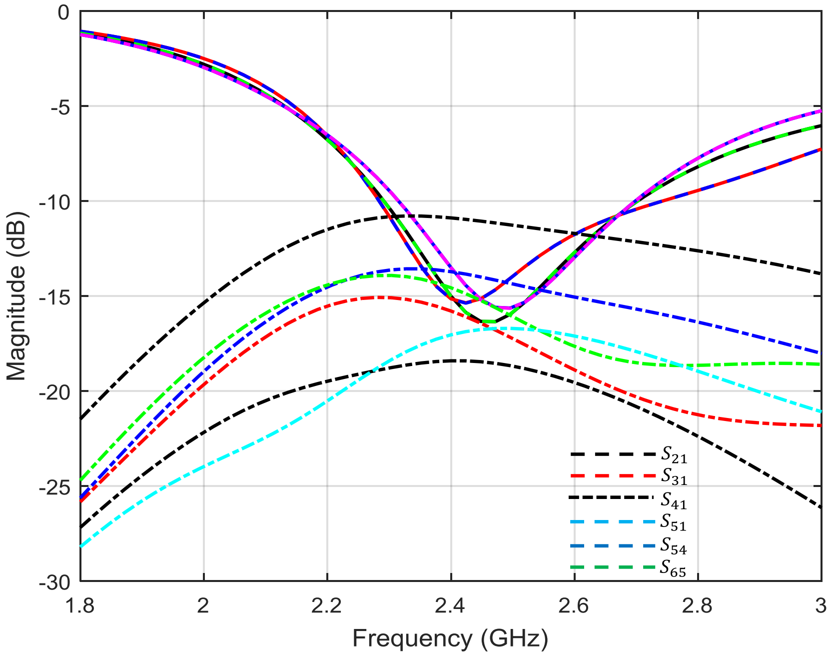

Figure 4.5: S-parameter values for nested sparse circular array.

$$\mathbf{Z} = \begin{bmatrix} 34.987+3.073i & -11.371+1.263i & 5.195-4.063i & -4.919+0.749i & 1.076+5.496i & 5.325-3.741i \\ -11.371+1.263i & 35.044+2.652i & -11.56+1.227i & 5.189-4.062i & 0.983+5.219i & -5.253+0.610i \\ 5.195-4.063i & -11.559+1.228i & 35.044+2.633i & -11.363+1.271i & -5.250+0.615i & 0.984+5.221i \\ -4.919+0.750i & 5.189-4.062i & -11.363+1.271i & 34.959+2.960i & 5.317-3.746i & 1.076+5.490i \\ 1.076+5.496i & 0.984+5.220i & -5.250+0.615i & 5.317-3.745i & 35.045+3.482i & 5.254-3.545i \\ 5.325-3.741i & -5.253+0.610i & 0.984+5.221i & 1.076+5.490i & 5.254-3.545i & 35.057+3.460i \end{bmatrix} \tag{4.18}$$

$$\mathbf{C} = \begin{bmatrix} 0.304-0.034i & 0.083-0.003i & 0.004+0.031i & 0.049+0.010i & -0.031-0.053i & -0.012+0.032i \\ 0.083-0.003i & 0.330-0.043i & 0.088-0.027i & 0.004+0.031i & -0.021-0.062i & 0.043-0.014i \\ 0.004+0.031i & 0.088-0.027i & 0.330-0.043i & 0.083-0.002i & 0.043-0.014i & -0.021-0.062i \\ 0.049+0.010i & 0.004+0.031i & 0.083-0.002i & 0.304-0.033i & -0.012+0.032i & -0.031-0.054i \\ -0.031-0.053i & -0.021-0.062i & 0.043-0.014i & -0.012+0.032i & 0.272-0.031i & -0.027+0.026i \\ -0.012+0.032i & 0.043-0.014i & -0.021-0.062i & -0.031-0.054i & -0.027+0.026i & 0.272-0.031i \end{bmatrix} \times 10^{-1} \tag{4.19}$$

4.5.4 Mutual Coupling Matrix - EM Software Simulation

In the performance assessment of the system in terms of underdetermined DOA estimation with mutual coupling compensation, we consider two cases. The first case, Case 1 is when the mutual coupling matrix is derived from the impedance matrix **Z** in (4.18) with all 36 values. In the second case, Case 2 the proposed banded–like circulant mutual cou-

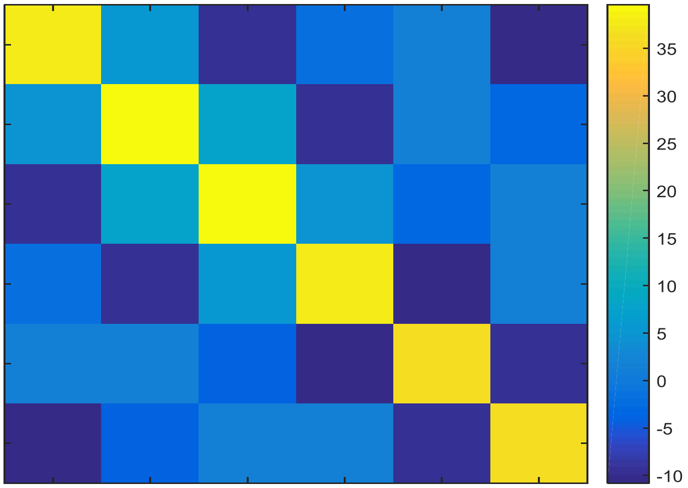

Figure 4.6: Mutual coupling matrix plot with all values.

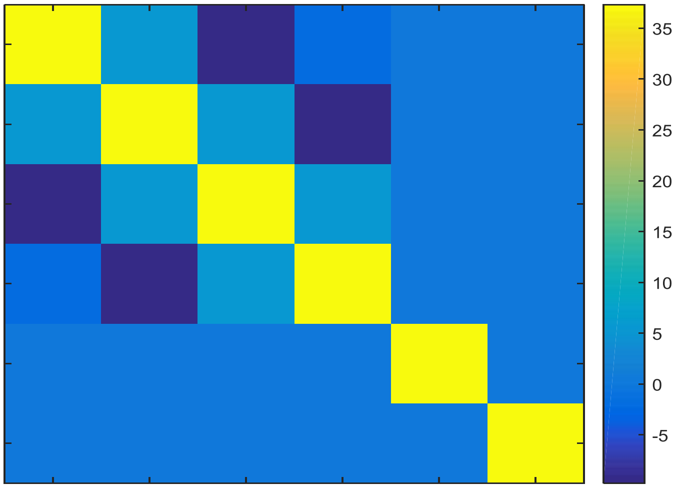

Figure 4.7: Mutual coupling matrix plot with proposed simple banded–like circulant mutual coupling matrix.

pling matrix with 4 values extracted from the impedance matrix $\mathbf{Z}$ in (4.18) is utilized. The impedance vector is found to be $\mathbf{z} = [34.987+3.073i\ -11.371+1.263i\ 5.195-4.063i\ -4.919+0.749i]$ which is extracted from z_{11}, z_{12}, z_{13}, and z_{14}. Thus, the mutual coupling matrix for a 6–element nested sparse circular array will have the form as shown in (4.7). Figure 4.6 shows the plot of mutual coupling matrix case 1 with all values whilst Fig. 4.7 shows a plot with the proposed banded-like circulant mutual coupling matrix scenario.

4.5.5 Underdetermined DOA Estimation Spectrum

4.5.5.1 Uncalibrated Mutual Coupling

The first example in this subsection, an underdetermined DOA estimation spectra without mutual coupling compensation (or uncalibrated mutual coupling) is considered. In Fig. 4.8(a), MUSIC algorithm's performance is assessed whilst in Fig. 4.8(b), we examine the performance of ℓ_1–based optimization method. In both methods as illustrated in Fig. 4.8, we observe that the methods are not able to accurately estimate the directions of the impinging signals. Despite the fact ℓ_1–based optimization method obtains higher dynamic range, only three DOAs of the eight are accurately estimated. Hence, there is a necessity for mutual coupling compensation such that the performance of the DOA estimation algorithms in the presence of mutual coupling can be improved. In the succeeding examples, two scenarios (case 1 and case 2) for mutual coupling compensation is considered.

4.5.5.2 Calibrated Mutual Coupling

Figure 4.9(a) exhibits the spectra plot of the subspace based approach MUSIC for underdetermined DOA estimation in the presence of mutual coupling using case 1. The problem addressed in this example is related to DOA estimation with mutual coupling compensation whereby all 36 coupling values are considered as shown in Fig. 4.6. In this scenario, we observe that we are able to resolve all DOAs and some peaks are sharp but the dynamic range is low. In Fig. 4.9(b) we observe the spectra of ℓ_1–based optimization of sparse signal recovery for underdetermined DOA estimation in the presence of mutual coupling using case 1 as well. In the case of utilizing the ℓ_1–based optimization, all DOAs are resolved and some of the DOAs are accurately estimated. The peaks in ℓ_1–based optimization method are very sharp and a very high dynamic range is achieved. Both methods in Fig. 4.9 expose some errors in DOA estimation.

In Fig. 4.10, we asses the performance by utilizing Case 2 (in which the mutual

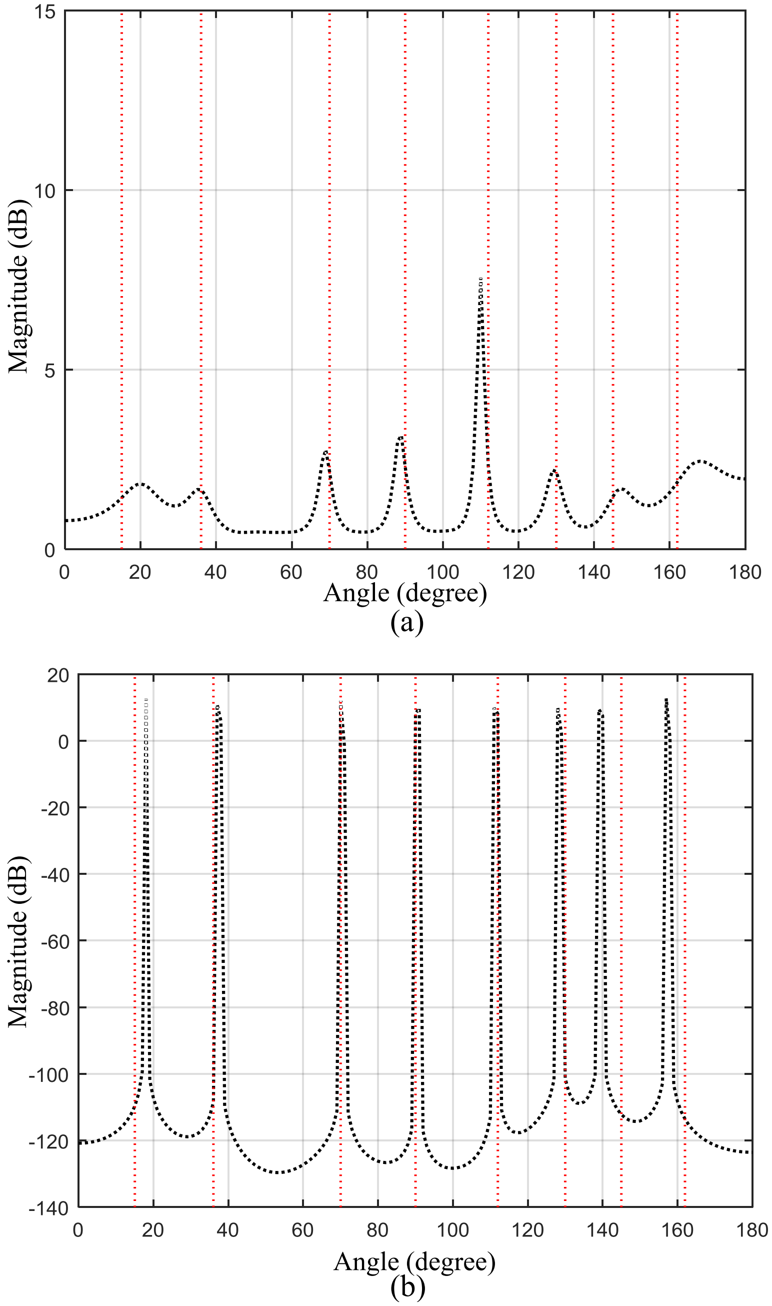

Figure 4.8: Spectra for underdetermined DOA estimation for nested sparse circular array - for uncalibrated mutual coupling with snapshots = 1000, and SNR = 0 dB for (a) MUSIC and (b) ℓ_1–based optimization.Red denotes true DOAs.

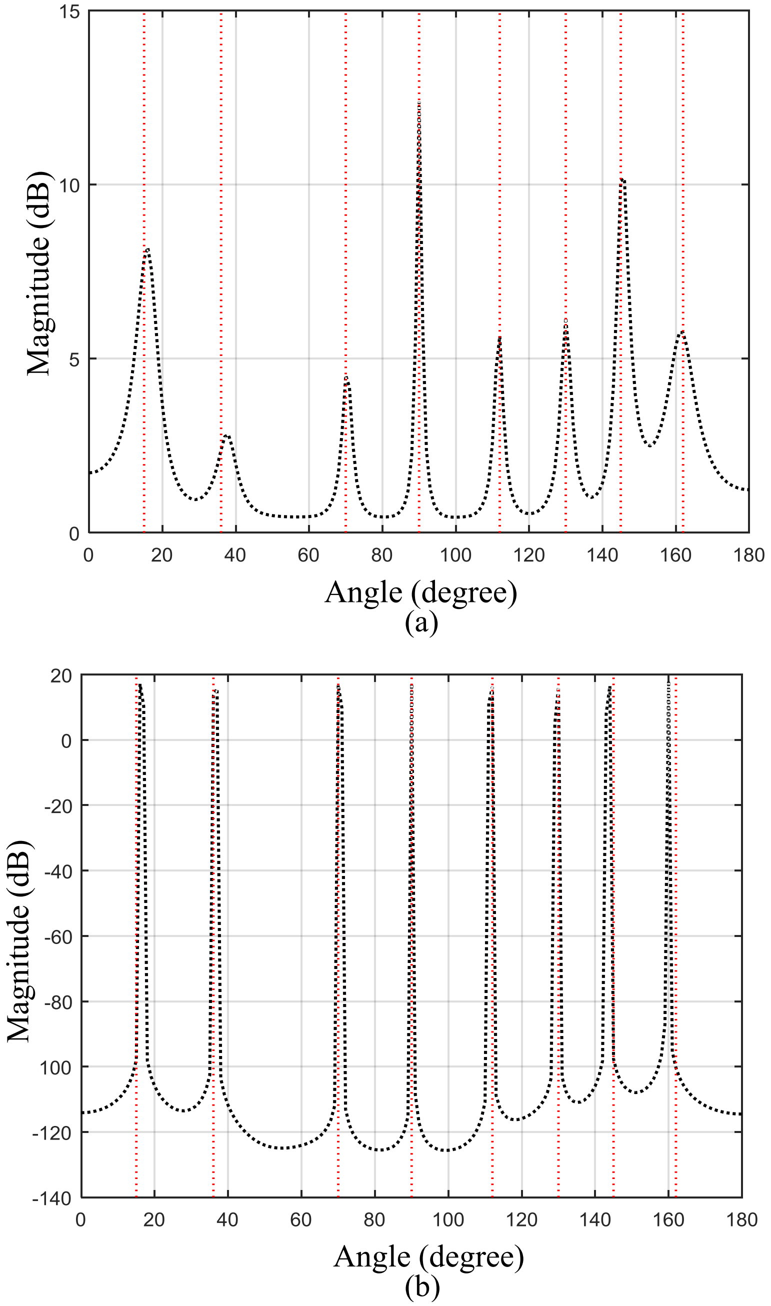

Figure 4.9: Spectra for underdetermined DOA estimation for nested sparse circular array - Case 1 with snapshots = 1000, and SNR = 0 dB for (a) MUSIC and (b) ℓ_1–based optimization.

coupling matrix is given by the proposed banded–like circulant mutual coupling matrix – Fig. 4.7). In Fig. 4.10(a), a plot of subspace based method MUSIC is presented whilst Fig. 4.10(b) presents a plot of ℓ_1–based optimization method. As compared to Fig. 4.9, better performance is observed in terms of DOA estimation accuracy. This is mainly recognized by comparing the dynamic range of Fig. 4.10(a) and Fig. 4.9(a), in which MUSIC algorithm for Case 2 obtains higher dynamic range. In the situation where ℓ_1–based optimization method is used and MCM of Case 2 (Fig. 4.10(b)), a better performance is observed since Fig. 4.9(b) has errors at 145° and 162°. For Fig. 4.10(b), we observe no estimation error at 145° and a very small estimation error at 162°. By comparing Case 1 and Case 2, we conclude that from spectra plots Fig. 4.9 and Fig. 4.10, Case 2 obtains better DOA estimation in an underdetermined scenario.

4.5.6 RMSE Performance Comparison for Underdetermined DOA Estimation with Mutual Coupling

In this subsection, we examine the performance of nested sparse circular array in relation to the RMSE of the angle estimates. We therefore evaluate this RMSE as a function of SNR and number of snapshots for underdetermined DOA estimation in the presence of mutual coupling. The cramer–rao lower bound (CRLB) [112], [137] is used as the benchmark in this case. We consider eight signals impinging on the array when the number of physical elements $M = 6$. In this case, we consider an SNR of 20 dB with 100 monte carlo simulations. The RMSE is defined as

$$\text{RMSE} = \sqrt{\frac{1}{T_r}\sum_{tr=1}^{T_r}\left\{\frac{1}{D}\sum_{d=1}^{D}(\hat{\phi}_d - \phi_d)^2\right\}} \tag{4.20}$$

where T_r is number of trials, $\hat{\phi}_d$ represents estimated DOAs and ϕ_d represents true DOAs. The CRLB [138] is given by;

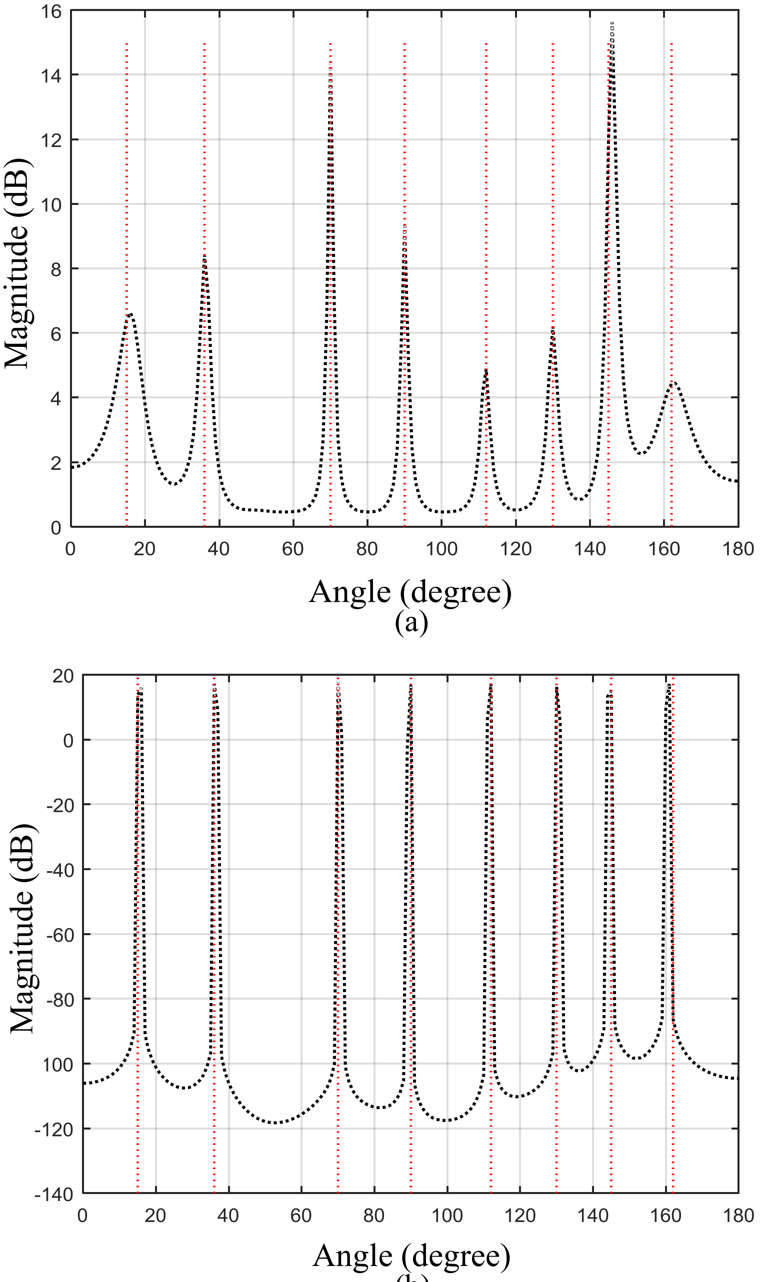

(a)

(b)

Figure 4.10: Spectra for underdetermined DOA estimation for nested sparse circular array - Case 2 with snapshots = 1000, and SNR = 0 dB for (a) MUSIC and (b) ℓ_1-based optimization.

$$\begin{aligned}\mathbf{CRLB} &= FIM^{-1} = N\text{Tr}\left\{\mathbf{R}_{xx}^{-1}\frac{\partial \mathbf{R}_{xx}}{\partial[\alpha]_p}\mathbf{R}_{xx}^{-1}\frac{\partial \mathbf{R}_{xx}}{\partial[\alpha]_l}\right\} \\ &= N\left[\text{vec}\left(\frac{\partial \mathbf{R}_{xx}}{\partial[\alpha]_p}\right)\right]^H(\mathbf{R}_{xx}^{-T}\otimes\mathbf{R}_{xx}^{-1})\text{vec}\left(\frac{\partial \mathbf{R}_{xx}}{\partial[\alpha]_l}\right) \\ &= \frac{1}{N}(\Lambda^H\Pi_{\Gamma}^{\perp}\Lambda)^{-1} \qquad (4.21)\end{aligned}$$

where $\Pi_{\Gamma}^{\perp} = \mathbf{I} - \Gamma(\Gamma^H\Gamma)^{-1}\Gamma^H$, FIM is the Fisher information matrix, Tr is the trace, α is the unknown parameter vector. A through derivation of the CRLB for nested sparse circular arrays is found in [138].

4.5.6.1 RMSE against SNR Performance Comparison

We asses the Underdetermined DOA estimation accuracy of the two algorithms; MUSIC and ℓ_1–based optimization in presence of mutual coupling by comparing the RMSE versus SNR performance. In Fig. 4.11(a), the performance is presented when the mutual coupling compensation utilizes Case 1 whilst in Fig. 4.11(b) we present the scenario when Case 2 is used. We observe that Case 2 obtains better RMSE performance. From this comparison, it follows that Case 2 as shown in Fig. 4.11(b) has better Underdetermined DOA estimation accuracy using NSCA.

4.5.6.2 RMSE against Snapshots Performance Comparison

In Fig. 4.12(a) we observe RMSE versus number of snapshots when Case 1 is utilized. In this scenario, as the number of snapshots increases, RMSE performance becomes better. We note that the RMSE of ℓ_1–based optimization method in Fig. 4.12(a) is better as compared to that of subspace based method MUSIC.

In the succeeding figure, Fig. 4.12(b), the RMSE performance of the proposed banded–like circulant mutual coupling matrix (Case 2) is considered. For the case of subspace based method MUSIC, we observe very little improvement in DOA estimation accuracy

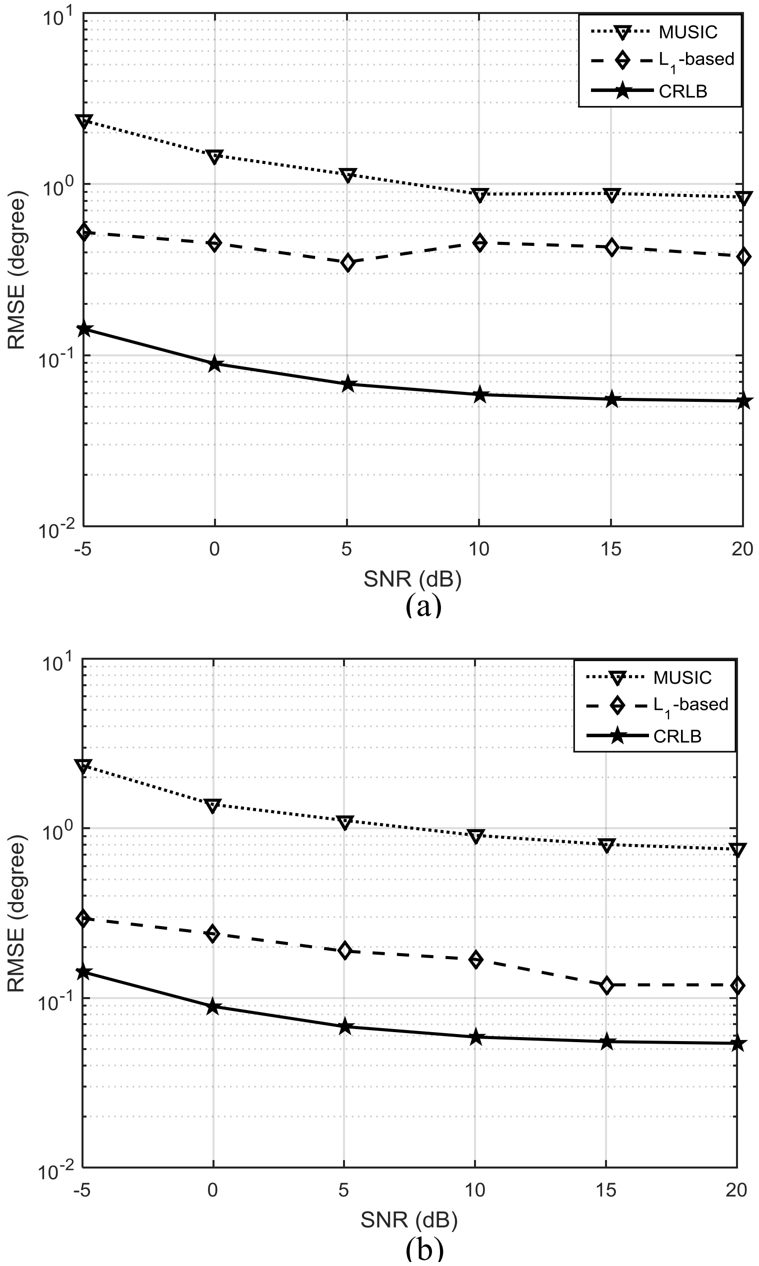

(a)

(b)

Figure 4.11: RMSE performance versus SNR utilizing MUSIC and ℓ_1–based optimization for underdetermined DOA estimation with $M = 6$, SNR = 20 dB for (a) Case 1, and (b) Case 2.

for Cases 1 and 2. In terms of ℓ_1–based optimization method, we observe better RMSE performance comparing Fig. 4.12(a) and Fig. 4.12(b). In both Case 1 and Case 2, a similar observation and conclusion can be made in which the increase in the number of snapshots leads to better RMSE performance but the ℓ_1–based optimization method has better RMSE than subspace based technique MUSIC.

4.5.7 Performance Evaluation of Sparse Signal Reconstruction with Mutual Coupling

As already observed in performance analysis and evaluation presented in preceding subsections, ℓ_1–based optimization method outperforms MUSIC algorithm. In this subsection, we carry out RMSE performance considering ℓ_1–based optimization as the number of signals (DOAs) arriving on the nested sparse circular array are increased. Since we examine an underdetermined DOA estimation scenario, the cases of six to ten signals impinging on the array are considered. In order to confirm that the method also works for an overdetermined DOA estimation scenario, a case of five DOAs has been added to the analysis. Figure 4.13 shows the RMSE performance when the number of DOAs increase from six to ten signal sources. In this figure, we observe that the proposed banded–like circulant mutual coupling matrix (case 2) has better RMSE performance for all signal sources impinging on the array. We also observe in Fig. 4.13 that nested sparse circular array is capable of overdetermined DOA estimation (5 DOAs impinging on the array). The performance of both cases (overdetermined and underdetermined) in the presence of MC shows that case 2 is better. Thus the proposed banded–like circulant mutual coupling matrix exhibit better performance as we compare the two cases.

In Fig. 4.14, the average run–time as compared to the number of DOAs is investigated. Conventionally, SSR based algorithms possess higher average run-time characteristics in DOA estimation. In a normal situation, ℓ_1–based optimization takes more time to execute as compared to MUSIC algorithm. In Fig. 4.14, we observe that the proposed case 2 obtains reduced average run–time as the number of DOAs increases compared to

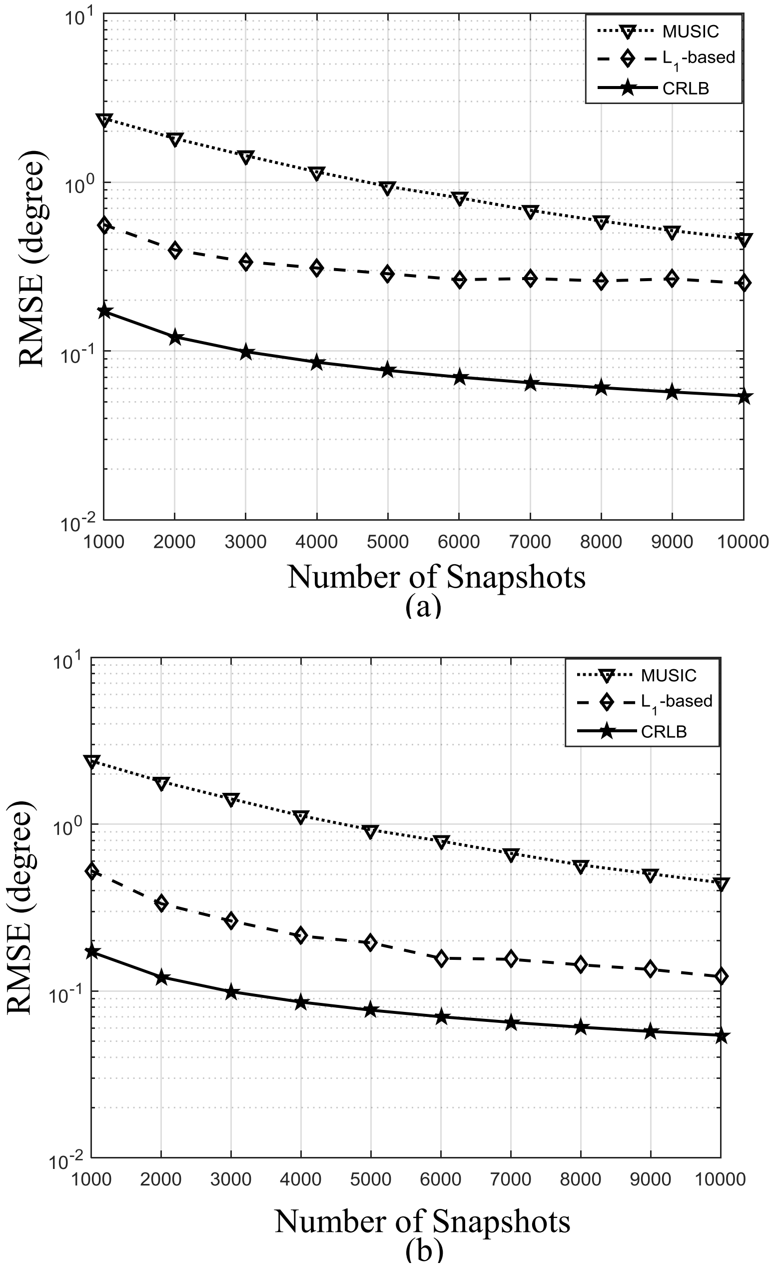

Figure 4.12: RMSE performance versus number of snapshots utilizing MUSIC and ℓ_1–based optimization for underdetermined DOA estimation with $M = 6$, SNR = 20 dB for (a) Case 1, and (b) Case 2.

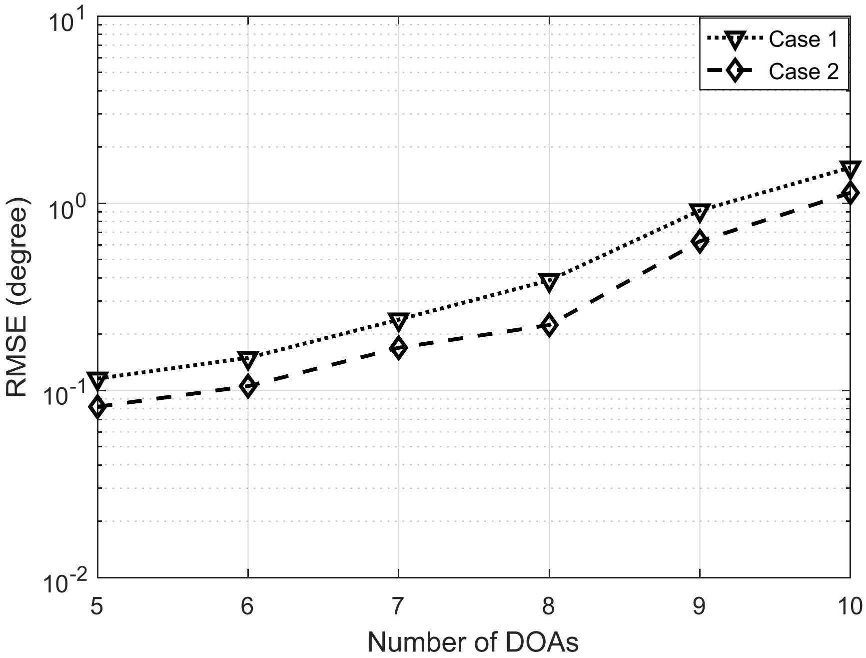

Figure 4.13: Comparison of RMSE performance versus number of DOAs for ℓ_1-based optimization using Case 1 and Case 2 with snapshots = 3000.

case 1. From this performance improvement, the proposed banded–like circulant mutual coupling matrix not only improves the RMSE performance or DOA estimation accuracy but also reduces the average run–time of the DOA estimation algorithm.

4.6 Summary

In this chapter, first of all, a simple banded–like circulant mutual coupling matrix was proposed. This MCM improves underdetermined DOA estimation estimation performance and accuracy in the presence of mutual coupling. This mutual coupling compensation method functions well with nested sparse circular arrays. Impedance matrix values were extracted from an electromagnetic simulation software and mutual coupling matrix values evaluated. Rather than utilizing all 36 coupling values for a 6–element nested sparse circular array, using only 4 values obtains better performance with the proposed method in this paper. The proposed technique achieves improved DOA estimation

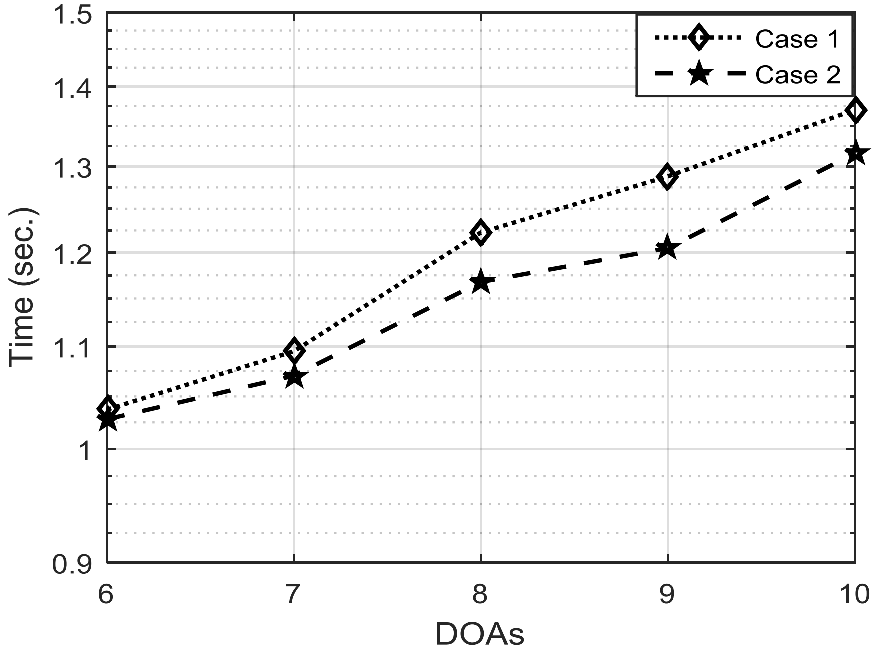

Figure 4.14: Average run–time versus DOAs comparison for ℓ_1–based optimization using Case 1 and Case 2.

performance, better RMSE as well as lower average run–time. RMSE performance as related to number of snapshots was also investigated. As the number of snapshots increases, the RMSE performance becomes better. Hence, nested sparse circular array is capable of performing DOA estimation for more sources than sensors in the presence of mutual coupling without degrading the estimation performance using a simple banded–like circulant mutual coupling matrix compensation method.

Chapter 5

Underdetermined Wideband DOA Estimation

5.1 Introduction

In Chapter 3 and Chapter 4, we considered underdetermined DOA estimation problem for narrowband signals. In most of sparse signal recovery (SSR) based methods, the techniques applied involve only narrowband signals and the literature for wideband signals is less sufficient. Despite the fact that wideband DOA estimation utilizing sparse signal recovery based techniques is not new, earlier works hardly address the underdetermined DOA estimation case [93].

In this chapter, we investigate a wideband model for the signal received by an antenna array, as opposed to the narrowband model that has so far been the topic under consideration. A wideband signal is defined as any signal whose energy is distributed over a bandwidth that is large in comparison to the signal's center frequency [139]. As an example, ultrawideband (UWB) noise radars use wideband signals offering low probability of detection (LPD), at the same time achieving good target detection and high resolution [140]. We therefore extend the algorithms studied in the foregoing chapters to problems related to wideband array processing.

In the wideband DOA estimation problem, when the incoming signals are wideband, the most attractive approach is to decompose the wideband signal into narrowband constituents and wideband DOA estimation problem in this case is mainly concerned with determining a way to use the multiple correlation matrices at different frequencies to get accurate DOA estimates [45]. One of the methods that is applied is the incoherent signal subspace method (ISSM) [141]. ISSM is one of the simplest wideband technique that estimates the source DOAs separately at each narrowband frequency. It then constructs the final estimate of the DOAs by taking an average [45]. This approach works well at high SNR levels. However, the performance suffer severely at lower SNR levels because even a single outlier from one narrowband component can potentially lead to inaccurate estimates through the averaging process [45]. Another disadvantage of this method is that it is incapable of handling coherent sources.

To overcome the drawbacks of this method, a sparse signal recovery techniques proposed in Chapter 3 is extended to wideband signals. In this chapter, we address the wideband underdetermined DOA estimation problem by incorporating the frequency–domain approach [84], [142] and dividing the wideband received signal data into narrowband signals [143]. With the increase in DOFs as shown in Chapter 3, we re–formulate the underdetermined DOA estimation to wideband signals and a similar technique as in [141] is used to decompose the wideband signal into different narrowband components. Then, we use the proposed NSCA at different frequency bins and apply the proposed ℓ_1–based optimization technique to perform underdetermined DOA estimation.

5.2 Ideal Case for Wideband DOA Estimation

5.2.1 Problem Formulation

For wideband signal sources, suppose that D far–field wideband signals impinge onto an M-element array from the directions of $\Phi_d = (\phi_1), (\phi_2), ..., (\phi_D)$ corrupted by additive white gaussian noise [142], [144], [145]. At time t, the received signal at the m-th array element is given by

$$\boldsymbol{x}_m(t) = \sum_{d=1}^{D} \mathbf{s}_d(t - \tau_{md}) + \mathbf{n}_m(t) \tag{5.1}$$

where $\boldsymbol{x}_m(t)$ is the waveform of the dth source, τ_{md} is the propagation delay of the mth element of the array with respect to the reference element, $\mathbf{n}_m(t)$ is the additive white gaussian noise [122]. The observation time T is divided into L sub–segments such that each sub–segment has an observation time T_d, therefore $T = LT_d$. When we transform T_d of l–th segment into frequency domain, we have J non–overlapping narrowband components. The frequency domain received data at frequency f_j is given by

$$\mathbf{X}_l(f_j) = \mathbf{A}(\phi, f_j)\mathbf{S}_l(f_j) + \mathbf{N}_l(f_j) \tag{5.2}$$

where $l = 1, 2, ..., L$ and $j = 1, 2, ..., J$, where $\mathbf{X}_l(f_j)$, $\mathbf{S}_l(f_j)$, and $\mathbf{N}_l(f_j)$ are derived from the Discrete Fourier Transform (DFT) of the received data, signals and noise respectively. From this array model, the wideband array model is given by

$$\mathbf{A}(\phi, f_j) = [\mathbf{a}(\phi_1, f_j), \mathbf{a}(\phi_2, f_j), ..., \mathbf{a}(\phi_D, f_j)] \tag{5.3}$$

where $\mathbf{a}(\phi_d, f_j)$ is the kth steering vector at frequency bin f_j. From the frequency domain received data $\mathbf{X}_l(f_j)$, the wideband covariance matrix is given by

$$\begin{aligned}\mathbf{R}(f_j) &= \frac{1}{L}\sum_{l=1}^{L} \mathbf{X}_l(f_j)\mathbf{X}_l^H(f_j) \\ &= \mathbf{A}(\phi, f_j)\mathbf{R}_s(f_j)\mathbf{A}^H(\phi, f_j) \\ &\quad + \sigma_n^2(f_j)\mathbf{I}\end{aligned} \tag{5.4}$$

where $\mathbf{R}_s$ is the wideband signal covariance matrix given by the diagonal of signal powers and $\mathbf{I}$ is an identity matrix. By using the Khatri–Rao product from Section 3.2.3, we vectorized the wideband covariance matrix in (5.4) such that

$$\mathbf{y} = \text{vec}(\mathbf{R}(f_j))$$

$$= \mathrm{vec}(\mathbf{A}(\phi, f_j)\mathbf{R}_s(f_j)\mathbf{A}^H(\phi, f_j)) + \mathrm{vec}(\sigma_n^2(f_j)\mathbf{I}) \tag{5.5}$$

From this output signal, we can apply the DOA estimation at each frequency bin using DOA estimation algorithms.

5.2.2 MUSIC and ℓ_1–based Technique in Wideband DOA Estimation

5.2.2.1 Extended MUSIC Algorithm

In the frequency–domain approach, an essential step is to merge the subspaces at various frequencies to obtain a DOA spectrum fusion. In order to compute DOA spectrum, the following formula is used;

$$P(\phi) = \frac{1}{\sum_{j=1}^{J} \left\| \mathbf{U}_n^H(f_j)\mathbf{F}^{\frac{1}{2}}\mathbf{b}(\phi, f_j) \right\|^2} \tag{5.6}$$

where $\mathbf{U}_n(f)$ denotes the noise subspace with f being fixed, $\mathbf{b}(\phi, f)$ is an extended steering vector.

5.2.2.2 Extended ℓ_1–based Technique

From (5.5), let the estimation error of $\hat{\mathbf{y}}$ be $\Delta\mathbf{y}$. This implies that

$$\hat{\mathbf{y}}_i = \mathbf{y}_i + \Delta\mathbf{y}_i \tag{5.7}$$

where, $\mathbf{y}_i = \mathbf{B}(\phi, f_i)\mathbf{p}_i + \mathrm{vec}(\sigma_n^2\mathbf{I})$ from the formulation in 5.2.1 and Section 3.2.3.

In order to extend our approach to wideband sparse signal recovery or ℓ_1–penalization, we need to appropriately choose the optimization criteria which is

$$\min \left\|\mathbf{p}_j\right\|_1 \text{ subject to } \left\|\mathbf{y}_j - \mathbf{B}\mathbf{p}_j\right\|_2^2 \leq \beta^2 \tag{5.8}$$

The sparsity of the signal behaves only in the spatial domain instead of the frequency domain. Thus, we can employ the ℓ_1–norm minimization formulation for sparse signal recovery. In this case, the wideband DOA estimation can be reduced to

$$\min_{\hat{\mathbf{p}}} \left\|\hat{\mathbf{p}}_j\right\|_1 \text{ subject to } \left\|\mathbf{W}^{-\frac{1}{2}}\left[\hat{\mathbf{y}}_j - \mathbf{B}(\phi, f_j)\hat{\mathbf{p}}_j\right]\right\|_2^2 \leq \beta^2 \tag{5.9}$$

In the next subsection, we consider numerical simulation for wideband DOA estimation. Subspace based MUSIC algorithm and sparse signal recovery based approach ℓ_1–based optimization is used in these simulation examples. From the formulation, we are able to perform underdetermined DOA estimation for wideband signals.

5.2.3 Numerical Simulations for Wideband DOA Estimation

From the above formulation, we show the performance of the NSCA for a wideband underdetermined DOA estimation. We consider lower frequency to be 2 GHz and higher frequency 3 GHz with 6 frequency bins. We observe how MUSIC based method and the ℓ_1–based optimization approach estimate DOAs for the array with 6 elements for 8 DOAs impinging on the array from directions $\phi = [15°, 36°, 70°, 90°, 112°, 130°, 145°, 162°]$.

5.2.3.1 Wideband DOA Estimation Spectrum and RMSE

In this subsection, the wideband DOA estimation of the two algorithms is compared. Firstly, we compare whether all the DOAs are resolved and dynamic range by plotting the DOA spectrum. Then, we compare the accuracy of the wideband underdetermined DOA estimation by plotting the RMSE against SNR. Figure. 5.1(a) shows spectrum of MUSIC based technique whilst Fig. 5.1(b) shows spectrum of ℓ_1–based technique. In Fig. 5.1(b) all DOAs are resolved with sharp peaks and noise level is less that -100 dB and dynamic range is very high whilst for Fig. 5.1(a), the spectrum is not sharp although all the DOAs are resolved with very low dynamic range. MUSIC method therefore is not good candidate for underdetermined wideband DOA estimation for low SNR levels.

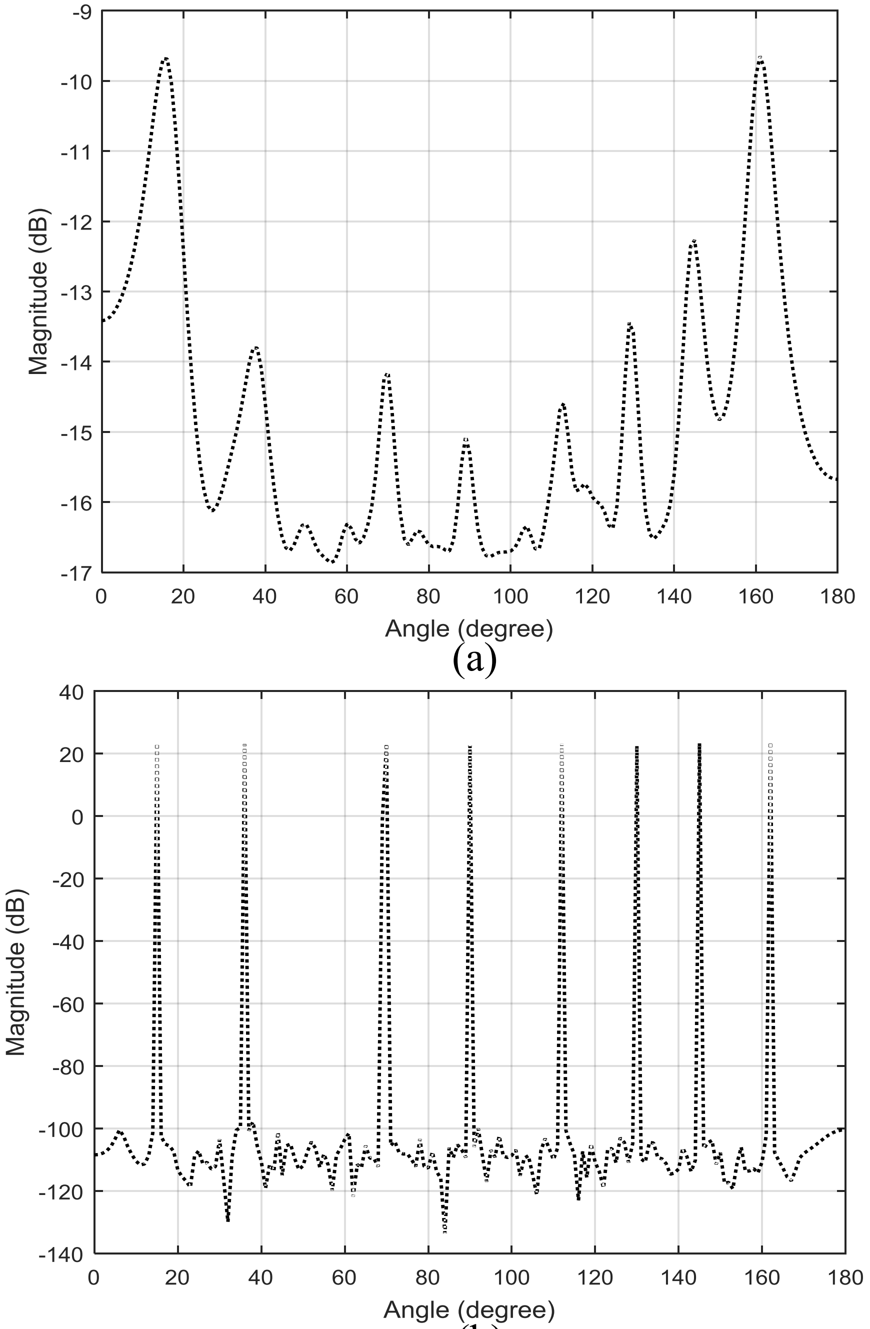

(a)

(b)

Figure 5.1: Underdetermined Wideband DOA estimation using NSCA. $M = 7$, $D = 8$, snapshots = 2000, and SNR = 0 dB for for (a) MUSIC based technique and (b) ℓ_1-based optimization.

In Fig. 5.2, the performance of MUSIC and ℓ_1–based technique is compared to CRLB for underdetermined DOA estimation. The RMSE performance for MUSIC is not as good as that of ℓ_1–based technique which is very close to CRLB. This is attributed to low peak level in which there is less difference between noise and spectrum peaks as observed in Fig. 5.1(a). Thus, the proposed NSCA is capable of performing wideband undetermined DOA estimation in the case when we use ℓ_1–based technique.

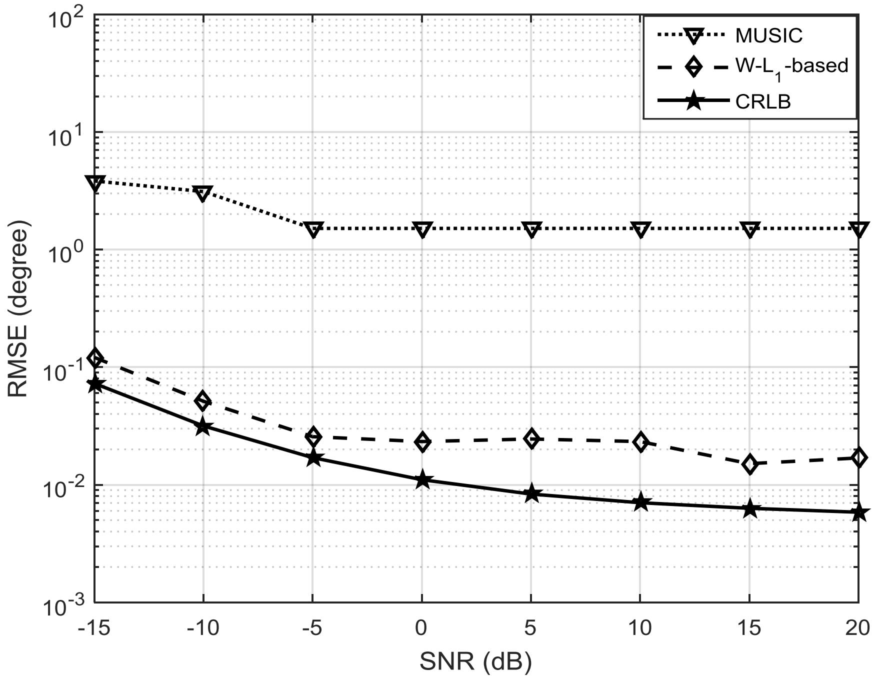

Figure 5.2: RMSE of underdetermined Wideband DOA estimation using NSCA. $M = 7$, $D = 8$ and Snapshots = 10000.

5.2.3.2 Wideband DOA Estimation Aliasing Free Test

In order to achieve high resolution in DOA estimation, array spacing may introduces ambiguity in identifying the source directions due to the aliasing components. We investigate the effect of spatial aliasing on the direction of arrival spectrum due to wideband sources. We have to note that the extent of aliasing is frequency dependent. In Fig. 5.3, we plot the frequency–bearing images at an SNR of 0 dB for frequency of 2–4 GHz band.

We observe that spatial aliasing appears when MUSIC algorithm is applied as shown in Fig. 5.3(a) but no aliasing is observed in the ℓ_1–based technique Fig. 5.3(b).

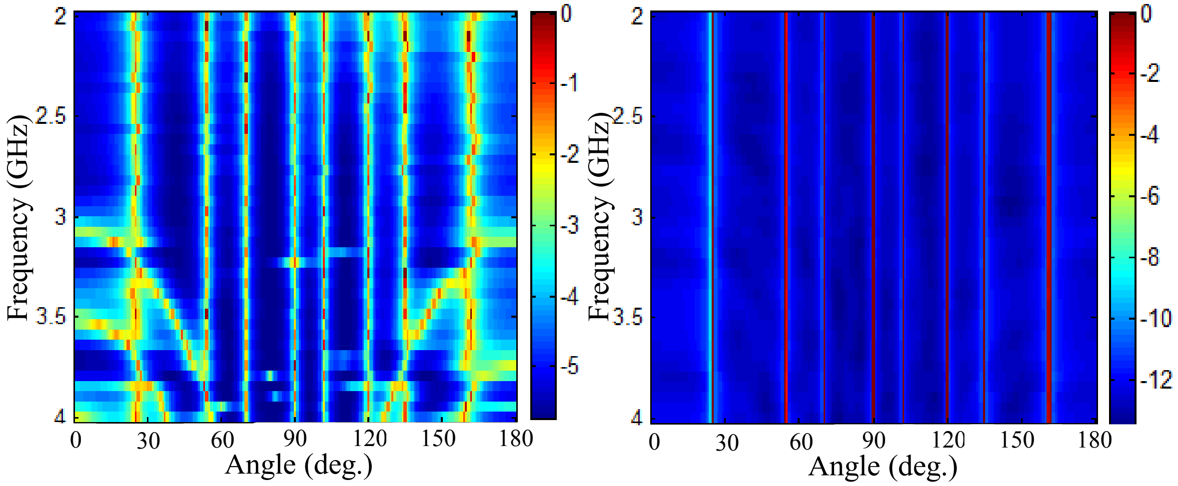

(a) (b)

Figure 5.3: Frequency–bearing images for underdetermined Wideband DOA estimation using NSCA.

5.3 Mutual Coupling Effects in Underdetermined Wideband DOA Estimation

Over the last few years, compressive sensing [56], has continued to enjoy popularity and is a rapidly expanding field in modern signal processing [60]. The key idea in this field is based on the fact that majority of real–life signals can be approximated by sparse vectors. Therefore, if we exploit the sparse signal structure, signal acquisition cost can be reduced, and accurate signal reconstruction can be accomplished in a computationally efficient way [60]. The emerging field of sparse representations therefore, has given restored interest to the DOA estimation problem [136]. A recursive weighted minimum–norm algorithm called FOCUSS was proposed in [146] to achieve sparsity for the problem of DOA estimation. The idea of enforcing sparsity to a general framework using ℓ_1–SVD method which has applications in a wide variety of practical DOA estimation problems was extended in [95]. In this chapter, we reformulate the underdetermined DOA estimation problem for wideband signals in the sparse signal reconstruction framework. We further develop the ℓ_1–based optimization to underdetermined DOA estimation such that we can utilize the increase in degrees of freedom from the Khatri–Rao approach in the presence of mutual coupling. We consider (5.5) as a sparse signal representation problem which is given by

$$\mathbf{y} = (\tilde{\mathbf{A}}^* \odot \tilde{\mathbf{A}})\mathbf{p} + \sigma_m^2 \mathbf{1}_m^T \tag{5.10}$$

In order to extend ℓ_1 penalization to (5.10), an optimization criteria is required to be determined appropriately that is

$$\min \|\mathbf{p}\|_1 \text{ subject to } \left\|\mathbf{y} - \tilde{\mathbf{A}}^* \odot \tilde{\mathbf{A}}\mathbf{p}\right\|_2^2 \leq \beta^2 \tag{5.11}$$

where β is a parameter specifying how much noise we wish to allow. Consequently, an unconstrained form of this objective function is

$$\min \left\|\mathbf{y} - \tilde{\mathbf{A}}^* \odot \tilde{\mathbf{A}}\mathbf{p}\right\|_2^2 + \lambda \|\mathbf{p}\|_1 \tag{5.12}$$

The ℓ_2 term in (5.12) forces the residual to be small and λ controls the tradeoff between the sparsity of the spectrum and residual norm [109].

In a practical setting, $\boldsymbol{y}$ in (5.10) can be estimated from N snapshots such that $\Delta\mathbf{y} = \hat{\mathbf{y}} - \mathbf{y}$. The estimate error is asymptotically normal distribution (AsN), thus

$$\Delta\mathbf{y} = \text{vec}(\Delta\mathbf{R}_{xx}) \sim AsN\left(0_{M^2,1}, \frac{1}{N}\mathbf{R}_{xx}^T \otimes \mathbf{R}_{xx}\right) \tag{5.13}$$

which leads to

$$\mathbf{W}^{-\frac{1}{2}}\Delta\mathbf{y} \sim AsN\left(0_{M^2,1}, \mathbf{I}_{M^2}\right) \tag{5.14}$$

where the weighting matrix $\mathbf{W}^{-\frac{1}{2}} = \sqrt{N}\mathbf{R}_{xx}^{-\frac{T}{2}} \otimes \mathbf{R}_{xx}^{-\frac{1}{2}}$ with $\mathbf{W} = \frac{1}{N}\mathbf{R}_{xx}^{T} \otimes \mathbf{R}_{xx}$. Let $\hat{\mathbf{p}}$ be the estimate of $\mathbf{p}$. From (5.14) we can deduce that

$$\mathbf{W}^{-\frac{1}{2}} \left[\hat{\mathbf{y}} - \tilde{\mathbf{A}}^{*} \odot \tilde{\mathbf{A}}\hat{\mathbf{p}}\right] \sim AsN\left(0_{M^2,1}, \mathbf{I}_{M^2}\right) \tag{5.15}$$

which then results in

$$\mathbf{W}^{-\frac{1}{2}} \left\|\hat{\mathbf{y}} - \tilde{\mathbf{A}}^{*} \odot \tilde{\mathbf{A}}\hat{\mathbf{p}}\right\|_2^2 \sim As\chi^2(M^2) \tag{5.16}$$

where $As\chi^2(M^2)$ denotes the asymptotic chi-square distribution with M^2 degrees of freedom. Therefore, DOA estimation can be reduced to

$$\min_{\hat{\mathbf{p}}} \|\hat{\mathbf{p}}\|_1 \text{ subject to } \left\|\mathbf{W}^{-\frac{1}{2}} \left[\hat{\mathbf{y}} - \tilde{\mathbf{A}}^{*} \odot \tilde{\mathbf{A}}\hat{\mathbf{p}}\right]\right\|_2^2 \le \beta^2 \tag{5.17}$$

where $\beta = \sqrt{\chi^2(M^2)}$. The problem (5.17) is therefore a second–order cone program problem.

5.3.1 Numerical Results

From the formulation in previous sections, we evaluate the performance of the nested sparse circular array for underdetermined DOA estimation of wideband signals in the presence of mutual coupling. We consider the wideband signals to be gaussian processes with zero mean with center frequency $f_0 = 2.5$ GHz and the bandwidth $BW = 200$ MHz, lower frequency to be 2 GHz and higher frequency 3 GHz with 5 frequency bins. We examine the performance of the sparse signal reconstruction method ℓ_1-based optimization approach in DOA estimation. We consider an array with 6 elements, 1000 snapshots and an SNR of 0 dB. 7 wideband signal sources impinging on the array from directions $\phi = [20^\circ, 35^\circ, 65^\circ, 80^\circ, 110^\circ, 130^\circ, 148^\circ]$. The radius of the sparse circular array is $r = \lambda/2$.

5.3.1.1 Spectra of Underdetermined Wideband DOA Estimation with Mutual Coupling

The underdetermined DOA estimation performance in the presence of mutual coupling is considered. Figure 5.4 shows spectra of wideband DOA estimation in the presence of mutual coupling in the case when ℓ_1–based technique is used. In this figure, we observe that we are capable of resolving all DOAs correctly and the peaks are sharp. The noise level is about -100 dB and dynamic range is very high.

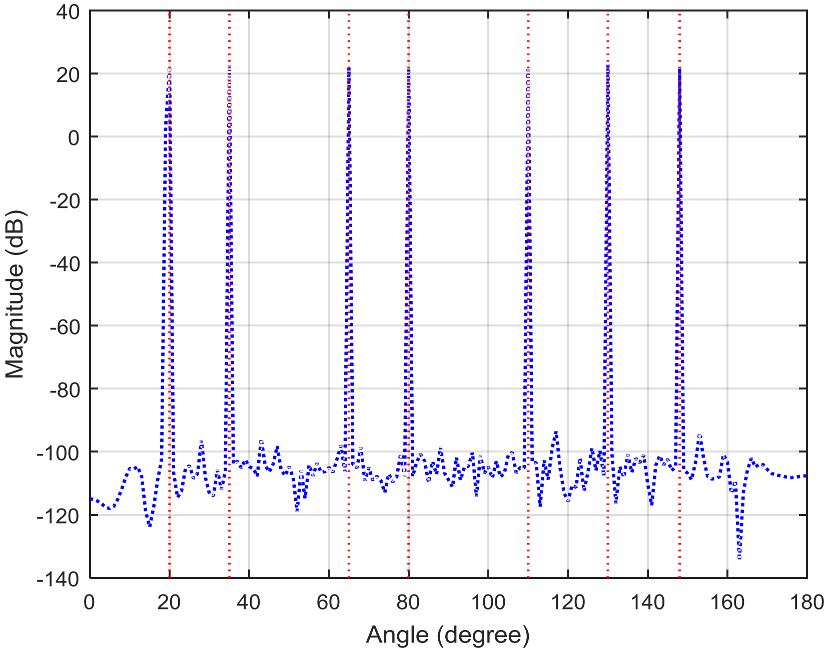

Figure 5.4: Spectra for underdetermined wideband DOA estimation using NSCA in presence of mutual coupling with $D = 7$, $M = 6$, snapshots = 1000, and SNR = 0 dB for ℓ_1–based optimization.

In Fig. 5.5, we present the spectra plot for 10 DOAs arriving on the array from the directions $\phi = [15°, 30°, 46°, 54°, 70°, 90°, 110°, 130°, 145°, 162°]$. In this figure as well, all DOAs are resolved correctly as can be observed from the comparison between the blue graph (estimated DOAs) and red lines (true DOAs). Thus, we verify the wideband DOA estimation in the presence of mutual coupling using ℓ_1–based technique as well in this example. We observe that all DOAs are resolved correctly and we obtain very high dynamic spectrum. Even when the number of sources increases, the proposed approach obtains good DOA estimation performance with mutual coupling compensation using the proposed method.

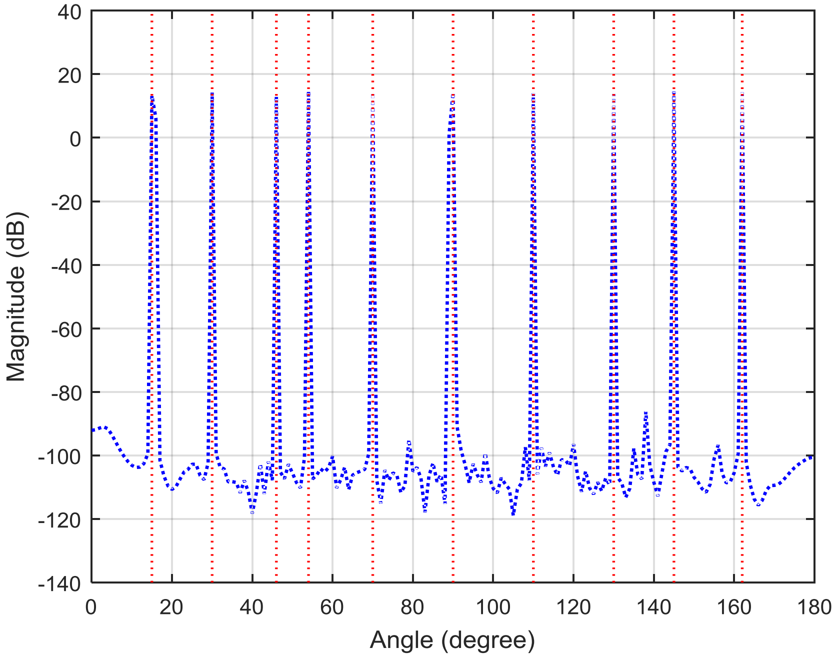

Figure 5.5: Spectra for underdetermined wideband DOA estimation using nested sparse circular array in presence of mutual coupling with $D = 10$, $M = 6$, snapshots $= 1000$, and SNR $= 0$ dB for ℓ_1–based optimization.

5.3.1.2 Average Run–time

In the next example, we consider the average run time as compared to the number of frequency bins. This comparison is shown in Fig. 5.6. In this figure, we observe that as the number of frequency bins increases, there is a tremendous increase in the average run–time. From roughly 5 seconds with 2 frequency bins, to about 12 seconds for 6 frequency bins. In both 100 and 1000 snapshots cases, there is very little difference in the average run–time. Thus, an increase in the number of snapshots has a limited effect in the average run–time as compared to an increase in the number of frequency bins.

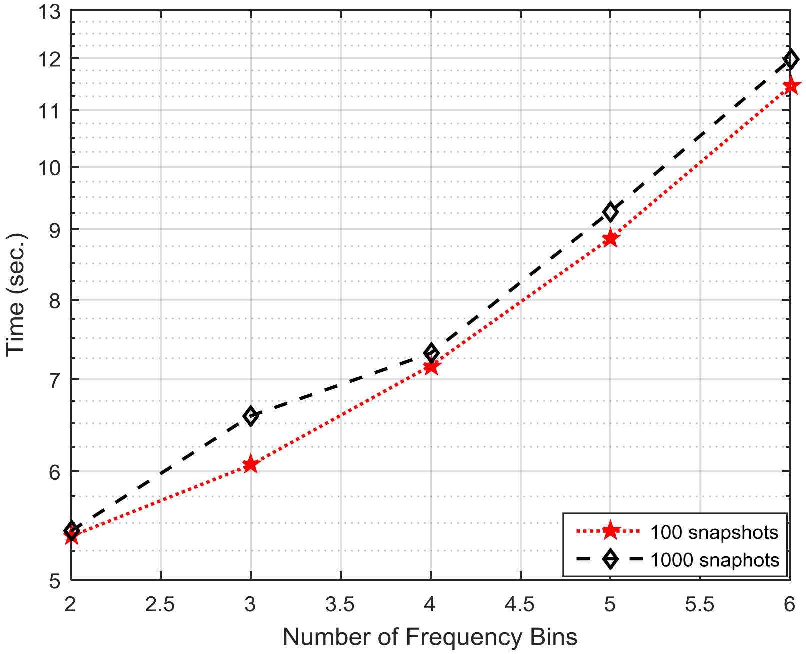

Figure 5.6: Average run time versus number of frequency bins for underdetermined wideband DOA estimation in presence of mutual coupling with $D = 7$, $M = 6$, SNR = 0 dB for ℓ_1–based optimization.

5.3.1.3 SNR Dependency for DOA Estimation

In this subsection's examples, we examine the RMSE performance of ℓ_1–based optimization technique. Firstly, we compare the RMSE accuracy when we consider two cases of mutual coupling matrix as illustrated in Chapter 5. Figure 5.7 show the two cases of the mutual coupling matrix. In terms of Case 1, all 36 coupling values are used. For Case 2, the proposed simple banded–like circulant mutual coupling matrix in Chapter 5 with 4 coupling values is used.

In Fig. 5.8, the underdetermined DOA estimation accuracy for the two cases is presented. In this figure, we observe that Case 2 achieves a better RMSE accuracy as compared to case 1. For wideband signals similar to narrowband signal sources, Case 2 obtains better DOA estimation accuracy and performance.

Secondly, We compare the RMSE of underdetermined DOA estimation as a function of SNR in uncalibrated case as well as the proposed mutual coupling compensation case

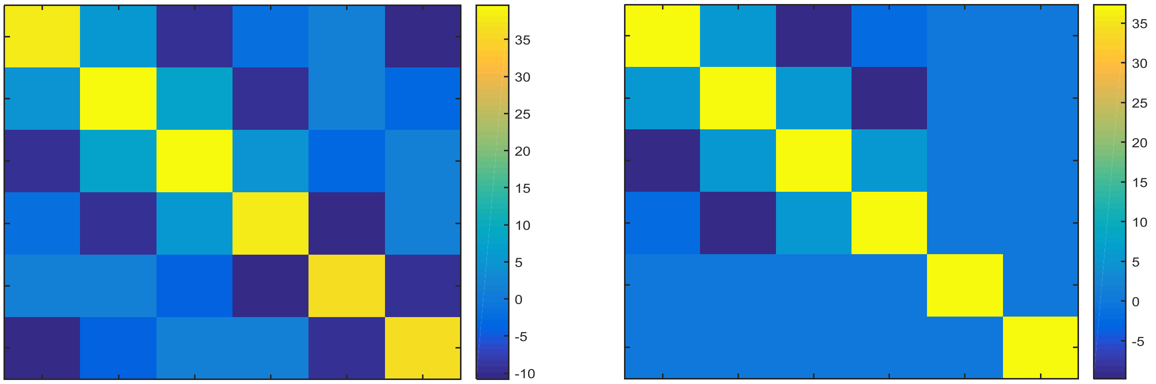

Figure 5.7: Mutual coupling matrix plot (left) Case 1, and (right) Case 2.

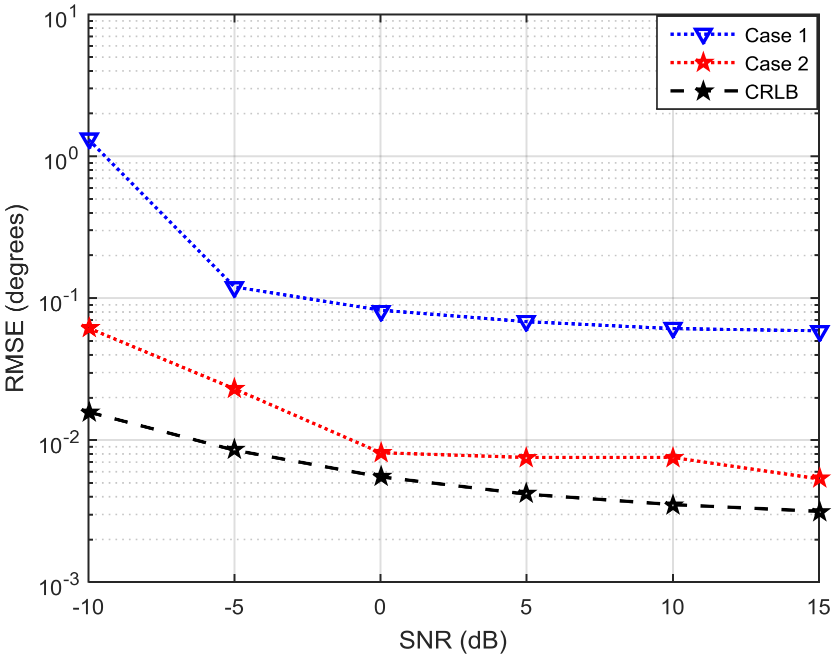

Figure 5.8: RMSE versus SNR comparison for Case 1 and Case 2 MCM with M = 6, D = 7, snapshots = 1000.

(Case 2) to the Cramer Rao lower bound (CRLB). In this simulation experiment, the number of trials is 50. In Fig. 5.9, we observe the RMSE of ℓ_1–based optimization as a function of SNR for an underdetermined DOA estimation case in the presence of mutual coupling. Seven wideband signal sources are impinging on the NSCA. The case in which the mutual coupling is uncalibrated obtains poor RMSE performance as compared to the proposed simple mutual coupling compensation. The proposed case's performance is close to the CRLB. In Fig. 5.9, we verify that the performance of the proposed simple mutual compensation for nested sparse circular arrays improves as the SNR is increasing for underdetermined DOA estimation.

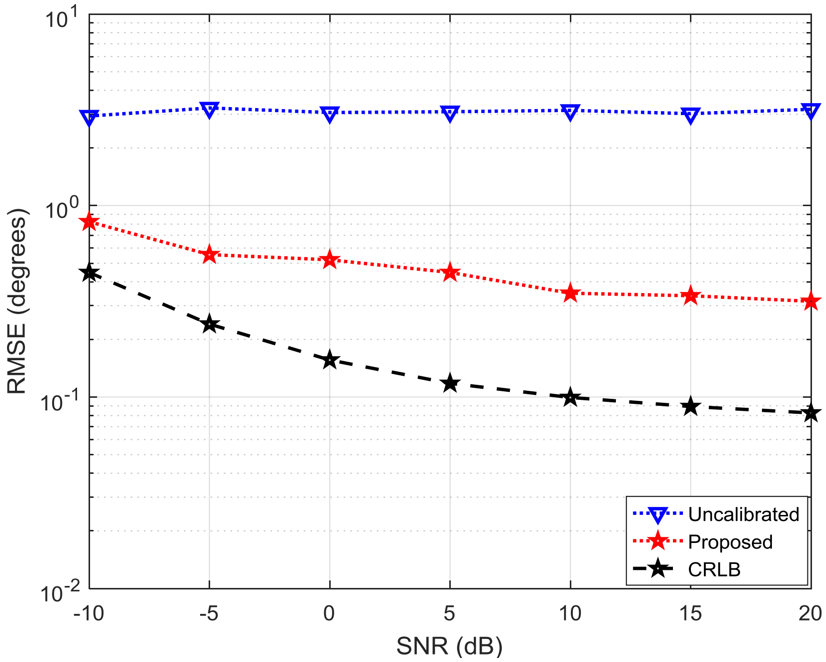

Figure 5.9: RMSE performance versus SNR in an uncalibrated case and simple mutual coupling compensation case with $M = 6$, $D = 7$, snapshots = 100.

5.4 Summary

In this chapter, the problem of underdetermined wideband DOA estimation has been considered. In the approach used, wideband signals were decomposed the into narrowband components multiple correlation matrices were found at different frequencies to get accurate DOA estimates. To overcome some drawbacks of this method, a sparse signal recovery techniques proposed in chapter 3 was extended to wideband signals. Furthermore, a new mutual coupling compensation method for wideband signals using nested sparse circular arrays. A simple mutual coupling matrix proposed in chapter was used for underdetermined direction of arrival estimation. By using the banded-like circulant mutual coupling matrix in the wideband underdetermined DOA estimation problem, the nested sparse circular array is capable of estimating more sources than sensors in the presence of mutual coupling. From simulation experiments, we verified that the proposed approach achieves better RMSE performance as well as excellent DOA estimation accuracy. This method is cost–effective and easy to implement whilst achieving better DOA estimation performance.

Chapter 6

Hemispherical Near Field Measurements for Far Field Estimation

6.1 Introduction

In a wireless communication system, wave transmission over free space is accomplished by an antenna system [33]. For different communication systems, the specifications for an antenna system is different. Because of these specifications, antennas of different types, size and shapes are required for example satellite communication, personal communication (such as smart phone), IoT sensors, etc. Although many theoretical models are available to describe the performance of these antenna systems, experimental measurements are required to validate these models [33]. In this case, antenna measurements are performed to validate an antenna if it meets specifications. Far field radiation pattern is one of the most important parameters to characterize an antenna's performance. In most cases, it is impractical or impossible to measure an antenna's far field using a conventional far field range. This may be as a result of the distance to the radiating far field being too long, or practically not possible to move the antenna from its operating environment to an antenna range [37]. Thus, it is often necessary to ascertain the far field patterns from measurements made in the radiating near field region of the antenna.

The problem of antenna radiation pattern reconstruction or restoration from near field measurements by means of a near–field far–field (NF–FF) transformation has extensively been investigated [38], [40], [42], [78], [81], [147]. The near field far field method is utilized to a wide range of antenna systems such as cellular phone antennas, vehicle mounted antennas, large phased arrays and many others. In most cases, near field data is collected on a plane surface, cylindrical surface, or spherical surface [36], [147], [148]. Of these techniques, the planar technique is perhaps the most fully developed [149]. The near field far field methods have proved to be efficient and attractive alternatives to conventional far field and compact range measurements. Another important aspect of the near field far field methods is that they can be performed in a controlled environment, such as an anechoic chamber, which eliminates the effect of the environment (changing weather conditions, and electromagnetic (EM) interference) that cannot be eliminated in the case of outdoor far field measurements [150].

Spherical near field (SNF) measurement techniques allows the complete characterization of antenna designs. By sampling data on a spherical surface surrounding the antenna–under–test (AUT), the antenna performance is assessed under its real operating conditions [151]. However, near field ranges suffer from the disadvantage that a full sphere needs to be acquired so as to apply a near field far field transformation, making often the measurement time unaffordable [152]. In order to perform this transformation, the spherical wave expansion needs to be evaluated in an asymptotic way [38], [147], [152], using the whole sphere data. This method is time consuming and also prone to errors for very large antenna systems such as antennas mounted on a vehicle.

In spherical near field measurement technique, the earliest works were based on wave mode expansion [38], [147], [153], [154], [155]. In this technique, measured near field information is used to determine wave mode coefficients of the AUT [38]. From these wave mode coefficients, one can be able to calculate the antenna radiation pattern at any distance. On the contrary, when using these techniques, spatial sampling rate should satisfy Nyquist criterion. Therefore, when the number of sampling points are reduced from that criterion, the transformation procedure is deteriorated.

Source reconstruction method (SRM) is another near field far field transformation technique [42], [156], [157]. In this method, equivalence principle is applied in which the equivalent currents at an antenna aperture are reconstructed from known near field information. From the reconstructed equivalent currents at an antenna aperture, far field radiation pattern of the AUT can be calculated at any distance. Source reconstruction method (SRM) is an inverse radiation problem based on electric field integral equation. It is a technique that was developed for antenna diagnostics and as well as to carry out near field to far field transformation. In SRM, one establishes an equivalent current distribution that radiates the same fields as the actual currents induced in the AUT by applying electromagnetic equivalence principle [156]. Knowledge of equivalent currents allows the determination radiating elements, as well as prediction of AUT's radiated fields outside the equivalent currents domain [157]. In this method, equivalent currents at the AUT aperture are discretized based on the known basis functions and then these currents are determined with the inverse method of moments (MoM) techniques [81].

In most antenna far field measurements and analysis, the effect of the earth is not included. In real use case scenarios, the antenna's performance is affected by the earth. Thus, the effect of the earth on the far field pattern of the antenna is of particular importance [158], [159]. According to [158], when the radiation patterns of several different antennas mounted on finite size metallic ground planes were measured in the presence of the earth, it was found out that the radiation pattern was affected by the earth at low elevation angles. In [82], a procedure to extend the methods of moments (MOM) by linear approximation of conductor surface to include the case in which an antenna is located over a lossy half–space.

The far field of the antenna can be calculated if the real source distribution of the antenna is known. As a method of estimating the current distribution on the conductor surface, there is an inverse problem estimation [78], [82] using the near field. However, in this method, increase in the number of measurement points according to the number of current elements and decrease in estimation accuracy due to regularization can become a problem.

In this chapter, hemispherical near field measurement technique is utilized which reduces the amount of time it takes to perform near field measurements and complexity. The surface current distribution reconstruction problem falls into the ill–posed condition due to lack of near field information at lower elevation part. We therefore propose an ℓ_2–norm least squares solution which utilizes the Moore–Penrose pseudoinverse. By using this technique, an accurate equivalent current distribution is obtained. In order to include the effect of real ground, mirror image source is used by applying reflection coefficient method (RCM) to the equivalent electric current in order to reconstruct far field on real ground. Validation of the method is confirmed in simulation and measurement results.

6.2 Conventional Far Field Measurement Methods

In antenna measurements, the radiation pattern can be obtained by measurements and the radiation of the source regardless of its actual complexity can be characterized efficiently. In conventional far field measurements, open site antenna measurements and anechoic chamber measurements are the most common. In the open site method, far field measurement is carried out outdoors with sufficient space. The object to be measured is placed on a rotating table and measured as a receiving antenna. For electronically large antennas, the size and wavelength of the AUT is large, thus, the required distance increases and it becomes difficult to secure measurement space. The existence of ground reflected waves is inevitable in outdoor measurements. Therefore, it is necessary to introduce a configuration such as a high–level measurement field, a ground level measurement field, and a slant range [160] to reduce this influence. Furthermore, variations due to weather changes also affect outdoor far field measurements.

Anechoic chamber is a facility that simulates the free space of radio waves indoors by attaching a radio wave absorber to the wall surface of a radio wave shielded room and suppressing reflection of radio waves. As compared to open site method, anechoic chamber is advantageous because it is not affected by weather and surrounding scatterers, measurement environment is stable, reproducibility is good, and foreign noises can be avoided. However, there are limitations on the target size and measurement frequency, as well as high costs. In addition, since the measurement is performed on the metal surface, it is impossible to evaluate the far field assuming the earth.

6.3 Near Field Antenna Measurements

6.3.1 Hemispherical Near Field Method

The near field measurement is a method of measuring an antenna's radiation in the near field region of the measurement object and determining the far field by numerical processing. In general, near field measurement often refers to the near-field far field method which determines the far field characteristics by performing calculation processing on the amplitude / phase data measured in the near field. This method provides a solution to weather and space problems related to open site and anechoic chamber. Although this is the case, it is not easy to measure because the device used for measurement is expensive, takes long time and it is numerically complex.

Spherical near field measurement techniques allows the complete characterization of antenna designs. It is the most accurate and complex techniques as compared to other near field measurement techniques. It is used for omnidirectional and low gain antennas. In order to utilize the advantages of spherical near field measurements as well as overcome some of its drawbacks, hemispherical near field measurement technique is utilized in this chapter. It reduces the amount of time it takes to perform near field measurements and complexity. The hemispherical near field measurement set up is shown in Fig. 6.1.

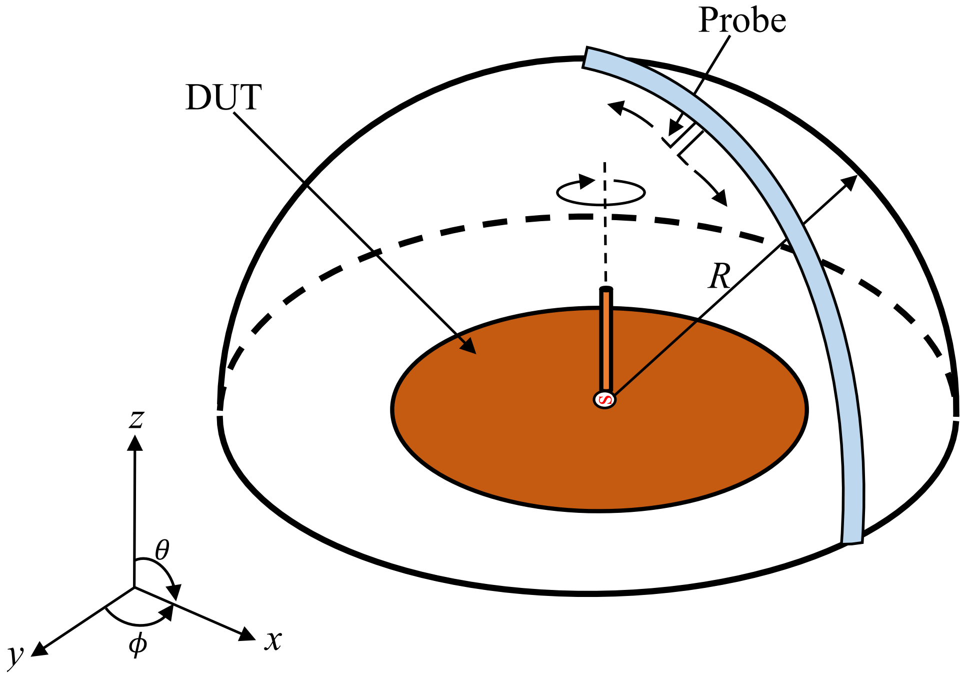

Figure 6.1: Measurement equipment and set up for hemispherical near field scan.

6.3.2 Wire Grid Model

In electromagnetic field analysis, it is necessary to discretize the analysis target. One of the discretization methods in moment method, is dividing a linear conductor along a line and replacing a planar conductor with a grid network (wire grid). This allows all linear and planar conductors to be considered as a collection of linear elements. The current flowing is therefore regarded as a linear current. Such approximation is called thin line approximation and is widely used for analysis of linear antenna. In our analysis, in order to derive wave source information on real surface, we consider approximating the conductor surface with a linear conductor element. The current distribution on the linear conductor is represented by $[\boldsymbol{J}]$, which is dicretized current. Figure 6.2 below shows the equivalent wire grid model for the AUT.

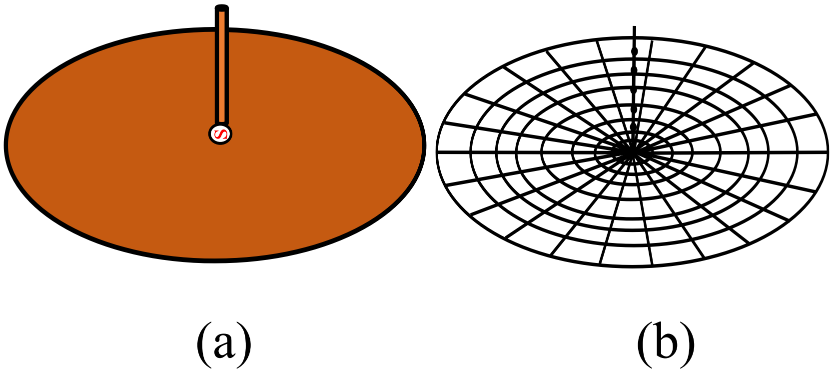

Figure 6.2: AUT and equivalent wire grid model of AUT. (a) Planar Model, and (b) wire grid model.

6.3.3 Moore–Penrose Inverse Method

We derive wave source information on real surface from hemispherical near field measurements performed in an anechoic chamber. From Maxwell equation, the electric field $\boldsymbol{E}$ at observation point $\boldsymbol{r}$’ by current distribution $\boldsymbol{J}$ on conductor surface in region $\boldsymbol{v}$ at the position $\boldsymbol{r}$ is expressed by the following integral equation:

$$\boldsymbol{E}(\boldsymbol{r}') = -\frac{j\eta}{k}\int_v \left\{k^2\boldsymbol{J}(\boldsymbol{r}) + \nabla\nabla\cdot\boldsymbol{J}(\boldsymbol{r})\right\}\boldsymbol{G}(\boldsymbol{r},\boldsymbol{r}')dv \tag{6.1}$$

where $\boldsymbol{G}(\boldsymbol{r},\boldsymbol{r}') = \frac{e^{-jk|\boldsymbol{r}-\boldsymbol{r}'|}}{4\pi|\boldsymbol{r}-\boldsymbol{r}'|}$ and $\nabla = \left(\frac{\partial}{\partial x}, \frac{\partial}{\partial y}, \frac{\partial}{\partial z}\right)$, η is the intrinsic impedance 120π, and k is wave number. Derivation of the actual wave source information is performed using near field information measured in anechoic chamber. Therefore, we assume an antenna on earth (realistic ground), and calculate the current distribution from measured near field. The real ground is assumed to be a lossy half–space. In order to obtain the transformation matrix for the hemispherical technique, the radial component of the measured near field is neglected. Thus, θ and ϕ components of the electric (magnetic) field distribution are given by;

$$\begin{bmatrix} E_\theta(H_\theta) \\ E_\phi(H_\phi) \end{bmatrix} = \begin{bmatrix} \cos\theta\cos\phi & \cos\theta\sin\phi & -\sin\theta \\ -\sin\phi & \cos\phi & 0 \end{bmatrix} \begin{bmatrix} E_x(H_x) \\ E_y(H_y) \\ E_z(H_z) \end{bmatrix} \tag{6.2}$$

In deriving the wave source information on the real surface, we consider approximating the conductor surface with a linear conductor element. The current distribution on the linear conductor is represented by $[\boldsymbol{J}]$, from which the following relation is established through discretization of the moment method [78], [82], [161] and (6.1).

$$\begin{bmatrix} E_\theta \\ E_\phi \end{bmatrix} = \begin{bmatrix} A_{x\theta} & A_{y\theta} & A_{z\theta} \\ A_{x\phi} & A_{y\phi} & A_{z\phi} \end{bmatrix} \begin{bmatrix} J_x \\ J_y \\ J_z \end{bmatrix} \tag{6.3}$$

where $[E]$ represents the measured electric field distribution, $[A]$ represent the coefficients of the radiation from each element and is determined by the approximate model shape obtained from wire grid model. In this paper, the approximate model used is a wire grid model of the DUT. By solving this matrix equation for the current vector, it is possible to acquire the surface current on the DUT. In conventional methods, the matrix equation (6.3) is solved by using generalized inverse matrix as,

$$[J] = ([A]^H[A])^{-1}[A]^H[E] \tag{6.4}$$

where $[A]^H$ is the Hermitian conjugate matrix of $[A]$. The, current distributions on the DUT are reconstructed using measured hemispherical electric field. The surface current distribution reconstructed at this step falls into the ill–posed condition due to the lack of near–field information at the lower elevation part. Thus, accurate surface current distribution can not be obtained.

We propose a method in which $[J]$ is calculated using the Moore–Penrose pseudoinverse [162] to ensure that solution exist for the linear system created. The Moore–Penrose pseudoinverse is a matrix that acts as a partial replacement for the matrix inverse in cases where it does not exist [162]. It chooses the minimum norm solution (find solution with smallest norm) to a system of linear equations with multiple solutions. The pseudoinverse provides a least squares solution to a system of linear equations. For an underdetermined scenario, applying the Moore–Penrose pseudoinverse yields the solution with the smallest ℓ_2–norm among all vectors $[J]$ satisfying $[E] = [A][J]$ such that;

$$\min_{[J]} \|[J]\|_2 \text{ subject to } [E] = [A][J] \tag{6.5}$$

where, the Moore–Penrose pseudoinverse provides the minimum ℓ_2–norm representation $[A]^+[E]$ of $[E]$, where $[A]^+$ is the pseudoinverse. The pseudoinverse thus, solves the problem as

$$\|[A][J] - [E]\|_2 \geq \|[A][q] - [E]\|_2 \tag{6.6}$$

where $[q] = [A]^+[E]$ which holds if and only if $[J] = [A]^+[E] + [I - A^+A]w$, where I is identity matrix and $\boldsymbol{w}$ is an arbitrary vector.

6.4 Antenna Far Field Estimation on Earth using Reflection Coefficient Method (RCM)

Far field is usually defined by the far electric field (E_θ, E_ϕ). It is obtained by setting the observation point at infinity point ($R = \infty$) in the near electric field equation. The method of moments for a scattered conductor in a semi–infinite space where $z = 0$ is a complete conductor ground plane as shown in Fig. 6.3. When there is a wave source on the ground plane, a mirror image source can be considered at symmetrical positions on the $z = 0$ plane from the boundary condition for the perfect conductor plate (mirror image method).

When a plane wave is incident from the medium I at the boundary surface where the medium I (ϵ_1, μ_1, σ_1) and the medium II (ϵ_2, μ_2, σ_2), and the tangential component of the magnetic field are continuous, the reflected wave and the transmitted wave are obtained from boundary conditions [161], [163]. In the semi–infinite space where the upper half is the free space and the lower half is the earth (dielectric) as shown in Fig. 6.3, the reflection coefficient method is used [164], [165]. In terms of the earth, the permittivity , permeability, and conductivity are assumed to be $\epsilon_s\epsilon_0$, μ_0, and σ. The complex relative permittivity of the earth is therefore given by;

$$\epsilon_r = \epsilon_s - j\frac{\sigma}{\omega\epsilon_0} \tag{6.7}$$

Therefore, the plane wave reflection coefficient R_{TM} and R_{TE} for the ground is given by;

$$R_{TM} = \frac{\epsilon_r \cos\theta - \sqrt{\epsilon_r - \sin^2\theta}}{\epsilon_r \cos\theta + \sqrt{\epsilon_r - \sin^2\theta}} \tag{6.8}$$

$$R_{TE} = \frac{\cos\theta - \sqrt{\epsilon_r - \sin^2\theta}}{\cos\theta + \sqrt{\epsilon_r - \sin^2\theta}} \tag{6.9}$$

Here, R_{TM} and R_{TE} represent reflection coefficients of the TM wave and the TE wave with respect to the earth. In the reflection coefficient method, the spherical wave is regarded as a TM wave, and the reflection term by the earth is approximated by multiplying the green function of the mirror image source by R_{TM}. By introducing these reflection coefficients, image current below the earth can be assumed as shown in Fig. 6.3. We therefore perform radiation integration from these currents and derive the far-field. Thus, the far field is therefore estimated by:

$$E_\theta(\theta,\phi) = \frac{jZ_0ke^{-jkr}}{4\pi r}F_\theta(\theta,\phi) \tag{6.10}$$

$$E_\phi(\theta,\phi) = \frac{jZ_0ke^{-jkr}}{4\pi r}F_\phi(\theta,\phi) \tag{6.11}$$

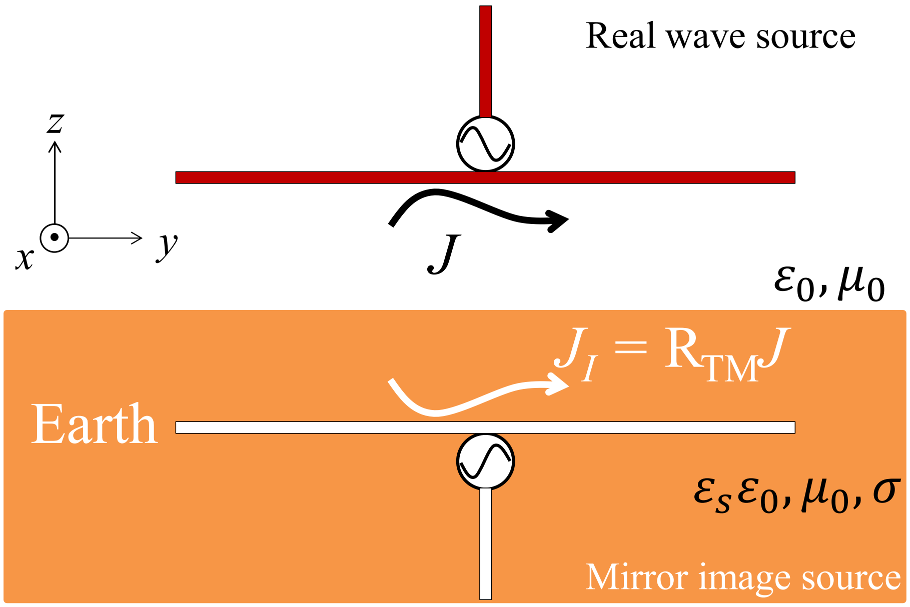

Figure 6.3: Mirror image source for AUT above lossy half–space (earth).

$$F_\theta(\theta,\phi) = \sum_{n=1}^{N} \boldsymbol{J}_n \left\{ \left(\boldsymbol{l}_n \cdot \hat{\theta} \right) e^{jk r_n \cdot \hat{r}} - R_{TM} \left(\boldsymbol{l}''_n \cdot \hat{\theta} \right) e^{jk r''_n \cdot \hat{r}''} \right\} \tag{6.12}$$

$$F_\phi(\theta,\phi) = \sum_{n=1}^{N} \boldsymbol{J}_n \left\{ \left(\boldsymbol{l}_n \cdot \hat{\phi} \right) e^{jk r_n \cdot \hat{r}} + R_{TE} \left(\boldsymbol{l}''_n \cdot \hat{\phi} \right) e^{jk r''_n \cdot \hat{r}''} \right\} \tag{6.13}$$

where $\boldsymbol{J}_n$ is discretized complex current on DUT and $\boldsymbol{l}_n$ is the length of line current element from wire grid model of the DUT. Far field on earth is calculated from equivalent current on a closed surface and equivalent image current under earth.

6.5 Results and Discussion

6.5.1 Synthesized/Simulation Results

The measurement of the near field is performed by scanning the estimation target hemispherically with a scan radius of $R \geq 3/2\lambda$ in an anechoic chamber as shown in Fig. 6.4. The far field F_θ is estimated by scanning the hemispherical shape with the interval $\Delta\theta = \Delta\phi = 2°$ for an elevation of $(0° \leq \theta \leq 90°)$, and azimuth $(0° \leq \phi \leq 360°)$ to measure the electric near field. The simulated near field in the analysis is obtained by using the current distribution derived from wire grid model in EEM–MOM software [166]. The estimation target, is a monopole antenna as shown in Fig. 2.1. The relative permittivity of the ground is $\epsilon_s = 4$, and conductivity $\sigma = 0.001$ S/m for dry earth.

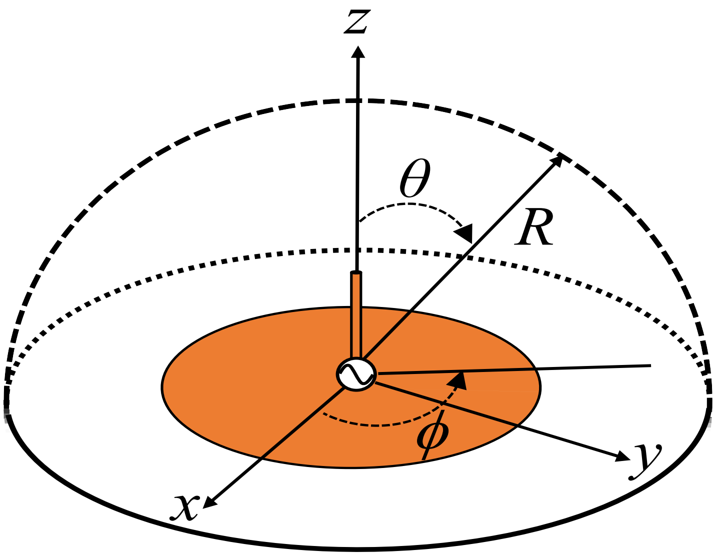

Figure 6.4: Near field measurement of estimation target.

In order to set the near field measurement radius R, we synthesized near field measurements at different distances (i.e changing the radius R of the hemisphere) and calculate the residual error. Figure 6.5 shows the residual error for two cases (conventional and proposed). The residual error (ϵ) is calculated by;

$$\text{Residual Error}(\epsilon) = \frac{\| J(\text{ref.}) - J(\text{est.}) \|_2}{\| J(\text{ref.}) \|_2} \times 100\% \tag{6.14}$$

where $[\boldsymbol{J}](\text{ref.})$ is the reference current distribution, and $[\boldsymbol{J}](\text{est.})$ is the estimated current distribution using the proposed method. In this figure, we observe that as the radius R is equal or greater than $3/2\lambda$, the residual error for both cases remains constant. Thus, performing hemispherical near field measurements at $R = 3/2\lambda$ will give better results.

Figure 6.6 shows a comparison of the near electric field distribution on the monopole antenna for different values of R. We observe that both the real part and the imaginary

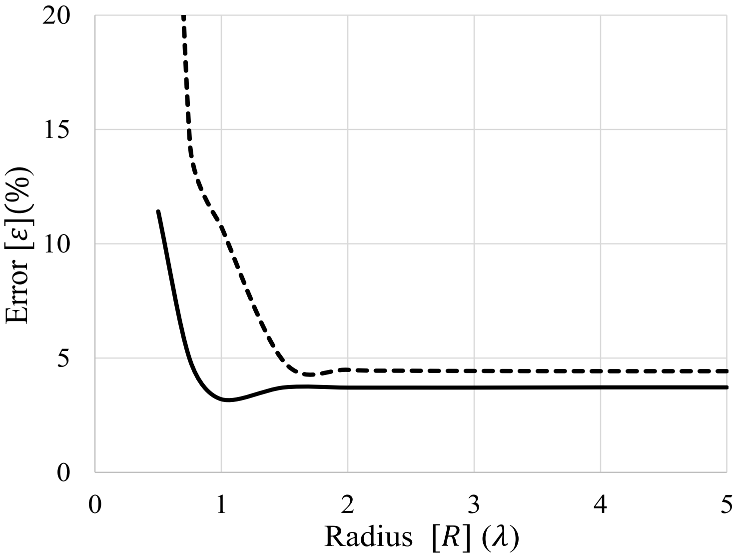

Figure 6.5: Derived results for measurement radius R.

part are roughly in good agreement. However, as the elevation angle (θ) is changed, there is a small difference in the near electric field distribution which is larger at $\theta = \pm 45°$ with the value 0.0178 V/m in the real part and $\theta = \pm 25°$ in imaginary part but with a lower value. This may be due to fluctuation of input impedance because of applying an approximate ground plane.

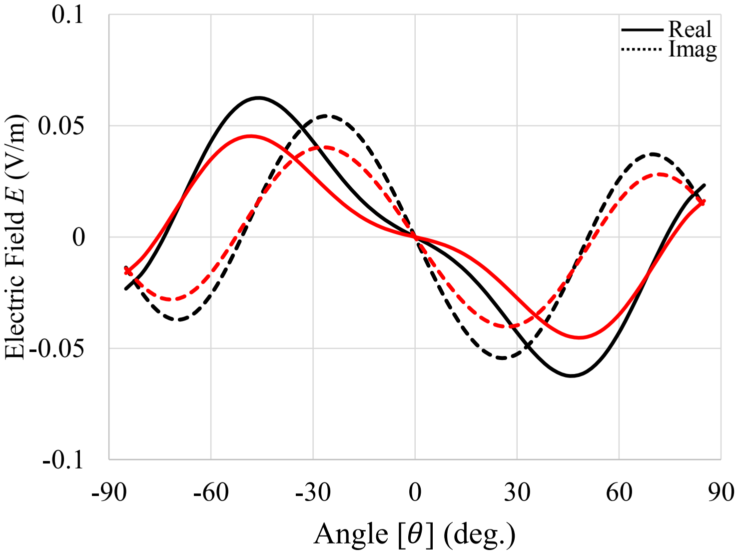

Figure 6.6: Comparison of near electric field distribution on yz plane at different hemispherical radius (a) $R = 3\lambda$ black color and (b) $R = 4\lambda$ black color.

In the next example shown in Fig. 6.7, we compare we compare near electric field distribution at $R = 3\lambda$ by using (a) reference current distribution and (b) calculated current distribution. The near electric field distribution is in good agreement which confirms the validity of the numerical processing.

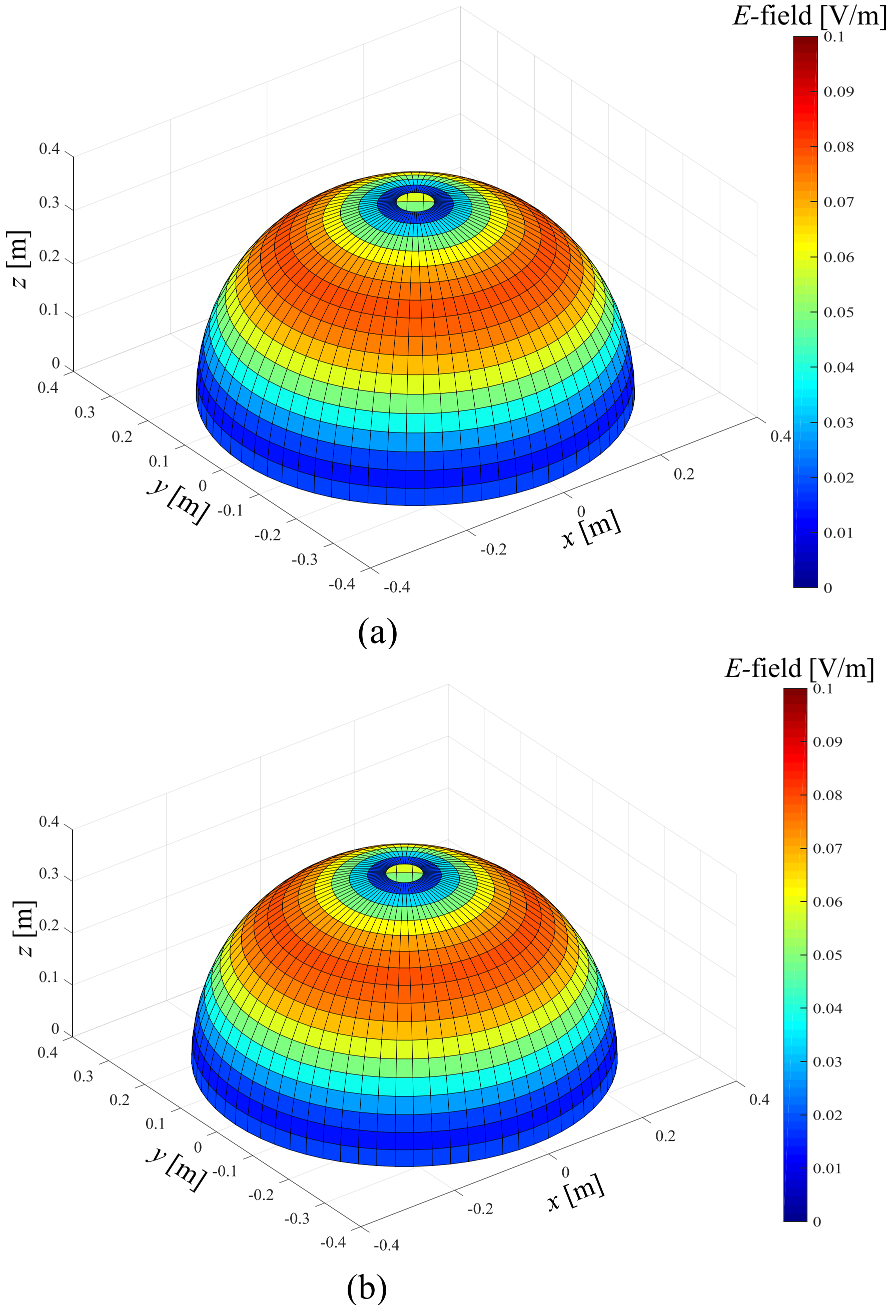

Figure 6.7: Near electric field distribution (a) reference and (b) numerical.

Next, we compare the amplitude of surface current distribution reconstructed using the proposed method. This distribution is compared to reference distribution as well as conventional surface current distribution. In Fig. 6.8, we observe an accurate current distribution reconstructed using the proposed method. This is confirmed by comparing it to the reference surface distribution in the same figure. In the case of conventional method, we observe a huge disparity between the reconstructed surface current with the reference. This disparity in conventional reconstruction method may lead to poor far field estimation accuracy. On the other hand, using the proposed method, the amplitude of surface currents on the radiating elements is reconstructed exactly as the amplitude of reference which ensures accurate far field estimation.

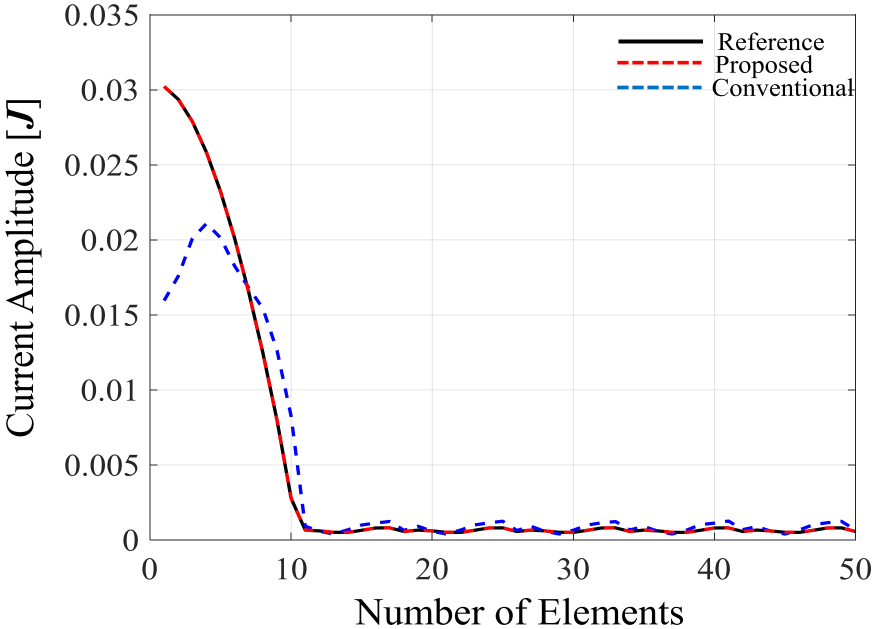

Figure 6.8: Reconstructed current distribution for AUT.

In order to verify the performance of the technique described in this chapter, we estimate the far field of the AUT (shown in Fig. 2.1) using simulated near field in this example and then measurement results in the next section. The estimated far field utilizes the RCM to include the effect of real ground (earth). We thus use the current distribution on the AUT surface. In Fig. 6.9 and Fig. 6.10, we show the result of the estimated far field on earth. In order to compare the performance of different methods, reference values for far field for an antenna above earth are derived from FEKO [167]. The reference results obtained in FEKO are solved using the Sommerfeld integrals. Thus, in Fig. 6.9(a), the estimated far field using conventional technique is compared to reference far field. In this figure, we observe poor performance of the conventional technique. This is attributed to poor current distribution reconstruction as observed in Fig. 6.8.

In Fig. 6.9(b), we compare far field estimation using reference far field and the far field reconstructed using the proposed technique. In this case, it is verified that a very good agreement between reference and estimated far field is achieved. A very good reconstructed current distribution contributes to the estimation performance. Thus, the proposed hemispherical near field method for far field estimation of an antenna above earth can accurately estimate the far field. In Fig. 6.10, we have a similar observation for both cases (a) conventional and (b) proposed. Therefore, the same explanation as above for Fig. 6.9 holds for the case when the AUT is very close to earth in Fig. 6.10.

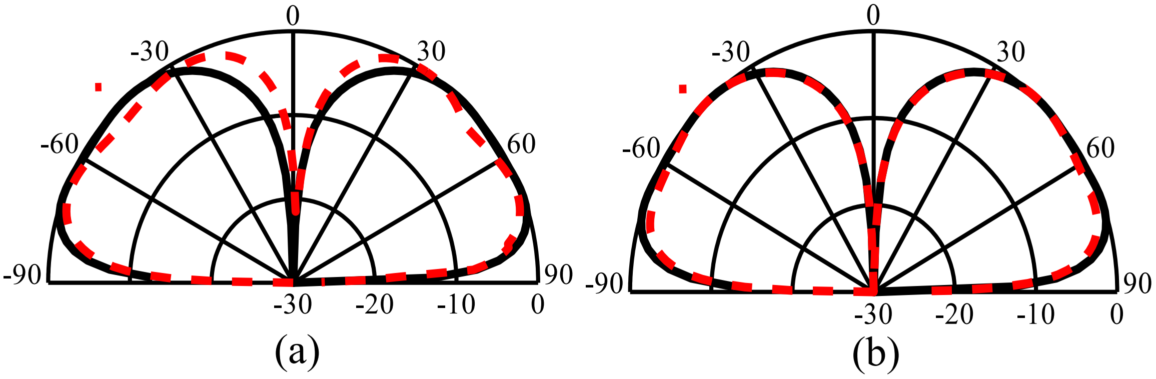

Figure 6.9: Estimated far field above real ground ($2m$) for AUT (zx/yz plane) (a). conventional and (b). proposed method.

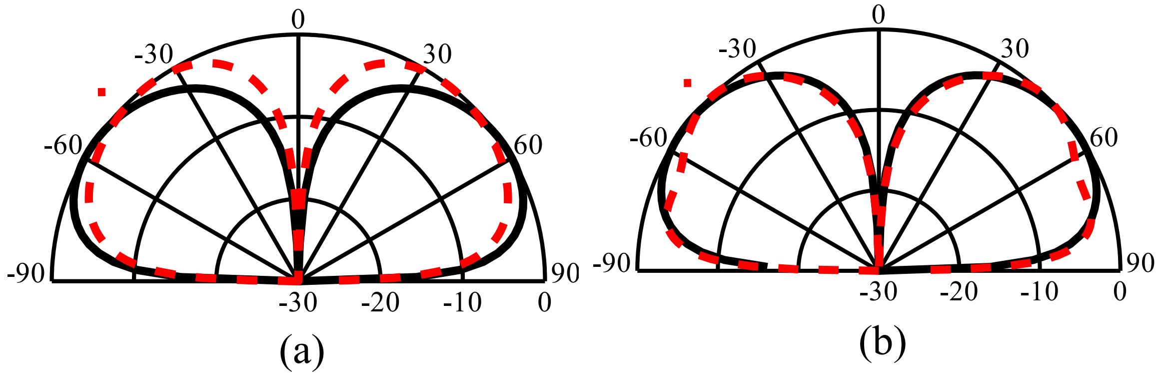

Figure 6.10: Estimated far field above real ground (very close) for AUT (zx/yz plane) (a). conventional and (b). proposed method.

6.5.2 Measurement Results

In this subsection, we consider the confirmation of the validity of the proposed technique by reconstructing the current distribution and then calculating/estimating the far field using measured near field information. From antenna measurement equipment point, it is not possible to perform a direct far field measurements including the effect of real ground. We thus, measure the near field hemispherically in an anechoic chamber and then use the proposed technique to estimate far field above real ground.

6.5.2.1 Measurement Set–up

In terms of the measurements, Fig. 6.11 shows the measurement set–up. For the AUT, a monopole antenna is used as an AUT. A frequency of 2.5 GHz is used as a measurement frequency. A non–resonant probe is used for near field measurements. In our case, a standard dipole for 5 GHz frequency band is used as a non–resonant probe. The hemispherical measurement radius of the system is 36 cm. This translates to a hemispherical radius of $R = 3\lambda$.

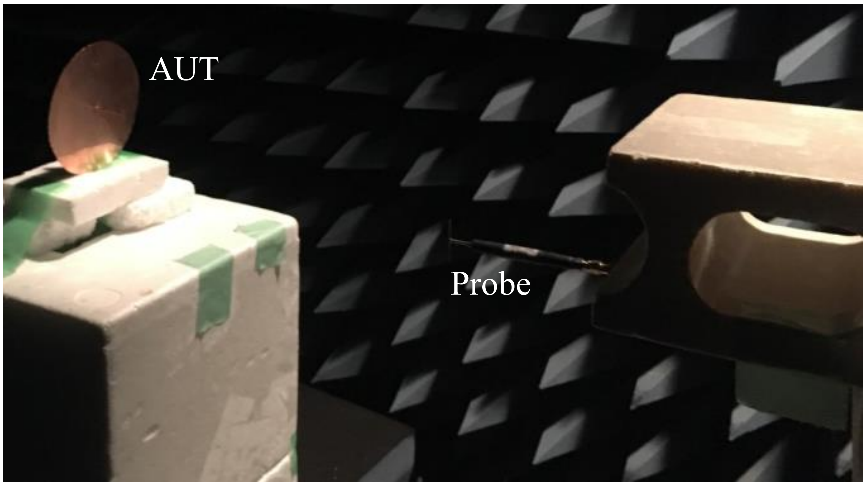

Figure 6.11: Near Field measurement set up in anechoic chamber.

6.5.2.2 Estimated Far Field from Measured Near Field

In Fig. 6.12, the estimated far field from hemispherically measured near field information is presented. In this figure, we observe that for conventional method, the estimated far field does not have a good agreement as compared to reference far field as shown in Fig. 6.12(a). On the other hand, in Fig. 6.12(b), the estimated far field using the proposed method have a very good agreement with reference. Therefore, we confirm the validity of the proposed technique for far field estimation using hemispherical near field measurements. From these results, in the case of using very large systems, and / or antennas with low gain, it is possible to estimate the far field using hemispherically measured near field information. This method is fast and include practical use scenario since the effect of real ground (earth) is included in the estimated far field.

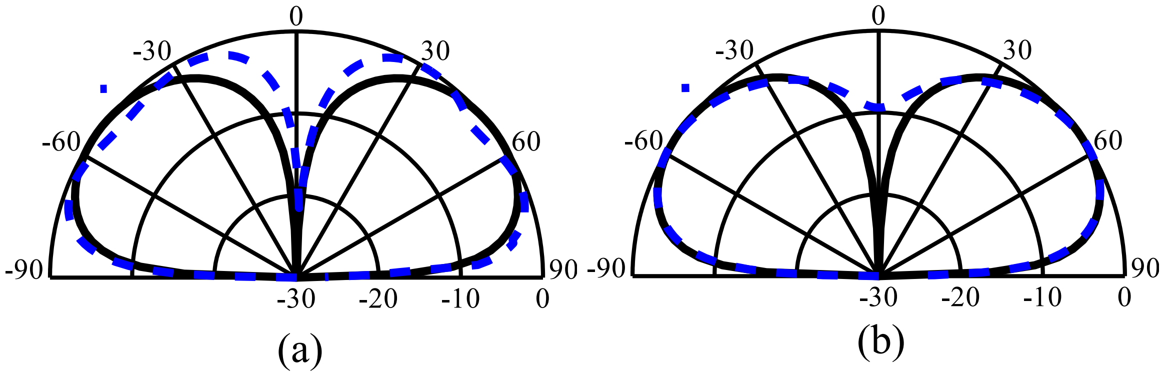

Figure 6.12: Estimated far field above real ground for AUT (zx/yz plane) using measured near field (a). conventional and (b). proposed method.

6.6 Summary

In antenna measurements, near field measurements provide fast and accurate method for the measurement of electronically large antennas whose far field measurements cannot fit in conventional anechoic chamber. In most cases, near field is measured using planar scan, cylindrical scan and spherical scan. From measured near field, far field is estimated using different numerical processing. In this chapter, we developed a novel technique in which far field of an AUT is estimated from near field information that is measured hemispherically. From the measured hemispherical near field information, an equivalent electric current source is determined over the hemispherical surface encompassing the AUT. Reflection coefficient method is applied to reconstructed surface current distribution to estimate far field above real ground. To verify the accuracy of the proposed method, numerical simulations as well as measurement experiments were conducted for a monopole antenna which acted as AUT. From the results, the validity of the proposed technique was verified in which accurate estimation of far field for an AUT above real ground was achieved from hemispherical near field measurements.

Chapter 7

Vehicular Antenna Far Field Estimation on Earth from Near Field Information

7.1 Introduction

In everyday life, transportation is essential in order to carry out various activities. As a consequence, vehicles are increasingly equipped with on–board computing devices [168]. In recent years, we have witnessed that the demand for connectivity to/in vehicles has grown rapidly, both from business and consumers. In order to enhance the safety and comfort of automobiles in conjunction with the development of information communication technology, antennas operating in different frequency bands are mounted inside and outside the vehicle [169], [170]. Some of the examples are broadcast reception, wireless communication, control, etc as shown in Fig. 7.1. Thus, antennas are used to receive AM/FM broadcast and television broadcast. On top of that, vehicles can receive real–time road traffic information about congestion and regulation, using the VICS (Vehicle Information and Communication System) [171].

For wireless communication applications, GPS (Global Positioning System) is used for car navigation system, ETC (Electronic Toll Collection System) [172] for Toll roads, mobile communication using mobile communication infrastructure along the road and

Wimax. Another new addition is the control systems. In order to realize fully automatic operation, millimeter wave radar is mounted in the vehicle [82]. Thus, antennas in automobile technology are positioned as an indispensable part of the industry for improving safety, performance, and comfort [170]. It is therefore important to evaluate the performance of these in–vehicle antennas.

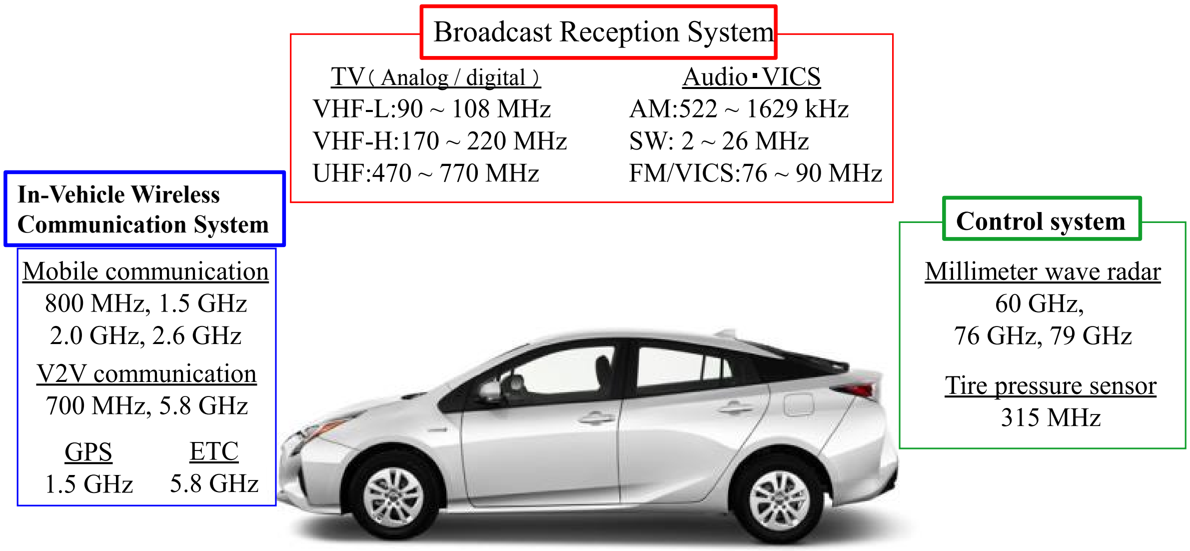

Figure 7.1: Frequency bands of various antennas installed in an automobile.

In antenna field or electromagnetics, directivity is a fundamental antenna parameter. It measures the degree to which the radiation emitted is concentrated in a single direction [173]. For in–vehicle antennas, the radiation directivity of the antenna is one of the characteristics in evaluating the system performance. The directivity of the antenna is evaluated from the measurement of the far field [82], [169]. In this case, the far field is measured when the antenna is mounted on the vehicle. For an antenna mounted on–vehicle, the whole car operates as an antenna due to the current flowing not only on the surface of antenna but also on the surface of the car body. As compared to a stand alone antenna, the characteristics of an on–vehicle mounted antenna change significantly [172], [174], [175]. Thus, it is necessary to perform measurement on the whole system including the automobile. However, to measure the far field, a sufficiently long measurement distance is required [82].

In addition, although it is necessary to consider the existence of the earth at the time of practical use, it is impossible to evaluate the effect including the influence on the measurement in an anechoic chamber's far field measurements. In this chapter, we therefore consider a simple car model as shown in Fig. 7.2. We calculate the current distribution on the surface of this model and then estimate the far field from the currents. Near field information is measured hemispherically and influence of the earth is as well included in the far field estimation. From the model considered in Fig. 7.2, we apply the same technique to a real car model which is considered in Section 7.6.

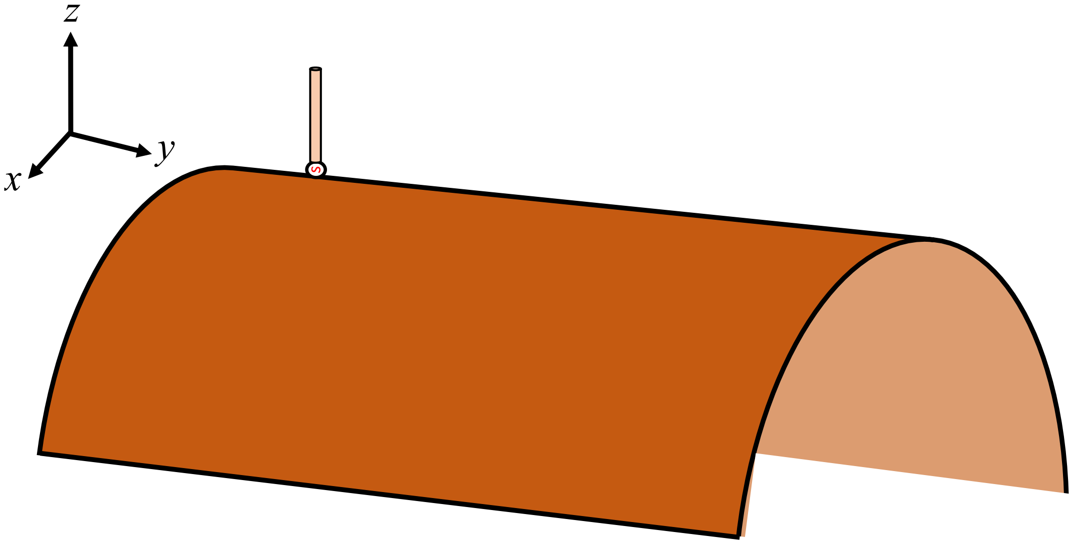

Figure 7.2: Simple Car model.

7.1.1 Wire Grid Model for Car

As described in the previous chapter, a wire grid model is used to discretize the analysis target. A planar conductor is replaced with a grid network (wire grid). Thus, a planar conductor modeled using $3D$ Electromagnetic software is considered as a collection of linear elements. In this case, near field behavior of the wire grid model of a conducting surface is examined.

In our analysis, FEKO [167] is used for the design and analysis of planar car model. An equivalent wire grid model is designed in EEM-MOM software [166]. In Fig. 7.2, a simple car modelled by FEKO is shown. An equivalent wire grid model of the model shown in Fig. 7.2 is shown in Fig. 7.3 below. In these figures, a simple model design of a planar conductor model and wire grid model are shown together with vehicular mounted antenna.

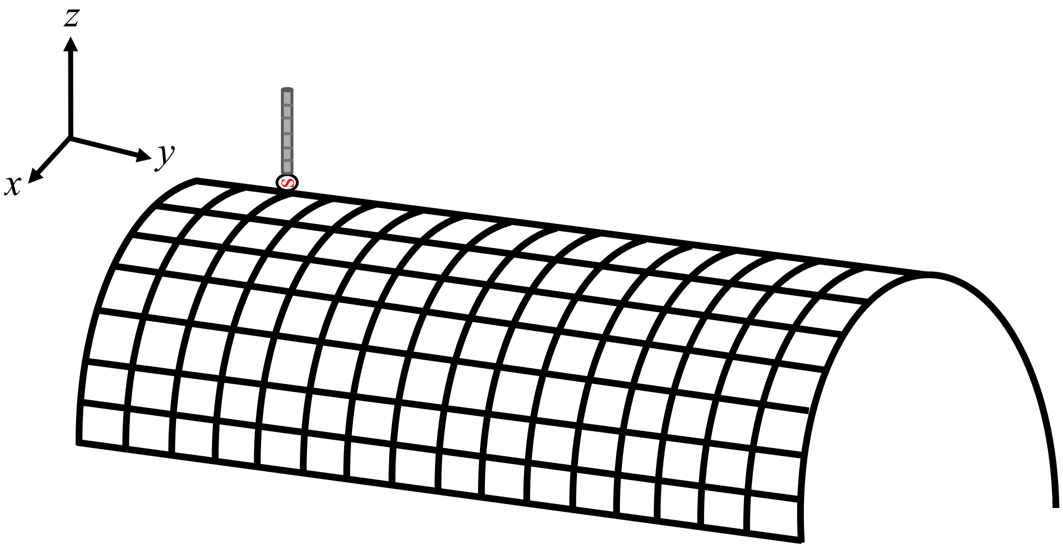

Figure 7.3: Wire grid model for simple car.

Figure 7.4: Hemispherical Near Field Measurement.

7.2 Derivation of Real Wave Source Information from Hemispherical Near Field

Wave source information on real surface is derived from near field measurements. By considering the Maxwell equation, electric field $\boldsymbol{E}$ at an observation point $\boldsymbol{r}$' by current distribution $\boldsymbol{J}$ on conductor surface in region $\boldsymbol{v}$ at the position $\boldsymbol{r}$ is expressed by the following integral equation:

$$\boldsymbol{E}(\boldsymbol{r}') = -\frac{j\eta}{k}\int_v \left\{k^2\boldsymbol{J}(\boldsymbol{r}) + \nabla\nabla\cdot\boldsymbol{J}(\boldsymbol{r})\right\}\boldsymbol{G}(\boldsymbol{r},\boldsymbol{r}')dv$$

$$\boldsymbol{G}(\boldsymbol{r},\boldsymbol{r}') = \frac{e^{-jk|\boldsymbol{r}-\boldsymbol{r}'|}}{4\pi\left|\boldsymbol{r}-\boldsymbol{r}'\right|} \tag{7.1}$$

where, η is the intrinsic impedance 120π, and k is wave number. When current distribution is represented by $[\boldsymbol{J}]$, using MoM [78], [82], [161] and (7.1);

$$[Z][J] = [V] \tag{7.2}$$

$$[E] = [A][J] \tag{7.3}$$

The impedance matrix $[Z_E]$ on the ground required for derivation is divided into the term of the real wave source and the term of the mirror image source as shown in Fig. 7.5.

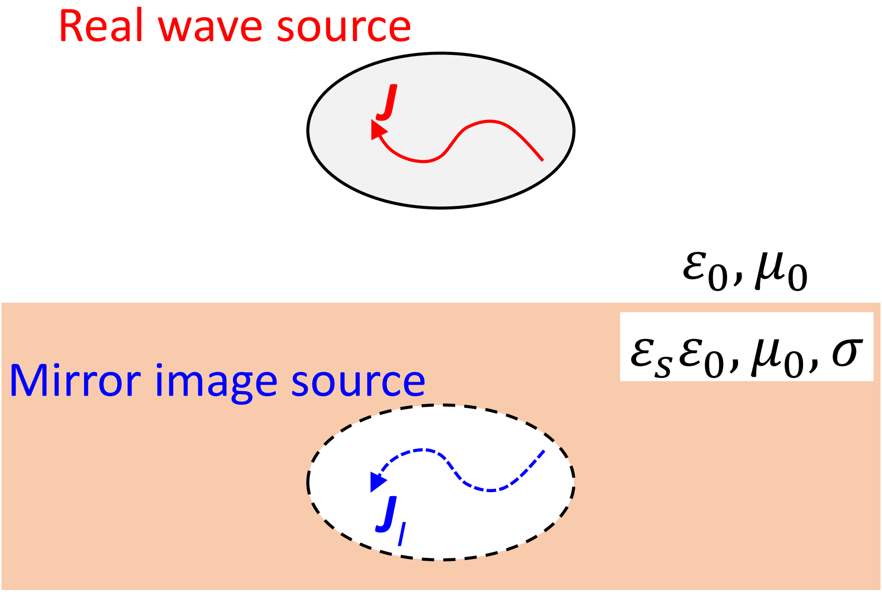

Figure 7.5: Mirror image source for DUT above real ground.

In order to reconstruct the surface current on the DUT. We consider using the measured electric field distribution so that we can reconstruct surface current. The integral equation (7.1) is reformed such that from known measurement electric field vector $[\boldsymbol{E}]$, coefficient matrix $[\boldsymbol{A}]$ and unknown current vector $[\boldsymbol{J}]$, the following matrix equation is acquired similar to (7.3);

$$\begin{bmatrix} E_\theta \\ E_\phi \end{bmatrix} = \begin{bmatrix} A_{x\theta} & A_{y\theta} & A_{z\theta} \\ A_{x\phi} & A_{y\phi} & A_{z\phi} \end{bmatrix} \begin{bmatrix} J_x \\ J_y \\ J_z \end{bmatrix} \tag{7.4}$$

In this case, it is possible to acquire the surface current distribution of the DUT by solving the matrix equation above.

7.3 Far Field Estimation on Earth

The far field of an antenna is conventionally considered to be the region where the outgoing wavefront is planar and the antenna radiation pattern has a polar variation and is independent of the distance from the antenna [176]. Consequently, in order to generate a local plane wave in the far field, the radial component of the electric field must be negligible compared to the transverse component. The far field is usually defined by the far electric field (E_θ, E_ϕ). In this case, the ratio of the electric and the magnetic far fields therefore should be equal to the intrinsic impedance of the medium. These two requirements; (i) that the radial component of the field should be negligible when compared with the transverse component and (ii) the ratio of the electric and the magnetic fields equal the intrinsic impedance of the medium – must hold in all angular directions from the antenna [176]. In order to determine the starting distance for the far field, we need to examine the simultaneous satisfaction of these two properties for all θ and ϕ angular directions, where θ is the angle measured from the z-axis and ϕ is the angle measured from the x-axis.

The far electric field is obtained by setting the observation point at the infinite point $(r = \infty)$ in the near electric field equation. In the far field observation system, the radiation direction from the wave source at the position $\mathbf{r}_n$ to the observation point $\mathbf{r}$ is uniquely represented by $\hat{r}$. Therefore, the phase change due to the wave source position with respect to the observation point is determined by the inner product of $\mathbf{r}_n$ and $\hat{r}$.

In addition, the electric field component (E_θ, E_ϕ) generated at the observation point by the wave source in the $\hat{l}_n$ direction is the inner product $(\hat{l}_n \cdot \hat{\theta}, \hat{l}_n \cdot \hat{\phi})$. Therefore, the far field by the linear wave source is estimated by:

$$E_\theta(\theta,\phi) = \frac{jZ_0 k e^{-jkr}}{4\pi r} F_\theta(\theta,\phi) \tag{7.5}$$

$$E_\phi(\theta,\phi) = \frac{jZ_0 k e^{-jkr}}{4\pi r} F_\phi(\theta,\phi) \tag{7.6}$$

$$F_\theta(\theta,\phi) = \sum_{n=1}^{N} \boldsymbol{J}_n \left\{ \left(\boldsymbol{l}_n \cdot \widehat{\theta}\right) e^{jkr_n \cdot \widehat{r}} - R_{TM} \left(\bar{\boldsymbol{l}}_n \cdot \widehat{\theta}\right) e^{jkr_n \cdot \widehat{r}} \right\} \tag{7.7}$$

$$F_\phi(\theta,\phi) = \sum_{n=1}^{N} \boldsymbol{J}_n \left\{ \left(\boldsymbol{l}_n \cdot \widehat{\phi}\right) e^{jkr_n \cdot \widehat{r}} + R_{TE} \left(\bar{\boldsymbol{l}}_n \cdot \widehat{\phi}\right) e^{jkr_n \cdot \widehat{r}} \right\} \tag{7.8}$$

7.4 Numerical Results

The measurement of the near field is performed by placing the estimation target in an anechoic chamber as shown in Fig. 7.6 and the hemispherical near field measured at a radius R. The far field F_θ is estimated by scanning the hemispherical shape with the scanning interval $\Delta\theta = \Delta\phi = 2^\circ$ to measure the electric field E_θ. The measured value of the near field in this analysis is obtained by using the current distribution derived from EEM-MOM [166]. The estimation target consists of a monopole element incorporated on top of a simple cylindrical car model. The antenna operates in the UHF/VHF band. The earth ground with $\varepsilon_s = 4$, and $\sigma = 0.001$ S/m representing a dry ground.

7.4.1 Current Distribution

Surface current distribution of the DUT shown in Fig. 7.6 is discussed in this subsection. The source reconstruction method is applied to retrieve an equivalent currents distribution on the antenna array aperture plane [177]. The reconstructed equivalent currents will be related to the extreme near field and hence, to the nominal excitations of the antenna. By using the equivalence principle [81], an equivalent electric current

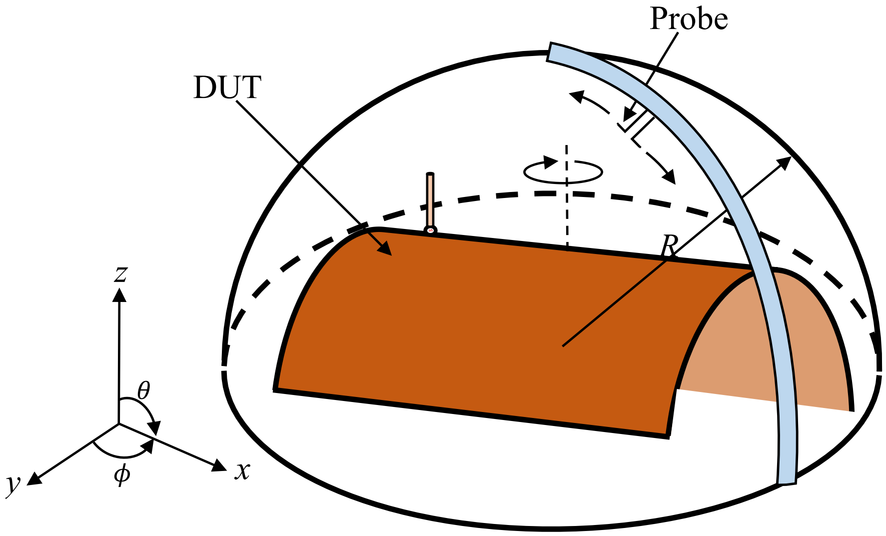

Figure 7.6: Near field measurement set up of vehicle mounted antenna.

is used to replace the radiating antenna. The assumption that is made is that the near field is produced by the equivalent electric current and, therefore, via Maxwells equation from the measured near field data, the current source can be determined [42]. From the solution of the surface distribution of the AUT, the near field and the far field of the radiating antenna in all regions in space of the radiating antenna can be determined directly from the equivalent electric current.

In the figure below, Fig. 7.7, we show the amplitude of the current distribution from reference data and analytical data. In this figure, amplitude on the radiating elements is reconstructed and a very good agreement is observed. From this analysis (Fig. 7.7), we can conclude that the analytical model, i.e. the wire grid model and the numerical consideration is correct and therefore can be applied to the far field estimation problem.

7.4.2 Near Field Simulation

Firstly, in order to consider the influence on the near field for different measurement radius positions of the hemisphere. In this example, we compare the electric near field distribution measured at $0.8m$ and $1.6m$. Fig. 7.8 shows a comparison of the electric

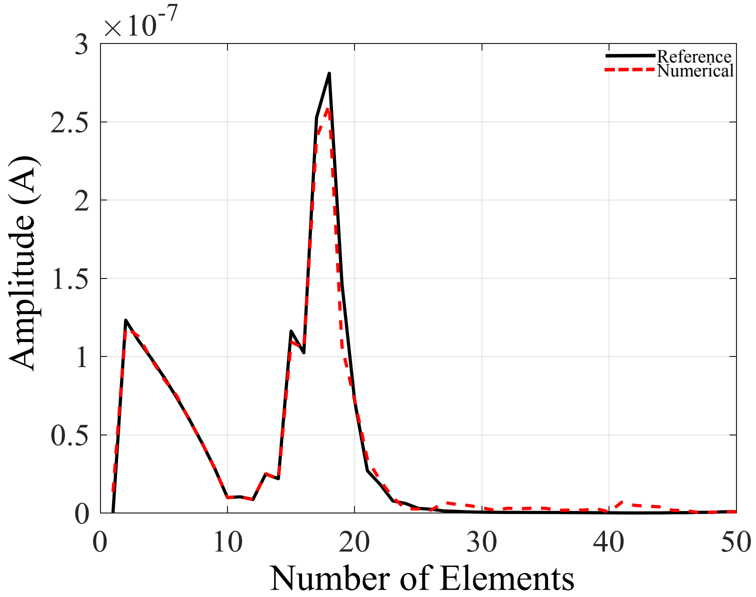

Figure 7.7: Reconstructed amplitude of current distribution.

field distribution for the case of $0.8m$. In Fig. 7.8(a) the reference near field distribution and in Fig. 7.8(b) the distribution calculated using our method from wire grid model. In both cases, Fig. 7.8(a) and Fig. 7.8(b), a very good agreement between the near field is observed. In this case, improving the estimation accuracy of the reconstructed current distribution on the DUT surface will ensure improved accuracy in the far field that is estimated from these currents.

In the next example, Fig. 7.9, we have a similar results but at a different radius of $1.6m$. In this figure, similar observations and conclusions are made as the one in Fig. 7.8 in which both the reference and numerical models have a very good agreement. By comparing Fig. 7.8 and Fig. 7.9, some fluctuations are observed in terms of the magnitude of electric near field distribution.

7.4.3 Far Field Estimation in Freespace

In order to verify the modeling performance of our wire grid model. We compare the far field pattern of the simple car models from Fig. 7.2 and Fig. 7.3. The two models that are being compared were modeled in FEKO for the planar car model whilst an

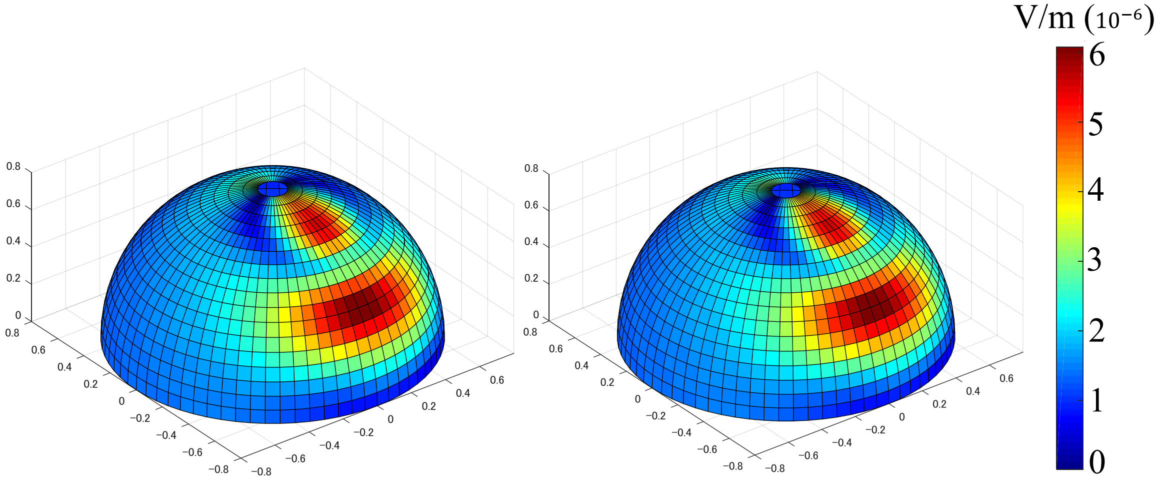

(a)

(b)

Figure 7.8: Near electric field distribution at $0.8m$ (a) reference and (b) numerical.

equivalent wire grid model for the simple car is modeled in EEM–MOM. To verify the performance of the two models, we compare the free–space far field of the two models.

In Fig. 7.10, observe the far field pattern for the two models. A very good agreement between the reference pattern (FEKO model) and the estimated pattern using the wire grid model is obtained. From the free space far field result, we verify that the two models are equivalent and we can therefore use the wire grid model for analysis using our method to estimate the far field pattern from measured hemispherical near field information. This also ensures that modelling errors are minimized. We thus, use the wire grid model in our numerical analysis in the next subsection and compare the reference results to the numerical one.

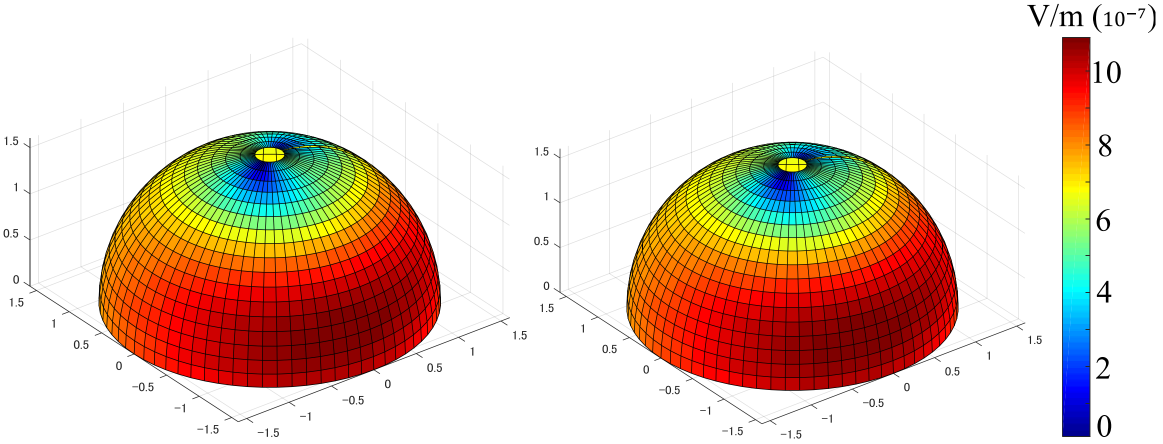

(a)

(b)

Figure 7.9: Near electric field distribution at 1.6m (a) reference and (b) numerical.

7.4.4 Far Field Estimation from Near Field on Earth

7.4.4.1 Simulated Results

Figure 7.11 shows a comparison of the far field between reference and estimated on earth. In this figure, an accurate estimation of far field including the effect of real ground is obtained. In Fig. 7.11, the analysis is obtained at 100 MHz. When we increase the frequency of interest Fig. 7.12, the reconstruction performance slightly deteriorates. This is due to the mesh size. As we frequency of interest increases, the number of meshes for the wire grid increases and errors occurs either in the zx–plane or the yz–plane.

7.4.4.2 Measured Results

In this example, measured near field is used to compare the performance of the proposed method. The term “measured” in this subsection only is used haphazardly since the near

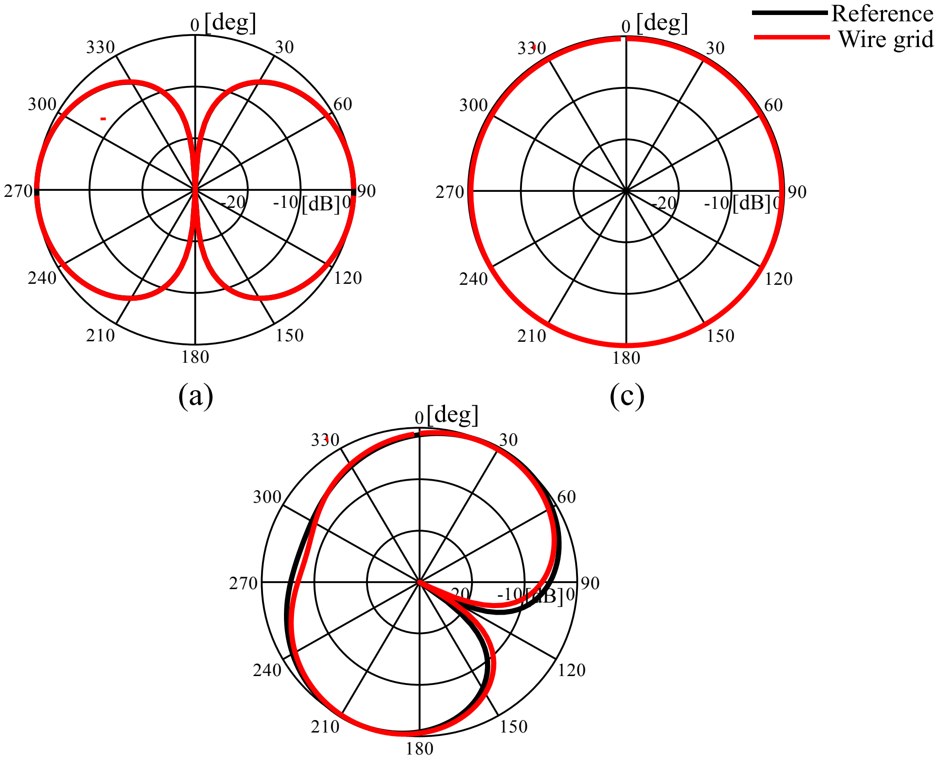

(a) (c)

(c)

Figure 7.10: Freespace far field for simple car model (a) $E_\theta(\phi = 0°)$, (b) $E_\phi(\phi = 0°)$, and (c) $E_\theta(\phi = 90°)$.

field information is obtained from EM software. Although there will some slight differences as related to data obtained in anechoic chamber measurements, the differences are assumed not significant. In the reconstructed far field result on earth from hemispherical near field information as shown in Fig. 7.13, we have a very good reconstruction performance. This results therefore verifies that our method can reconstruct the far field of a vehicular mounted antenna including the effect of the earth on the performance of the antenna from hemispherical near field measurements. In Fig. 7.14, we show the performance at different frequency points. In this case, an improvement between the simulation and the measurement is observed which can be attributed to errors in mesh sizes.

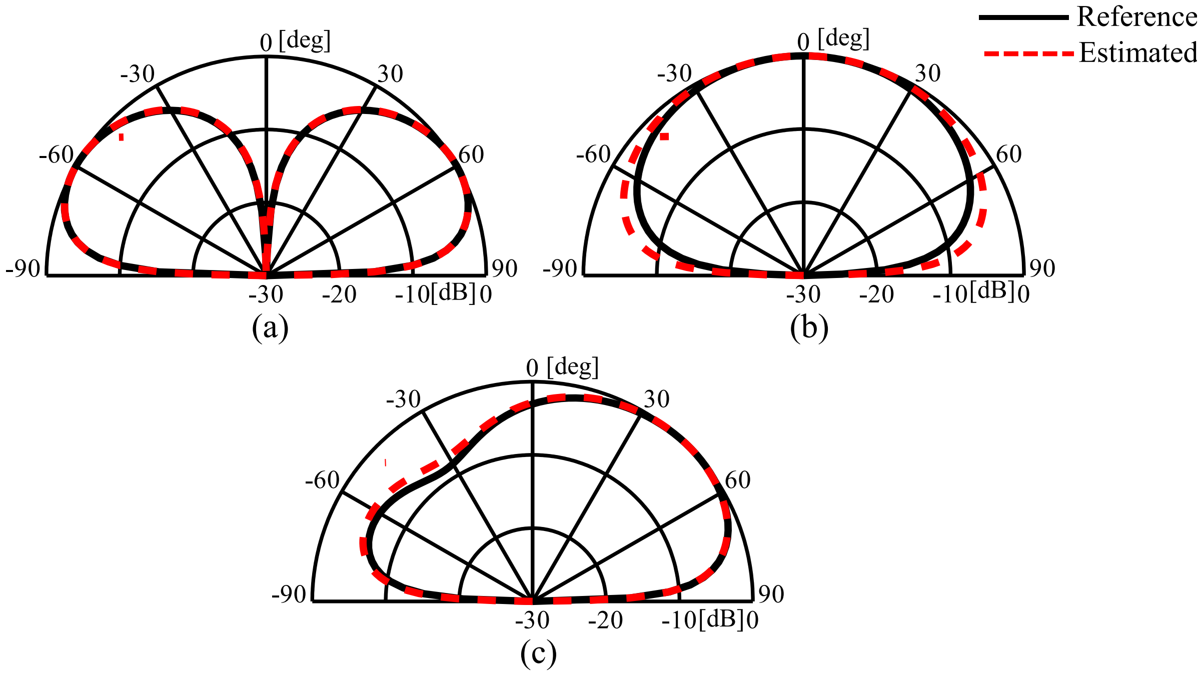

Figure 7.11: Estimated far field on earth from near field measurements (numerical) for 100MHz (a) $E_\theta(\phi = 0°)$, (b) $E_\phi(\phi = 0°)$, and (c) $E_\theta(\phi = 90°)$.

7.5 Windscreen Based Antenna Model

For vehicular antennas, some antennas are embedded in the car's windscreen. In windscreen based antennas, the windscreen glass affects the performance of the antenna. In some instances, antennas may have defects which may also contribute to difficulties in directivity measurements [169]. In these cases, it is imperative to use a Black Box model in order to estimate the directivity of the antenna. Therefore, in this section, we estimate the far field of an automotive windscreen based antenna on earth using a very simple car model. The conductor surface is linearly approximated and radiation obtained from the current distribution evaluated. The near field is measured in a hemispherical scanning manner as is the case in previous sections. In this section, the effectiveness of the method is examined when using windscreen antennas and the accuracy of estimating

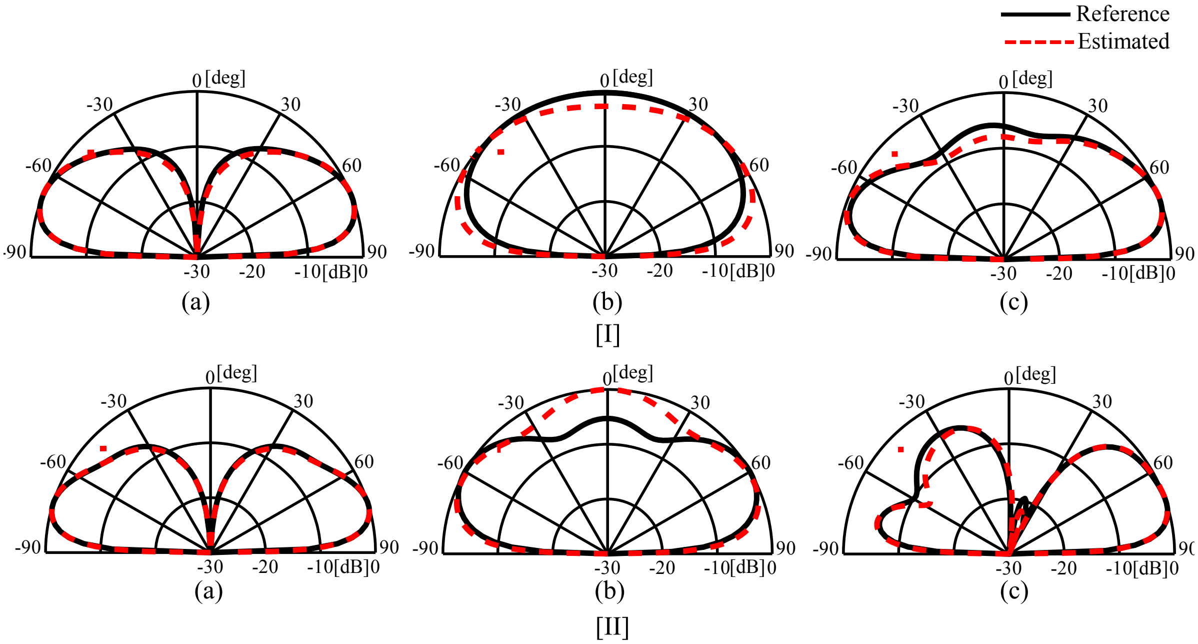

Figure 7.12: Estimated far field on earth from near field measurements (numerical) for (I) 300MHz and (II) 500MHz (a) $E_\theta(\phi = 0°)$, (b) $E_\phi(\phi = 0°)$, and (c) $E_\theta(\phi = 90°)$.

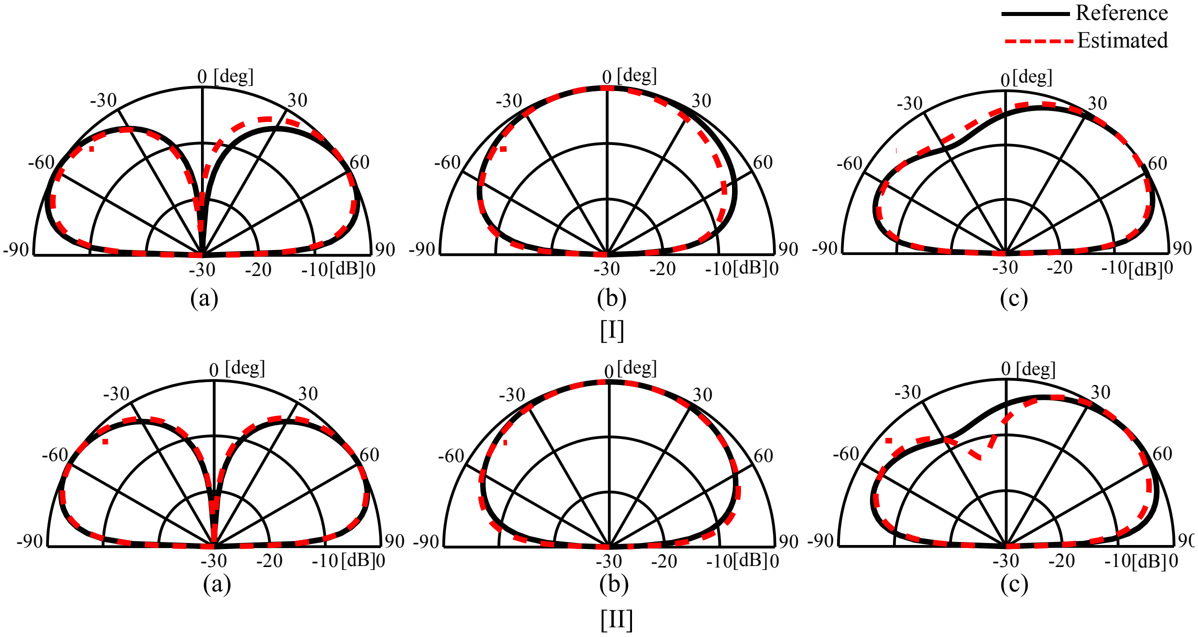

Figure 7.13: Estimated far field on real ground from measured Near field at 100 MHz (I) 0.8m and (II) 1.6m (a) $E_\theta(\phi = 0°)$, (b) $E_\phi(\phi = 0°)$, and (c) $E_\theta(\phi = 90°)$.

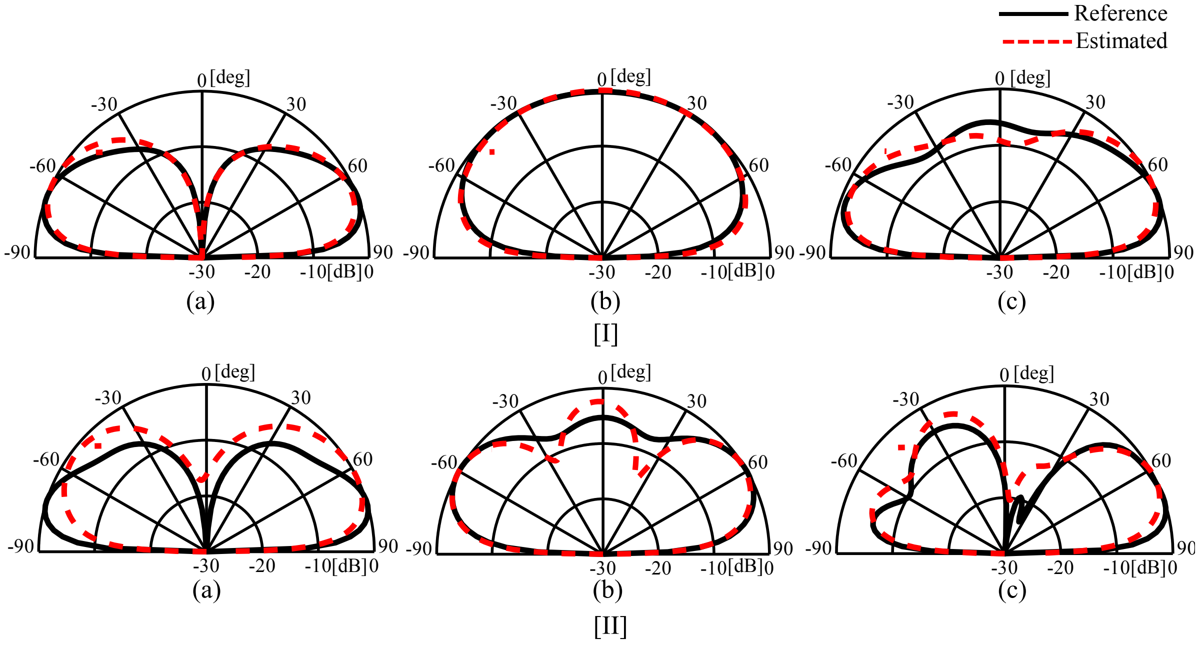

Figure 7.14: Measured far field on earth from near field measurements at 1.6m for (I) 300MHz and (II) 500MHz (a) $E_\theta(\phi = 0°)$, (b) $E_\phi(\phi = 0°)$, and (c) $E_\theta(\phi = 90°)$.

the far field using an arbitrary antenna model (Black Box model) is also considered.

In the case of using a Black box model, an infinitesimal dipole array is used to emulate the blackbox antenna model. This can be used to reconstruct the directivity of a windscreen based antenna which has been broken or one that is faulty. By calculating the norm error of the current distribution, a proper feeding position is obtained. This feeding position is then used as the feeding point of the antenna.

In our analysis, the estimation target consists of a monopole element incorporated in a car's windscreen. The antenna operates in the VHF band, and the car is placed on earth ground with $\varepsilon = 4$, and $\sigma = 0.001$ S/m. In order to verify that we can use an arbitrary antenna (Black Box model) to estimate the far field of windscreen based antenna, we use three car models to compare the far field estimation performance. Firstly, a reference model (FEKO) is used having a monopole incorporated onto a windscreen. Secondly, a wire grid model based on EEM–MOM modelling is used with monopole antenna similar to reference model. Lastly, a Black Box model is used to estimate the far field of a windscreen based antenna as shown below in Fig. 7.15.

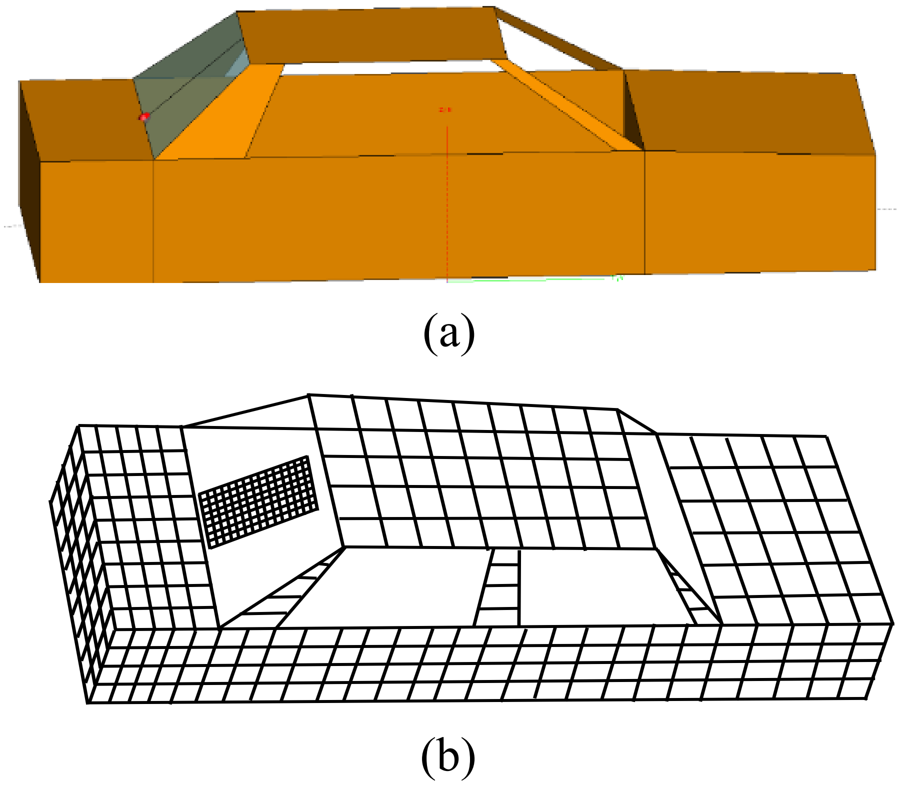

Figure 7.15: Car models used for windscreen analysis (a) reference model (FEKO), and (b) Black Box Model.

In Fig. 7.16, the near field measurement is shown for a monopole antenna on a cars windscreen. We observe that for all the three cases, we obtain a very close near field measurement. For the Black Box model, there is a little deviation which is attributed to the shape of the model which consists of infinitesimal dipole elements. From this near field measurement, we estimate the far field obtained as shown in Fig. 7.17. In both zx-plane and yz–plane, we observe a good agreement in far field estimation from reference model obtained using FEKO, the model obtained from EEM–MOM and black box antenna model. Even if we do not know the characteristics of the antenna (due to defects), we can accurately estimate the far field pattern of the antenna using near field data obtained from near field measurements.

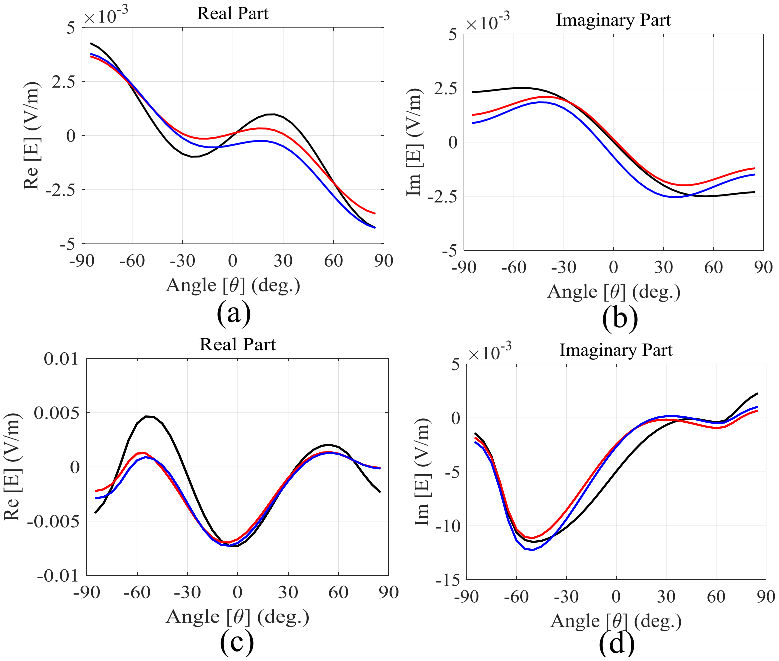

Figure 7.16: Near field measurement (a) Real part, and (b) imaginary part. black: reference model, red: Black Box Model vertical feed, blue: Black Box Model horizontal feed.

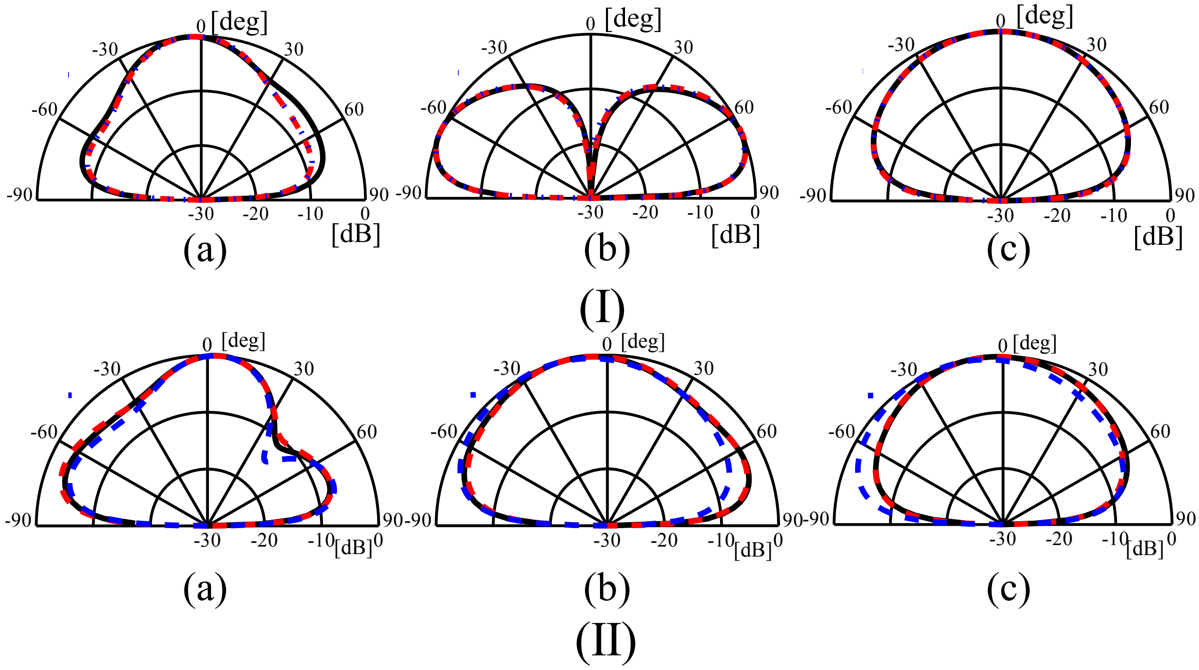

Figure 7.17: far field estimation on earth ground (a) zx Plane, (b) yz Plane. black: reference model (FEKO), red: EEM-MOM Monopole Model, blue: Black Box Model.

7.6 Real Car Model

In the initial consideration of vehicular mounted antennas, a simple car model was used to verify the accuracy of the propose technique. In this section, we consider a real car model. A prius car model is used as a DUT. In Fig. 7.18, the CAD model for Prius car is shown. This model is used in FEKO as a simulation model.

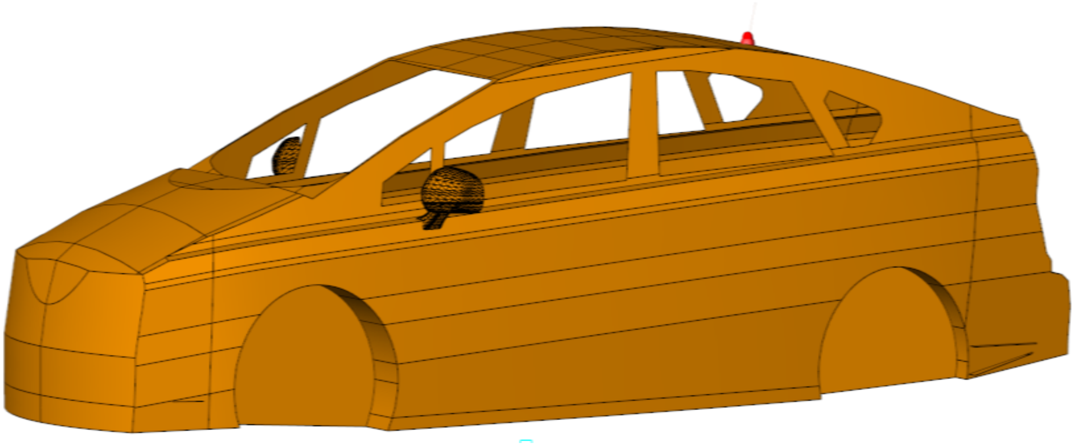

Figure 7.18: Prius car simulation model.

In our analysis, we consider approximating the conductor surface with a linear conductor element in deriving wave source information on the real surface. Therefore, the current distribution on the linear conductor can be represented by a matrix representation from discretization of the method of moments. In order to consider the wire grid model, a similar wire grid model as shown in Fig. 7.19 was modeled in EEM–MOM to compare the validity of the algorithm in estimating the far field on earth.

7.6.1 Surface Current and Near Field Distribution on Real Car

Surface current distribution of the DUT for the real car model is discussed in this subsection. As discussed earlier, the source reconstruction method is applied to retrieve an

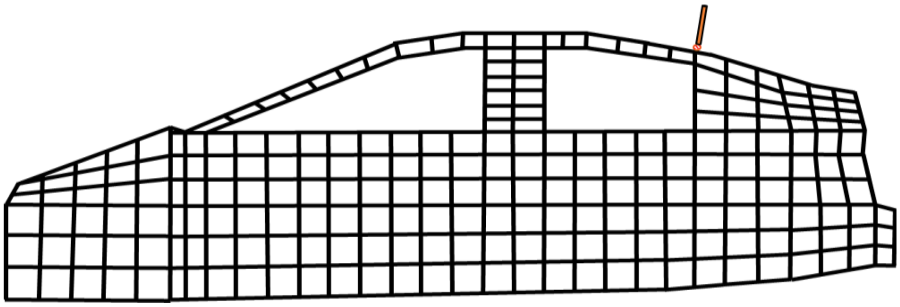

Figure 7.19: Equivalent wire grid model for Prius (used as analytical model).

equivalent currents distribution on the antenna array aperture plane. From the surface current distribution on the DUT, the near field and the far field of the radiating antenna can be determined. The current distribution on the antenna of the DUT is shown in Fig. 7.20. The amplitude in Fig. 7.20(a) and phase Fig. 7.20(b) of the current distribution from (a) reference data and (b) analytical data is observed. In both Fig. 7.20(a) and Fig. 7.20(b), the result is same which confirms the accuracy of the analytical (or numerical) consideration.

In the figures below, we compare near electric field distribution at $0.8m$ in Fig. 7.21 and $1.6m$ in Fig. 7.22 by using reference current distribution in (a) and calculated current distribution in (b). In this figure, it is verified that the near electric field have the same result. In the case when the measurement distance is near to the DUT, the electric field is strong near to the antenna region. On the other hand, when the distance is increased, the field strength starts to become uniform around the DUT. This may reduce the accuracy of the determined currents around the DUT when the measurement distance is very far away from the DUT.

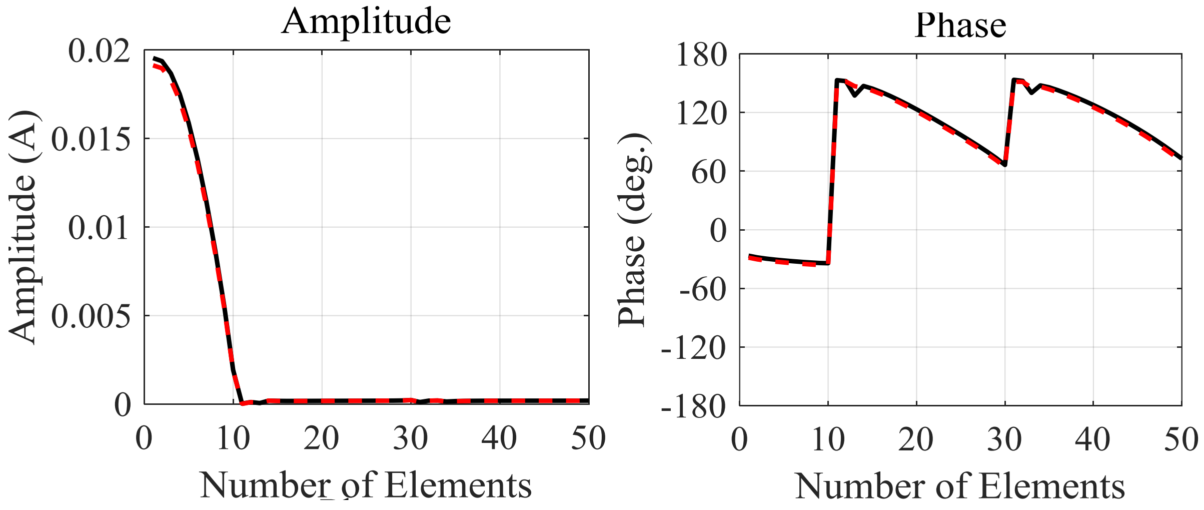

(a) (b)

Figure 7.20: Surface current distribution on real car.

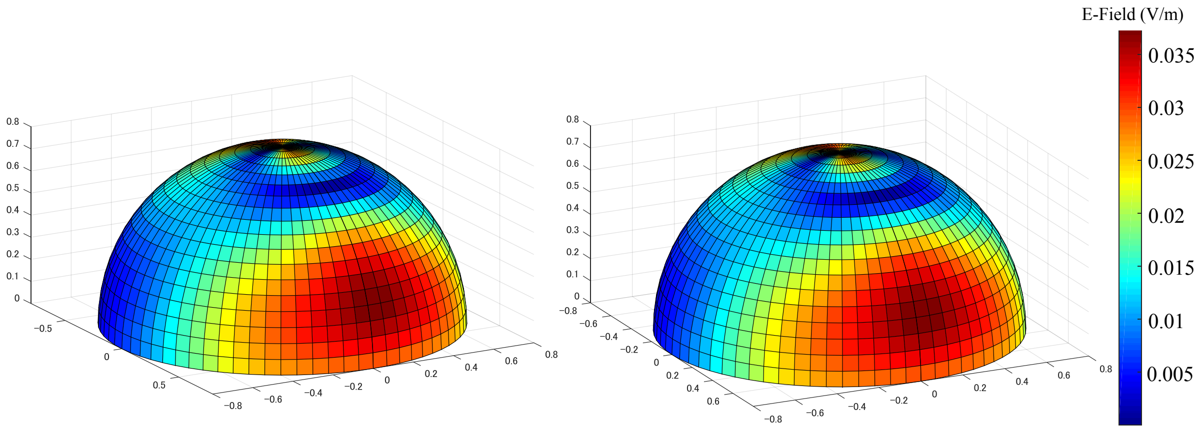

(a) (b)

Figure 7.21: Near field distribution for real car at $0.8m$ (a) reference and (b) calculated.

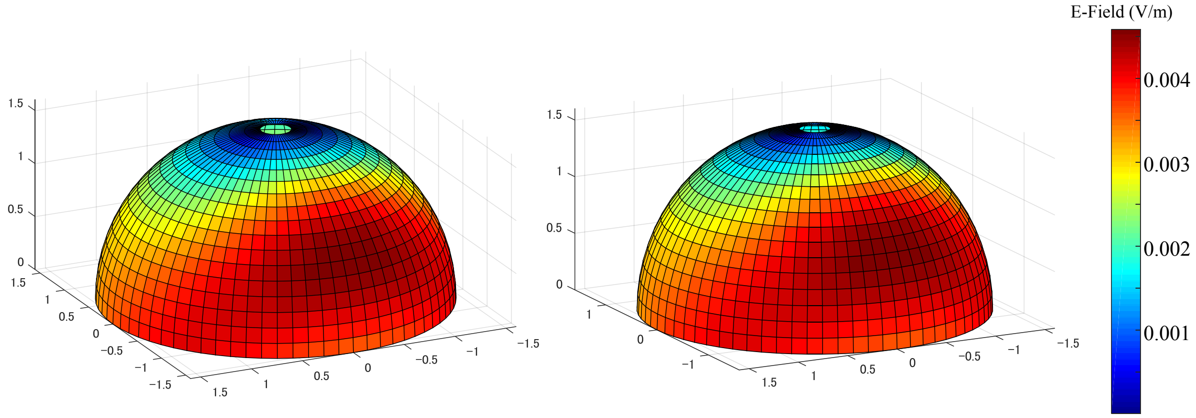

(a)

(b)

Figure 7.22: Near field distribution for real car at $1.6m$ (a) reference and (b) calculated.

7.6.2 Far Field Estimation in Freespace

In order to verify the modeling performance of our wire grid model. We compare the far field pattern of the two car models. The first model is planar car model which is modeled in FEKO. An equivalent wire grid model is modeled in EEM-MOM. We therefore verify the far field in freespace in order to verify the performance.

In the case of different frequency points as shown in Fig. 7.23, we obtain a very good agreement in the reference pattern and the estimated pattern using the proposed method. This therefore entails that using the wire grid model for our method to estimate the far field pattern from measured hemispherical near field information would produce agreeable results. Thus, in free space pattern, the results verifies that the two models are equivalent. We thus, use the wire grid model in our numerical analysis in the next subsection and compare the reference results to the numerical one.

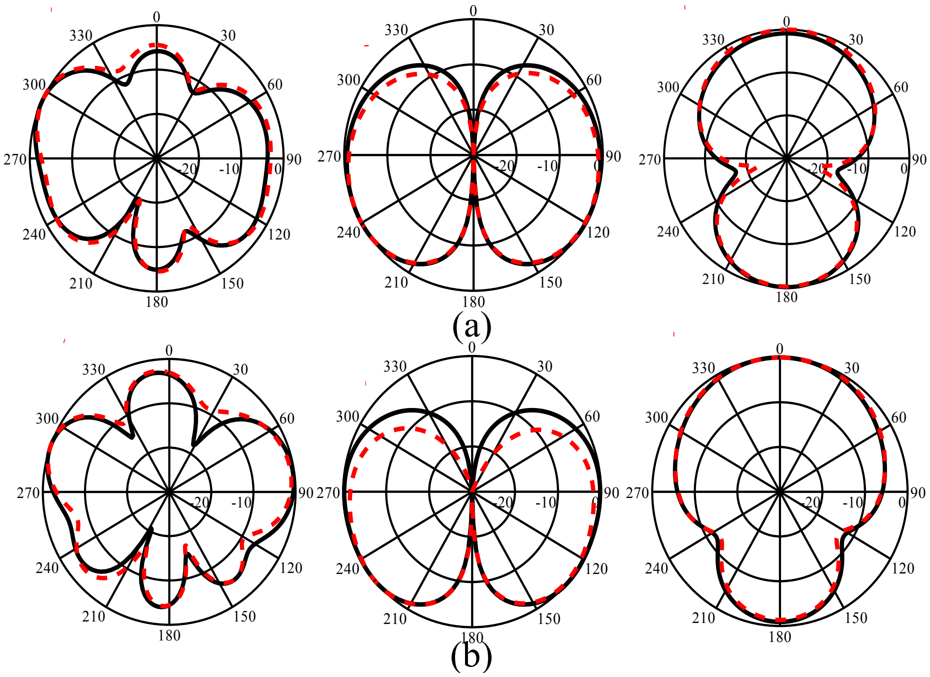

Figure 7.23: Freespace far field in for different frequency.

7.6.3 Far Field Estimation from Near Field on Earth

From the acquired hemispherical near field information, we estimate the far field pattern using RCM to include the effect of real ground. In the reconstructed far field result on earth from hemispherical near field information as shown in Fig. 7.24 and Fig. 7.25, we have a very good estimation performance. This therefore confirms the validity of the method which reconstruct the currents and estimate far field of a vehicular mounted antenna including the effect of real ground from hemispherically measured near field information.

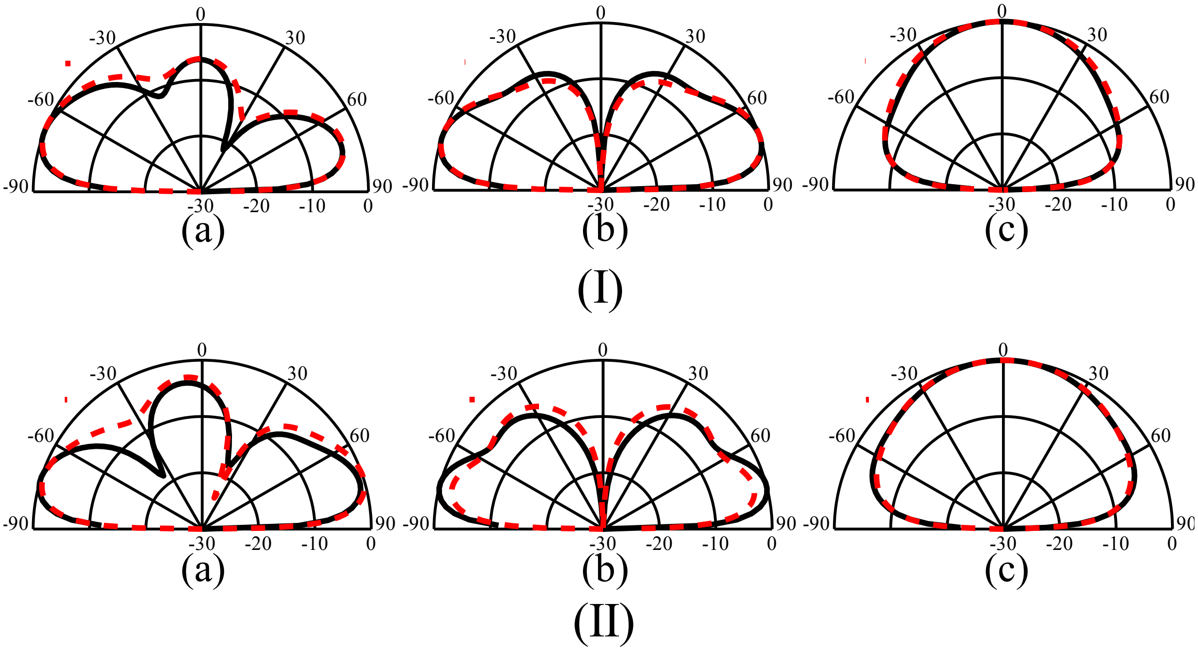

(a) (b) (c)

(I)

(a) (b) (c)

(II)

Figure 7.24: Estimated far field on earth from near field measurements for lower frequency points.

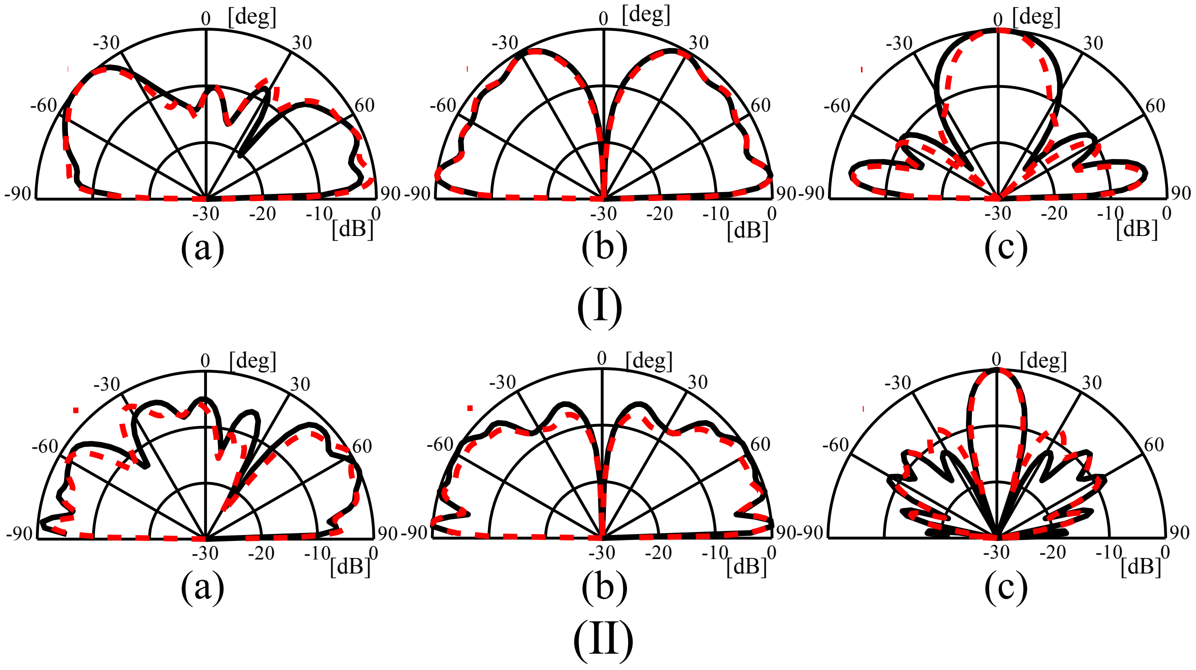

(a) (b) (c)

(I)

(a) (b) (c)

(II)

Figure 7.25: Estimated far field on earth from near field measurements for higher frequency points.

7.6.4 Prius Measurement Model and Set–up

In this subsection, we verify the validity of the proposed method by comparing the simulated and/or the numerical data with measured near field information in anechoic chamber. In the reference pattern, it is impossible to measure the far field pattern of a car including of the earth. We therefore, measure the near field data hemispherically, then reconstruct the surface current distribution of the car and then calculate the far field of the vehicle mounted antenna including the effect of the earth.

In Fig. 7.26, the measurement model of the Prius car is shown. In the measurement model, a $\frac{1}{5}$ size of the actual model was used. The car is made from copper material and resin. In this figure, the measurement set–up is also presented. The radius of measurement was at $R = 0.8m$ and $R = 1.265m$. The measurement data was obtained for $\theta = 0 - 90°$ (elevation) and $\phi = 0 - 360°$ (azimuth). The sampling interval is given by $\Delta\theta = \Delta\phi = 2°$. A Satimo horn antenna is used a measurement probe.

Figure 7.26: Prius car measurement model.

In the measurement comparison, the result of estimating the far field from the derived actual wave source information is compared from numerically simulated result in FEKO. From this comparison, we show in the next subsections the far field results obtained.

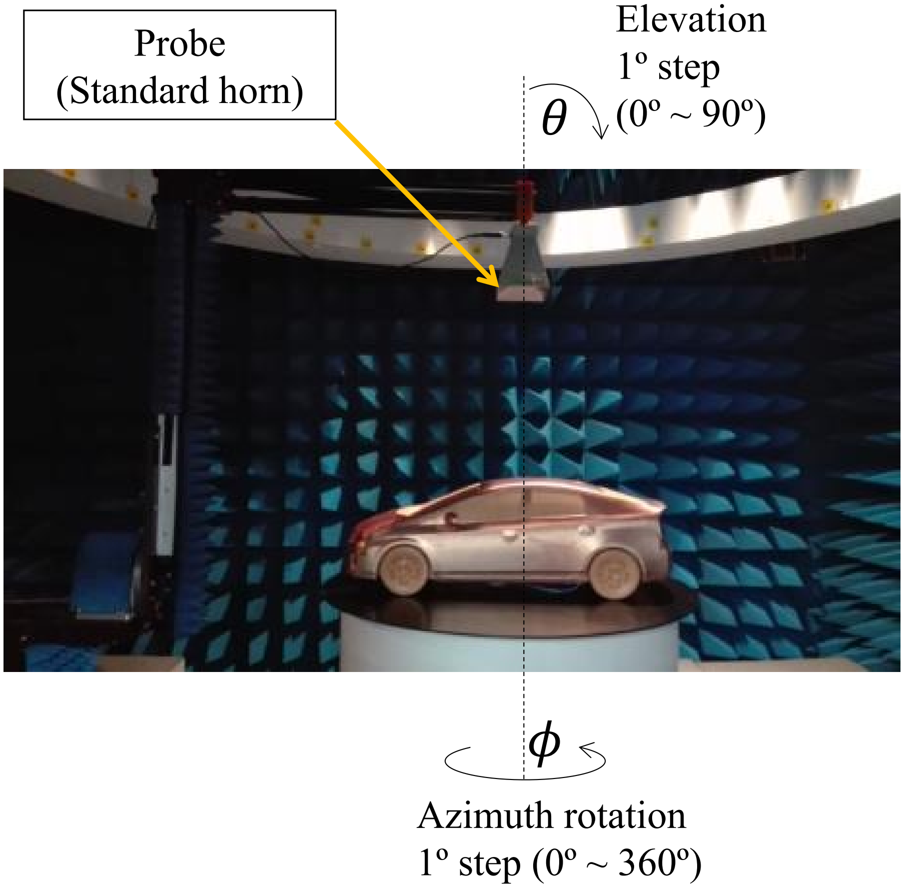

Figure 7.27: Prius car measurement model and set up.

7.6.5 Measured Far Field in Freespace

Before verifying or comparing the performance of the proposed method, we firstly, compare the far field of the simulated model in FEKO and manufactured model used for measurements. In this comparison, we consider far field in free space simulated in FEKO as well as measured in an anechoic chamber. The frequency of consideration is 1.5 GHz. Fig. 7.28 shows the simulated far field (black line) as well as measured far field (red line) in free space. We obtain a roughly comparable far field in free space for the two models.

Errors can be attributed to short measurement distance for the far field measurement due to space constraints in anechoic chamber as well as some differences in the FEKO model and measurement model. One of the important points to note is that FEKO simulation model was coarse mesh model while the measurement model was manufactured using a fine CAD mesh model which contained very detailed information about the car model.

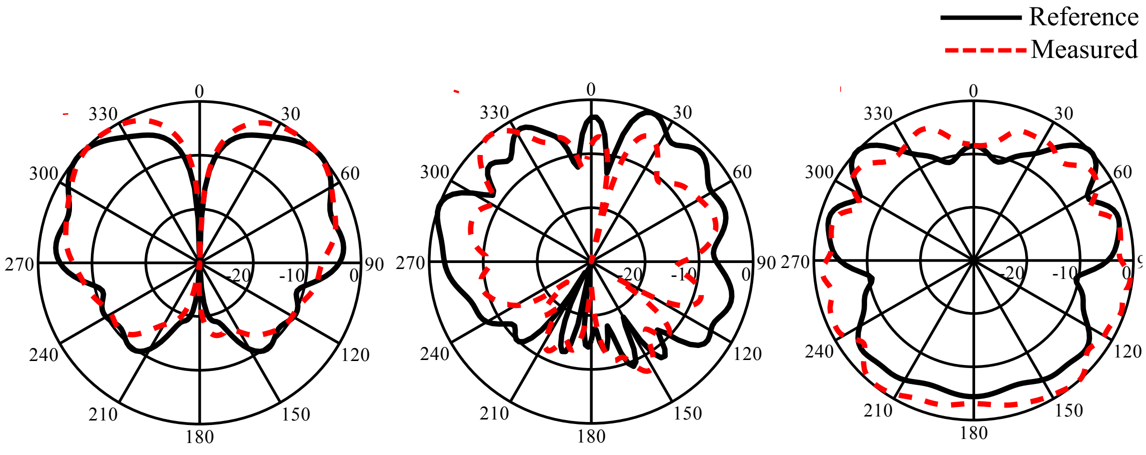

(a) (b) (c)

Figure 7.28: Measured freespace far field for vehicular mounted antenna. (a) $E_\theta(\phi = 0°)$, (b) $E_\theta(\phi = 90°)$, and (c) $E_\theta(\theta = 90°)$.

7.6.6 Estimated Far Field on Earth from Measured Near Field

In this subsection, we compare the performance of the method by using measured near field information. From the measured near field data, we calculate surface current distribution of the estimation target. We then apply reflection coefficient method to the surface current distribution to estimate the far field on earth for a vehicular mounted antenna. In Fig. 7.29, we observe the result for different frequency points 100 MHz and 200 MHz for a measurement radius of $0.8m$. Although we obtain small estimation errors, we have reconstructed the far field with good accuracy. Therefore, it can be confirmed that the far field is roughly in agreement (between the numerically simulated and measured data).

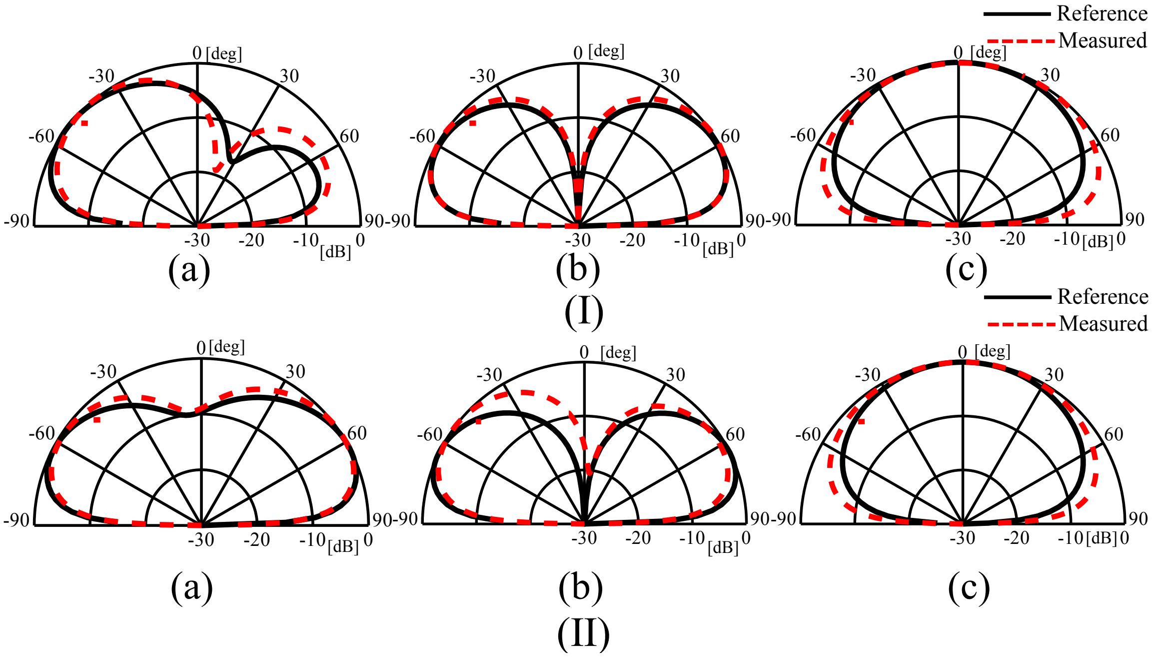

(a) (b) (c)
(I)

(a) (b) (c)
(II)

Figure 7.29: Reconstructed far field on earth from measured near field data for vehicular mounted antenna at 100 (top) and 200 MHz (bottom). (a) $E_\theta(\phi = 0°)$, (b) $E_\phi(\phi = 0°)$, and (c) $E_\theta(\phi = 90°)$.

In the following example, we consider near field information measured at a hemispherical of $0.8m$ as well and a frequency of 500MHz. In Fig. 7.30, we observe a good estimation in (a) and (b) while (c) has errors between $0 - 30°$. This corresponds to weak near field around the windscreen part of the car. On top of that, the mesh size of the wire grid model is not consistent and therefore leads to estimation error in high frequency cases.

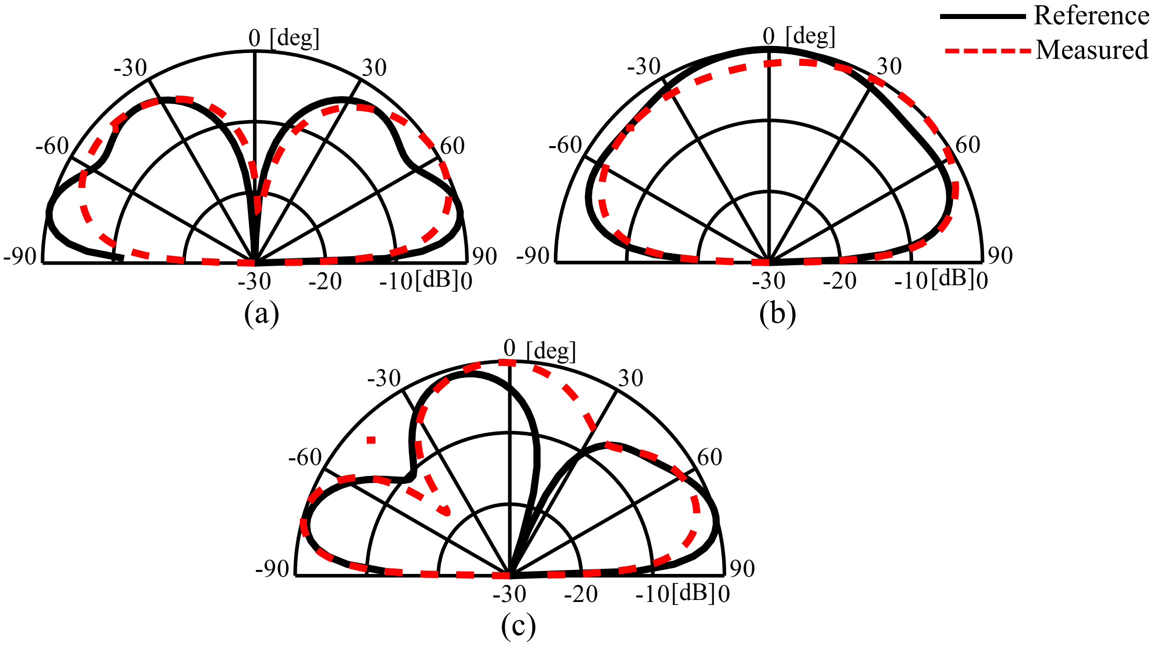

Figure 7.30: Reconstructed far field on earth from measured near field data for vehicular mounted antenna at 500 MHz. (a) $E_\theta(\phi = 0°)$, (b) $E_\phi(\phi = 0°)$, and (c) $E_\theta(\phi = 90°)$.

7.7 Summary

In this chapter, a method to derive actual wave source information on real surface derived from near field measurements is discussed. The near field information is measured in a hemispherical manner for a vehicular mounted antenna. The method is based on the assumption of scanning current distribution based on the moment method, and to estimate far field on earth (realistic ground) from the mirror image source. We have examined three different types of models. (I) is a simple car model with an antenna mounted on top. (II) is an arbitrary antenna model (Black Box model) which is used to estimate the far field of windscreen based antenna. (III) is a real Car model (complex model). In this model, a monopole antenna is mounted on a Prius car and its far field estimated from near field measurements including the effect of the earth (realistic ground). It is confirmed that accurate estimation can be made using an arbitrary antenna to reconstruct far field of a windscreen based antenna on earth as well as complex DUT model. We have therefore verified the effectiveness of the proposed method for a vehicular mounted antenna and a windscreen based monopole antenna model to estimate far field on earth from hemispherical near field measurements.

Chapter 8

Conclusion

Wireless communication technology continues to play an important role in people's lives. It continues to influence and/or affect our social and economic lives. In wireless communications, mathematical models are the backbone of algorithms used in this technology. In this dissertation, we have developed robust mathematical models that can improve the performance of wireless systems. This chapter presents an overview of the conclusions drawn from the analysis and results of the preceding chapters.

In Chapter 3, the problem of direction of arrival estimation in the case where the number of sources is larger than the number of sensors was considered. Firstly, a circularly configured nested sparse circular array was proposed. The concentric extension of the NSCA provides the virtual sensors, which are synthesized on a non–uniform concentric circular array. By utilizing the virtual sensors in the concentric extension, NSCA achieves increased degrees of freedom. Furthermore, we developed mathematical models to explore the increased degrees of freedom to undertake underdetermined DOA estimation. Thus, two strategies were utilized together with the NSCA; subspace based technique MUSIC and ℓ_1–based optimization method. In both methods, it was verified that the NSCA is capable of estimating more number of sources in comparison to the number of physical sensors. In the numerical examples, we investigated the RMSE performance as related to SNR and number of snapshots in which the number of snapshots played a crucial role in the underdetermined DOA estimation. We further compared the performance of different circularly configured arrays in order to find an optimal circular array configuration. It was discovered that the NSCA is capable of resolving closed spaced signal and obtains better RMSE performance for underdetermined DOA estimation. The discussion in this chapter is connected to the discussion in Chapter 4 and Chapter 5.

In Chapter 4, a mutual coupling compensation method for nested sparse circular array was proposed. This method is based on a simple mutual coupling matrix which is symmetric banded–like circulant matrix. The banded–like circulant mutual coupling matrix improves underdetermined DOA estimation accuracy in the presence of mutual coupling. In an ideal case, the effect of mutual coupling is not considered in the DOA estimation problem as in Chapter 3. By including the effect of the mutual coupling, the performance of DOA estimation is seriously degraded. The effects of mutual coupling can neither be eliminated nor its variability predicted since the electromagnetic environment surrounding the antenna is continuously changing. If calibration procedures to estimate and compensate for the mutual coupling are available, design constraints with respect to coupling could be relaxed by antenna designers to improve other aspects of the antenna, without affecting the performance of the algorithms. The mutual coupling compensation method proposed in this chapter works well with nested sparse circular arrays. In the case of a 6 element array, the mutual coupling matrix has 36 values. In the proposed method, only 4 values are used to compensate for the mutual coupling effects and obtains better performance. The method achieved improved DOA estimation performance, better RMSE as well as lower average run–time. The discussion in this chapter is connected to Chapter 5 since the signals considered were narrowband signals.

The discussion in Chapter 5 stems from the discussions in Chapter 3 and Chapter 4. In this chapter, wideband signals were considered. Furthermore, we extended the DOA estimation algorithm in Chapter 3 from narrowband signal sources to the case of wideband signals. We further, consider the mutual coupling compensation method in

Chapter 4 in the case of using wideband signals. We verified that underdetermined DOA estimation is possible in the case of wideband signals in the discussion from this chapter. This also applies when mutual coupling is assumed in the array. From simulation experiments, we verified that the proposed approach achieves better RMSE performance as well as excellent DOA estimation accuracy. This method is cost effective and easy to implement whilst achieving better DOA estimation performance.

In Chapter 6, a hemispherical near field measurement technique was discussed. Near field measurements, provide fast and accurate method for the measurements of large antennas whose far field measurements cannot fit in conventional anechoic chamber. In this chapter, a method of far field estimation for an antenna above the earth from hemispherical near field measurements was discussed. Furthermore, we proposed a method to calculate current distribution on the AUT; the Moore–Penrose pseudo–inverse method. From measured near field information, we determine an equivalent electric current source over a hemispherical surface encompassing the antenna. By using plane wave reflection coefficient method, we are capable of reconstructing the far field of an antenna above earth. The accuracy of the proposed method was verified by using synthetic data as well as data measured in an anechoic chamber for a monopole antenna model.

In device–mounted antennas, the whole system affect the performance on the antenna. In most cases, performance of the antenna is evaluated without considering the whole system. In Chapter 7, a vehicular mounted antenna was discussed. The car body affect the performance of the antenna. In terms of measuring far field of a vehicle–mounted antenna, a very huge anechoic chamber is required, which is very expensive. We thus utilized the hemispherical near field measurement technique in Chapter 6. This technique reduces the measurement cost as well as complexity as compared to full spherical near field measurement. From the hemispherically measured near field data, we reconstructed the far field by including the effect of the car body as well as real ground. Far field results from simulation and measurement data is compared in both freespace case and on real ground (earth). In real use scenario, the earth affects performance of the antenna on vehicle and considering effect of real ground in the far field reconstruction problem helps antenna engineers to evaluate the real performance of antennas before deployment for specific use cases.

From the results presented in this dissertation, robust mathematical models have been proposed which improves the performance of wireless communication system. The performance of DOA estimation algorithms has been proved in the case when we have more sources as compared to the number of sensors. Furthermore, the effect of mutual coupling has been considered in which the effect of mutual coupling can be reduced for both narrowband and wideband signal sources. In antenna measurement application, mathematical models were proposed in which far field is estimated from hemispherically measured near field and the effect of real ground on the far field is included.

Appendix A

Cramer–Rao Lower Bound (CRLB) for NSCA

The Cramer–Rao lower bound (CRLB) sets a lower bound on the variance of unbiased estimators. It has been extensively studied in the field of array signal processing especially for direction of arrival (DOA) estimation using uniform or non–uniform linear arrays. We consider an underdetermined signal model for circularly configured planar arrays and investigate the conditions under which CRLB exist. In this appendix, we derive a new closed–form expression for the CRLB.

A.1 Cramer–Rao Lower Bound

The expressions for CRLB comes from the inversion of the Fisher information matrix (FIM), which contains information about all the unknown parameters. In this appendix, we are interested in the stochastic CRLB of circularly configured planar array for underdetermined DOA estimation in which $D \geq M$. Let $\boldsymbol{\alpha} = [\boldsymbol{\phi}^T, \quad \rho_d^T, \quad \sigma]^T$ denote unknown parameter vector where $d = 1, 2, ..., D$. The (η, ℓ)–th entry of the Fisher information matrix (FIM) $\mathfrak{I}(\boldsymbol{\alpha})$ is defined as

$$\mathfrak{J}(\boldsymbol{\alpha}) = N \bullet \mathrm{Tr}\left\{\mathbf{R}_{xx}^{-1}\frac{\partial \mathbf{R}_{xx}}{\partial[\boldsymbol{\alpha}]_{\eta}}\mathbf{R}_{xx}^{-1}\frac{\partial \mathbf{R}_{xx}}{\partial[\boldsymbol{\alpha}]_{\ell}}\right\} \tag{A.1}$$

Tr{} is the trace which can be defined as;

$$\begin{aligned}\mathrm{Tr}\left\{\mathbf{WXYZ}\right\} &= \mathrm{vec}(\mathbf{X}^{H})^{H}(\mathbf{W}^{T}\otimes\mathbf{Y})\mathrm{vec}(\mathbf{Z})\\ (\mathbf{W}\otimes\mathbf{X})^{-1} &= (\mathbf{W})^{-1}\otimes(\mathbf{X})^{-1}\end{aligned}$$

for non–singular $\mathbf{W}$ and $\mathbf{X}$. Therefore (A.1) can be written as

$$\begin{aligned}\mathfrak{J}(\boldsymbol{\alpha}) &= N\left[\mathrm{vec}\left(\frac{\partial \mathbf{R}_{xx}}{\partial[\boldsymbol{\alpha}]_{\eta}}\right)\right]^{H}(\mathbf{R}_{xx}^{-T}\otimes\mathbf{R}_{xx}^{-1})\mathrm{vec}\left(\frac{\partial \mathbf{R}_{xx}}{\partial[\boldsymbol{\alpha}]_{\ell}}\right)\\ &= N\left[(\mathbf{R}_{xx}^{T}\otimes\mathbf{R}_{xx})^{-\frac{1}{2}}\left(\frac{\partial \mathbf{y}}{\partial[\boldsymbol{\alpha}]_{\eta}}\right)\right]^{H}(\mathbf{R}_{xx}^{T}\otimes\mathbf{R}_{xx})^{-\frac{1}{2}}\left(\frac{\partial \mathbf{y}}{\partial[\boldsymbol{\alpha}]_{\ell}}\right)\end{aligned} \tag{A.2}$$

The derivatives of $\mathbf{y}$ with respect to $\boldsymbol{\alpha}$ is given by

$$\frac{\partial \mathbf{y}}{\partial[\boldsymbol{\alpha}]} = \left[\frac{\partial \mathbf{y}}{\partial\phi_1},\frac{\partial \mathbf{y}}{\partial\phi_2},\cdots,\frac{\partial \mathbf{y}}{\partial\phi_D},\frac{\partial \mathbf{y}}{\partial\rho_1},\frac{\partial \mathbf{y}}{\partial\rho_2},\cdots,\frac{\partial \mathbf{y}}{\partial\rho_D},\frac{\partial \mathbf{y}}{\partial\sigma^2}\right] \tag{A.3}$$

Let $\boldsymbol{\Lambda}$ and $\boldsymbol{\Gamma}$ denote:

$$\begin{aligned}\boldsymbol{\Lambda} &= (\mathbf{R}_{xx}^{T}\otimes\mathbf{R}_{xx})^{-\frac{1}{2}}\left[\frac{\partial \mathbf{y}}{\partial\phi_1},\frac{\partial \mathbf{y}}{\partial\phi_2},\cdots,\frac{\partial \mathbf{y}}{\partial\phi_D}\right]\\ \boldsymbol{\Gamma} &= (\mathbf{R}_{xx}^{T}\otimes\mathbf{R}_{xx})^{-\frac{1}{2}}\left[\frac{\partial \mathbf{y}}{\partial\rho_1},\frac{\partial \mathbf{y}}{\partial\rho_2},\cdots,\frac{\partial \mathbf{y}}{\partial\rho_D},\frac{\partial \mathbf{y}}{\partial\sigma^2}\right]\end{aligned}$$

The FIM therefore becomes;

$$\mathfrak{J}(\boldsymbol{\alpha}) = N\begin{bmatrix}\boldsymbol{\Lambda}^{H}\\ \boldsymbol{\Gamma}^{H}\end{bmatrix}[\boldsymbol{\Lambda}\quad\boldsymbol{\Gamma}] = N\begin{bmatrix}\boldsymbol{\Lambda}^{H}\boldsymbol{\Lambda} & \boldsymbol{\Lambda}^{H}\boldsymbol{\Gamma}\\ \boldsymbol{\Gamma}\boldsymbol{\Lambda}^{H} & \boldsymbol{\Gamma}^{H}\boldsymbol{\Gamma}\end{bmatrix} \tag{A.4}$$

If the FIM is non–singular, then the CRLB for the DOAs $\boldsymbol{\phi} = [\phi_1,\phi_2,...,\phi_D]^{T}$ can be expressed as the inverse of the Schur complement of the block $\boldsymbol{\Lambda}^{H}\boldsymbol{\Lambda}$ of $\mathfrak{J}(\boldsymbol{\alpha})$. Therefore the CRLB will be given by

$$\text{CRLB}(\phi) = \mathfrak{J}(\boldsymbol{\alpha})^{-1} = \frac{1}{N}(\boldsymbol{\Lambda}^H \boldsymbol{\Pi}_{\boldsymbol{\Gamma}}^{\perp} \boldsymbol{\Lambda})^{-1} \tag{A.5}$$

where $\boldsymbol{\Pi}_{\boldsymbol{\Gamma}}^{\perp} = \mathbf{I} - \boldsymbol{\Gamma}(\boldsymbol{\Gamma}^H\boldsymbol{\Gamma})^{-1}\boldsymbol{\Gamma}^H$. The non–singularity of the FIM is equivalent to non–singularity of $\boldsymbol{\Lambda}^H\boldsymbol{\Lambda}$ and $\boldsymbol{\Lambda}^H\boldsymbol{\Pi}_{\boldsymbol{\Gamma}}^{\perp}\boldsymbol{\Lambda}$.

Bibliography

[1] M. Helfenstein and G. S. Moschytz, *Circuits and Systems for Wireless Communications.* Kluwer Academic Publishers, 1999.

[2] L. Eriksson, M. Elmusrati, and M. Pohjola, “Introduction to wireless automation,” Helsinki University of Technology, Tech. Rep. Report 155, 2007.

[3] C. White, *Data Communications and Computer Networks: A Business User’s Approach.* Cengage Learning, 2015.

[4] S. Mishra, N. K. Singh, and V. Rousseau, *System on Chip Interfaces for Low Power Design.* Morgan Kaufmann, 2015.

[5] “Alliance for telecommunications industry solutions,” http://www.atis.org/glossary/definition.aspx?id=231.

[6] G. Wen, *Foundations For Radio Frequency Engineering.* World Scientific Publishing, 2015.

[7] W. Gosling, *Radio Spectrum Conservation.* Newnes, 2000.

[8] Carrie MacGillivray, “The internet of things is poised to change everything, says idc,” Business Wire, 2013.

[9] D. M. West, “How 5G technology enables the health internet of things,” https://www.brookings.edu/wp-content/uploads/2016/07/How-5G-tech-enables-health-iot-west.pdf, 2016.

[10] Charles McLellan, “The Internet of Things and Big Data,” https://www.zdnet.com/article/the-internet-of-things-and-big-data-unlocking-the-power/, 2015.

[11] Ian King, “5g networks will do much more than stream better cat videos,” Bloomberg News, 2016.

[12] ShareTechnote, “IoT (Internet Of Things) - Definition,” http://www.sharetechnote.com/html/IoT/, 2015.

[13] H. Boche and A. Eisenbltter, “Mathematics in wireless communications,” in *Production Factor Mathematics*, M. Grtschel, K. Lucas, and V. Mehrmann, Eds. Berlin: Springer, 2010, pp. 266–290.

[14] N. R. Council, *Renewing U.S. Telecommunications Research*, R. W. Lucky and J. Eisenberg, Eds. Washington, DC: The National Academies Press, 2006. [Online]. Available: https://www.nap.edu/catalog/11711/renewing-us-telecommunications-research

[15] J. W. Plunkett, *Plunkett's Telecommunications Industry Almanac 2009: Telecommunications Industry Market Research, Statistics, Trends and Leading Companies.* Plunkett Research, 2008.

[16] C. A. Balanis and P. I. Ioannides, “Introduction to smart antennas,” *Synthesis Lectures on Antennas*, vol. 2, no. 1, pp. 1–175, 2007.

[17] A. Mathur and R. Trivedi, *Antenna And Wave Propagation.* Scientific Publishers, 2011.

[18] X. Zang, J. Yu, and G. Chen, “Design and implementation of mobile sink node in sdma applications,” in *Ubiquitous Intelligence and Computing*, Z. Yu, R. Liscano, G. Chen, D. Zhang, and X. Zhou, Eds. Xi'an, China: 7th International Conference Proceedings, 2010, pp. 215–227.

[19] F. Gross, *Smart Antennas for Wireless Communications: With MATLAB.* McGraw Hill Professional, 2005.

[20] T. Kaiser, *Smart Antennas: State of the Art.* Hindawi Publishing Corporation, 2005.

[21] S. Bellofiore, J. Foutz, R. Govindarajula, I. Bahceci, C. A. Balanis, A. S. Spanias, J. M. Capone, and T. M. Duman, “Smart antenna system analysis, integration and performance for mobile ad-hoc networks (manets),” *IEEE Transactions on Antennas and Propagation*, vol. 50, no. 5, pp. 571–581, May 2002.

[22] Skyler Frink, “Smart Antenna technology relies on digital signal processing,” http://www.militaryaerospace.com/articles/print/volume-24/issue-5/technology-focus/smart-antenna-technology-relies-on-digital-signal-processing.html, 2013.

[23] T. Anderson, *Plasma Antennas.* Artech House, 2011.

[24] T. E. Tuncer and B. Friedlander, *Classical and Modern Direction-of-Arrival Estimation.* New York: Academic Press, 2009.

[25] H. Krim and M. Viberg, “Two decades of array signal processing research: the parametric approach,” *IEEE Signal Processing Magazine*, vol. 13, no. 4, pp. 67–94, Jul. 1996.

[26] J. Foutz, A. Spanias, and M. K. Banavar, “Narrowband direction of arrival estimation for antenna arrays,” *Synthesis Lectures on Antennas*, vol. 3, no. 1, pp. 1–76, 2008.

[27] C. A. Balanis, *Antenna Theory, Analysis and Design*, 2nd ed. New York: John Wiley and Sons, Inc., 1997.

[28] T. Basikolo, “A study of reactance based uniform circular array antenna for doa estimation,” Master’s thesis, Yokohama National University, Japan, 2015.

[29] R. Hansen, *Phased array antennas*, 2nd ed. Hoboken, United States: John Wiley and Sons, 2009.

[30] L. C. Godara, “Application of antenna arrays to mobile communications. ii. beamforming and direction-of-arrival considerations,” *Proceedings of the IEEE*, vol. 85, no. 8, pp. 1195–1245, Aug 1997.

[31] H. L. Van Trees, *Optimum Array Processing, Detection, Estimation and Modulation Part IV.* New York: John Wiley and Sons, 2002.

[32] F. Gao and A. B. Gershman, “A generalized esprit approach to direction-of-arrival estimation,” *IEEE Signal Processing Letters*, vol. 12, no. 3, pp. 254–257, March 2005.

[33] R. L. Yadava, *Antenna and Wave Propagation.* PHI Learning Pvt. Ltd., 2011.

[34] T. A. Milligan, *Modern Antenna Design*, 2nd ed. Hoboken, New Jersey: Wiley-IEEE Press, 2005.

[35] J. D. Kraus and R. J. Marhefka, *Antennas For All Applications*, 3rd ed. McGraw-Hill Science, 2002.

[36] F. Agostino, F. Ferrara, C. Gennarelli, R. Guerriero, and M. Migliozzi, “Spherical near-field - far-field transformation for quasi-planar antennas from irregularly spaced data,” *Journal of Electromagnetic Analysis and Applications*, vol. 4, no. 4, pp. 147–155, Apr. 2012.

[37] R. C. Johnson, H. A. Ecker, and J. S. Hollis, “Determination of far-field antenna patterns from near-field measurements,” *Proceedings of the IEEE*, vol. 61, no. 12, pp. 1668–1694, Dec 1973.

[38] A. Yaghjian, “An overview of near-field antenna measurements,” *IEEE Transactions on Antennas and Propagation*, vol. 34, no. 1, Jan. 1986.

[39] D. Paris, W. Leach, and E. Joy, "Basic theory of probe-compensated near-field measurements," *IEEE Transactions on Antennas and Propagation*, vol. 26, no. 3, pp. 373–379, May 1978.

[40] D. Slater, *Near-Field Antenna Measurements.* Artech House, Boston, 1991.

[41] Y. Sugimoto, "A study on estimating electrical characteristics of wave source and its applications using electromagnetic information in near-field," Ph.D. dissertation, Yokohama National University, 2018.

[42] T. K. Sarkar and A. Taaghol, "Near-field to near/far-field transformation for arbitrary near-field geometry utilizing an equivalent electric current and mom," *IEEE Transactions on Antennas and Propagation*, vol. 47, no. 3, pp. 566–573, Mar. 1999.

[43] J. A. Hansen, "On cylindrical near-field scanning techniques," *IEEE Transactions on Antennas and Propagation*, vol. 28, no. 2, pp. 231–234, Mar 1980.

[44] A. M. Zoubir, M. Viberg, R. Chellappa, and S. Theodoridis, *Academic Press Library in Signal Processing: Volume 3 Array and Statistical Signal Processing.* Academic Press, 2014.

[45] P. Pal, "New directions in sparse sampling and estimation for underdetermined systems," Ph.D. dissertation, California Institute of Technology, 2013.

[46] F. Belloni and V. Koivunen, "Beamspace transform for uca: Error analysis and bias reduction," *IEEE Transactions on Signal Processing*, vol. 54, no. 8, pp. 3078–3089, Aug 2006.

[47] T. Basikolo, K. Ichige, and H. Arai, "Direction of arrival estimation for quasi-stationary signals using nested circular array," in *2016 4th International Workshop on Compressed Sensing Theory and its Applications to Radar, Sonar and Remote Sensing (CoSeRa)*, Sept 2016, pp. 193–196.

[48] J. van de Laar, M. Moonen, and P. C. W. Sommen, "Mimo instantaneous blind identification based on second-order temporal structure," *IEEE Transactions on Signal Processing*, vol. 56, no. 9, pp. 4354–4364, Sept 2008.

[49] R. Schmidt, "Multiple emitter location and signal parameter estimation," *IEEE Trans. Antennas and Propagation*, vol. 34, no. 3, pp. 276–280, Mar. 1986.

[50] Z. Chen, G. Gokeda, and Y. Yu, *Introduction to Direction-of-Arrival Estimation.* Boston: Artech House, 2010.

[51] C. P. Mathews and M. D. Zoltowski, "Signal subspace techniques for source localization with circular sensor arrays," ECE Technical Reports, Tech. Rep. Paper 172, 1994.

[52] Y. Sugimoto, S. Miyabe, T. Yamada, S. Makino, and F. Juang, "Underdetermined doa estimation by the non-linear music exploiting higher-order moments," in *IWAENC 2012; International Workshop on Acoustic Signal Enhancement*, Sept 2012, pp. 1–4.

[53] Y. Sugimoto, "A study on underdetermined doa estimation techniques based on higher-order correlation analysis utilizing non-linear mapping," Ph.D. dissertation, University of Tsukuba, 2016.

[54] Z. Yang, J. Li, P. Stoica, and L. Xie, "Sparse methods for direction-of-arrival estimation," 2016.

[55] E. J. Candes, J. Romberg, and T. Tao, "Robust uncertainty principles: exact signal reconstruction from highly incomplete frequency information," *IEEE Trans. Information Theory*, vol. 52, no. 2, pp. 489–509, Feb. 2006.

[56] D. L. Donoho, "Compressed sensing," *IEEE Transactions on Information Theory*, vol. 52, no. 4, pp. 1289–1306, April 2006.

[57] D. L. Donoho and M. Elad, "Optimally sparse representation in general (nonorthogonal) dictionaries via l1 minimization," *Proceedings of the National Academy of Sciences*, vol. 100, no. 5, pp. 2197–2202, 2003.

[58] R. G. Baraniuk, "Compressive sensing [lecture notes]," *IEEE Signal Processing Magazine*, vol. 24, no. 4, pp. 118–121, July 2007.

[59] Y. C. Eldar, *Sampling Theory: Beyond Bandlimited Systems.* Cambridge, United Kingdom: Cambridge University Press, 2015.

[60] I. Rish and G. Grabarnik, *Sparse Modeling: Theory, Algorithms, and Applications.* CRC Press, 2015.

[61] S. Foucart and H. Rauhut, *A Mathematical Introduction to Compressive Sensing.* New York: Springer, 2013.

[62] M. Vetterli, J. Kovacevic, and V. K. Goyal, *Foundations of Signal Processing*, 3rd ed. Cambridge, UK: Cambridge University Press, 2014.

[63] Y. C. Eldar and G. Kutyniok, *Compressed Sensing: Theory and Applications.* New York: Cambridge University Press, 2012.

[64] S. Boyd and L. Vandenberghe, *Convex Optimization.* Cambridge, UK: Cambridge University Press, 2004.

[65] M. Grant and S. Boyd, "Cvx: Matlab software for disciplined convex programming," Apr. 2010.

[66] S. G. Mallat and Z. Zhang, "Matching pursuits with time-frequency dictionaries," *IEEE Transactions on Signal Processing*, vol. 41, no. 12, pp. 3397–3415, Dec 1993.

[67] Y. C. Pati, R. Rezaiifar, and P. S. Krishnaprasad, "Orthogonal matching pursuit: recursive function approximation with applications to wavelet decomposition," in *Proceedings of 27th Asilomar Conference on Signals, Systems and Computers*, Nov 1993, pp. 40–44 vol.1.

[68] D. Wu, W. P. Zhu, and M. N. S. Swamy, "The theory of compressive sensing matching pursuit considering time-domain noise with application to speech enhancement," *IEEE/ACM Transactions on Audio, Speech, and Language Processing*, vol. 22, no. 3, pp. 682–696, March 2014.

[69] D.Needell and J.A.Tropp, "Cosamp: Iterative signal recovery from incomplete and inaccurate samples," *Applied and Computational Harmonic Analysis*, vol. 26, no. 3, pp. 301–321, May 2009.

[70] D. L. Donoho, Y. Tsaig, I. Drori, and J. L. Starck, "Sparse solution of underdetermined systems of linear equations by stagewise orthogonal matching pursuit," *IEEE Transactions on Information Theory*, vol. 58, no. 2, pp. 1094–1121, Feb 2012.

[71] D. Needell and R. Vershynin, "Uniform uncertainty principle and signal recovery via regularized orthogonal matching pursuit," *Foundations of Computational Mathematics*, vol. 9, pp. 317–334, 2009.

[72] T. Blumensath and M. E. Davies, "Iterative thresholding for sparse approximations," *Journal of Fourier Analysis and Applications*, vol. 14, no. 5, pp. 629–654, Dec 2008.

[73] T. T. Lam, "Optimization in l1- norm for sparse recovery," Master's thesis, University of Oslo, Norway, 2014.

[74] C. A. Balanis, *Modern Antenna Handbook*. Hoboken, New Jersey: John Wiley and Sons, Inc., 2008.

[75] F. D'Agostino, F. Ferrara, C. Gennarelli, G. Riccio, and C. Savarese, "Direct far-field reconstruction from data measured by a cylindrical scanning facility," in *2002 9th International Symposium on Antenna Technology and Applied Electromagnetics*, July 2002, pp. 1–5.

[76] D. Paris, W. Leach, and E. Joy, "Basic theory of probe-compensated near-field measurements," *IEEE Transactions on Antennas and Propagation*, vol. 26, no. 3, pp. 373–379, May 1978.

[77] W. P. M. N. Keizer, "An overview of test techniques for characterizing active phased array antennas," in *Perspectives on Radio Astronomy: Technologies for Large Antenna Arrays*, April 1999, pp. 191–199.

[78] K. Mei, "On the integral equations of thin wire antennas," *IEEE Transactions on Antennas and Propagation*, vol. 13, no. 3, pp. 374–378, May 1965.

[79] J. Richmond, "A wire-grid model for scattering by conducting bodies," *IEEE Transactions on Antennas and Propagation*, vol. 14, no. 6, pp. 782–786, Nov 1966.

[80] R. F. Harrington, "Matrix methods for field problems," *Proceedings of the IEEE*, vol. 55, no. 2, pp. 136–149, Feb 1967.

[81] ——, *Field Computation by Moment Methods.* Orlando, FL: Krieger, 1987.

[82] Y. Matsuda and H. Arai, "Far field estimation on the earth using real source information derived by near field," *IEICE Technical Report*, vol. 116, no. 526, pp. 43–46, Mar. 2017.

[83] D. H. Johnson and D. E. Dudgeon, *Array Signal Processing: Concepts and Techniques.* New Jersey: Prentice-Hall, 1993.

[84] H. Wang and M. Kaveh, "Coherent signal-subspace processing for the detection and estimation of angles of arrival of multiple wide-band sources," *IEEE Trans. Acoust. Speech and Signal Process.*, vol. 33, no. 4, pp. 823–831, Aug. 1985.

[85] E. D. Di Claudio and R. Parisi, "Waves: weighted average of signal subspaces for robust wideband direction finding," *IEEE Trans. Signal Processing*, vol. 49, no. 10, pp. 2179–2191, Oct. 2001.

[86] P. Pal and P. Vaidyanathan, "Nested arrays: A novel approach to array processing with enhanced degrees of freedom," *IEEE Trans. Signal Process.*, vol. 58, no. 8, pp. 4167–4181, Aug. 2010.

[87] ——, "Nested arrays in two dimensions, part i: Geometrical considerations," *IEEE Trans. Signal Process.*, vol. 60, no. 9, pp. 4694–4705, Sept. 2012.

[88] ——, "Nested arrays in two dimensions, part ii: Application in two dimensional array processing," *IEEE Trans. Signal Process.*, vol. 60, no. 9, pp. 4706–4718, Sept. 2012.

[89] Z. Tan, Y. Eldar, and A. Nehorai, "Direction of arrival estimation using co-prime arrays: A super resolution viewpoint," *IEEE Trans. Signal Process.*, vol. 62, no. 21, pp. 5565–5576, Nov. 2014.

[90] B. H. Wang, H. T. Hui, and M. S. Leong, "Decoupled 2d direction of arrival estimation using compact uniform circular arrays in the presence of elevation-dependent mutual coupling," *IEEE Trans. Antennas and Propagation*, vol. 58, no. 3, pp. 747–755, Mar. 2010.

[91] S. C. Chan and H. H. Chen, "Uniform concentric circular arrays with frequency-invariant characteristics –;theory, design, adaptive beamforming and doa estimation," *IEEE Trans. Signal Process.*, vol. 55, no. 1, pp. 165–177, Jan. 2007.

[92] W.-K. Ma, T.-H. Hsieh, and C.-Y. Chi, "Doa estimation of quasi-stationary signals with less sensors than sources and unknown spatial noise covariance: A khatri-rao subspace approach," *IEEE Trans. Signal Process.*, vol. 58, no. 4, pp. 2168–2180, Apr. 2010.

[93] Z.-Q. He, Z.-P. Shi, L. Huang, and H. C. So, "Underdetermined doa estimation for wideband signals using robust sparse covariance fitting," *IEEE Signal Process. Lett.*, vol. 22, no. 4, pp. 435–439, Apr. 2015.

[94] P. Vaidyanathan and P. Pal, "Sparse sensing with coprime arrays," in *Proc. Asilomar Conference on Signals, Systems and Computers*, Nov. 2010.

[95] D. Malioutov, M. Cetin, and A. Willsky, "A sparse signal reconstruction perspective for source localization with sensor arrays," *IEEE Trans. Signal Process.*, vol. 53, no. 8, pp. 3010–3022, Aug. 2005.

[96] X. Wang, M. G. Amin, F. Ahmad, and E. Aboutanios, "Bayesian compressive sensing for doa estimation using the difference coarray," in *2015 IEEE International Conference on Acoustics, Speech and Signal Processing (ICASSP)*, April 2015.

[97] E. J. Candes, J. K. Romberg, and T. Tao, "Stable signal recovery from incomplete and inaccurate measurements," *Communications on pure and applied mathematics*, vol. 59, no. 8, p. 12071223, Aug. 2006.

[98] M.-Y. Cao, L. Huang, C. Qian, J.-Y. Xue, and H. So, "Underdetermined doa estimation of quasi-stationary signals via khatrirao structure for uniform circular array," *Signal Processing*, vol. 106, pp. 41–48, Jan. 2015.

[99] A. Firoozabadi and H. Abutalebi, "A novel nested circular microphone array and subband processing-based system for counting and doa estimation of multiple simultaneous speakers," *Circuits, Systems, and Signal Processing*, vol. 35, no. 2, pp. 573–601, Feb. 2016.

[100] D. Romero, R. Lpez-Valcarce, and G. Leus, "Compression limits for random vectors with linearly parameterized second-order statistics," *IEEE Transactions on Information Theory*, vol. 61, no. 3, pp. 1410–1425, March 2015.

[101] H. C. Pumphrey, “Design of sparse arrays in one, two and three dimensions,” *J. Acoust. Soc. Amer.*, vol. 93, no. 3, pp. 1620–1628, Mar. 1993.

[102] R. T. Hoctor and S. A. Kassam, “The unifying role of the coarray in aperture synthesis for coherent and incoherent imaging,” *Proc. IEEE*, vol. 78, no. 4, pp. 735–752, Apr. 1990.

[103] S. Pillai, Y. Bar-Ness, and F. Haber, “A new approach to array geometry for improved spatial spectrum estimation,” *Proceedings of the IEEE*, vol. 73, no. 10, pp. 1522–1524, Oct. 1985.

[104] Y. Abramovich, D. Gray, A. Gorokhov, and N. Spencer, “Positive-definite toeplitz completion in doa estimation for nonuniform linear antenna arrays. i. fully augmentable arrays,” *IEEE Trans. Signal Process.*, vol. 46, no. 9, pp. 2458–2471, Sept. 1998.

[105] Z. Tan and A. Nehorai, “Sparse direction of arrival estimation using co-prime arrays with off-grid targets,” *IEEE Signal Process. Lett.*, vol. 21, no. 1, pp. 26–29, Jan 2014.

[106] S. Qin, Y. D. Zhang, and M. G. Amin, “Generalized coprime array configurations for direction-of-arrival estimation,” *IEEE Trans. Signal Process.*, vol. 63, no. 6, pp. 1377–1390, March 2015.

[107] B. Porat and B. Friedlander, “Direction finding algorithms based on high-order statistics,” *IEEE Trans. Signal Process.*, vol. 39, no. 9, pp. 2016–2024, Sept. 1991.

[108] R. J. Kozick and S. A. Kassam, “Coarray synthesis with circular and elliptical boundary arrays,” *IEEE Trans. Image Process.*, vol. 1, no. 3, pp. 391–405, Jul. 1992.

[109] J. Yin and T. Chen, “Direction-of-arrival estimation using a sparse representation of array covariance vectors,” *IEEE Trans. Signal Process.*, vol. 59, no. 9, pp. 4489–4493, Sept. 2011.

[110] B. Ottersten, P. Stoica, and R. Roy, “Covariance matching estimation techniques for array signal processing applications,” *Digital Signal Processing*, vol. 8, no. 3, pp. 185 – 210, 1998.

[111] J. F. Sturm, “Using sedumi 1.02, a matlab toolbox for optimization over symmetric cones,” *Optim. Method Softw.*, vol. 11, no. 12, pp. 625–653, 1999.

[112] P. Stoica, E. G. Larsson, and A. B. Gershman, “The stochastic crb for array processing: a textbook derivation,” *IEEE Signal Processing Letters*, vol. 8, no. 5, pp. 148–150, May 2001.

[113] P. Stoica and A. Nehorai, “Music, maximum likelihood, and cramer-rao bound,” *IEEE Trans. Acoust. Speech and Signal Process.*, vol. 37, no. 5, pp. 720–741, May 1989.

[114] S. Valaee, B. Champagne, and P. Kabal, “Parametric localization of distributed sources,” *IEEE Transactions on Signal Processing*, vol. 43, no. 9, pp. 2144–2153, Sep 1995.

[115] Y. U. Lee, J. Choi, I. Song, and S. R. Lee, “Distributed source modeling and direction-of-arrival estimation techniques,” *IEEE Transactions on Signal Processing*, vol. 45, no. 4, pp. 960–969, Apr 1997.

[116] T. Basikolo, K. Ichige, and H. Arai, “Distributed source doa estimation for more sources than sensors using sparse circular arrays,” in *2017 International Symposium on Antennas and Propagation (ISAP)*, Oct 2017, pp. 1–2.

[117] Q. T. Zhang, “Probability of resolution of the music algorithm,” *IEEE Transactions on Signal Processing*, vol. 43, no. 4, pp. 978–987, Apr 1995.

[118] T. Basikolo, K. Ichige, and H. Arai, “Optimal circular array configuration for underdetermined doa estimation,” in *32nd Symposium on Signal Processing*, Nov. 2017, pp. 101–102.

[119] Y. I. Abramovich and N. K. Spencer, “Detection-estimation of more uncorrelated sources than sensors in noninteger sparse linear antenna arrays,” in *Proceedings of the Tenth IEEE Workshop on Statistical Signal and Array Processing (Cat. No.00TH8496)*, 2000, pp. 99–103.

[120] A. Moffet, “Minimum-redundancy linear arrays,” *IEEE Transactions on Antennas and Propagation*, vol. 16, no. 2, pp. 172–175, Mar 1968.

[121] J. L. Allen and B. L. Diamond, “Mutual coupling in array antennas,” Lincoln Laboratory, M.I.T., Lexington, MA, Technical Rep. 424 ESD-TR-66443, 1966.

[122] P. Ioannides and C. A. Balanis, “Wideband beamforming using circular arrays,” in *Antennas and Propagation Society International Symposium, 2004. IEEE*, vol. 3, June 2004, pp. 2627–2630.

[123] B. Liao and S. C. Chan, “Adaptive beamforming for uniform linear arrays with unknown mutual coupling,” *IEEE Antennas and Wireless Propagation Letters*, vol. 11, pp. 464–467, 2012.

[124] I. Gupta and A. Ksienski, “Effect of mutual coupling on the performance of adaptive arrays,” *IEEE Transactions on Antennas and Propagation*, vol. 31, no. 5, pp. 785–791, Sep 1983.

[125] E. M. Friel and K. M. Pasala, “Effects of mutual coupling on the performance of stap antenna arrays,” *IEEE Transactions on Aerospace and Electronic Systems*, vol. 36, no. 2, pp. 518–527, Apr 2000.

[126] F. Sellone and A. Serra, “A novel online mutual coupling compensation algorithm for uniform and linear arrays,” *IEEE Transactions on Signal Processing*, vol. 55, no. 2, pp. 560–573, Feb 2007.

[127] B. Friedlander and A. J. Weiss, “Direction finding in the presence of mutual coupling,” *IEEE Transactions on Antennas and Propagation*, vol. 39, no. 3, pp. 273–284, Mar 1991.

[128] T. Su, K. Dandekar, and H. Ling, “Simulation of mutual coupling effect in circular arrays for direction-finding applications,” *Microwave and Optical Technology Letters*, vol. 26, no. 5, pp. 331–336, 2000.

[129] M. Wang, X. Ma, S. Yan, and C. Hao, “An autocalibration algorithm for uniform circular array with unknown mutual coupling,” *IEEE Antennas and Wireless Propagation Letters*, vol. 15, pp. 12–15, 2016.

[130] E. BouDaher, F. Ahmad, M. G. Amin, and A. Hoorfar, “Mutual coupling effect and compensation in non-uniform arrays for direction-of-arrival estimation,” *Digital Signal Processing*, vol. 61, pp. 3 – 14, 2017, special Issue on Coprime Sampling and Arrays.

[131] R. Arita, K. Ichige, and H. Arai, “On the accuracy of doa estimation via blind calibration,” in *The 2009 International Symposium on Antennas and Propagation (ISAP 2009)*, Oct. 2009, pp. 1099–1102.

[132] K. M. Pasala and E. M. Friel, “Mutual coupling effects and their reduction in wideband direction of arrival estimation,” *IEEE Transactions on Aerospace and Electronic Systems*, vol. 30, no. 4, pp. 1116–1122, Oct 1994.

[133] M. Wax and T. Kailath, “Detection of signals by information theoretic criteria,” *IEEE Trans. Acoust. Speech and Signal Process.*, vol. 33, no. 2, pp. 387–392, Apr. 1985.

[134] H. Yamada, Y. Ogawa, and Y. Yamaguchi, “Mutual impedance of receiving array and calibration matrix for high-resolution doa estimation,” in *IEEE/ACES International Conference on Wireless Communications and Applied Computational Electromagnetics, 2005.*, April 2005, pp. 361–364.

[135] H. T. Hui, “Improved compensation for the mutual coupling effect in a dipole array for direction finding,” *IEEE Transactions on Antennas and Propagation*, vol. 51, no. 9, pp. 2498–2503, Sep 2003.

[136] J. Dai, D. Zhao, and X. Ji, "A sparse representation method for doa estimation with unknown mutual coupling," *IEEE Antennas and Wireless Propagation Letters*, vol. 11, pp. 1210–1213, 2012.

[137] Z. Q. He, Z. P. Shi, and L. Huang, "Covariance sparsity-aware doa estimation for nonuniform noise," *Digital Signal Processing*, vol. 28, pp. 71–85, May 2014.

[138] T. Basikolo, K. Ichige, and H. Arai, "A note on crlb formulation for nested sparse circular array," *IEICE Communications Express*, submitted, 2017.

[139] S. Chandran, *Advances in Direction-of-Arrival Estimation.* Artech House, London, United Kingdom, 2006.

[140] D. S. Garmatyuk and R. M. Narayanan, "Eccm capabilities of an ultrawideband bandlimited random noise imaging radar," *IEEE Transactions on Aerospace and Electronic Systems*, vol. 38, no. 4, pp. 1243–1255, Oct 2002.

[141] M. Wax, T.-J. Shan, and T. Kailath, "Spatio-temporal spectral analysis by eigenstructure methods," *IEEE Trans. Acoust., Speech, Signal Process.*, vol. 32, no. 4, pp. 817–827, Aug 1984.

[142] Y.-S. Yoon, L. M. Kaplan, and J. H. McClellan, "Tops: new doa estimator for wideband signals," *IEEE Trans. Signal Process.*, vol. 54, no. 6, pp. 1977–1989, June 2006.

[143] M. A. Doron and A. J. Weiss, "On focusing matrices for wide-band array processing," *IEEE Trans. Signal Process.*, vol. 40, no. 6, pp. 1295–1302, Jun 1992.

[144] Z. M. Liu, Z. T. Huang, and Y. Y. Zhou, "Direction-of-arrival estimation of wideband signals via covariance matrix sparse representation," *IEEE Trans. Signal Process.*, vol. 59, no. 9, pp. 4256–4270, Sept 2011.

[145] X. Gan, Luand Wang, "Doa estimation of wideband signals based on slice-sparse representation," *EURASIP Journal on Advances in Signal Processing*, vol. 2013, no. 1, pp. 1–10, 2013.

[146] I. F. Gorodnitsky and B. D. Rao, "Sparse signal reconstruction from limited data using focuss: a re-weighted minimum norm algorithm," *IEEE Transactions on Signal Processing*, vol. 45, no. 3, pp. 600–616, Mar 1997.

[147] J. Hansen(ed.), *Spherical Near-Field Antenna Measurements.* Peter Peregrinus Ltd., London, United Kingdom, 1988.

[148] J. E. Hansen and F. Jensen, "Spherical near-field scanning at the technical university of denmark," *IEEE Transactions on Antennas and Propagation*, vol. 36, no. 6, pp. 734–739, Jun. 1988.

[149] A. C. Newell and C. F. Stubenrauch, “Effect of random errors in planar near-field measurement,” *IEEE Transactions on Antennas and Propagation*, vol. 36, no. 6, pp. 769–773, Jun 1988.

[150] F. D’Agostino, F. Ferrara, C. Gennarelli, R. Guerriero, M. Migliozzi, and G. Riccio, “An innovative spiral scanning over an oblate ellipsoid for nf-ff transformation,” in *2006 Intern. Symposium on Antenna Technology and Applied Electromagnetics*, July 2006.

[151] M. A. Qureshi, C. H. Schmidt, and T. F. Eibert, “Efficient near-field far-field transformation for nonredundant sampling representation on arbitrary surfaces in near-field antenna measurements,” *IEEE Transactions on Antennas and Propagation*, vol. 61, no. 4, pp. 2025–2033, April 2013.

[152] T. Salmern-Ruiz, M. Sierra-Castaer, F. Saccardi, S. Burgos, F. J. Cano-Fcila, and L. J. Foged, “A fast single cut spherical near-field-to-far-field transformation using cylindrical modes,” in *The 8th European Conference on Antennas and Propagation*, Apr. 2014, pp. 2476–2480.

[153] Y. Rahmat-Samii, V. Galindo-Israel, and R. Mittra, “A plane-polar approach for far-field construction from near-field measurements,” *IEEE Transactions on Antennas and Propagation*, vol. 28, no. 2, pp. 216–230, March 1980.

[154] T. K. Sarkar, P. Petre, A. Taaghol, and R. F. Harrington, “An alternate spherical near-field to far-field transformation,” in *Progress in Electromagnetic Research*, vol. 16, Boston, MA, 1997, p. 268284.

[155] Y. Alvarez, F. Las-Heras, and M. R. Pino, “On the comparison between the spherical wave expansion and the sources reconstruction method,” *IEEE Transactions on Antennas and Propagation*, vol. 56, no. 10, pp. 3337–3341, Oct 2008.

[156] Y. A. Lopez, F. L.-H. Andres, M. R. Pino, and T. K. Sarkar, “An improved super-resolution source reconstruction method,” *IEEE Transactions on Instrumentation and Measurement*, vol. 58, no. 11, pp. 3855–3866, Nov 2009.

[157] A. Gati, Y. Adane, M. F. Wong, J. Wiart, and V. F. Hanna, “Inverse source characterization for electromagnetic near field reconstruction and interaction with the environment,” in *2006 IEEE Antennas and Propagation Society International Symposium*, July 2006, pp. 1065–1068.

[158] R. J. Coe and W. L. Curtis, “Effect of lossy earth on antenna gain,” *Radio Science*, vol. 68D, no. 2, pp. 251–255, Feb. 1964.

[159] R. W. P. King and S. S. Sandler, “The electromagnetic field of a vertical electric dipole over the earth or sea,” *IEEE Transactions on Antennas and Propagation*, vol. 42, no. 3, pp. 382–389, Mar 1994.

[160] P. Arnold, “The ”slant” antenna range,” *IEEE Transactions on Antennas and Propagation*, vol. 14, no. 5, pp. 658–659, Sep 1966.

[161] A. Rudge, “Input impedance of a dipole antenna above a conducting half space,” *IEEE Transactions on Antennas and Propagation*, vol. 20, no. 1, pp. 86–89, Jan. 1972.

[162] A. B.-I. T. N. E. Greville, *Generalized Inverses: Theory and Applications.* Springer-Verlag, New York, 2003.

[163] P. Parhami and R. Mittra, “Wire antennas over a lossy half-space,” *IEEE Transactions on Antennas and Propagation*, vol. 28, no. 3, May 1980.

[164] E. Miller, “Analysis of wire antennas in the presence of a conducting half-space. parti. the vertical antenna in free space,” *Canadian J. Physics*, vol. 50, p. 879, Mar 1972.

[165] R. K. Moore and W. E. Blair, “Dipole radiation in a conducting half space,” *Radio Propagation*, vol. 65D, no. 6, pp. 547–563, Nov. 1961.

[166] “Eem (3.4),” 2016. [Online]. Available: http://www.e-em.co.jp

[167] “Altair engineering inc.,,” 2017. [Online]. Available: http://www.altairhyperworks.com/product/FEKO

[168] D. N. Cottingham, “Vehicular wireless communication,” University of Cambridge, Tech. Rep., 2009.

[169] T. Basikolo and H. Arai, “Far field estimation on earth from near field measurements for car windscreen based antenna,” in *2017 IEEE Conference on Antenna Measurements Applications (CAMA)*, Dec 2017, pp. 194–195.

[170] Y. Matsuda, “Estimation of far field on the earth about car antennas by derivation of real source information using near field,” Master’s thesis, Yokohama National University, Japan, 2017.

[171] “Vehicle information and communication system center,” http://www.vics.or.jp/en/.

[172] R. Ehmann, B. Wagner, and T. Weiland, “Farfield calculations for car antennas at different locations,” *IEEE Transactions on Magnetics*, vol. 33, no. 2, pp. 1508–1511, Mar 1997.

[173] F. Khoury and A. Zgheib, *Building a Dedicated GSM GPS Module Tracking System for Fleet Management: Hardware and Software.* CRC Press, 2018.

[174] F. G. Bogdanov, D. D. Karkashadze, R. G. Jobava, A. L. Gheonjian, E. A. Yavolovskaya, N. G. Bondarenko, and C. Ullrich, "Validation of hybrid mom scheme with included equivalent glass antenna model for handling automotive emc problems," *IEEE Transactions on Electromagnetic Compatibility*, vol. 52, no. 1, pp. 164–172, Feb 2010.

[175] K. Nishikawa and Y. Asano, "Vertical radiation patterns of mobile antenna in uhf band," *IEEE Transactions on Vehicular Technology*, vol. 35, no. 2, pp. 57–62, May 1986.

[176] M. N. Abdallah, T. K. Sarkar, M. Salazar-Palma, and V. Monebhurrun, "Where does the far field of an antenna start? [stand on standards]," *IEEE Antennas and Propagation Magazine*, vol. 58, no. 5, pp. 115–124, Oct 2016.

[177] Y. Alvarez, F. Las-Heras, and C. Garcia, "The sources reconstruction method for antenna diagnostics and imaging applications," in *Solutions and Applications of Scattering, Propagation, Radiation and Emission of Electromagnetic Waves*, A. Kishk, Ed. Rijeka: InTech, 2012, ch. 06.

Acknowledgments

When I was a young boy, an idea of doing a PhD never crossed my mind. Through the years, I was privileged to encounter people who challenged my ideas, thoughts, and way of thinking. I have also been motivated by people around me who by all means managed to be strong and happy in the face of so many adversaries. On the center of my motivation, my mum has been central. She has motivated me indirectly through the years and her motivation continues to grow as time passes. This motivation has tremendously sustained me in this long but adventurous journey of advanced studies in a foreign land.

I thank GOD for the gift of life and everything that I need. Through HIS blessings, I managed to get a scholarship at a time where getting one seemed impossible. HE has blessed me with a group of caring people. I would like to express my sincere gratitude to all those who provided warm support and encouragement up to this day.

First and foremost, I would like to express my sincere gratitude to my academic supervisor Professor Hiroyuki Arai. He accepted me as a student in his Lab. He has taught, helped, encouraged, and motivated me throughout the years. Over the years, he has advised and helped me grow in different ways. He made sure I had a balanced lifestyle which kept my motivation levels high. On top of this, he gave me chances to attend local and international conferences where I met various people from academia and industry. This enhanced my writing and communication skills. I was lucky as well to go for internships in companies during my PhD period. I managed to enhance my confidence levels as an engineer.

Secondly, I would like to thank Associate Professor Koichi Ichige. He co–supervised part of my work and we collaborated well on different projects. His approach to academic work left me in awe. His door was always open to talk on academic as well as personal matters. The one on one meetings as well as problem solving during nomikai were just amazing.

I would like to express my appreciation to the committee members which composed of Professor Takehiko Adachi, Professor Toshihiko Baba, Associate Professor Koichi Ichige,

and Associate Professor Nobuhiro Kuga for the time they spared to look into my work, their comments and suggestions were invaluable.

Throughout the years, I have received a lot of support from my family. Financially, emotionally, socially, spiritually, and all sorts of support. My family has been the pillar in all of my work. Your prayers has made it possible for me to reach this far. There were moments you could not understand what I am up to but you guys kept on inquiring and encouraging. Mum, Dad, Lovemore, Charity, Leah, Theresa, Peter, and Emmanuel. You guys rock!

A special appreciation to Atsuko and Mwayi. You guys have been amazing all this time. You have supported me through thick and thin. You provided an ear when I just wanted to talk random stuff, and comfort during my low moments. Your support, encouragement, and the thought of achieving a dream for the future kept me going. Thank you once again.

My studies in Japan could not have been possible without the scholarship I received from Japanese Government (Monbukagakusho Scholarship). I would like to thank MEXT for the scholarship to study Masters as well as PhD in Japan. It has been a worthwhile journey. Thanks also to Japanese embassy in Malawi especially Yuki Asano, who was instrumental in the scholarship process.

I would like to thank NEC C & C foundation for the research grant I received in fiscal year 2017. It was amazing to be one of the recipients of Grants for Non–Japanese Researchers. Within the grant period, I achieved more and the grant helped me to travel to various parts of the world to present my research work. On top of this, I thank NEC Corporation especially the Data Science Research Group for the internship opportunity. The Manager, Toshiyuki Nomura (Information and Media Processing Lab), who made initial contact and showed interest in my work. Dr. Masayuki Ariyoshi, Dr. Kazumine Ogura, Dr. Akihiko Sugiyama and everyone in the group. The atmosphere was welcoming and I enjoyed my time there.

I would like to express my gratitude to Microwave Factory (MWF) for the internship position. MWF President Toshiyasu Tanaka, the team members which composed of Sakurai–san, Yoshida–san, Takaoka–san and many others who made me feel at home. It was an interesting experience to be part of real life engineers, solving real life problems that affect millions of people. I was really surprised and happy by the welcoming environment I received at MWF. The support of MWF staff was invaluable.

Over the years, I have met, talked and received encouragement from a lot of people. Dr. Chomora Mikeka is one of them. He has motivated and treated me like a brother. I am always fascinated by his communication skills. He is in a class of his own. Dr. Levis Eneya encouraged me to advance my mathematical competence. Through his encouragement, my motivation for mathematics peaked. Mr. Mlatho (Physics Technician), who taught me how to repair computers, his daily encouragement of me being an engineer elevated my desire to pursue this career. Dr. J.S.P. Mlatho, Elias Mwakilama, William Nyirenda, Limiton Mhone, your company and various experiences shared over the course of time will never be forgotten.

Living in a foreign land for a long period of time poses a lot of challenges. This has been easier because of the family of Malawians living in Japan. Ankolo (Fred Sato) and Symon Mkandawire, you guys have been special in many ways. Continue being the close family you are. Isaac Yami Chilima, Steven Wandale, Angella Faith Lapukeni and other Malawians in Japan, I truly appreciate the time and moments we shared. This also extends to the African brothers and sisters who became family over the years, Chris Cyusa, and many more people.

In the university especially Arai Lab, I was privileged to have shared interesting moments with a lot of people. Dr. Rohani Bakar, you hold a very special place in my heart. I can not thank you enough. Since my arrival in the Lab, you have taken care of me in different ways. We have shared ideas, eating out, random talks and your trip to Malawi left me speechless. Tran Thi Lan, it has been a great 3 years doing the PhD together. Goodluck in your future endeavors. Dr. Daisuke Uchida, Dr. S. Wang, Gu–san, Okura–san, and many other OB from Arai Lab. A special thank you to the current Arai Lab members for the support you have rendered in various ways. Hiroshi Hashiguchi, Yuka Shinozaki, M2, M1, and B4 members.

It Hasn't Been An Easy Road

Thomas Basikolo

July, 2018

List of Publications and Awards

Published Work

Journal Papers

1. Thomas Basikolo, Koichi Ichige, and Hiroyuki Arai, "A Novel Mutual Coupling Compensation Method for Underdetermined Direction of Arrival Estimation in Nested Sparse Circular Arrays," in *IEEE Transactions on Antennas and Propagation*, Vol. 66, No. 2, pp. 909–917, Feb. 2018.

2. Thomas Basikolo, Koichi Ichige, and Hiroyuki Arai, "Nested Circular Array and Its Concentric Extension for Underdetermined Direction of Arrival Estimation," in *IEICE Transactions on Communications*, Vol.E101-B, No.4, pp. 1076–1084, Apr. 2018.

3. Thomas Basikolo, Koichi Ichige, and Hiroyuki Arai, "A Note on CRLB Formulation for Underdetermined DOA Estimation in Circularly Configured Planar Arrays," in *IEICE Electronics Express*, Vol. 15, No. 6, pp. 1–6, Mar. 2018.

4. Thomas Basikolo and Hiroyuki Arai, "APRD-MUSIC Algorithm DOA Estimation for Reactance based Uniform Circular Array," in *IEEE Transactions on Antennas and Propagation*, Vol. 64, No. 10, pp 4415–4422, Oct. 2016.

International Conferences

1. Thomas Basikolo, Hiroyuki Arai, Satoshi Hori, and Shinya Iwanaga, "Far Field from Hemispherical Near Field Measurements for Vehicular Mounted Antenna," *2018 International Symposium on Antennas and Propagation (ISAP2018),* Busan, South Korea, Oct., 2018.

2. Thomas Basikolo, Hiroyuki Arai, Satoshi Hori, and Shinya Iwanaga, “Reconstruction of Far Field Radiation Pattern from Hemispherical Near Field Measurements,” *2018 IEEE International Workshop on Electromagnetics: Applications and Student Innovation Competition (iWEM),* Nagoya, Japan, Aug., 2018.
3. Thomas Basikolo and Hiroyuki Arai, “Far Field Estimation on Earth from Near Field Measurements for Car Windscreen based Antenna,” *2017 IEEE Conference on Antenna Measurements and Applications (CAMA),* Tsukuba, Japan, Dec. 2017.
4. Thomas Basikolo, Koichi Ichige, and Hiroyuki Arai, “Distributed Source DOA Estimation for More Sources than Sensors Using Sparse Circular Arrays,” *2017 International Symposium on Antennas and Propagation (ISAP2017),* Phuket, Thailand, Oct. 2017.
5. Thomas Basikolo, Koichi Ichige, and Hiroyuki Arai, “Underdetermined DOA Estimation in the Presence of Mutual Coupling for Sparse Circular Array,” *2017 IEEE International Symposium on Antennas and Propagation and USNC-URSI Radio Science Meeting,* San Diego, California, Jul. 2017.
6. Thomas Basikolo, Koichi Ichige, and Hiroyuki Arai, “Underdetermined DOA Estimation for Uniform Circular Array Based on Sparse Signal Reconstruction,” *2016 International Symposium on Antennas and Propagation (ISAP2016),* Okinawa, Japan, Oct. 2016, pp. 1012-1013.
7. Thomas Basikolo, Koichi Ichige, and Hiroyuki Arai, “Direction of Arrival Estimation for Quasi-Stationary Signals using Nested Circular Array,” *2016 4th International Workshop on Compressed Sensing Theory and its Applications to Radar, Sonar and Remote Sensing (CoSeRa),* Aachen, Germany, Sept. 2016, pp. 193-196.
8. Thomas Basikolo and Hiroyuki Arai, “A compact reactance based UCA antenna system for null steering and DOA estimation,” *2016 IEEE International Workshop on Electromagnetics: Applications and Student Innovation Competition (iWEM),* Nanjing, China, May, 2016. (**Best Paper Award**)

Local Conferences

1. Thomas Basikolo, Koichi Ichige, and Hiroyuki Arai, “Optimal Circular Array Configuration for Underdetermined DOA Estimation,” *32nd Symposium on Signal Processing,* Morioka, Japan, Nov. 2017.
2. Thomas Basikolo and Hiroyuki Arai, “Automotive Windscreen Antenna Far Field Estimation from Near Field on Earth Ground,” *IEICE Society Conference, B-4-9,* Tokyo City University, Tokyo, Sept. 2017.

3. Thomas Basikolo, Koichi Ichige, and Hiroyuki Arai, "Sparse Signal Reconstruction based Underdetermined Direction of Arrival Estimation," *IEICE General Conference, B-1-129,* Meijo University, Nagoya, Mar. 2017.
4. Thomas Basikolo and Hiroyuki Arai, "Blind Adaptive Null Forming Based on Maximum Moment Criterion Orthogonal Constant Modulus Algorithm for Reactance based UCA Antenna," *IEICE General Conference, B-1-182,* Kyushu University, Kyushu, Mar. 2016.
5. Thomas Basikolo and Hiroyuki Arai, "DOA Estimation with Optimal Reactance values for Reactance based UCA Antenna System," *IEICE Society Conference, B-1-52,* Tohoku University, Sendai, Sept. 2015.
6. Thomas Basikolo and Hiroyuki Arai, "Performance Analysis of DOA Estimation by Active Ports Reactance Domain Music Algorithm," *IEICE General Conference, B-1-188,* Ritsumeikan University, Kusatsu, Mar. 2015.
7. Thomas Basikolo and Hiroyuki Arai, "DOA Estimation using Reactance Based Uniform Circular Array Antenna," *IEICE Society Conference, B-1-171*, Tokushima University, Tokushima, Japan, Sept. 2014.

The Other Research Activities

Internship

1. Internship at NEC Data Science Research Laboratories, Jun. 2017 - Aug. 2017.
2. Internship at Microwave Factory, April, 2016.

Awards

1. Best Student Award, 2017 IEEE AP-S Japan Student Award.
2. NEC C& C Foundation, Recipient of Grants for Non-Japanese Researchers -2017 Fiscal Year, 2017 - 2018.
3. Best Paper Award, 2016 IEEE International Workshop on Electromagnetics (iWEM 2016), Nanjing, China, May, 2016.